

DISSERTATION

Multi-Scale Modeling and Simulation of Metallic Foams

ausgeführt zum Zwecke der Erlangung des akademischen Grades eines
Doktors der technischen Wissenschaften unter der Leitung von

O.Univ.Prof. Dipl.-Ing. Dr.techn. Franz G. RAMMERSTORFER

E317

Institut für Leichtbau und Flugzeugbau

eingereicht an der Technischen Universität Wien

Fakultät für Maschinenbau

von

Dipl.-Ing. Thomas DAXNER

Matrikelnummer: 8825624

Rembrandtstraße 30/3/40

A-1020 Wien

Wien, im Juli 2002

Thomas Daxner

Kurzfassung

Metallschäume sind zelluläre Metalle, die als Leichtbauwerkstoffe stetig an Bedeutung gewinnen. Ihre hervorstechendsten mechanischen Eigenschaften sind hohe spezifische Steifigkeit bzw. Festigkeit sowie ein hohes Stoßaufnahmevermögen, welches eine Folge ihrer hohen Verformbarkeit darstellt. Metallschäume bestehen aus einem Skelett aus solidem Material, welches entweder schwammartig aus verbundenen Stegen oder schaumartig aus geschlossenen Zellen aufgebaut ist. Der hohe Hohlraum-Anteil macht sie zu hochgradig inhomogenen Materialien und führt zu thermomechanischen Eigenschaften, welche sich deutlich von jenen massiver Metalle unterscheiden.

Da der schwammartige bzw. geschlossenporige mikrostrukturelle Aufbau die mechanischen Eigenschaften von Metallschaum wesentlich mitbestimmt, wurden in der vorliegenden Arbeit Simulationen des mechanischen Verhaltens auf der mikrostrukturellen Ebene durchgeführt, wobei sowohl analytische als auch Finite Elemente Modelle, insbesondere in Verbindung mit Einheitszellen-Modellierungsstrategien Anwendung fanden. Die Untersuchungen geben Einblick in die lokalen Deformations- und Lastumlagerungs-Mechanismen sowie deren Auswirkung auf das effektive mechanische Verhalten des Metallschaums, repräsentiert beispielsweise durch die Gestalt der effektiven Fließfläche oder das effektive Verhalten unter mehrachsiger Belastung. Es werden sowohl vorteilhafte als auch nachteilige Topologien und Werte von mikrogeometrischen Parametern identifiziert und damit wertvolle Erkenntnisse für das Werkstoffdesign und die Entwicklung neuer Metallschäume gewonnen.

Auf der Längenskala von Werkstoffproben und Bauteilen, die zwei oder drei Größenordnungen größer sind als einzelne Schaumzellen, wurde das effektive Werkstoffverhalten simuliert, wobei zwei im Finite Element Programm ABAQUS implementierte Stoffgesetze an Hand der Simulation von Aufprallversuchen mit Bezug zum Insassenschutz in Automobilen evaluiert wurden. Die Untersuchungen zeigen unter anderem das Vorhandensein von optimalem Energieaufnahmeverhalten - im Sinne einer möglichst hohen Energieaufnahme bei niedrigem Spitzenkraftniveau - bei einer bestimmten, von der Art des Metallschaums abhängigen, effektiven Schaumdichte.

Auf derselben Längenskala wurde ein Algorithmus zur Optimierung der Dichteverteilung in Metallschaum-Strukturen entwickelt und zur Berechnung von steifigkeits- und festigkeitsoptimierten Bauteilen herangezogen. Der Ansatz, den Optimierungsalgorithmus als Materialgesetz im Sinne eines selbstadaptierenden Werkstoffes in Analogie zu lebendem Gewebe (Knochen) zu implementieren, bringt starke Geschwindigkeitsvorteile gegenüber bestehenden Methoden.

Eine Untersuchung der Auswirkungen von mesoskopischen Inhomogenitäten in der Dichteverteilung auf das statische und dynamische Stauchverhalten von Metallschaum-Körpern rundet das Spektrum der Arbeit ab. Hier wurden unter anderem dynamische Effekte wie Wellenausbreitungsphänomene untersucht, und wertvolle Rückschlüsse für die Auslegung von stoßabsorbierenden Metallschaum-Strukturen gezogen.

Abstract

The subjects of the present thesis are metallic foams, which have entered the stage of practical application, their most important mechanical properties being high energy absorption capacity as well as high specific strength and stiffness. Metallic foams consist of a solid skeleton formed by struts and/or cell walls and a high volume fraction of voids, making them highly inhomogeneous materials. Their heterogeneity leads to thermomechanical responses, that are markedly different from those of bulk solids, and gives rise to material properties that have made cellular materials attractive for many engineering applications. It also presents an obvious target for modeling studies aimed at gaining an improved understanding of the mechanical behavior of cellular materials and of structures made of them.

In the present thesis, simulations of the mechanical responses of cellular metals are carried out at different length scales. In micromechanical approaches, their inhomogeneous structure is accounted for at the level of individual cells, cell walls, struts, and vertices. At this length scale, discrete geometrical models of the cellular microstructure are examined with the Finite Element method in combination with unit cell approaches, providing information on the local deformation and load transfer behavior. The micromechanical behavior is correlated to the mechanical behavior at the structural level, for example, in the form of overall yield surfaces or the effective behavior under multiaxial loading conditions. Advantageous and detrimental topologies and values of microgeometrical parameters are identified for supporting materials design and development.

At the macromechanical level, that is, the level of samples and components that are two or three orders of magnitude larger than the typical size of individual cells, only the overall thermomechanical behavior is accounted for. Constitutive models for metallic foams, which are implemented in the Finite Element code **ABAQUS**, are evaluated with regard to their performance in simulating impact tests related to passenger protection in motor vehicles. Among other results, the investigation shows the existence of optimum crash-absorption behavior, described by high energy absorption capability at a low peak force, for a well-defined foam-specific apparent density.

At the same macroscopic level, an algorithm for the optimization of foam density distributions in components made of or containing metallic foam is presented along with examples of structures that are improved with regard to strength or stiffness. The implementation of the algorithm as a material law, which is self-adapting in analogy to living tissue (bone), yields distinct speed benefits in comparison to existing methods.

In addition, questions involving the spatial variations or gradients of cell sizes and shapes within a given sample or structure are studied at length scales that are intermediate between microscale and macroscale. A section of the present thesis is devoted to the influence of mesoscopic inhomogeneities on the mechanical behavior of bodies made of metallic foams under crush and crash loads.

Acknowledgements

This thesis was prepared in the course of my employment at the Institute of Lightweight Structures and Aerospace Engineering (ILFB) at the Vienna University of Technology. As the head of the Institute and the advisor of the thesis, Prof. Dr. F.G. Rammerstorfer had the strongest, and always positive influence on my work. I am deeply indebted to him for his support and encouragement as well as for his being a great example of a generous and kindhearted person.

I also want to express my gratitude to Prof. Dr. H.P. Degischer, who, both as the co-advisor of the thesis and in many past discussions, provided valuable input and insight on the practical aspects of foam production and testing. Along with Prof. Degischer, I want to thank the members of the Institute of Materials Science and Testing of Vienna University of Technology, in particular Dr. B. Kriszt, Ing. K. Faure, Dr. B. Foroughi, as well as DI A. Kottar for sharing information in many valuable discussions.

Additionally, I would like to express my thanks to Prof. Dr. H.J. Böhm, who did not fail to impress me with the thoroughness and the quality of his reviews of the present text. His readiness to provide assistance and spot-on auxiliary information must not pass unnoticed. The same applies for the technical competence and the support of Ing. G. Schneider, the system administrator of the ILFB, who can be trusted to solve any technical problem within minutes, and, thus, has provided an optimal working environment for the Institute.

In addition to the named persons, special thanks go to all the former and current colleagues at the ILFB for the valuable discussions and for the many enjoyable hours we spent together in our spare time. They are all both great engineers and great friends.

Many of the results presented in this contribution were obtained in connection with the Brite/EURAM project “EAMLIFe” (BE96–3605). The funding of this project by the Commission of the European Union is gratefully acknowledged. I would also like to thank the Institut für Verbundwerkstoffe (IVW) in Kaiserslautern, Germany, and, in particular, Mr. Ralf Denzer, for the excellent collaboration in the course of the “EAMLIFe” project.

An informal “Thank you!” goes out to the creators of the Unix tools `locate` and `grep`, to Stephen Wolfram for creating `Mathematica`, and to the creators of `LaTeX`.

Furthermore, I do not want to miss the opportunity to thank my parents, Ing. Karl Daxner and Mrs. Elfi Daxner, for their ongoing care and selfless support of the whole family! Last but not least, I want to express my heartfelt thanks to my fiancée, Miss Alexandra Mikedaki, for being an extraordinary partner, friend, and companion.

Vienna, July 2002

Für meine Großmutter
Frau Margarethe Öchsel

Contents

1	Introduction	1
1.1	Modeling and Simulation for Material Design	3
1.2	Modeling and Simulation for Component Design	5
2	Micromechanical Modeling and Simulation	7
2.1	Introduction	7
2.2	Classification of Microgeometries	8
2.3	Methods for Micromechanical Modeling	12
2.4	Influence of Material Distribution in the Cell Walls	28
2.5	Influence of Non-Uniform Cell Wall Thickness	47
2.6	Influence of Wavy and Curved Cell Walls	49
2.7	Influence of Irregular Vertex Positions	54
2.8	Interaction of Cells of Different Sizes	56
2.9	Influence of Holes and Solid-Filled Cells	64
2.10	Influence of Fractured or Missing Cell Walls	64
2.11	Overall Yield and Collapse Surfaces	66
2.12	Fracture Simulations for Metallic Foams	72
2.13	Summary and Outlook	76
3	Modeling of Mesoscopic Density Inhomogeneities	77
3.1	Introduction	77
3.2	Experimental Data	80
3.3	Method	81

3.4	Results	86
3.5	Summary	106
4	Macroscopic Modeling of Metallic Foams	109
4.1	Introduction	109
4.2	Nonlinear Macroscopic Behavior of Metallic Foams	110
4.3	Constitutive Modeling	117
4.4	Low Energy Impact on Metallic Foam Paddings	128
4.5	Design Optimization with Metallic Foams	150
5	Conclusions	171
	Bibliography	173

Chapter 1

Introduction

Cellular materials are a class of materials that can be found in nature and in technical applications alike, see Figure 1.1. Their cellular structure gives rise to excellent weight-specific properties, such as high specific stiffness and high specific strength. Beyond these most obvious advantageous properties of cellular materials, a range of additional beneficial properties such as excellent deformability, formability, insulation, small absolute density and, therefore, good buoyancy, makes them suitable for a multitude of thermo-structural applications like packaging, cores in lightweight structural sandwich panels, thermal insulations, crush and crash elements, and many more.

Since cellular materials consist of an interconnected network of solid struts or plates their overall properties scale with those of the solid bulk material. Hence, the creation of cellular materials with a solid phase of high (specific) stiffness and strength is of special interest. Solid metals and, in particular, aluminum provide the required properties, and the design and production of metallic foams is gaining momentum. In addition to their advantageous mechanical properties metallic foams show good thermal stability, high fire retardance and considerable potential for recycling. By various production routes, they can be manufactured both in simple shapes like panels, as well as in more complex shapes, see Figure 1.1 (right). Owing to their metallic bulk phase, they are compatible with metal face sheets, stimulating the design of integral structures and lost cores for advanced casting technologies.

Metallic foams are produced both in the form of spongy, open-cell foams, see Figure 1.2, and in the form of closed-cell foams, compare Figure 1.3. A special class of cellular metals are metal honeycombs, which can be used as core materials in high-performance sandwich panels.

The modeling and simulation of cellular metals is a field of research that has drawn considerable interest from researchers, research groups and industry, from foam manufacturers to industrial end-users. Two major directions of research can be distinguished, the “design” of metallic foams on the one hand and the design of components made of cellular metals

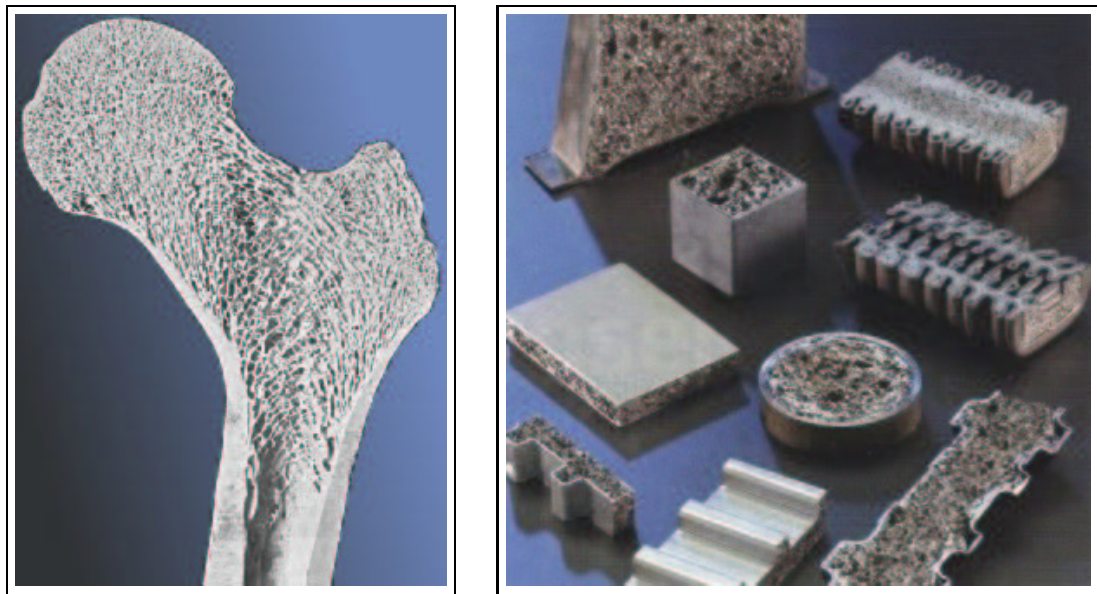


Figure 1.1: Cross-section of the head of a human femur (left) and samples of shell structures with in-situ foam cores (right, courtesy of LKR).

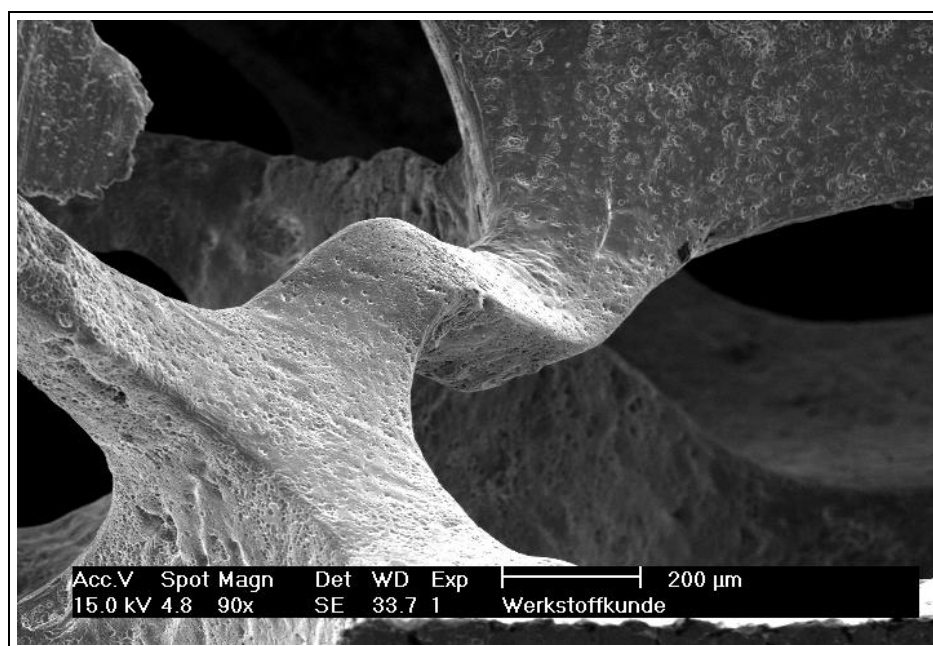


Figure 1.2: REM image of a bent strut in an open-cell metallic foam; (image courtesy of Institute of Materials Science and Testing, Vienna University of Technology.)

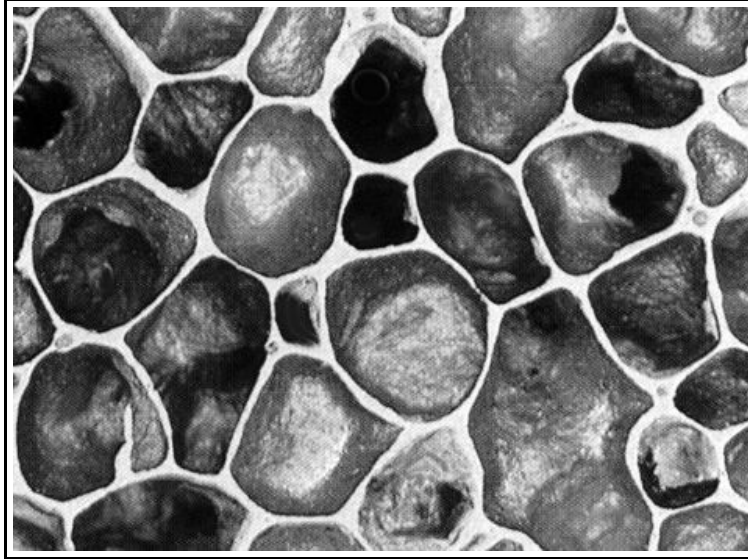


Figure 1.3: Microscopic cross-section through a closed-cell aluminum foam (image courtesy of Neuman Aluminium).

on the other hand.

1.1 Modeling and Simulation for Material Design

From the point of view of the manufacturers, the design of mechanically efficient metallic foams is the paramount aspect of foam modeling and simulation, the aim being the development of “optimum” cellular metals. The most important design variables are production technologies and the choice of the metal constituting the solid phase of the foam. Besides the apparent mass density and the properties of the metal, the mechanical behavior of metallic foams is determined by the geometrical arrangement of voids and solid regions in the material, which will be referred to as the microgeometry in the following. Consequently, a considerable number of studies has aimed at exploring the connections between the microgeometry and the mechanical properties of cellular materials and thus belong to a research field known as micromechanics of materials.

At the length scale of the voids, the deformation of cellular materials tends to be dominated by local mechanisms (Figure 1.4) that must be accounted for in any modeling effort. Because detailed descriptions of the microgeometries of large structures or components made of foam are far in excess of present capabilities, the most fruitful approaches for simulating the thermomechanical behavior of metallic foams have aimed at studying representative regions of appropriate model materials. Most commonly, actual foams are approximated by periodic microgeometries that can be described via unit cells subjected to appropriate

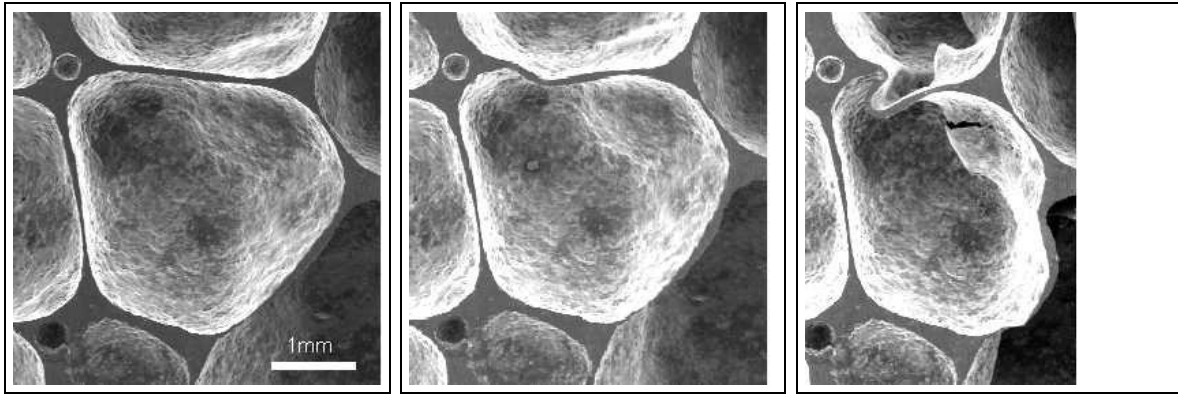


Figure 1.4: Deformation sequence of a wrought alloy aluminum foam (*ALULIGHT*TM) showing post-buckling collapse of a cell wall oriented in deformation direction; images courtesy of Institute of Materials Science and Testing, Vienna University of Technology [61].

boundary conditions. Alternatively, a geometrically detailed microregion may be embedded in a larger region for which a much simpler description is employed, leading to embedded cell models. A discussion of such micromechanical approaches will be presented in Chapter 2.

Microgeometrical models covering a wide range of complexity can be studied with the above methods to give predictions for the overall mechanical behavior of metallic foams and link it to specific local deformation processes. In addition, microscale geometrical imperfections such as curved cell walls can be introduced in a controlled way and assessed for their influence on the macromechanical material response, making it possible to isolate the influence of individual parameters. It has been found difficult, however, to make fully quantitative predictions on the basis of micromechanical simulations, the main reason being the high geometrical complexity of actual foams and the dearth of reliable data on the in-situ material behavior of the metallic phase. Nevertheless, micromechanical approaches have provided important instruments for gaining a better understanding of the thermomechanical behavior of metallic foams, see Chapter 2.

If the mean cell size or the effective mass density of the foam exhibits spatial variations or gradients over a sample or component, additional information can be obtained by explicitly considering length scales that lie between the micro- and macroscales. Such mesomechanical studies are described in Chapter 3.

1.2 Modeling and Simulation for Component Design

Designers of components made of metallic foams (Figure 1.1, right) are interested in easy-to-use methods for describing the constitutive behavior of these materials, for example in the form of constitutive material laws for use with general purpose Finite Element codes. For such purposes it is neither possible nor desirable to account for details of the foams' microgeometry at every position in the component. Instead, the material behavior of the foam is described in terms of a (fictitious) equivalent homogeneous material. Such macroscopic constitutive models may be derived from micromechanical studies by homogenization, or they may take the form of phenomenological macroscopic descriptions that employ material parameters which have to be obtained from experiments. Because metallic foams typically show a limited elastic range, such constitutive models have to be nonlinear for general application.

For some purposes full constitutive descriptions are not required and material characterization can provide the necessary information. This can take the form of experimentally based relations, for example in the form of stress versus strain relations parametrized by the effective mass density of the foam. Alternatively, micromechanical reasoning may be used to derive generic mathematical relationships, which can then be fitted to experimental results and provide physically based regression formulae.

Knowledge of the effective elastic stiffness on the continuum level is sufficient for linear stress analysis, where the foam is treated as a homogeneous, linear elastic solid. Depending on the complexity of the problem, such structural analyses can either be performed analytically or numerically, for example by using the Finite Element method. If only the macroscopic stresses within the component are of interest, the knowledge of the homogenized material properties (in this case the tensor of elasticity) will be sufficient. These macroscopic stresses have to be assessed with respect to failure of the structure by yielding, fracture or buckling, so that additional information in the form of macroscopic strength data is required.

More sophisticated structural analysis must take into account the nonlinear behavior of metallic foams; this is an absolute necessity when large strains are present, for example in crushing or crash situations, compare Figure 1.5. Here, incremental macroscopic constitutive laws, that is, relationships between increments of stresses and strains, must be available to allow the use of typical numerical analysis tools. Several constitutive material laws describing the overall behavior of cellular metals have been proposed and applied in the simulation of components consisting of or containing metallic foams. Obviously, the selection of a particular constitutive law is governed by the number of material parameters it requires and by the effort necessary for calibrating them by experiments or via micromechanical studies. Because they are based on the use of an equivalent homogeneous continuum, macroscopic constitutive laws should only be used for studying components or samples that are considerably larger (and thicker) than the typical cell size of the foam. Macroscopic constitutive laws for foams are the focus of Chapter 4, where the advantageous

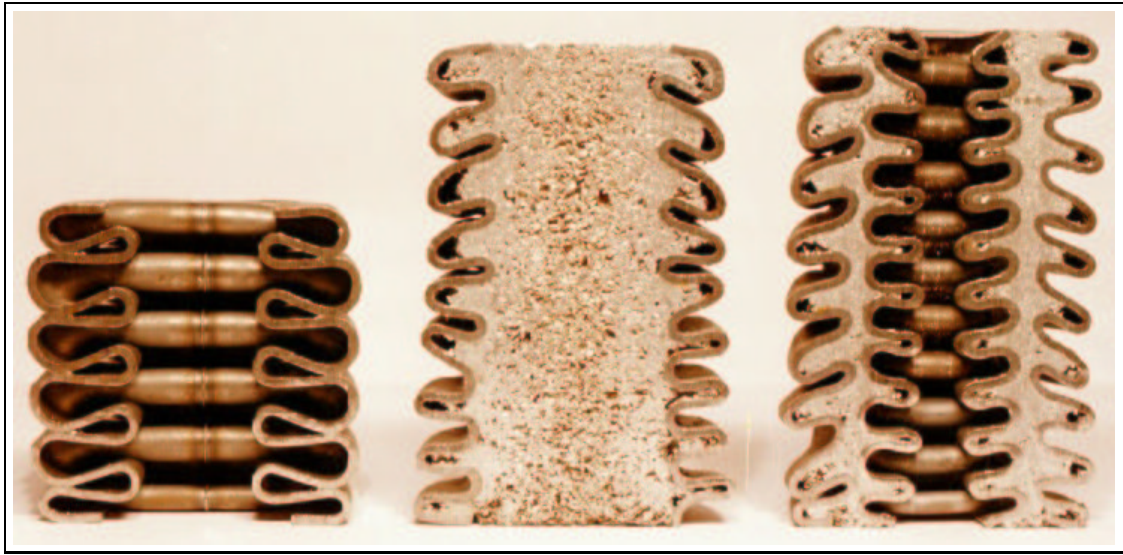


Figure 1.5: Crushed square steel profiles in empty monotubal (left), foam-filled monotubal (center) and foam-filled bitubal design (right); from [100].

use of metallic foams in energy absorbing structures, and modeling strategies for assessing crashworthiness are discussed.

Because metallic foams show some potential for controlled spatial variation of their effective mass density and, as a consequence, of their mechanical properties, they offer the possibility of designing functionally graded cellular materials in analogy to bone tissue (Figure 1.1, left). Some considerations pointing in this direction can be found in Section 4.5. Considering all the facts mentioned above, the structural analysis of components made of or employing metallic foams is likely to become a standard procedure in Finite Element simulations. Chapter 4 will present some steps in this direction.

Chapter 2

Micromechanical Modeling and Simulation of Metallic Foams

2.1 Introduction

From the point of view of micromechanical modeling, cellular metals fall into three groups: honeycombs, which can be studied by two-dimensional models, open cell foams, the solid scaffold of which is dominated by beam-like members, and closed cell foams, in which membrane- or shell-like cell walls are present. All of these materials typically show a limited elastic range, and their mechanical behavior tends to be dominated by local deformation mechanisms such as bending, buckling, plastic yielding, and fracture of cell struts and walls. These deformation mechanisms, in turn, are highly sensitive to details of the microgeometry, which, in practice, may be quite regular for some honeycombs, but tends to be complex and highly non-uniform in the case of metallic foams.

The mean field and Hashin–Shtrikman-type methods, that play an important role in continuum micromechanics of composites and materials with small volume fractions of pores, compare [86], have seen only limited use for cellular materials. Hashin–Shtrikman upper bounds for the elastic moduli can be evaluated for macroscopically isotropic cellular materials by prescribing vanishing stiffness for the void phase (the lower bounds, however, vanish trivially). Typically, the elastic moduli of metallic foams lie considerably below these upper bounds, but for honeycombs it was possible to identify microgeometries that realize the upper bounds, see [112].

As a consequence, most micromechanical studies of cellular materials in general and of metallic foams in particular have been based on discrete microgeometrical models. Due to the high geometrical complexity and irregularity of actual metallic foams such model microgeometries tend to be highly idealized. One common modeling strategy is based on studying periodic “model foams”, the thermomechanical behavior of which is fully described by appropriate unit cells, see Section 2.3.2. Alternatively, cells or geometrical

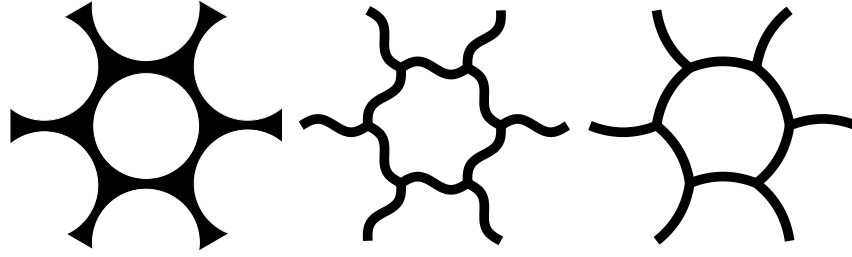


Figure 2.1: Schematic representation of imperfections at the level of individual cell walls: Plateau borders (left), corrugated cell walls (center) and curved cell walls (right).

units may be studied in isolation without requiring them to be space filling. A third type of approach employs a geometrically fully resolved microregion (“core”) that is embedded in a much larger region in which the microgeometry is not resolved and smeared-out material behavior is used (“embedded cell models”). Discrete microgeometrical modeling approaches facilitate the controlled variation of selected geometrical parameters in order to assess their effect on the mechanical response. These modeling strategies, which have well-established equivalents in continuum micromechanics of composite materials, allow studying both the local deformation mechanisms and the corresponding overall behavior, which can be obtained by homogenization.

2.2 Classification of Microgeometries

This section represents an attempt at systematically classifying the most important types of cellular microgeometries that have been or may be used for unit cells or in the core regions of embedded cell models. The main classification criteria are the dimensionality (two-dimensional versus three-dimensional) and the microscale morphology (regular periodic, perturbed periodic, random and “real structure” arrangements) of the geometrical models.

Two-dimensional discrete microgeometry models are directly applicable for investigating the mechanical behavior of honeycombs. Due to their relative simplicity they have also been used as tools for studying metallic foams in a qualitative way (in the following planar models are generally referred to as “honeycombs”). The “baseline” regular morphology are periodic hexagonal honeycombs, which show in-plane elastic isotropy and, in the context of two-dimensional liquid foams, may be viewed as surfaces of minimal surface energy. Because hexagonal honeycombs (albeit of reduced symmetry) are applied routinely as sandwich cores, cellular metals of this type have been closely studied both experimentally and analytically, compare [80]. Alternative regular microgeometries for two-dimensional cellular materials were also discussed in the literature [14; 40].

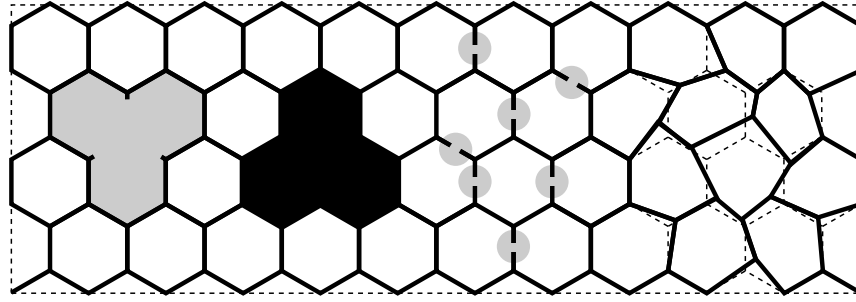


Figure 2.2: Schematic representation of a honeycomb containing imperfections in the form of a large hole, cells filled with material, fractured cell walls and geometrical perturbations (from left to right).

In contrast to the regular microgeometry of idealized models, real cellular metals are subject to morphological defects that tend to lead to softer and weaker mechanical responses. Periodic two-dimensional models have been an important means for studying the influence of imperfections such as curved or corrugated cell walls [11; 39; 107], perturbed cell shapes [42], and non-uniform material distribution between cell walls and cell vertices (Plateau borders) [106] as sketched in Figure 2.1. Within such honeycomb models local defects can be introduced into cell walls [11; 12; 95], individual cell walls can be eliminated [12; 104], vertices and the adjoining cell walls can be removed to leave large voids in the honeycomb structure [12; 87], and cells or groups of cells can be filled with solid material to assess the influence of nodal inclusions [12], compare Figure 2.2.

In addition, periodic arrangements of large and small cells [17] may be used to study influences of relative cell sizes.

Random honeycomb arrangements can be generated on the basis of Voronoi tessellations [11; 95; 104; 105], which may be interpreted in terms of geometries that emerge when the fronts of bubbles growing with the same linear rate from randomly distributed nuclei meet. A different type of random microgeometry are Johnson–Mehl cells [63], a tessellation that corresponds to cases where new cell nuclei are added while others are in the process of growing.

Finally, two-dimensional microgeometries may be based on micrographical sections of metallic foams [20]. Such “real structure” unit cells typically require some manipulation in the boundary regions in order to achieve periodicity.

Planar models obviously can emulate the behavior of three-dimensional microgeometries only to a limited extent (note, for example, that in the two-dimensional case there are no equivalents of open cell and closed cell topologies). Accordingly, there has been growing research interest in three-dimensional models of cellular materials despite their high demands on computational resources. In the case of open cell foams, beam theory or beam

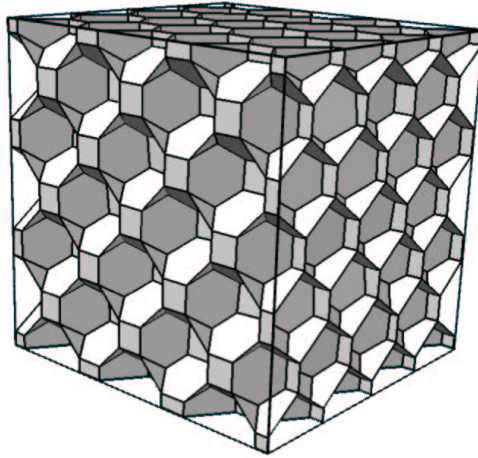


Figure 2.3: Regular tetrakaidecahedral model for a closed cell foam [20].

Finite Elements provide comparatively inexpensive solutions for describing the mechanical behavior of the solid skeleton. Micromechanical studies of closed cell foams, however, require an appropriate modeling of the cell faces and, consequently, shell theories must be invoked or shell elements must be used, which increases the complexity of the simulations.

Perfectly regular three-dimensional periodic microgeometries can be generated from space filling regular polyhedra, leading to models based on cubes, rhombic dodecahedra and regular tetrakaidecahedra (Kelvin structures). None of these arrangements is elastically isotropic, but tetrakaidecahedral geometries have the advantage of giving face and edge counts per cell that are similar to the average values found in actual polyhedral foams [116]. Accordingly, tetrakaidecahedral microgeometries have been widely used for studying open cell [1; 115] and closed cell [20; 71] foams, compare Figure 2.3. Somewhat more complex microgeometries were also proposed in the form of regular arrangements of two populations of polyhedral voids of different size [94].

Most three-dimensional studies of the effects of imperfect periodic cellular arrangements have been based on closed cell tetrakaidecahedral microgeometries subjected to various kinds of perturbations. Unit cell models of varying levels of complexity were used to study the effects of Plateau borders [106], of curved or corrugated cell walls [39; 107], of perturbed cell shapes [20; 42], and of cell walls that have randomly assigned thicknesses [41].

In analogy to two-dimensional models, Voronoi diagrams may be used to generate irregular three-dimensional microgeometries for open cell [103; 121] and closed cell foams [22; 42; 59]. Because they typically require large numbers of shell elements, investigations of this type tend to be computationally expensive.

Three-dimensional real structure models of cellular materials can be generated on the basis of microtomographical data, each voxel being typically mapped to a Finite Element. Anal-

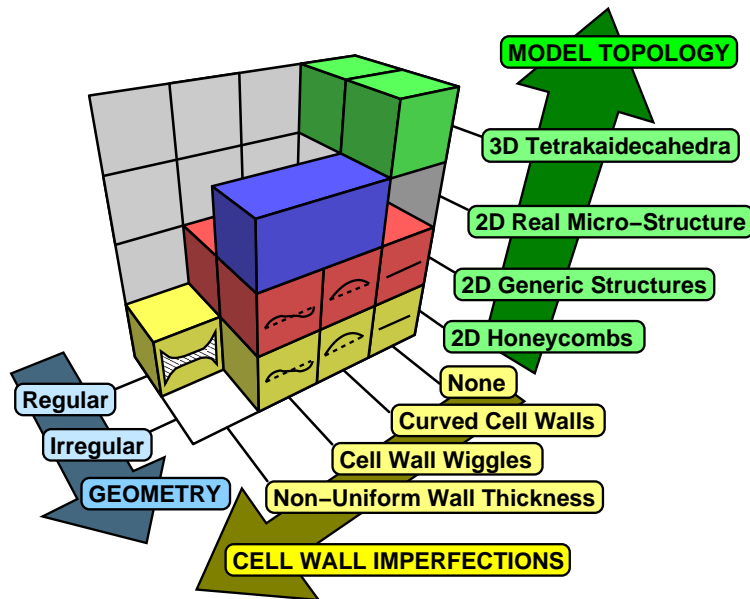


Figure 2.4: Classification of micro-mechanical simulation models.

yses of this kind were pioneered by groups studying the mechanical behavior of cancellous bone [54; 75], which may be viewed as an open cell foam, and were recently also reported for closed cell metallic foams [65]. This modeling strategy typically gives rise to ragged surfaces of the solid skeleton of cellular materials, which may lead to difficulties in analyses involving large deformations and large strains.

As was outlined in this section, microstructural models for cellular materials can be classified according to their topology, the regularity of their geometry as well as the nature and the degree of their imperfection(s). In compliance with the above criteria, Figure 2.4 sketches the classification of the microstructural models developed for this thesis. At present it is not feasible to examine the combined influence of all parameters that influence the microstructural geometry. Therefore, the influence of individual imperfections, such as curved cell walls, is generally studied in isolation. Models following this principle are symbolized by individual cubes in Figure 2.4. If the prediction of the effective behavior of real metallic foams is the aim of a microstructural simulation, it is reasonable to include as many natural imperfections as possible in the model. An example for this category of models is the 2D “real structure” model presented in Section 2.11.

2.3 Methods for Micromechanical Modeling

2.3.1 Analytical and Semi-Analytical Methods

When a sufficiently high degree of abstraction is introduced into discrete microgeometry models of cellular materials, the mathematical description of the micromechanical system becomes accessible to analytical methods, and closed-form solutions [118] can be obtained. For cellular 2D structures and open-cell 3D foams the application of linear elastic beam theory is a typical analytical modeling strategy.

A by now classical example of an analytical modeling approach is the work of Gibson and Ashby [33], who based their models on single cells, that do not necessarily give rise to space-filling periodic arrangements, and developed a large body of results on the elastic deformation, elastic buckling, plastic collapse, brittle fracture, visco-elastic deformation, creep, and creep buckling of honeycombs, open cell and closed cell foams, see also [7; 31]. Developments of this class of models have included, among others, large deformation analyses of the buckling collapse of honeycombs [120] and studies on the power-law creep of honeycombs [5].

Analytical formulae for the elastic behavior of a number of perfectly regular periodic cellular geometries were given by Grenestedt [40], and scaling relations for arrangements of this type were published by Christensen [14]. Tetrakaidecahedral cells were used in a series of papers by Zhu et al. to describe the elastic behavior [123] and the finite deformation compressive response of periodic open cell [124] and closed cell [71] foams, numerical methods being used to resolve the resulting equations in some cases.

In addition to studying perfectly regular cellular microgeometries, imperfections of the cells, such as waviness of cell walls and struts, can be accounted for, compare [11; 39]. Analytical methods may also be applied to predict the plastic collapse of cellular structures as was proposed by Santosa and Wierzbicki [94] who presented a kinematic model for the crushing of a column of truncated cubes.

The attribute *semi-analytical* is used in this thesis for describing analytical problems, the solution of which can only be found by numerical techniques. Although a closed-form solution is preferable in most situations, such approaches are often helpful to determine the governing mechanisms in a mechanical problem, especially in comparison with more sophisticated, purely numerical methods like the Finite Element method.

2.3.2 Finite Element Unit Cell Methods

Introduction to the Unit Cell Method

Generally, analytical descriptions can only be used for relatively simple generic microgeometries. More complex geometrical arrangements typically have to be analyzed via

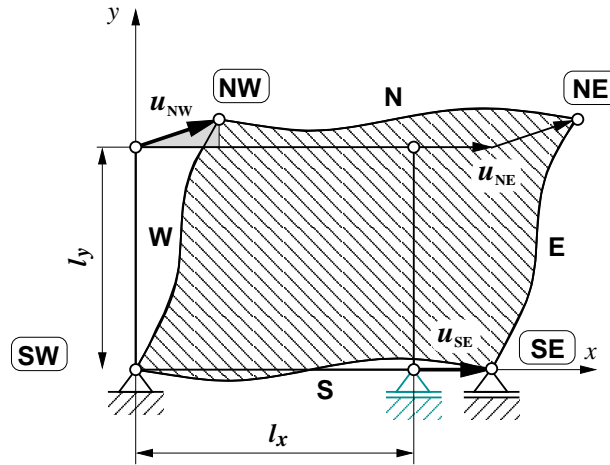


Figure 2.5: Idealized 2D unit cell in the undeformed and the deformed configurations. Displacement vectors and codes for the corner and edge nodes are given. Single letter codes denote edges, two-letter codes denote corners.

numerical engineering methods, the Finite Element method [8; 55; 125] having proven the most popular tool for this purpose. In some Finite Element based studies of honeycombs it was possible to simulate actual experimental setups, compare [79]. In most cases, however, unit cell methods were employed.

The unit cell method is a modeling approach for the prediction of the thermo-mechanical behavior of infinite periodic structures on both the microscale and the macroscale. The method assumes that the behavior of an infinite periodic structure or phase arrangement can be represented by a model of finite size constituting a periodically repeating building block of the geometry in combination with appropriate boundary conditions, which ensure the periodicity of the structure. The combination of representative building blocks and boundary conditions is referred to as a *unit cell*. Unit cells are designed to fill the problem space seamlessly both in the initial undeformed and in all subsequent simulation states. For mechanical problems this means that the displacement of those points on the boundary of the unit cell, which can be mapped onto each other by a translation along a linear combination of the vectors of periodicity, have to be coupled by kinematic constraints. Figure 2.5 illustrates the periodicity of the boundary of a deformed rectangular unit cell.

The boundary of the rectangular unit cell in Figure 2.5 consists of the four edges N, S, W, and E, as well as the four corners NW, SW, NE, SE. The letters in this naming scheme are abbreviations for the four cardinal points North, South, West, and East. The displacements of the corners SW and SE are constrained to restrict rigid body movement modes. Under these constraints, the unit cell can still deform in horizontal and vertical direction, as well as in a shear-like manner without violating the periodicity of the boundary. It is convenient

to relate these global deformation modes to the displacement of Finite Element nodes at the corners of the model. These nodes are commonly called “master nodes”. In Figure 2.5 the nodes NW and SE are master nodes, and their contribution to the overall deformation of the unit cell is indicated by bold arrows.

To maintain geometrical periodicity, pairs of parallel edges of a rectangular unit cell have to be coupled in terms of their displacements. In such a pair the degrees of freedom (DOF) of one edge remain unconstrained. The degrees of freedom of corresponding points on the opposite “slave” edge are constrained to be identical to those of the unconstrained edge except for a constant additional offset vector, which is related to the global deformation DOFs of the unit cell. In the idealized unit cell in Figure 2.5 these offset vectors are $\mathbf{u}_{NW} = \{u_{NW}, v_{NW}\}$ and $\mathbf{u}_{SE} = \{u_{SE}, 0\}$, the components of which are related to the macroscopic strain state $\boldsymbol{\epsilon} = \{\epsilon_{xx}, \epsilon_{yy}, \gamma_{xy}\}$ of the unit cell by:

$$\epsilon_{xx} = \frac{u_{SE}}{l_x}, \quad \epsilon_{yy} = \frac{v_{NW}}{l_y}, \quad \gamma_{xy} = \frac{u_{NW}}{l_y}, \quad (2.1)$$

Constraining the corner node SW and the vertical DOF of the corner node SE, choosing the remaining DOFs of node SE as well as NW as macroscopic master DOFs and the edges S and W as unconstrained edges leaves the edges N and E to be slaved to the former entities:

$$\mathbf{u}_E(y) = \mathbf{u}_W(y) + \mathbf{u}_{SE} \quad (2.2)$$

$$\mathbf{u}_N(x) = \mathbf{u}_S(x) + \mathbf{u}_{NW} \quad (2.3)$$

The displacement of the corner node NE is a linear combination of the displacement vectors \mathbf{u}_{NW} and \mathbf{u}_{SE} of the two master nodes NW and SE:

$$\mathbf{u}_{NE} = \mathbf{u}_{NW} + \mathbf{u}_{SE} \quad (2.4)$$

In the case of Finite Element models involving rotational DOFs (for example beam or shell elements) additional coupling equations have to be provided. In the case of a rectangular unit cell the rotational DOFs φ of all corner nodes have to be identical:

$$\varphi_{NW} = \varphi_{NE} = \varphi_{SE} = \varphi_{SW} \quad (2.5)$$

The rotational DOFs of opposite sides have to be coupled accordingly:

$$\varphi_E(y) = \varphi_W(y), \quad \varphi_N(x) = \varphi_S(x) \quad (2.6)$$

A complete description of the set of boundary conditions necessary for a rectangular periodic 2D unit cell can be found in Table 2.1. Node groups with free DOFs are tabulated in the columns. Node groups with DOF constraints are listed in the rows. In the first row (“DOF=0”) the fully constrained DOFs of the master nodes are given. In the row “Free” the unconstrained degrees of freedom of the master or unconstrained nodes are given. The set of Equations (2.2)–(2.6) is represented by the subsequent rows, where each DOF index

Slave Node Sets	Master Node Sets				
	SW	SE	NW	W	S
Fully Constrained DOFs					
DOF=0	1,2	2			
Unconstrained DOFs					
Free	6	1	1,2	1,2,6	1,2,6
Dependent DOFs					
SE	6				
NW	6				
NE	6	1	1,2		
E		1		1,2,6	
N			1,2		1,2,6

Table 2.1: Degree of freedom (DOF) dependence matrix for general periodic boundary conditions on a rectangular 2D unit cell. The DOF indices 1,2 and 6 conform to **ABAQUS** conventions, where $\{u_1, u_2, u_6\} = \{u, v, \varphi_z\}$.

in the matrix indicates the addition of the respective displacement term to the constraint equation for the same DOF of the node (set) identified in the leading column.

The fact that all nodes along a boundary are coupled to the free DOFs of unconstrained nodes predestines the latter to serve as points of load application. It can be shown, that unit cell models react to concentrated loads on master DOFs like the infinite periodic structure would react to homogenized applied stresses [108]. Similar to Equation (2.1) the relationship between the homogenized stress state $\boldsymbol{\sigma} = \{\sigma_{xx}, \sigma_{yy}, \sigma_{xy}\}$ and the concentrated horizontal and vertical nodal forces H and V involves the side lengths l_x and l_y of the rectangular unit cell:

$$\sigma_{xx} = \frac{H_{SE}}{l_y}, \quad \sigma_{yy} = \frac{V_{NW}}{l_x}, \quad \sigma_{xy} = \frac{H_{NW}}{l_x}, \quad (2.7)$$

With the present definition of l_x and l_y as the initial side lengths of the unit cell, these stress components are defined as nominal stress measures. The extension to true stresses in the large strain domain is straightforward and involves the consideration of the actual side lengths.

The same scheme can be applied to three-dimensional unit cells. Figure 2.6 (left) shows a naming convention for identifying corners, edges, and faces on a cube-shaped unit cell. The identifiers Top and Bottom are introduced to account for the third spatial dimension. Three-letter identifiers denote vertices, two-letter identifiers denote edges and single letter identifiers denote faces. Figure 2.6 (right) depicts the same unit cell in a general

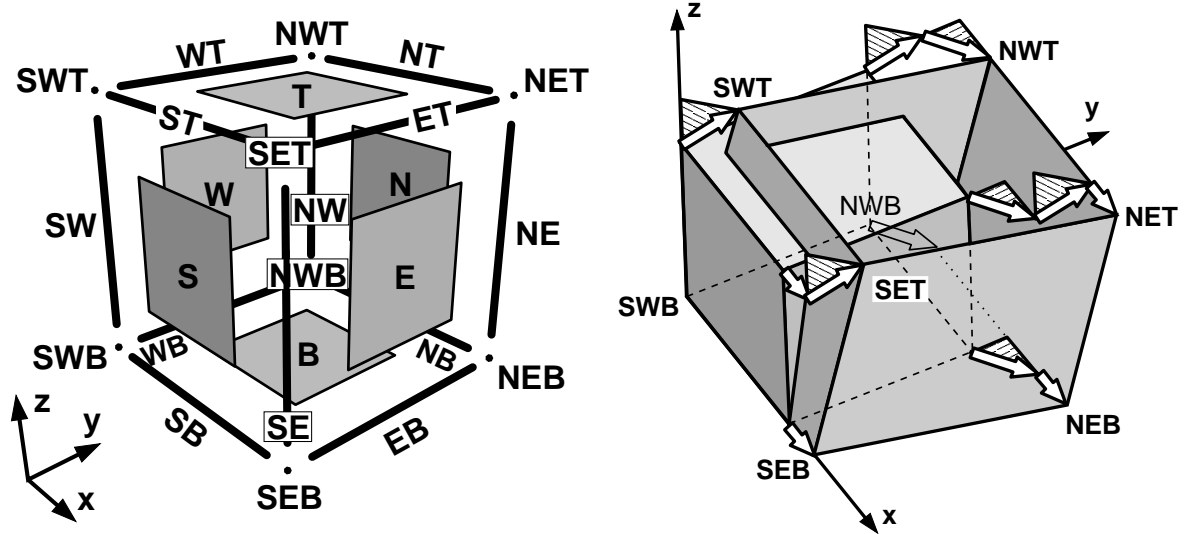


Figure 2.6: Default identifiers for the node sets on the unit cell cube (left) and general deformation state of the 3D unit cube (right).

macroscopic deformation state, with three normal and three shear deformation degrees of freedom being active. Unlike Figure 2.5, this figure does not show possible fluctuations of the local periodic deformation field.

A detailed table of the dependences of the DOFs of Finite Element node sets representing corners, edges and faces of the cube-shaped 3D unit cell can be found in Table 2.2. Each row of the table translates to constraint equations for the DOFs of the constrained node sets (left column) involving the marked DOFs of the master nodes and the unconstrained node sets as listed in the right columns. The constraint equation with the highest number of independent terms (3) can be found for the x -displacement u_{NET} of the corner NET:

$$u_{\text{NET}} = u_{\text{SEB}} + u_{\text{NWB}} + u_{\text{SWT}} \quad (2.8)$$

Figure 2.7 shows the successful validation of the proposed set of periodic kinematic boundary conditions; a large 3D unit cell model with a closed-cell tetrakaidecahedral topology is displayed. The cell walls are modeled using shell elements and, hence, periodic coupling conditions have to be provided for rotational DOFs. The principal deformation modes, uniaxial deformation and shear deformation, are shown to be handled correctly.

Some care is required in the selection of unit cells for a given problem. In order to provide reliable results the unit cell ideally should be a proper representative volume element, the geometry of which contains the full statistical information on the material's microgeometry, compare the discussion in [49]. For modeling the inelastic behavior of cellular materials,

Slave Node Sets	Master Nodes				Unconstrained Node Sets					
	SWB	SEB	NWB	SWT	SB	WB	SW	B	S	W
Fully Constraint Degrees of Freedom										
DOF=0	1,2,3	2,3	3							
Unconstrained Degrees of Freedom										
Free	4,5,6	1	1,2	1,2,3	1...6	1...6	1...6	1...6	1...6	1...6
Degree of Freedom Dependence at Corners										
SEB	4,5,6									
NEB	(3)4,5,6	1	1,2							
NWB	4,5,6									
SWT	4,5,6									
SET	4,5,6	1		1,2,3						
NET	4,5,6	1	1,2	1,2,3						
NWT	4,5,6		1,2	1,2,3						
Degree of Freedom Dependence at Edges										
EB		1				1...6				
NB			1,2		1...6					
SE		1					1...6			
NE		1	1,2				1...6			
NW			1,2				1...6			
ST				1,2,3	1...6					
ET		1		1,2,3		1...6				
NT			1,2	1,2,3	1...6					
WT				1,2,3		1...6				
Degree of Freedom Dependence at Faces										
E		1								1...6
N			1,2						1...6	
T				1,2,3				1...6		

1...6 ... Degrees of freedom $\{u, v, w, \varphi_x, \varphi_y, \varphi_z\}$

DOF=0 ... Fully constraint degrees of freedom

Table 2.2: Degree of freedom dependence matrix for general periodic boundary conditions on a cube-shaped 3D unit cell.

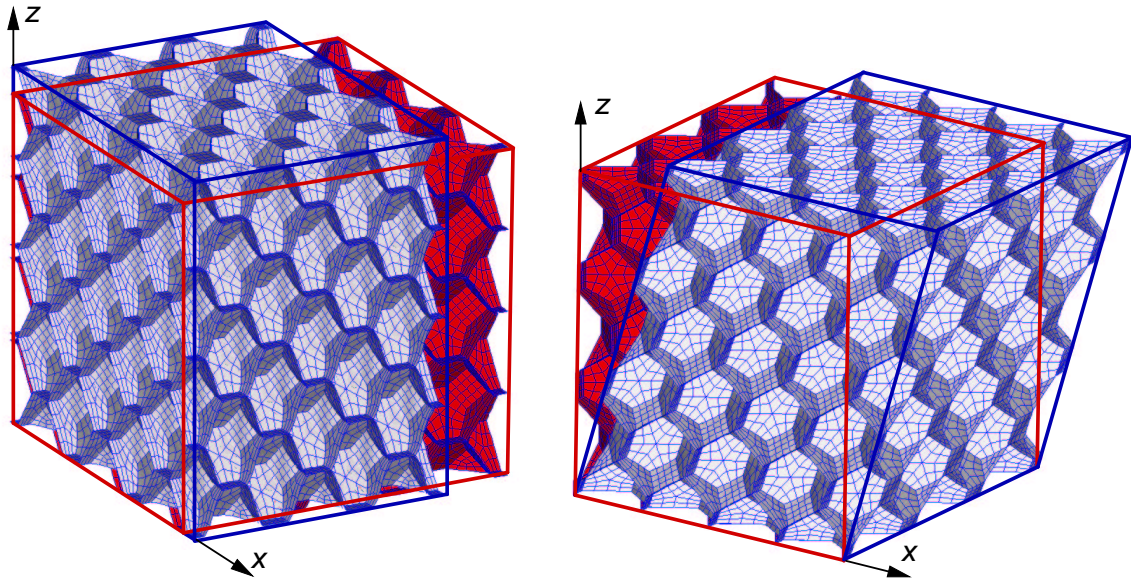


Figure 2.7: Predicted undeformed (dark) and deformed configurations of a 3D unit cell model composed of multiple tetrakaidecahedral cells. The deformed configurations for uniaxial compression (left) and combined shear (right) are shown.

the unit cell must be designed to allow for very large local deformations, and self contact between the cell walls has to be provided for if the behavior in the densification range is to be explored.

Figure 2.8 shows the predicted periodic deformation pattern of an irregular 2D honeycomb with two cell size populations and cell walls with geometric imperfections. The unit cell was subjected to a biaxial compressive deformation by prescribing the vertical displacement of corner NW and the horizontal displacement of corner SE. The resulting horizontal displacement of corner NW indicates the activation of a macroscopic shear deformation mode, and, hence, anisotropic behavior of the microstructure. The dashed line in Figure 2.8 outlines a cell which was approximately circular in the undeformed configuration and has collapsed completely during the deformation process.

In this example, the contact across the unit cell boundary could be captured quite well, but this is not necessarily always the case: cells that are split by the unit cell boundary lack a contact partner for self-contact in a conventional unit cell model. In Section 2.4 a modeling approach, which overcomes this problem, will be discussed.

The choice of the unit cell geometry is often influenced by the necessity of allowing for realistic deformation and buckling patterns, which in most cases precludes the use of simple symmetry boundary conditions [89]. Figure 2.9 shows predicted periodic buckling patterns for regular hexagonal honeycombs under uniaxial compression. While for compression in

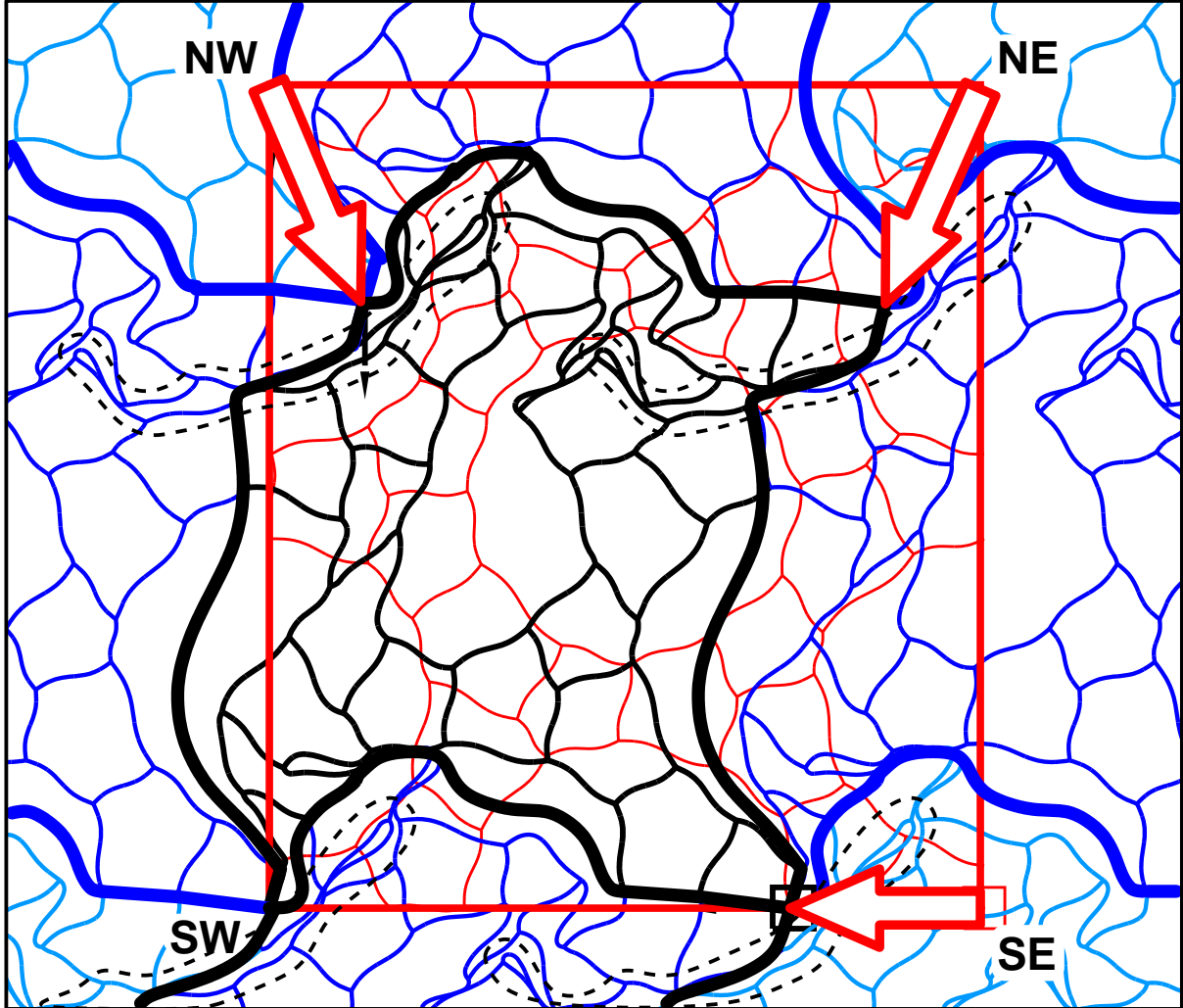


Figure 2.8: Predicted deformed configuration for an irregular 2D honeycomb unit cell model under biaxial compression. The undeformed configuration is depicted by red lines. Red arrows mark the displacement vectors of the corners of the unit cell. The black lines outline the deformed configuration of the actual Finite Element model, while the blue lines illustrate the periodic pattern, in which the unit cell fills the model space. The dashed line surrounds a cell which has collapsed completely.

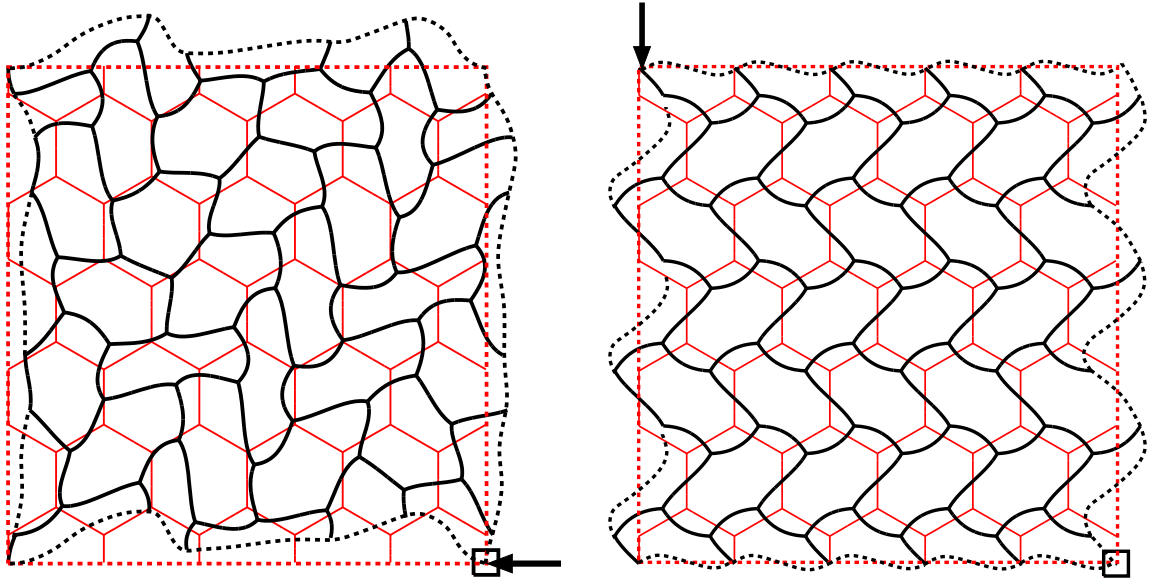


Figure 2.9: Predicted buckling patterns for unit cell models of regular hexagonal honeycombs under uniaxial compression in horizontal (left) and vertical direction (right).

horizontal direction (Figure 2.9, left) the periodicity of the buckling pattern is not readily apparent, the deformed configuration for compression in the vertical direction (Figure 2.9, right) suggests that a much smaller unit cell would suffice to describe the buckling patterns. In all cases, of course, there is a requirement to keep the complexity of the unit cell and thus the computational costs within acceptable limits.

When using unit cell descriptions it is important to keep in mind that the resulting models are periodic in all respects. As an example, inhomogeneous densification of cellular materials as predicted by unit cell models will always take place in periodic patterns, the period of which is strongly influenced by the choice of the size of the unit cell (compare Figure 2.8). Single crack tips (as opposed to periodic patterns of cracks) cannot be handled by periodic microgeometries, and free surfaces are restricted to layer-like geometries in which at least one direction is non-periodic. For these types of problems, embedded cell approaches are the methods of choice [1; 89].

Preprocessing Techniques

All micromechanical simulations in this study were performed with the Finite Element code **ABAQUS** [52]. For the simplification of some mesh and model generation tasks some preprocessing tools were developed which will be discussed briefly in the following.

Automatic Generation of Periodic Boundary Conditions. In the previous section an introduction to the definition of periodic boundary conditions on the boundary of rectangular 2D and cube-shaped 3D unit cells was presented. Preprocessing tools, which were developed in the course of the present thesis, provided for an automatic generation of input code containing the definition of constraint equations necessary for a successful unit cell analysis. This task involved the determination of the unit cell dimensions, the classification of the Finite Element nodes in corner nodes, edge nodes, face nodes and non-boundary nodes (mutually exclusive) as well as the correlation of unconstrained and constrained nodes.

The following bit flag based encoding scheme proved advantageous for the classification of the Finite Element nodes:

Identifier	T	B	E	W	N	S
Bit flag value	32	16	8	4	2	1

Employing this scheme, the node set membership of a Finite Element node can be coded without ambiguity. Masks of 6 bits can then be used to filter the required nodes from the database of the preprocessor. This is a prerequisite for a speed-efficient implementation of the algorithm that searches for the partner of unconstrained nodes.

Controlled Perturbation of Finite Element Meshes. For studying the influence of geometrical imperfections in a systematic way, it is advantageous to have a means of perturbing arbitrary Finite Element meshes in a geometrically and statistically well defined way. A preprocessing tool with the purpose of perturbing 2D beam Finite Element models was developed for this thesis. This tool allowed for an isolated, or combined, perturbation of Finite Element node positions by

- shifting the vertices of a 2D beam structure in a statistically well defined way while maintaining straight cell edges,
- shifting cell wall nodes to create cell walls with sinusoidal wiggles,
- shifting cell wall nodes to achieve curved cell walls.

Figure 2.10 (left) shows a regular hexagonal honeycomb prior to the perturbation preprocessing step. In Figure 2.10 (right) the same model is shown after a controlled disturbance of the node positions. Applications of the mesh perturbation tool will be demonstrated in Sections 2.6 to 2.8.

Automatic Creation of Contact Surfaces. For unit-cell simulations, which involve the deformation of unit cell models up to very high macroscopic strains, compare Figure 2.8, it is advantageous to have a tool which facilitates the creation of contact surfaces on the

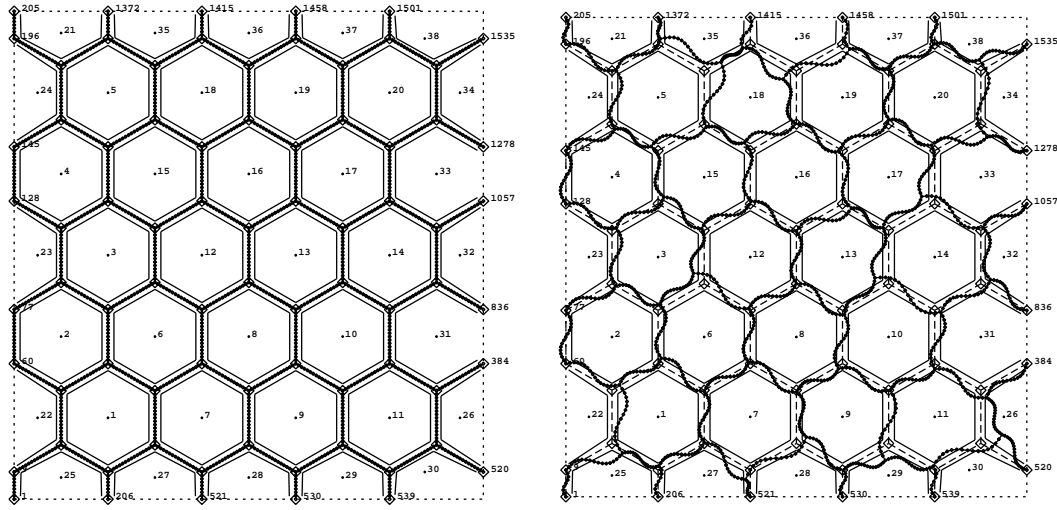


Figure 2.10: 2D Beam model of a hexagonal honeycomb; original geometry (left) and geometry perturbed by a custom preprocessing program (right).

unit cell models. For 2D beam models, this capability was implemented in a preprocessing tool which was able to identify the topology of a plane beam model by detecting the connectivity of the beam elements.

Figure 2.10 (left) shows a 2D unit cell comprised of hexagonal honeycombs. The surfaces on this beam model were correctly identified by the preprocessing tool; they are displayed as thin lines which are drawn with a small offset in the direction of the surface normal.

Prediction of the Elastic Behavior

The most basic aspect of the mechanical material characteristics of inhomogeneous materials is their linear elastic behavior, which can be described in terms of an overall elasticity tensor or appropriate effective moduli (compare Section 4.3.3). Linear analysis requires comparably little effort, and, therefore, the linear elastic properties of a wide range of cellular microgeometries are well researched. As a consequence, the focus of the microstructural investigations in this thesis rests on the prediction of the nonlinear behavior of cellular metals.

Prediction of the Onset of Yielding in the Microstructure

Cellular metals typically have small linear elastic ranges, beyond which nonlinear behavior sets in due to finite deformations, yielding, loss of stability or fracture at the microscale. In contrast to bulk metals, the elastic range of metallic foams is also limited under purely

hydrostatic loading. Micromechanical analyses of such behavior may be carried out in terms of material characterization by simulating, for example, uniaxial or multiaxial tests to obtain homogenized stress versus strain curves. In terms of the overall behavior the onset of nonlinear responses can generally be described via appropriate surfaces in stress space, of which the classical von Mises yield surface for plastic yielding of bulk metals is a well-known example. Analogous surfaces for cellular metals can be obtained from micromechanical analyses by monitoring the material response while following loading paths that are radial in macroscopic stress space. Deviations from linear overall behavior are mainly due to local yielding (typically at the transitions between cell walls and cell edges) or to local elastic buckling of the cell walls or struts. The onset of nonlinear behavior is, in fact, caused by yielding in the majority of cases, and microscale buckling plays an appreciable role only for highly regular microgeometries, for which the above surfaces may be viewed as “generalized yield surfaces”. If only the onset of plastic yielding is considered in this context the superposition of elastic solutions is possible, and only one simulation per dimension of the macroscopic stress space is required for determining the overall yield surface of macroscopically isotropic materials.

The algorithm for the determination of the initial yield surface and for tracing the evolution of the yield surface during a nonlinear deformation process will be outlined in the following. The term “yielding” is used in a very strict sense here, because fulfilling the (local) yield condition

$$F(\boldsymbol{\sigma}) = 0 \quad (2.9)$$

anywhere in the unit cell is interpreted as the onset of both local *and* macroscopic yielding. In Equation (2.9), the *yield function* $F(\boldsymbol{\sigma})$ is introduced as a scalar function, which returns negative values for stress states that do not cause yielding and zero for stress states which are able to cause plastic deformations (the framework of Plasticity Theory will be discussed in depth in Chapter 4). Often, the yield function takes the form

$$F(\boldsymbol{\sigma}) = \sigma_{\text{eqv}}(\boldsymbol{\sigma}) - \sigma_{\text{YS}}, \quad (2.10)$$

where the equivalent stress $\sigma_{\text{eqv}}(\boldsymbol{\sigma})$ is a scalar measure for the tendency of the (local) stress state $\boldsymbol{\sigma}$ to cause (local) yielding in the material. For use in Equation (2.10) this equivalent stress has to be formulated such that it can be directly compared to the uniaxial yield stress σ_{YS} of the bulk material.

In practice, it will be virtually impossible to detect local, initial yielding in experiments, which rely on the occurrence of measurable plastic deformations for the definition of the yield stress. Consequently, the determination of yield surfaces with micromechanical models is expected to show important trends in the influence of individual microgeometrical parameters on the macroscopic behavior of the foam.

For foams with a metallic solid phase, the von Mises yield criterion is applicable for determining the onset of local yielding. This local yield criterion can be expressed in Nye (vector) notation [77], that is, in terms of the vector of stress components $\boldsymbol{\sigma}^T =$

$\{\sigma_{xx}, \sigma_{yy}, \sigma_{zz}, \sigma_{yz}, \sigma_{zx}, \sigma_{xy}\}$, giving

$$F_{\text{Mises}}(\boldsymbol{\sigma}) = \frac{1}{2} \boldsymbol{\sigma}^T \mathbf{P} \boldsymbol{\sigma} - \sigma_{ys}^2 = 0, \quad (2.11)$$

where $\boldsymbol{\sigma}$ is a $n \times 1$ (pseudo) vector of local stress components and \mathbf{P} is a constant $n \times n$ matrix [15]. For general 3D stress states ($n = 6$) \mathbf{P} becomes:

$$\mathbf{P} = \begin{bmatrix} 2 & -1 & -1 & & & \\ -1 & 2 & -1 & & & \\ -1 & -1 & 2 & & & \\ & & & 6 & & \\ & & & & 6 & \\ & & & & & 6 \end{bmatrix} \quad (2.12)$$

Taking into account a possible local residual stress state $^{\text{RES}}\boldsymbol{\sigma}$, which is inside the local yield surface in stress space, and a linear elastic response of the bulk material, the total vector of stress components $\boldsymbol{\sigma}$ in Equation (2.11) can be expressed as the sum of $^{\text{RES}}\boldsymbol{\sigma}$ and the product of a load multiplier λ and a vector of load induced stress components $^{\text{D}}\boldsymbol{\sigma}$,

$$\boldsymbol{\sigma}(\lambda) = ^{\text{RES}}\boldsymbol{\sigma} + \lambda ^{\text{D}}\boldsymbol{\sigma}, \quad (2.13)$$

as long as $\boldsymbol{\sigma}(\lambda)$ is a stress state inside the von Mises yield surface, that is, $F_{\text{Mises}}(\boldsymbol{\sigma}(\lambda)) < 0$. The vector ($\lambda^{\text{D}}\boldsymbol{\sigma}$) describes the contribution of a stress field induced by an applied macroscopic load to the local stress state.

To calculate the load multiplier λ_y , which would cause the equivalent stress to reach the yield strength of the bulk material, the expression (2.13) can be inserted in the yield criterion Equation (2.11):

$$\frac{1}{2} (^{\text{RES}}\boldsymbol{\sigma} + \lambda_y ^{\text{D}}\boldsymbol{\sigma})^T \mathbf{P} (^{\text{RES}}\boldsymbol{\sigma} + \lambda_y ^{\text{D}}\boldsymbol{\sigma}) - \sigma_{ys}^2 = 0. \quad (2.14)$$

Since \mathbf{P} is a symmetric matrix, the product $(^{\text{RES}}\boldsymbol{\sigma}^T \mathbf{P} ^{\text{D}}\boldsymbol{\sigma})$ is equal to $(^{\text{D}}\boldsymbol{\sigma}^T \mathbf{P} ^{\text{RES}}\boldsymbol{\sigma})$ and Equation (2.14) can be rewritten in the form of a second order equation for λ_y :

$$\lambda_y^2 \underbrace{(^{\text{D}}\boldsymbol{\sigma}^T \mathbf{P} ^{\text{D}}\boldsymbol{\sigma})}_a + \lambda_y \underbrace{(2 ^{\text{RES}}\boldsymbol{\sigma}^T \mathbf{P} ^{\text{D}}\boldsymbol{\sigma})}_b + \underbrace{(^{\text{RES}}\boldsymbol{\sigma}^T \mathbf{P} ^{\text{RES}}\boldsymbol{\sigma} - 2 \sigma_{ys}^2)}_c = 0 \quad (2.15)$$

The two solutions $\lambda_y^{(1,2)}$ can then be calculated with the well-known formula:

$$\lambda_y^{(1,2)} = \frac{-b \pm \sqrt{b^2 - 4ac}}{2a} \quad (2.16)$$

For each stress evaluation point i in the Finite Element analysis it is possible to calculate a load multiplier $\lambda_y^{(i)}$, which in connection with the known applied macroscopic stress state

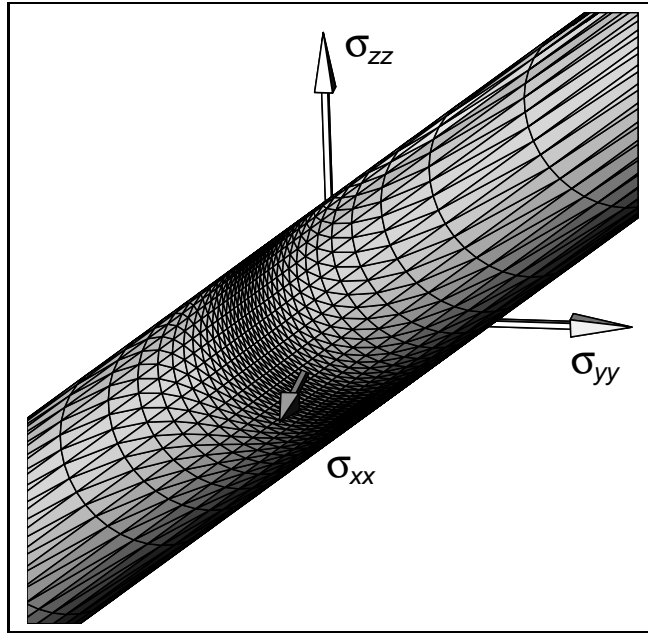


Figure 2.11: Verification example for the prediction of initial yield surfaces: cylindrical yield surface corresponding to the yield condition of J_2 plasticity in a solid material.

would lead to yielding in the evaluation point. The critical global load multiplier Λ_y causing the *first* local fulfillment of the yield condition in the structure can be found for a radial loading path as the local load multiplier with the smallest positive value: $\Lambda_y = \min(\lambda_y^{(i)})$ for all $\lambda_y^{(i)} \geq 0$.

Since, here, the determination of yield surfaces is based on the assumption of linear elastic deformation prior to the situation at which the local yield condition is met, the local load-induced stress states ${}^D\boldsymbol{\sigma}$ can be calculated by superimposing stress fields obtained by the analysis of unit load cases.

The outlined algorithm was implemented in a Finite Element postprocessor program. Figure 2.11 shows the result of a verification example based on a single element test and the application of the von Mises yield criterion. In three subsequent linear elastic analysis steps the element was loaded with a unit load in the direction of a different coordinate axis. By feeding the resulting stress states into the postprocessor it was possible to recover the yield surface of J_2 (von Mises) plasticity, which corresponds to a cylinder along the hydrostatic stress axis in the principal stress space, see Figure 2.11.

The above concept can also be used to follow the evolution of the yield surface for a prescribed macroscopic loading path. To do this, the macroscopic load is applied incrementally, and complete unloading is carried out after each step followed by an evaluation of the new yield surface under the consideration of the residual stress state in the microstructure.

This may again be done by superimposing elastic solutions.

A complete analysis for tracing the evolution of the yield surface consists of the following independent simulation runs:

1. An analysis performing a linear perturbation step for each global unit load component and subsequent calculation of the initial yield surface.
2. A nonlinear analysis for a given global radial load path, subdivided into increments each of which can be used as the starting configuration for step 3.
3. An analysis, which recovers an arbitrary deformation state from step 2, and performs an unloading step during which the applied load is removed. This way the residual stress state caused by the plastic deformations in the model is obtained.
4. A linear perturbation analysis for each global unit load component directly following step 3. With these results, the sequential yield surface can be predicted under consideration of the residual stress state $^{\text{RES}}\boldsymbol{\sigma}(x, y, z)$ obtained in step 3.

If desired, steps 3 and 4 can be repeated with different increments from step 2.

The evaluation of Equation (2.15) for determining the critical local load multiplier is only straightforward as long as the yield stress σ_{ys} remains constant during the deformation, that is, *hardening* does not occur (compare Chapter 4). Hence, the assumption of elastic-ideal plastic bulk material behavior simplifies the algorithm considerably.

Additionally, it should be noted, that the application of linear superposition analyses is limited to the small deformation regime. In cellular metals geometrical nonlinearities (caused, for instance, by marked bending of cell walls) may give rise to noticeably nonlinear overall responses even before yielding sets in.

Prediction of Collapse and Fracture

As soon as a foam is subjected to increasing compressive stresses a load will be reached at which the first collapse of a cell occurs. In metallic foams the initial collapse of a cell under these conditions tends to be followed by growth of the collapsed region, which typically takes place at stress levels that show only limited variation, giving rise to a so-called plateau region in the overall stress versus strain behavior. When a considerable percentage of cells have been “consumed” the foam densifies, the plateau region ends, and a much stiffer response sets in. The accumulation of considerable compressive strains at nearly constant stresses is of particular interest for cellular metals that are to be employed for impact energy absorption. Collapse stresses under uniaxial loading have been studied for many cellular morphologies and for various kinds of microgeometrical imperfections. For general load cases the initial collapse stress states form an envelope surrounding the initial yield surface, which may be called a collapse surface. For the point-wise evaluation

of collapse surfaces fully nonlinear analyses along individual load paths are required, see Section 2.11.

Relatively little work has been reported on the modeling of fracture of metallic foams, although it is the dominant failure mechanism under tensile macroscopic loading. Embedded cell models provide a flexible approach for studying cracks in idealized cellular metals, compare Section 2.12.

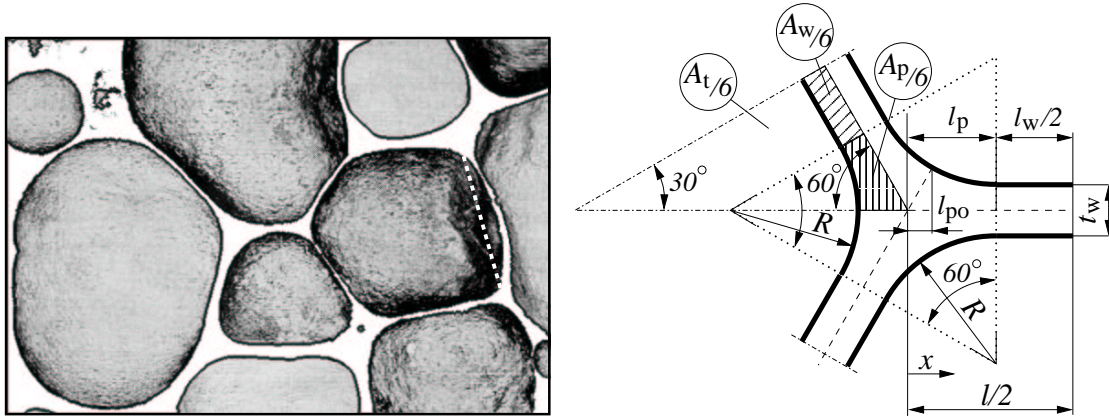


Figure 2.12: Left: Section through an aluminum foam produced by the powder metallurgical route (courtesy Institute of Materials Science and Testing, Vienna University of Technology). Right: Model geometry.

2.4 Influence of Material Distribution in the Cell Walls

2.4.1 Introduction

The production of metallic foams typically involves the solidification of a molten precursor material into an appropriate shape. In the liquid state a redistribution of material driven by surface tension and internal pressure results in the formation of concave transition regions between the cell walls, known as Plateau borders, and give rise to non-uniform cell wall thicknesses, compare Figure 2.12. This phenomenon may influence the mechanical behavior of the foam on both the micro- and the macroscales and has, accordingly, been the subject of research interest.

Simone et al. [106] developed unit cells for hexagonal honeycombs and tetrakaidecahedral foams in which Plateau borders were modeled by appropriate curved and parallel regions. Their results indicate that the distribution of material in the cell walls has little influence on the Young's modulus and only a moderate effect on the uniaxial yield strength of closed cell metallic foams. A different approach was followed by Chen et al. [11], who studied honeycombs with wall thicknesses that increase linearly between the middle of the walls and the vertices. This simplifies the mathematics of the problem sufficiently for closed-form analytical solutions to be obtained for the overall yield surfaces of the models.

In the following, several aspects of the influence of Plateau borders on the effective mechanical behavior of regular hexagonal honeycombs are studied, including the initial overall yield surface and the behavior under uniaxial crush deformation.

2.4.2 Method

Geometry

In the microstructural cross-section of a metallic foam in Figure 2.12 (left) the curved transitions between adjacent cell walls are apparent. The figure also shows other imperfections like non-uniform cell wall thickness (compare Section 2.5), curved cell walls (compare Section 2.6) and different cell sizes (compare Section 2.8). To study the influence of Plateau borders in isolation, a regular hexagonal honeycomb model is proposed. Figure 2.12 (right) shows a geometrical building block of this model.

The geometry of the model is fully described by the honeycomb edge length l , the concave radius of the cell wall transition R , which will be referred to as “Plateau border radius” in the following, and the thickness t_w of the straight part of the cell wall. The out-of-plane thickness b completes the set of geometrical parameters.

The dimensions of the model honeycomb have to be related to the apparent density ρ_{rel} on the one hand and a measure for the size of the Plateau border on the other hand. For this purpose, the in-plane area filled with solid material is partitioned into two sections: the area A_w contained in the straight cell walls and the area A_p contained in the cell vertex formed by the Plateau borders.

The total area A_p of a cell vertex with Plateau borders is given by

$$A_p = \sqrt{3} \left(R + \frac{t_w}{2} \right)^2 - \frac{R^2 \pi}{2} \quad (2.17)$$

The total area A_w of a straight cell wall section is

$$A_w = t_w \left(l - \frac{2R + t_w}{\sqrt{3}} \right) \quad (2.18)$$

A triangle containing one vertex and the symmetry halves of the three adjoining cell walls can be considered as a geometrical unit cell for the honeycomb. The total area A_t of the representative triangular cell is

$$A_t = \frac{3\sqrt{3}}{4} l^2 \quad (2.19)$$

The relative density ρ_{rel} of a cellular material is defined as the quotient ρ_F/ρ_S of its absolute apparent density ρ_F and the absolute density ρ_S of the bulk material. The relative density can also be expressed in terms of volume, or cross-sectional area fractions, the volume, or area, of the solid phase being the numerator and the volume, or area, of the overall volume being the denominator. With the definitions (2.17) to (2.19), the relative density ρ_{rel} can be calculated to

$$\rho_{\text{rel}} = \frac{A_p + \frac{3}{2}A_w}{A_t} \quad (2.20)$$

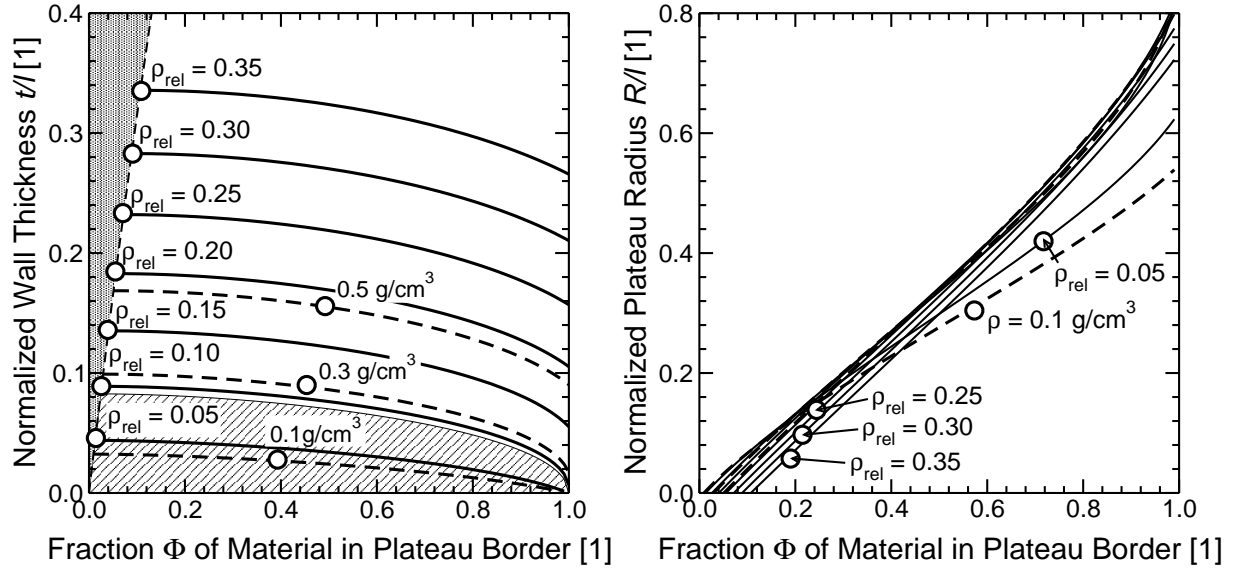


Figure 2.13: Geometrical parameters for aluminum honeycombs with Plateau borders. The shaded area indicates unrealizable combinations of t and Φ . The hashed area indicates relative densities below ρ_{rel}^* , that is, vanishing thickness t for $\Phi \rightarrow 1$.

Finally, the size of the Plateau border can be described by the ratio Φ of the area contained in the cell vertex and the total solid area in the representative triangular cell:

$$\Phi = \frac{A_p}{A_p + \frac{3}{2}A_w} \quad (2.21)$$

For a given honeycomb edge length l , a given relative density ρ_{rel} and a desired volume fraction Φ , the geometric parameters R and t_w can be determined by solving the system of equations (2.17)–(2.21) numerically for these parameters. Cell wall thickness values and Plateau border radii, both normalized with respect to the the honeycomb edge length, can be found in Figure 2.13 as functions of the Plateau border area fraction Φ and the honeycomb density. The absolute density values associated with the dashed lines in Figure 2.13 assume an aluminum bulk material with an absolute density of 2.7 g/cm^3 (2700 kg/m^3).

The range of admissible density and volume fraction values is limited by two boundary cases: (a) perfect honeycombs with a sharp corner ($R = 0$) instead of a smooth transition and (b) cases of vanishing cell wall thickness for $\Phi \rightarrow 1$.

For a perfect honeycomb ($R = 0$) with uniform cell wall thickness t_w along the honeycomb edge, the relative density ρ_{rel} is correlated to the cell wall thickness by

$$\rho_{\text{rel}}(t_w/l) = \frac{2}{\sqrt{3}} \left[\frac{t_w}{l} \right] - \frac{1}{3} \left[\frac{t_w}{l} \right]^2 \quad (2.22)$$

Lower limits of the Plateau material fraction Φ_{\min} and the cell wall thickness $t_w^{(\min)}$ for perfect honeycombs can be given directly in terms of the relative density ρ_{rel} :

$$\Phi_{\min}(\rho_{\text{rel}}) = \frac{1 - \sqrt{1 - \rho_{\text{rel}}}}{1 + \sqrt{1 - \rho_{\text{rel}}}} \quad (2.23)$$

$$t_w^{(\min)}(\rho_{\text{rel}}, l) = l\sqrt{3} \left(1 - \sqrt{1 - \rho_{\text{rel}}} \right) \quad (2.24)$$

The grey area in Figure 2.13 (left) covers Φ - t pairs that violate the condition $\Phi(\rho_{\text{rel}}) > \Phi_{\min}(\rho_{\text{rel}})$ and, hence, do not have a physical meaning.

For $\Phi = 1$ and relative densities below $\rho_{\text{rel}}^* = 1 - \pi/(2\sqrt{3}) = 0.0931$, the cell wall thickness is zero. In Figure 2.13 (left) the hashed area covers Φ - t curves for which the condition of vanishing cell wall thickness applies for $\Phi \rightarrow 1$. For relative densities above ρ_{rel}^* , the cell wall thickness for honeycombs with voids in the form of circular cylinders ($\Phi = 1$) is given by:

$$t_{\min} = \sqrt{3} - \sqrt{\frac{6\sqrt{3}(1 - \rho_{\text{rel}})}{\pi}} \quad (2.25)$$

The local cell wall thickness $t(x)$ within the Plateau border section can be expressed as a function of the distance x from the center of the honeycomb vertex:

$$t(x) = 2R + t_w - \frac{1}{\sqrt{3}} \sqrt{8R^2 - 4Rt_w - (t_w)^2 + 8\sqrt{3}Rx + 4\sqrt{3}t_w x - 12x^2} \quad (2.26)$$

Admissible values for x in Equation (2.26) are $l_{p0} \leq x \leq l_p$, where

$$l_{p0} = \frac{t_w + R(2 - \sqrt{3})}{2\sqrt{3}} \quad (2.27)$$

is the x -coordinate marking the intersection of the Plateau border and the symmetry plane, and l_p is the width of the Plateau border, that is, the axial location of the transition between Plateau border and cell wall:

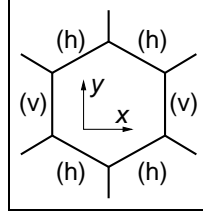
$$l_p = \frac{2R + t_w}{2\sqrt{3}} \quad (2.28)$$

The length $l_w = l - 2l_p$ denotes the length of that part of the honeycomb edge that shows a constant wall thickness.

Applied Stresses and Local Stress State

Subjecting a regular hexagonal honeycomb with variable cell wall thickness $t(x)$ to macroscopic stresses σ_{xx} and σ_{yy} in the horizontal and in the vertical directions causes local stresses, which can be split into contributions from bending moments, normal forces, and shear forces. Plane stress conditions are assumed in the following considerations.

In the schematic diagram below the global x and y directions are defined in relation to the vertical honeycomb edges (v) and the inclined honeycomb edges (h):



The stresses due to normal forces in the vertical honeycomb edges (v) and the inclined edges (h) can be related to the applied stress state by:

$$\begin{bmatrix} \sigma_n^{(h)} \\ \sigma_n^{(v)} \end{bmatrix} = \left(\frac{l}{t}\right) \begin{bmatrix} \frac{3\sqrt{3}}{4} & \frac{\sqrt{3}}{4} \\ 0 & \sqrt{3} \end{bmatrix} \begin{bmatrix} \sigma_{xx} \\ \sigma_{yy} \end{bmatrix} \quad (2.29)$$

Both components of the vector of applied stresses (σ_{xx}, σ_{yy}) cause bending moments in the oblique cell edges, but not in the vertical edges. Along the skeletal lines of the oblique edges, the bending moment varies linearly between a maximum value at the proximal corner and a moment of the same magnitude but opposite sign at the distal corner. In the middle of the oblique honeycomb edges ($x = l/2$) the bending moment changes its sign and, hence, vanishes: $M(l/2) = 0$. For uniaxial applied stress states the maximum moment M_{\max} relates to the applied stress σ by

$$M_{\max} = \frac{3}{8} b l^2 \sigma \quad (2.30)$$

The linear bending moment distribution along the cell wall is given by

$$M_i(x) = \sigma_i \frac{3lb}{4} \left[\frac{l}{2} - x \right] \quad (2.31)$$

The bending moments M_{xx} and M_{yy} caused by the two applied stress components σ_{xx} and σ_{yy} , respectively, have the same relative magnitude, but opposite sign. The total bending moment can be derived by a linear superposition of the individual bending moment contributions:

$$M(x) = M_{xx}(x) - M_{yy}(x) \quad (2.32)$$

The axial stresses σ_u and σ_l in the upper and the lower fibers of the cell edge can be calculated by superimposing the bending stresses $M(x)/W(x)$ and the normal stress distribution $\sigma_n^{(h)}$ from Equation (2.29):

$$\sigma_{u/l}(x) = \frac{\sqrt{3}}{4} \frac{l}{t(x)} (3\sigma_{xx} + \sigma_{yy}) \pm (\sigma_{xx} - \sigma_{yy}) \frac{9l}{t^2(x)} \left[\frac{l}{2} - x \right] \quad (2.33)$$

Shear stresses are generally neglected in this investigation.

Onset of Yielding (Effective Initial Yield Stress)

Considering a bulk material with a yield stress of σ_{ys} , the condition

$$\max(|\sigma_u|, |\sigma_l|) = \sigma_{ys} \quad (2.34)$$

has to be fulfilled for the onset of yielding at a critical position x^* , for which the optimality criterion $d\sigma(x)/dx = 0$ is fulfilled with $\sigma(x)$ being either $\sigma_u(x)$ or $\sigma_l(x)$. The critical axial positions of the locations with the highest axial stresses in the outer fibers of the cell wall can be determined numerically for general applied stress states. For the plane “hydrostatic” biaxial case $\sigma_{xx} = \sigma_{yy} = p$ the critical applied stress p^* can be given directly:

$$p^* = \pm \frac{\sigma_{ys}}{\sqrt{3}} \left[\frac{t_w}{l} \right] \quad (2.35)$$

If no strain hardening is assumed for the bulk material this macroscopic yield stress is equal to the macroscopic collapse stress in the regular hexagonal configuration, because, owing to the uniform distribution of axial stress for this loading case, the whole cross section of the cell wall yields at once as soon as the yield stress is reached at the thinnest portion of the cell wall.

The optimization problem posed by Equation (2.34) was solved numerically with the symbolic and numerical mathematics code *Mathematica* [117]. The minimization function `FindMinimum[f(x)]` was used at the core of the solution. Four cases of objective functions $f(x)$ were considered: $\sigma_u(x)$, $-\sigma_u(x)$, $\sigma_l(x)$, and $-\sigma_l(x)$. A calculation of absolute values for $\sigma_{u/l}(x)$ with the `Abs[f(x)]` function had to be abandoned, because the occurrence of spikes caused numerical problems. Furthermore, special provisions had to be taken to prevent execution problems owing to the occurrence of boundary extrema. Lastly, plane hydrostatic stress states $\sigma_{xx} = \sigma_{yy} = p^*$ caused uniform axial stress states in cell walls of uniform thickness, leading to an indefinite numerical problem. This case was trapped, and Equation (2.35) was applied directly.

Uniaxial Effective Collapse Stress

Loading beyond the elastic limit discussed above causes plastic deformation and the spreading of a plastic zone throughout the honeycomb wall sections. At a certain point, the cross-section cannot withstand any further increase of the applied loads and starts to collapse as soon as the admissible peak load is exceeded (see, for example, Mang and Hofstetter [66]). An estimate for this peak or limit load will be derived in the following.

The moment M_{pl} for a rectangular cross-section of height $t(x)$ and width b in the fully plastified state is given as:

$$M_{pl}(x) = \frac{b t^2(x)}{4} \sigma_{ys} \quad (2.36)$$

The critical axial force leading to plastic failure of the rectangular cross-section can be determined by

$$N_{\text{pl}}(x) = b t(x) \sigma_{\text{ys}} \quad (2.37)$$

For a constant axial force N the critical moment $M^*(x)$ can be found by solving the interaction relationship:

$$\frac{M^*}{M_{\text{pl}}(x)} + \left[\frac{N}{N_{\text{pl}}(x)} \right]^2 = 1 \quad (2.38)$$

for $M^*(x)$ [66]. For the regular hexagonal honeycomb, the axial force N can be expressed in terms of the applied stress σ_{yy} by

$$N = \frac{\sqrt{3}}{4} b l \sigma_{yy} \quad (2.39)$$

For a rectangular cross-section $b \times t(x)$ the applied stress, which would cause plastic failure of the cross-section, can be calculated by solving the identity relationship

$$M^*(x, \sigma_{yy}^*) = M_{\text{b}}(x, \sigma_{yy}^*) \quad (2.40)$$

for $\sigma_{yy}^*(x, \sigma_{\text{ys}})$, the necessary applied stress to cause *local* plastic failure. The global collapse stress σ_{yy}^* can then be calculated by minimizing $\sigma_{yy}^*(x)$ by variation of x . This operation was performed semi-analytically with the code `Mathematica` [117].

Finite Element Model

For a more detailed resolution of the stress fields in the honeycomb and a simulation of crushing deformation up to large strains, a Finite Element model of a regular hexagonal honeycomb with Plateau borders was developed.

Figure 2.14 shows the setup of the unit cell. The model consists of two neighboring honeycomb cells offset by $\sqrt{3}/2l$ in the vertical direction and sharing a cell edge. For this model to be a representative volume element of an “infinite”, space-filling honeycomb, appropriate boundary conditions have to be prescribed. These boundary conditions enable the unit cell to deform in a natural, periodic pattern, which was elsewhere demonstrated to appear in the uniaxial compression of elastomeric honeycombs, see Figure 2.15. The periodic coupling conditions are indicated by arrows in Figure 2.14. To trigger non-symmetric deformation patterns like the one depicted in the inset picture in Figure 2.14 it is necessary to introduce small geometric imperfections. The custom pre-processor developed for the generation of the unit cell models supports two kinds of imperfections: curved cell walls and cell wall wiggles. The initial deformations used to trigger the desired collapse mode for vertical uniaxial compression are overemphasized in Figure 2.14.

The Finite Element mesh was composed of 8-node solid 2D elements with bi-quadratic interpolation functions. Typically, six elements were used in edge thickness direction. Plane stress conditions were prescribed.

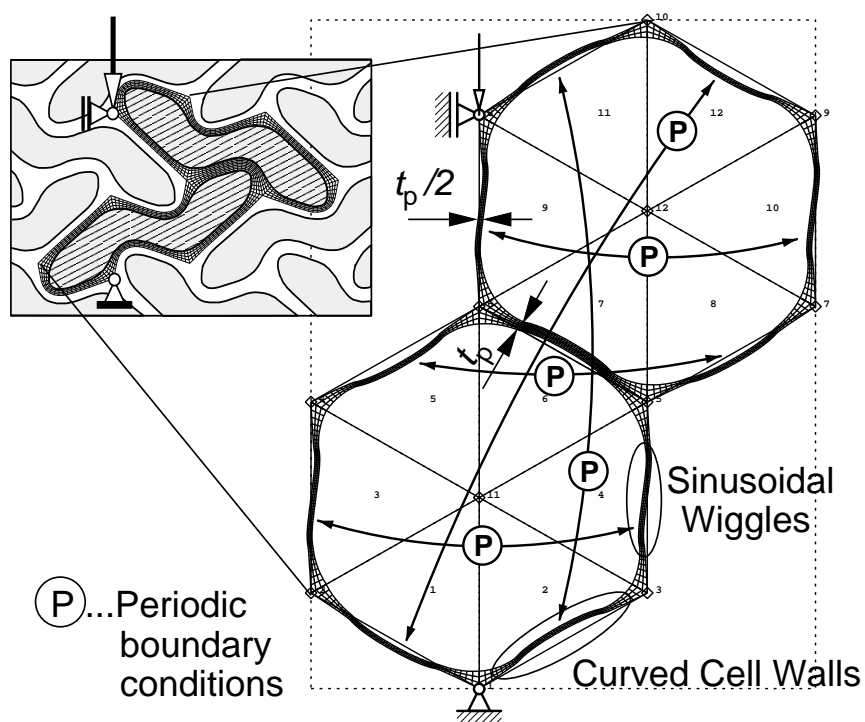


Figure 2.14: Deformation constraints and periodic boundary conditions on the Finite Element model of two honeycomb cells with Plateau borders.

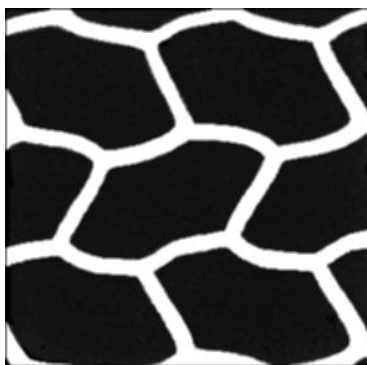


Figure 2.15: Periodic buckling mode of an elastic honeycomb under uniaxial compression in the vertical direction, from Gibson and Ashby [34].

Model Material Parameters	
Density	$\rho = 2.7 \text{ g/cm}^3$
Young's modulus	$E = 70 \text{ GPa}$
Poisson ratio	$\nu = 0.33$
Yield stress	$\sigma_{ys} = 200 \text{ MPa}$
Hardening modulus	$E_t = 700 \text{ MPa}$

Table 2.3: Bulk material parameters.

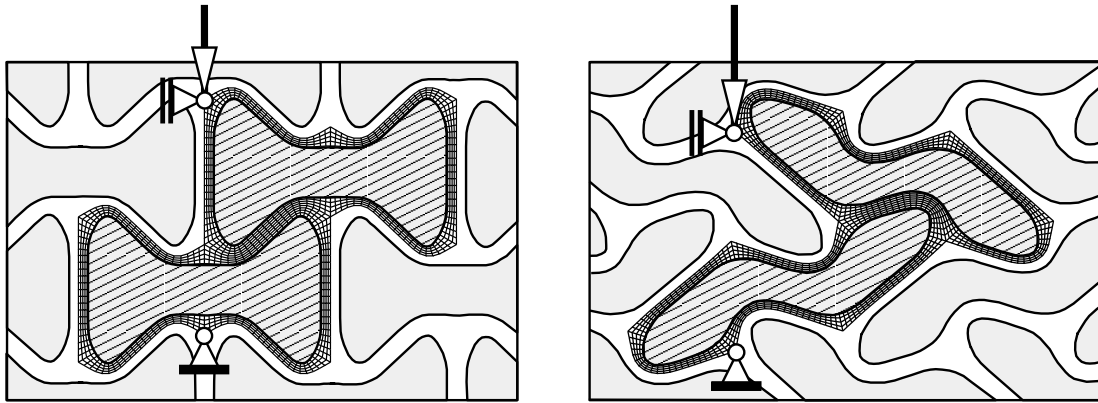


Figure 2.16: Predicted symmetric (left) and periodic (right) deformation modes of hexagonal honeycombs with Plateau borders.

J_2 plasticity with isotropic hardening was used as the constitutive theory for the cell wall material. The uniaxial stress–strain relationship was idealized as bilinear with a post-yield modulus E_t of $E/100$. The parameters listed in Table 2.3, which were used for the calibration of the bulk material, are intended to describe an idealized aluminum material.

Investigations of the deformation patterns of honeycombs in the large strain regime, which determine the materials' energy absorption capacity, can also be carried out with this unit cell model. In such simulations the initiation of densification can be identified from the occurrence of surface self-contact in the collapsed voids, the modeling of which required special provisions in terms of the unit cell geometry; in the proposed unit cell all boundaries run within the cell walls, which means that no contact has to be accounted for at the outer boundary of the model. The free surface on the inside of the honeycomb cells is a closed surface and, therefore, suitable for detecting self-contact. Such unit cells have been found to answer well for the self-contact problem, compare Figure 2.16 which shows symmetric and periodic deformation modes before the onset of densification. The main advantage of unit cells of the above type is that all free surfaces of the voids face inwards, allowing for a straightforward use of contact algorithms.

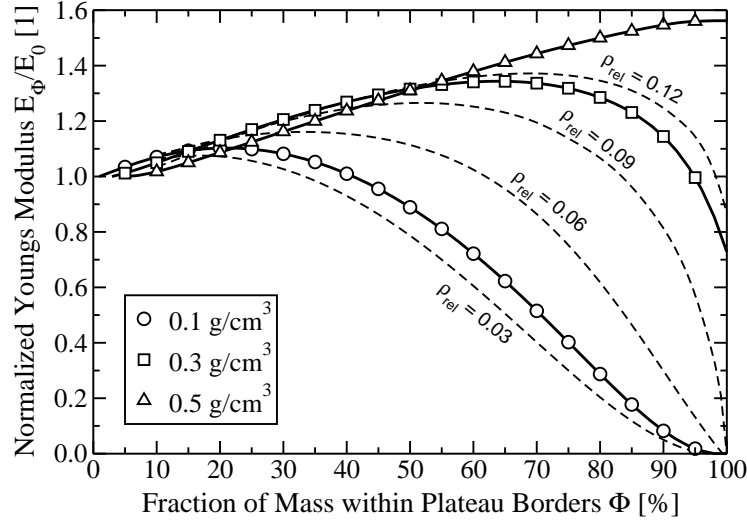


Figure 2.17: Predicted effective stiffness of hexagonal honeycombs normalized by the stiffness E_0 for $\Phi = \Phi_{\min}$ as a function of the material distribution between walls and cell vertices (Plateau borders).

2.4.3 Results and Discussion

Elastic Stiffness

The effective elastic stiffness of regular hexagonal honeycombs with Plateau borders was determined by compressing Finite Element models with perfect geometric symmetry, that is, without curved walls or wiggles, in the vertical direction. An example of the resulting symmetric deformation mode is depicted in Figure 2.16 (left).

The predicted structural stiffness is expressed by the normalized effective modulus E_Φ in Figure 2.17. The reference modulus E_0 for the curves in this diagram is the modulus determined for a perfect honeycomb without Plateau border transition regions ($R = 0$). The solid lines correspond to absolute densities of 0.1, 0.3, and 0.5 g/cm³, with aluminum ($\rho_s = 2.7$ g/cm³) being the bulk material. The dashed lines representing relative densities between 0.03 and 0.12 are results derived in a similar Finite Element study by Simone and Gibson [106]. They agree very well with the ones predicted by the proposed unit-cell model.

The results show an increase of the effective elastic modulus for volume fractions Φ up to approximately 25%. At this point, the predicted stiffness of the honeycomb with the lowest density shows a maximum and starts to drop for increasing volume fractions. The relative density of this honeycomb ($\rho_{\text{rel}} = 0.037$) is below the critical relative density $\rho_{\text{rel}}^* = 0.0931$ for vanishing cell wall thickness. Hence, the effective modulus tends towards zero for $\Phi \rightarrow 1$.

The honeycomb of intermediate density (0.3 g/cm^3) gains elastic stiffness up to a volume fraction of $\Phi \approx 65\%$, where the elastic stiffness is 35% above the one of the perfect reference honeycomb. For higher volume fractions, the effective elastic modulus drops again until it reaches a value of 70% E_0 at $\Phi = 1$. In this case $\Phi = 1$ means that the cell wall length l_w becomes zero, while the cell wall retains a finite thickness t_{\min} according to Equation (2.25).

For the honeycomb with the highest density (0.5 g/cm^3) an increase of the Plateau border volume fraction Φ leads to a monotonic increase of the effective stiffness, with the highest stiffness for $\Phi = 1$ being 55% higher than the stiffness of the corresponding perfect honeycomb. For this density, the formation of Plateau borders is beneficial for arbitrary values of Φ .

The influence of the mass distribution between the cell walls and the cell vertices on the predicted effective stiffness shows the two contrary effects caused by a redistribution of material in the honeycomb:

1. With increasing values of Φ , material is shifted from regions subjected to small local bending moments, such as the center of the edge, to regions, where the local bending moment is maximal, that is, close to the vertices. This redistribution leads to a stiffening of the microstructure.
2. On the other hand, increasing Φ implies a reduction of the thickness of the cell wall, thus reducing the stiffness of the straight-walled cell sections.

Which of these two mechanisms is the governing one depends on the relative density and on the vertex volume fraction Φ . For the aluminum honeycomb with 0.5 g/cm^3 absolute density the stiffening effect dominates for all values of Φ . For lower densities, the influence of the two mechanisms is more balanced, and the effective stiffness shows a maximum for intermediate Φ values.

Onset of Yielding

With the semi-analytical model governed by Equation (2.40) and the numerical method described in Section 2.3.2, it is possible to predict the onset of local yielding for proportional, that is, radial loading paths.

Figure 2.18 shows deformed configurations of a perfectly regular aluminum honeycomb with an absolute density of 0.5 g/cm^3 and three different vertex volume fractions ($\Phi=10\%$, 50% , and 90%). In the top row, the symmetric deformation modes under vertical uniaxial tension are depicted. In the bottom row, the deformed configurations for uniaxial tension in the horizontal direction are shown. All configurations were predicted by means of linear elastic analyses.

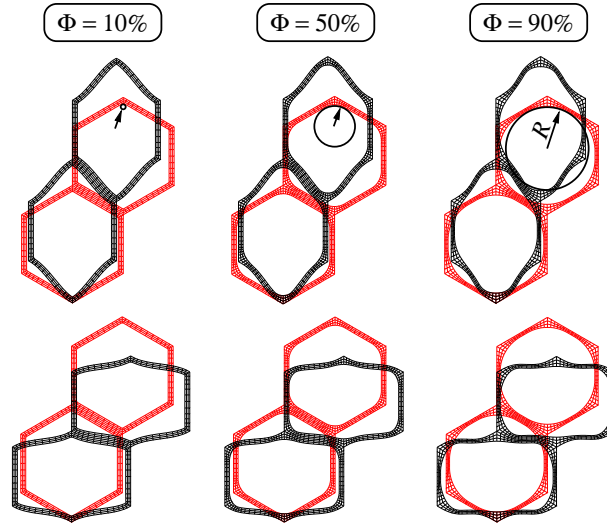


Figure 2.18: Predictions for undeformed and deformed configurations for uniaxial tension in “vertical” (top row) and “horizontal” direction (bottom row) for a honeycomb of 0.5 g/cm^3 density and different volume fractions Φ .

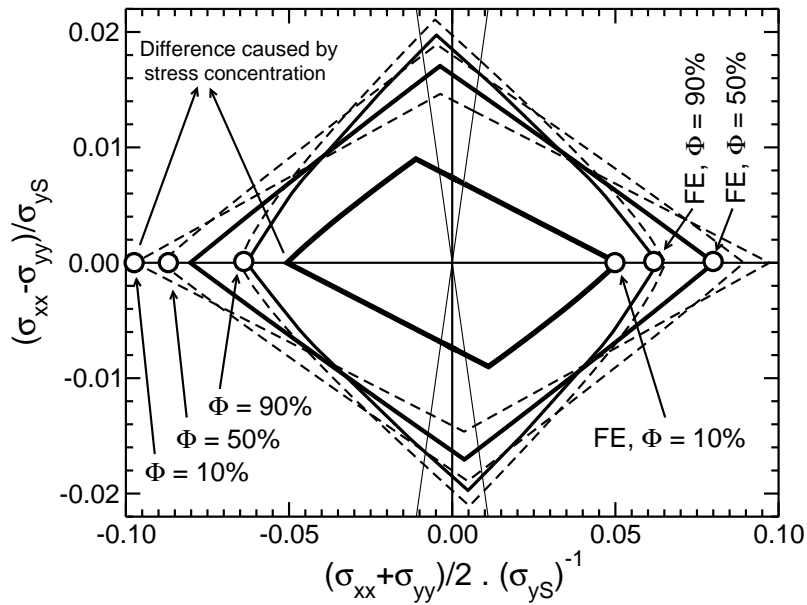


Figure 2.19: Applied macroscopic stress states $(\sigma_{xx}^*, \sigma_{yy}^*)$ leading to the onset of yielding in hexagonal aluminum honeycombs of a density of 0.5 g/cm^3 and different vertex volume fractions Φ . The dashed lines represent semi-analytical predictions.

The corresponding curves representing applied macroscopic stress states $(\sigma_{xx}^*, \sigma_{yy}^*)$, that lead to the onset of local yielding, are shown in Figure 2.19. In this diagram, the abscissa represents plane hydrostatic stress states $\sigma_{xx} = \sigma_{yy}$. The ordinate marks applied stress states of pure shear $\sigma_{xx} = -\sigma_{yy}$. Uniaxial stress paths are projected to straight lines with a gradient of $\pm 2:1$. Solid lines correspond to Finite Element results, and dashed lines represent semi-analytical predictions.

For uniaxial stress states, the semi-analytical model predicts yield stresses that are highest for the $\Phi=90\%$ honeycomb and lowest for the $\Phi=10\%$ honeycomb, indicating that, as it was the case for the effective stiffness, a shift of material from the cell wall to the vertex is beneficial, at least for the considered density of 0.5 g/cm^3 .

With increasing biaxiality the critical cross-section moves towards the middle of the cell edge, but remains within the Plateau border ($x < l_p$). The perfectly biaxial applied stress state $\sigma_{xx} = \sigma_{yy}$ is a special case, because it causes uniform normal stress states in the whole cell wall section between the Plateau borders. The mathematical model predicts macroscopic plane-hydrostatic yield stresses, which increase for decreasing vertex volume fractions Φ . This prediction is in line with the expectations, because (a) the biaxial applied stress state causes only normal stresses in the cell wall, and (b) the thickness of the cell wall decreases with increasing Φ . Hence, the perfect honeycomb has the highest biaxial yield strength at least according to linear elastic beam theory.

The predicted yield surfaces obtained by the evaluation of the Finite Element analyses agree very well with the mathematical results for intermediate and high vertex volume fractions. For the honeycomb “closest” to the perfect configuration, that is, for low Φ values, the yield surface predicted by the Finite Element method is much smaller than the respective analytical one. The reason for this discrepancy is the ability of the Finite Element method to resolve local stress concentrations. Figure 2.20 shows a detail of the vertex area of the honeycomb with a contour plot of the von Mises equivalent stress. Along the surface of the cell wall, the von Mises equivalent stress increases almost linearly as expected from the predictions of beam theory. In the small transition area between the cell edges, stress concentration effects cause a local stress peak with equivalent stress values that are 2.4 times as high as the nominal stresses in the immediate surrounding. Such local stress concentrations cause the macroscopic yield surface to shrink disproportionally for Φ values approaching Φ_{\min} . They are also liable to have a marked detrimental effect on the fatigue strength of the honeycomb.

Collapse under Uniaxial Compression

Beyond the yield limit discussed above, the mechanical response of the honeycomb structure becomes inelastic. Figure 2.21 shows predicted macroscopic stress-strain relationships for an aluminum honeycomb of 0.1 g/cm^3 apparent density and different vertex volume fractions Φ . The symmetry of the Finite Element models used for these simulations was perturbed with small geometrical imperfections to trigger a periodic deformation mode,

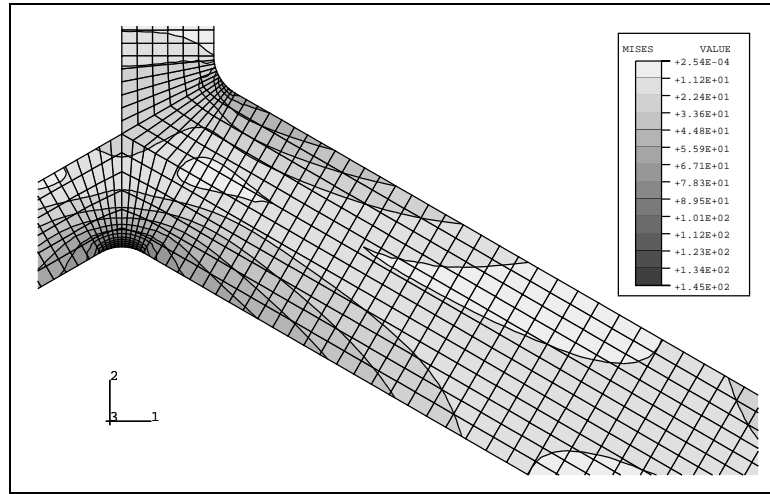


Figure 2.20: Predicted distribution of the von Mises equivalent stress in detail of a nearly perfect hexagonal honeycomb under uniaxial tension in the horizontal direction.

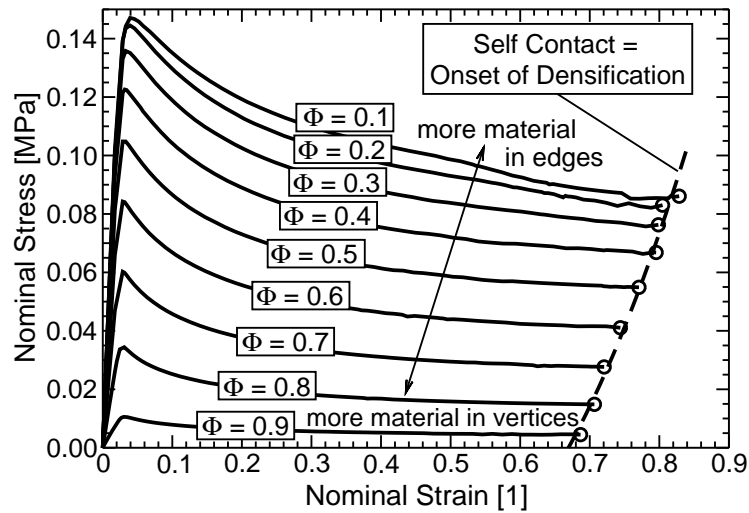


Figure 2.21: Predicted macroscopic stress–strain relationships of hexagonal aluminum honeycombs of 0.1 g/cm^3 apparent density and different vertex volume fractions Φ .

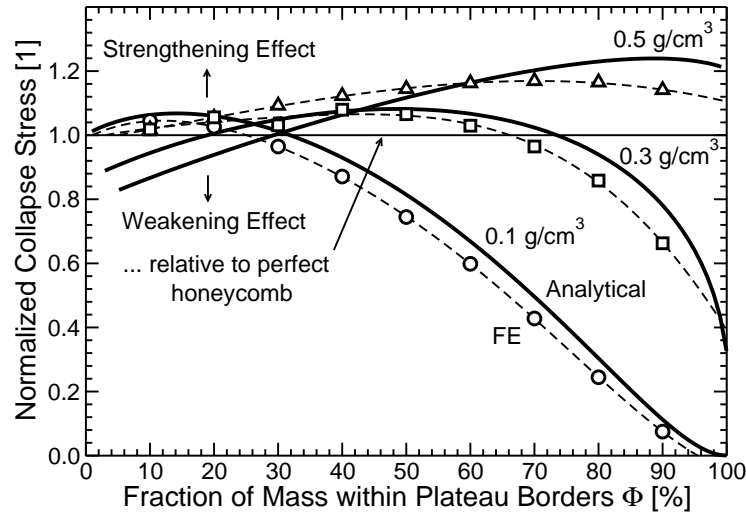


Figure 2.22: Normalized macroscopic collapse stresses predicted by a semi-analytical model (solid lines) and FE analyses (dashed lines) as functions of the material distribution between cell walls and cell vertices (Plateau borders) for three different apparent densities.

compare Figure 2.14.

The stress–strain relationships in Figure 2.21 exhibit a distinct peak between 3% and 4% nominal strain. Beyond this peak stress, the level of the macroscopic stresses drops steadily until self-contact occurs. At these points, which are connected by a dashed line in Figure 2.21, the stress level jumps instantly to values that are several orders of magnitude higher than the initial peaks. At this point, the simulations were stopped. The instantaneous densification is a consequence of the small number of cells in the model and of the applied periodic boundary conditions, both of which do not allow for a stepwise localization of the deformation.

For the aluminum honeycomb of 0.1 g/cm³ absolute density, the transfer of material to the cell vertices for increasing values of Φ consistently reduces the peak stress, as can be seen from Figure 2.21. Plotting the normalized collapse stresses for the two high densities, 0.3 g/cm³ and 0.5 g/cm³, shows that this is not a general rule, see Figure 2.22. As for the elastic stiffness, the simulations reveal a slight strengthening effect for small values of Φ . This effect is most pronounced for the highest density, where it leads to a relative increase of 15% in the strength of the honeycomb. Unlike the predictions of the elastic stiffness, the predicted strength shows a maximum for $\Phi = 70\%$.

Figure 2.22 also contains predictions for the uniaxial limit load obtained with beam theory (solid lines). For low and intermediate densities, the qualitative and the quantitative agreement with the Finite Element results is excellent. The predicted strength for the high density deviates from the simulation results for very low and very high Φ values. A

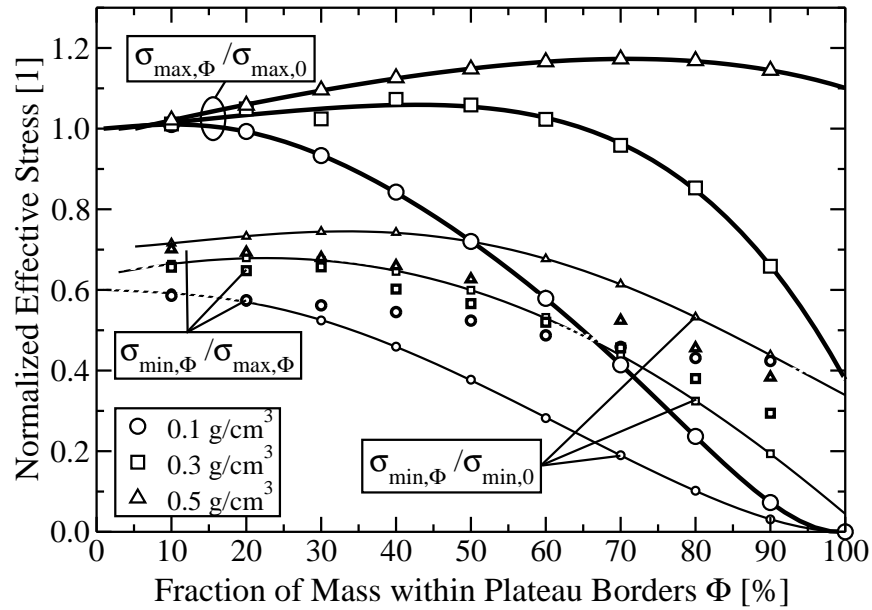


Figure 2.23: Predicted normalized macroscopic collapse stresses as functions of the material distribution between cell walls and cell vertices (Plateau borders) for three different apparent densities.

visual inspection of the models depicted in Figure 2.18 leads to the conclusion, that the applicability of beam theory has to be re-assessed for high apparent densities.

Uniaxial Compression until Densification

The specific unit cell setup used in this investigation allows for the extension of the crush deformation domain to the point of self-contact. The description of the effective mechanical behavior beyond the onset of yielding and before the moment of self-contact and, therefore, densification is important for the assessment of the energy absorption characteristics of the microstructure.

Two parameters govern the amount of energy that is necessary to deform the honeycomb up to the point of densification: (a) the macroscopic peak stress and (b) the overall strain, for which densification occurs, that is, the point, at which opposite cell walls get into contact. Figure 2.23 shows both the normalized macroscopic peak stress $\sigma_{\Phi, \max}$ for different densities and vertex volume fractions as well as the normalized stress $\sigma_{\Phi, \min}$ shortly before contact occurs. The ratio between those two stress levels is also shown. In all cases the macroscopic peak stress is distinctly higher than the stress prior to contact, indicating softening during the deformation process.

Figure 2.24 shows the dependency of the strain at the first moment of contact on the fraction of mass in the vertices/Plateau borders. For all densities, this strain decreases

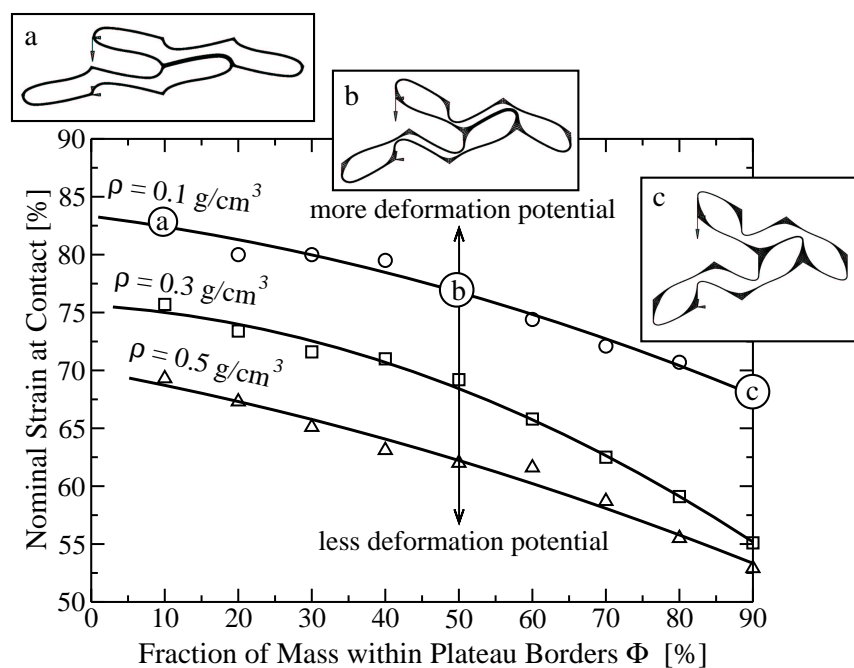


Figure 2.24: Predicted macroscopic nominal strains at first cell wall contact as functions of the material distribution between walls and cell vertices (Plateau borders) for three different apparent densities.

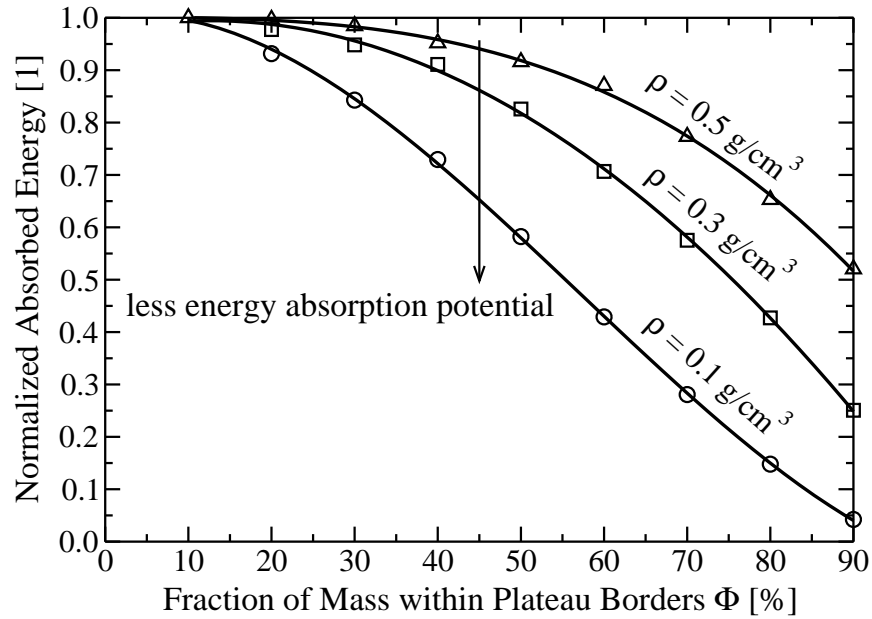


Figure 2.25: Predicted normalized absorbed energy (up to first cell wall contact) as functions of the material distribution between the cell walls and the cell vertices (Plateau borders) for three different apparent densities.

with an increasing fraction of material in the vertices. This is a result of the changing kinematics in the honeycomb, as the deformed configurations in Figure 2.24 demonstrate; the larger the vertex section is, the farther the yield hinge is situated away from the vertex center. This manifests itself in a smaller overall contact strain, and, hence, in a reduced stroke length usable for energy absorption.

The resulting influence of the material distribution between cell vertex and cell wall on the effective energy absorption behavior is demonstrated in Figure 2.25, where the amount of mechanical energy necessary to crush the unit cell up to the point of self contact is plotted. Perfect honeycombs without Plateau borders have the highest energy absorption capacity. Any shifting of material reduces this capacity. It has to be concluded that the reduction of the usable strain domain, or, in other words, of the usable stroke length, is the governing factor for this relationship. The increase of the peak stress, which was observed for the honeycomb of high absolute density and intermediate values of Φ (Figure 2.23), cannot compensate for the loss of deformation capacity owing to the influence of the Plateau borders on the deformation kinematics.

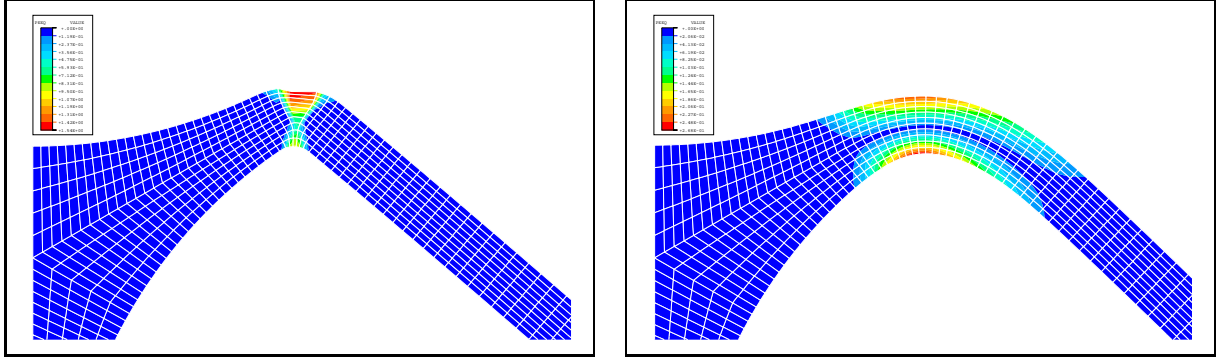


Figure 2.26: Formation of plastic hinges at the transition from the Plateau border and the cell wall for an ideally plastic material (left) and a material with isotropic hardening (right).

Influence of the Bulk Materials' Hardening Behavior

It has to be noted, that the hardening behavior of the bulk material does not only influence the plastic failure moment of a cross-section, but also the deformation kinematics. Figure 2.26 shows a detail of the predicted deformed configurations of honeycombs with Plateau borders and different degrees of hardening. In the left picture in Figure 2.26, the deformed configuration is given for an elastic-ideally plastic bulk material. The formation of a very localized yield hinge is apparent. As a matter of fact, the deformation localizes in a single column of Finite Elements, resulting in a sharp kink in the cell wall. Figure 2.26 (right), on the other hand, shows the deformed configuration predicted for a bulk material with linear hardening. Here, the plastic zone is extending over a comparatively wide area while the neutral axis of the beam remains elastic. This can be attributed to the fact that the outer regions of the edge increase in their yield strength as long as they experience growing plastic strains. This behavior leads to a deformation of the cell wall in the form of an arc of finite radius.

2.4.4 Conclusions

Drainage of the material into Plateau borders reduces the cell wall thickness, which is the governing parameter for the strength and the stiffness of honeycombs. This is especially important in the case of foams of very low density, for which the cell wall thicknesses approach zero. At higher densities, however, the redistribution of material towards the cell vertices and, therefore, into regions subjected to higher bending moments can be beneficial for the overall properties. Furthermore, smooth transitions with large radii of curvature were shown to reduce stress concentration effects in the transition region between adjacent honeycomb edges, which is beneficial for the yielding and the fatigue behavior of the

microstructure.

As more material is accumulated in the vertices, the plastic hinges tend to form more closely to the mid-region of the cell edges, so that the size of the nearly rigid regions around the vertex is increased. Although such a zone can rotate during compression it still takes up more space because the distance between the hinges and the vertex centers is increased. Together with changes in the folding kinematics this causes the cell walls to contact each other at lower strains than it is the case for microgeometries with less pronounced Plateau borders. This effect dominates the energy absorption potential as shown in Figures 2.23, 2.24, and 2.25.

Even in cases, where the collapse and pre-contact loads are increased by the material redistribution, the decrease of the usable deformation length reduces the amount of energy that can be converted by plastic deformation before the densification regime is reached. Strong mass concentrations in the edges reduce the weight efficiency of the material with respect to energy absorption.

2.5 Influence of Non-Uniform Cell Wall Thickness

Microscale fluctuations of the material distribution in cellular materials may, on the one hand, be due to thickness variations within individual cell walls as discussed above in connection with Plateau borders or can, on the other hand, be caused by individual cell walls having different thicknesses. The latter problem was addressed by Grenestedt and Bassinet [41], who developed a three-dimensional tetrakaidecahedral model of a closed cell foam that contains a total of 112 cell walls, the thicknesses of which could be assigned individually. Their results show that the stiffness of regular closed cell arrangements is rather insensitive to the presence of cell walls with different thickness. This was explained noting that such microgeometries deform primarily by cell wall stretching, which is less sensitive to cell wall thickness effects than bending modes induced, for example, by corrugated cell walls.

Meguid et al. [69] studied the crush behavior of closed cell metallic foam with a representative Finite Element model based on a modification of the truncated cube model [94] consisting of an array of cubic cells the corners of which are replaced by two pyramidal sections forming a smaller closed cell around the replaced cube corner. In [69] the pyramidal cell was replaced by a spherical one, and a multi-cell FE model consisting of $5 \times 5 \times 5 = 125$ individual unit cells was composed. To achieve different apparent densities in the model, the cell wall thickness was varied across the unit cells. The authors then simulated uniaxial compression tests. In comparison to experimental results they found the predicted force–displacement behavior to fit the measured one much better than force–displacement curves predicted with a reference model of uniform cell wall thickness, which overestimated the collapse force and showed very large oscillations caused by the layer-wise collapse of the microstructure (see also Section 2.8). Comparing the absorbed energy in all configurations, they achieved 5% accuracy with the randomized model as opposed to a 40%

difference between the prediction of the uniform model and the experiment.

Variation of the cell wall thickness in otherwise regular microstructures leads to deformation localization and lower yield and collapse stresses. Meguid et al. [69] showed that statistical variations of the cell wall thickness can improve the predictive quality of multi-cell Finite Element models significantly.

2.6 Influence of Wavy and Curved Cell Walls

2.6.1 Introduction

In addition to inhomogeneous thickness distributions, the geometries of cell walls may also be perturbed by deviations from simple linear (honeycombs) or planar (three-dimensional foams) connections between the vertices. Straight strut or plane wall geometries are in fact good approximations for low-density organic foams. In metallic foams, however, curved and corrugated (“wavy”) cell walls typically are present, compare the curved cell wall in Figure 2.12.

Grenestedt [39] studied the influence of wavy cell wall imperfections on the elastic stiffness of cellular solids and found that the bulk modulus decreases by some 50% when corrugations with an amplitude of twice the thickness of the cell walls are added. Simone and Gibson [107] documented the detrimental effect of curved and corrugated cell walls on the stiffness and strength of regular honeycombs and perfectly tetrakaidecahedral unit cell models. The Young’s modulus was shown to be more adversely affected by these imperfections than the collapse stress. Chen et al. [11] gave analytical expressions for the yield surfaces of regular honeycombs with wavy cell walls. They found that corrugations significantly reduce the hydrostatic yield strength of honeycombs, whereas the deviatoric yield stresses are hardly affected. Evidently, cell wall bending is activated in addition to membrane deformations even under overall hydrostatic loading.

In this section, the investigation of the effects of imperfect cell wall geometries on the onset of yielding and failure by elastic buckling will be extended to irregular honeycombs and general biaxial stress states.

2.6.2 Method

A periodic unit cell model of a regular hexagonal honeycomb was used as the reference geometry for the prediction of the influence of cell wall geometry imperfections. The model contained 30 individual cells as shown in Figure 2.27 (left; the other two topologies will be discussed in Section 2.8). Periodic boundary conditions were prescribed to achieve periodic plane-filling deformation patterns.

The honeycomb struts were modeled using 8 three-node beam elements with quadratic interpolation functions (ABAQUS element type B22). The cell edge length was set to 1.963 mm. The thickness of the rectangular beam sections was adjusted to achieve the desired apparent density. The model bulk material was characterized as an elasto-plastic solid described by J_2 -flow theory and isotropic, linear hardening. The bulk material properties were chosen as those of a generic aluminum alloy (see Table 2.3).

The initial overall yield surfaces of hexagonal honeycomb models with different geometrical imperfections were determined with the postprocessing method proposed in Section

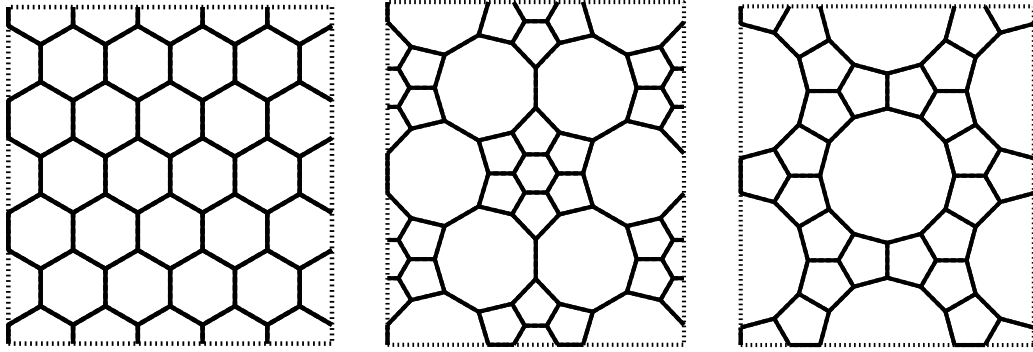


Figure 2.27: Honeycomb geometries for studying the interaction of cells of different sizes [17]: Regular hexagonal arrangement (“HC”, left), a cluster of small cells surrounded by big cells (“SBS”, center), and big cells surrounded by small cells (“BSB”, right).

2.3. At the same time, the effective elastic stiffness of the microstructure was calculated. Additionally, elastic buckling analyses were performed for a large number of radial stress paths in the compressive regime.

2.6.3 Results

The influence of the relative amplitude of geometrical cell wall imperfections was studied both on regular hexagonal honeycombs as well as irregular hexagonal honeycombs, that is, honeycombs, the regularity of which was disturbed by shifting cell vertices in a statistically controlled manner (see Figure 2.2, right). Specifically, the vertex positions were perturbed by random displacements following a Gaussian distribution with a given standard deviation of 15% of the honeycomb edge length ($\bar{r} = 0.3$ mm) in the radial direction and a normal distributed angle of translation.

Table 2.4 lists selected results for (a) a perfect regular honeycomb of 0.1 g/cm^3 density, (b) an irregular honeycomb with three different apparent densities, (c) the same irregular honeycomb with wiggles of a relative wiggle amplitude w_{rel} of up to 10% of the strut length, and (d) the same irregular honeycomb with curved cell walls and a curvature amplitude c_{rel} of up to 10% of the strut length. Simulations (c) and (d) were performed assuming an apparent foam density of 0.1 g/cm^3 . In the results Table 2.4, the following macroscopic stress values are given: $\sigma_{Y,x}$, $\sigma_{Y,y}$, and $\sigma_{Y,m}$, which are, respectively, the overall stresses causing initial micro-yielding under loading in x - and y -direction as well as under plane hydrostatic stress conditions, and $\sigma_{B,x}$, $\sigma_{B,y}$, $\sigma_{B,m}$, which are the macroscopic uniaxial stresses and the macroscopic biaxial stress causing elastic buckling. The two buckling modes of the regular honeycomb model were presented earlier, see Figure 2.9.

The dependence of the effective elastic stiffness on the amplitude of the cell wall imperfec-

ρ_F [g/cm ³]	\bar{r} [mm]	w_{rel} [%]	C_{rel} [%]	$\sigma_{Y,x}$	$\sigma_{Y,m}$	$\sigma_{Y,y}$	E_x
				$\sigma_{B,x}$	$\sigma_{B,m}$	$\sigma_{B,y}$	E_y
Perfect Hexagonal Honeycomb							
0.1	0.0	0	0	0.10235	3.68765	0.10379	5.30000
				0.69908	0.40527	0.48690	5.30000
Irregular Hexagonal Honeycombs of Different Density							
0.1	0.3	0	0	0.06075	0.12223	0.06612	5.73356
				0.62719	0.56021	0.48249	5.45780
0.3	0.3	0	0	0.53763	1.01962	0.59719	146.678
				16.7360	10.6066	12.9030	139.659
0.5	0.3	0	0	1.48478	2.64190	1.67785	614.428
				75.6770	48.2869	58.5990	586.239
Irregular Hexagonal Honeycombs with Cell Wall Wiggles							
0.1	0.3	2	0	0.05956	0.11592	0.06682	5.60501
				0.62707	0.39502	0.48173	5.35848
0.1	0.3	4	0	0.05884	0.11031	0.06805	5.34423
				0.61829	0.39079	0.47705	5.13871
0.1	0.3	6	0	0.05851	0.10538	0.06849	4.98826
				0.60256	0.38378	0.46887	4.82439
0.1	0.3	8	0	0.05824	0.10087	0.06918	4.57481
				0.58196	0.37448	0.45779	4.45010
0.1	0.3	10	0	0.05767	0.09267	0.07005	4.13927
				0.55825	0.36347	0.44453	4.05018
Irregular Hexagonal Honeycombs with Curved Cell Walls							
0.1	0.3	0	2	0.06154	0.13317	0.06725	5.69133
				0.62480	0.39771	0.48486	5.41431
0.1	0.3	0	4	0.06256	0.13770	0.06662	5.59947
				0.61997	0.39833	0.48559	5.31975
0.1	0.3	0	6	0.06382	0.12351	0.06612	5.46097
				0.61281	0.39798	0.48470	5.18091
0.1	0.3	0	8	0.06530	0.11224	0.06568	5.28443
				0.60351	0.39660	0.48224	5.00337
0.1	0.3	0	10	0.06367	0.10323	0.06532	5.07614
				0.59234	0.39415	0.47830	4.79688

Table 2.4: Selected results of the elastic yield and elastic buckling analysis under uni- (x,y) and biaxial (m) compression. All nominal stresses and the elastic moduli are given in [MPa].

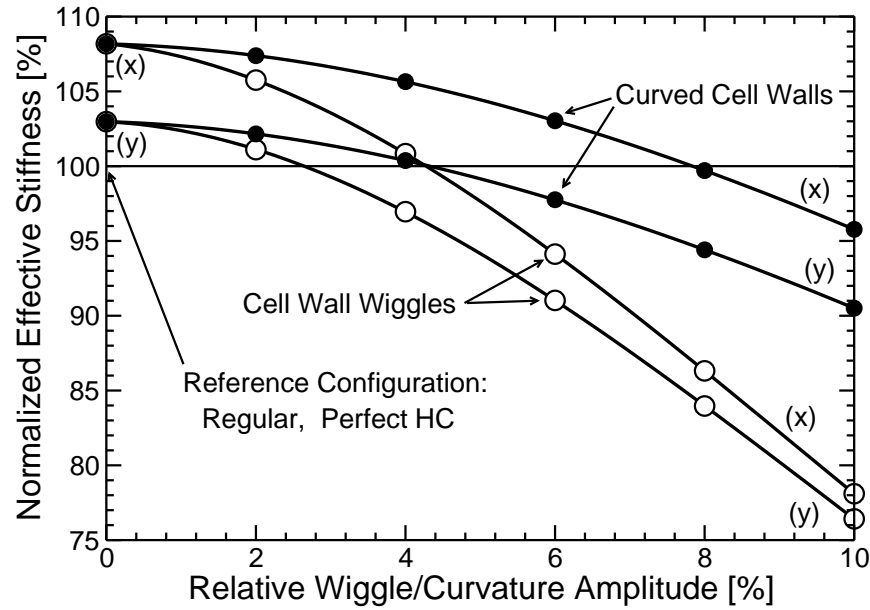


Figure 2.28: Effective stiffness of an irregular hexagonal honeycomb with cell wall wiggles and curved cell walls of different amplitude; (x) and (y) denote the loading direction.

tions is displayed in Figure 2.28. In this diagram, all effective stiffness values are normalized by the effective stiffness of a perfect regular honeycomb. The stiffness of 5.3 MPa, which was predicted by the Finite Element simulation for this configuration agrees very well with the analytical estimate

$$E_x = E_y = E_s \frac{4}{\sqrt{3}} \left[\frac{t}{l} \right]^3 = 5.33 \text{ MPa}, \quad (2.41)$$

where t is the cell wall thickness and l is the cell strut length of a regular hexagonal honeycomb [34]. It is obvious from Figure 2.28 that irregularities in the vertex positions make the microstructure slightly stiffer and introduce some anisotropy. Cell wall wiggles reduce the relative effective stiffness to a stronger extent than curved cell walls. With respect to the irregular configuration with straight cell walls, the relative decrease of stiffness with increasing imperfection amplitude is approximately the same in the two loading directions.

Apart from the elastic stiffness of the honeycombs general overall yield and buckling stress states were investigated and are displayed as curves in the normal stress plane in Figure 2.29. Figure 2.29(a) shows the overall yield and overall buckling curves for a regular hexagonal honeycomb with different wiggle amplitudes. Figure 2.29(b) shows the overall yield curves for an *irregular* hexagonal honeycomb with wiggles of different amplitude. The same irregular base geometry was analyzed in Figure 2.29(c), but parabolic cell walls of different curvature were superimposed. Figure 2.29(d) presents predicted overall yield surfaces for different irregular honeycombs. The standard deviation of the radial displacement of the

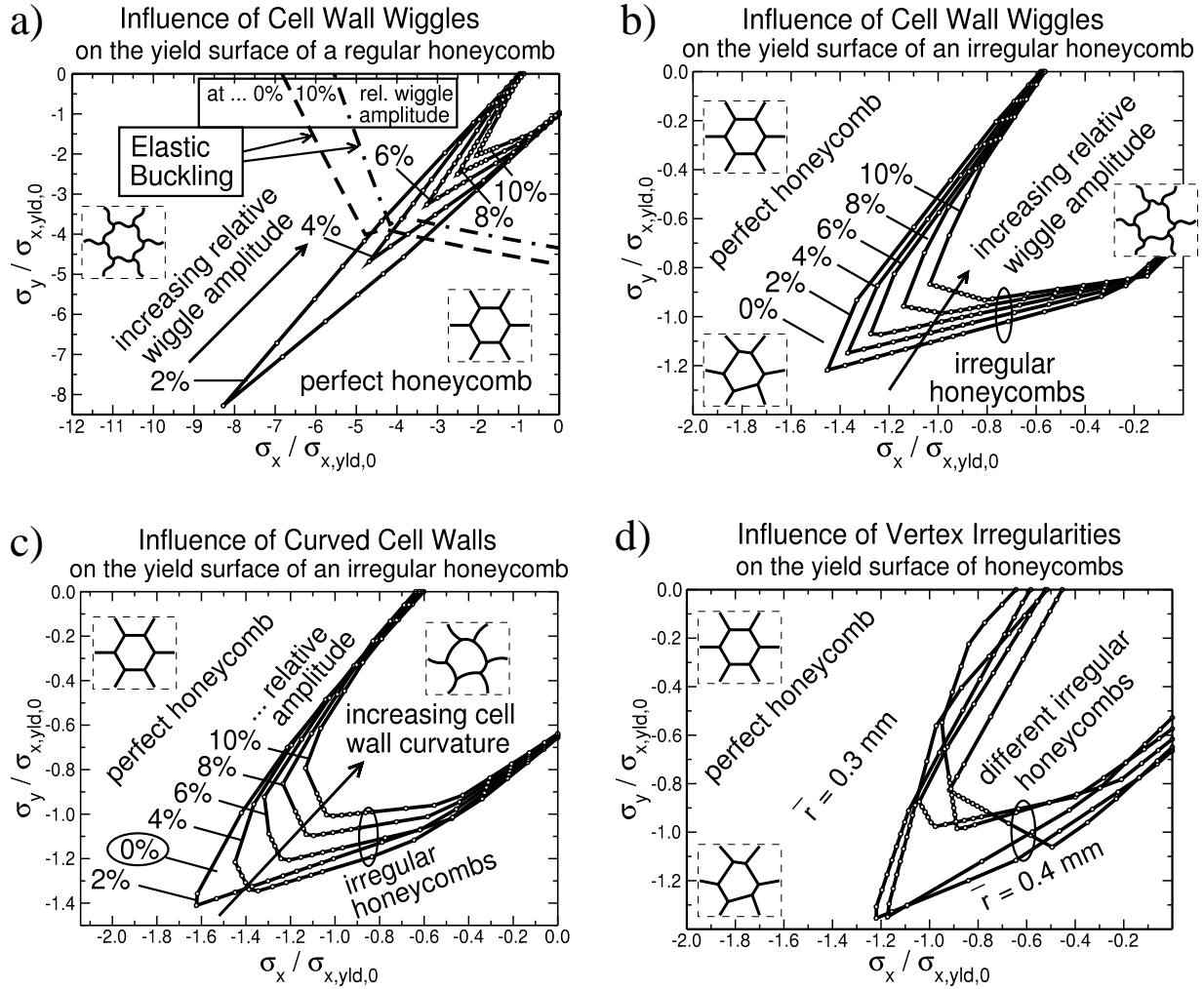


Figure 2.29: Predicted overall yield surfaces for regular and irregular honeycombs with different types and degrees of imperfections [17]. Dashed and dash-dotted lines denote elastic buckling stress states.

cell vertices was 20% of the honeycomb edge length ($\bar{r} = 0.4$ mm) for the overall yield curves represented by solid lines.

2.6.4 Discussion

The influence of corrugated and curved cell walls on the onset of nonlinear behavior was studied by evaluating initial yield surfaces according to the postprocessing method proposed in Section 2.3. Figure 2.29 shows such curves, which represent overall stress states that give rise to the local onset of yielding or to local elastic buckling in regular and perturbed honeycombs having curved and wavy cell walls of varying curvature.

In perfect regular honeycombs in-plane hydrostatic compression leads to pure membrane stresses in the cell walls, which gives rise to an elongated overall initial yield surface in the σ_x - σ_y stress plane. For low-density perfect honeycombs, this yield surface is truncated by the failure surface for elastic cell wall buckling, compare the dashed lines in Figure 2.29(a), which shows a kink due to the change of the buckling mode. The two buckling modes of a regular honeycomb were displayed earlier, see Figure 2.9. This type of behavior is maintained in the presence of small corrugations, but when the amplitudes of wiggles exceed about 5% of the wall thickness yielding alone determines the onset on nonlinearity.

The influence of wiggles and curved cell walls on the yield surfaces of honeycomb microgeometries, that are irregular from the outset, is much less pronounced, see Figures 2.29(b-c). Perturbing the geometry by randomly displacing cell vertices causes the yield surface to shrink even more than the presence of severe wiggles, compare Section 2.7. Corrugated or curved cell walls generally have little effect on the uniaxial yield strength, but severe wiggles can reduce the in-plane hydrostatic yield stress by some 35%. Curved cell walls typically give rise to similar effects as wiggles, see Figure 2.29(c), but cell walls incorporating only slight curvature can lead to minor increases of the in-plane hydrostatic yield stress.

2.7 Influence of Irregular Vertex Positions

Generic models for cellular materials are commonly based on regular periodic microgeometries, the simplest geometry being hexagonal honeycombs for the two-dimensional case. A comparison of such a honeycomb structure to a cross section of an actual metallic foam as shown in Figure 2.12 makes clear that the latter is far from being a regular structure. A standard assumption in modeling efforts is that different types of geometrical imperfections may be studied in isolation. Following this strategy, the present section concentrates on the effects of irregularities of the overall cell geometry while neglecting the cell wall imperfections discussed above.

It can be shown that the elastic stiffness of a honeycomb model is not very sensitive

to irregularities and perturbations of the vertex positions. In fact, upon comparing the elastic stiffnesses of hexagonal and Voronoi honeycombs, Silva et al. [105] reported that the overall elastic moduli are some 5 to 10% higher in the latter case, which is in excellent agreement with Figure 2.28. Zhu et al. [122] defined a measure for the irregularity of Voronoi honeycombs and correlated it to the predicted elastic properties. They found the effective Young's and shear moduli of periodic Voronoi honeycombs to increase with growing irregularity, whereas the effective bulk modulus decreases. In [121] they applied the same methodology to three-dimensional open cell foams and obtained analogous results. Grenestedt and Tanaka [42] examined the elastic behavior of three-dimensional closed cell Voronoi unit cells, finding a decrease in the bulk modulus of 5 to 10% compared to regular tetrakaidecahedra.

The uniaxial yield stress of honeycomb models can be reduced by some 40% by perturbing the positions of the cell vertices, compare Figure 2.29(d), where the initial overall yield curves for a number of perturbed hexagonal honeycombs are compared. Silva and Gibson [104] reported a similar decrease in the yield strength of Voronoi honeycombs compared to hexagonal honeycombs, but a less pronounced reduction for the uniaxial yield stress was obtained by Chen et al. [11], who attribute this difference to the use of periodic rather than mixed boundary conditions for their unit cells. In addition to Voronoi honeycombs, they studied configurations obtained from hexagonal arrangements by randomly shifting the vertices and predicted uniaxial compressive yield stresses that are in good agreement with Figure 2.29. Both planar Voronoi microgeometries and perturbed hexagonal arrangements give rise to strongly reduced yield stresses under in-plane hydrostatic loading as compared to regular honeycombs, because the deformation mode tends to be cell wall bending rather than membrane compression [11]. In the case of the 0.1 g/cm^3 reference honeycomb in Table 2.4, the overall plane hydrostatic yield stress of the perturbed model is only 3.3% of the respective yield stress of the regular model.

As mentioned above, randomly shifting the vertex positions of regular honeycombs typically leads to more pronounced reductions of the overall yield limits than does the introduction of corrugations of the cell walls. In addition, the collapse stress, which is closely related to the macroscopic plateau stress, is decreased. Again, the most affected loading condition is in-plane hydrostatic loading. Loss of stability due to elastic buckling plays a significant role only in extreme cases of near-perfect microgeometries and very thin cell walls. For microgeometries with significant irregularities of the vertex positions elastic buckling would require uniaxial applied stresses that are about one magnitude higher than the predicted yield stress.

Clearly, irregular microgeometries are required for obtaining realistic results from simulations of the mechanical behavior of metallic foams. This is especially true when multiaxial loads or deformations are to be studied. In the presence of irregular vertex positions other imperfections such as cell wall corrugations typically are relegated to secondary roles.

Model	Cell incircle radius		Unit cell dimensions [mm] \times [mm]	Unit cell area [mm ²]	Total beam length [mm]
	large [mm]	small [mm]			
BSB	2.500	0.965	15.00 \times 17.32	259.81	164.76
SBS	2.500	0.873	11.29 \times 13.03	147.09	108.56
HC	1.700		17.00 \times 17.67	300.33	176.67

ρ_{app}	0.1 g/cm ³	0.3 g/cm ³	0.5 g/cm ³
ρ_{rel}	0.037	0.1	0.185
Model	Beam thickness [mm]		
BSB	0.05840	0.17521	0.29202
SBS	0.05018	0.15054	0.25091
HC	0.06296	0.18889	0.31481

Table 2.5: Summary of geometric parameters for the perfect models.

2.8 Interaction of Cells of Different Sizes

2.8.1 Introduction and Method

In metallic foams the sizes of the cells are typically far from uniform, compare Figure 2.12, and often regions containing small cells as well as clusters of very large cells can be identified. In order to gain some understanding of the interaction between larger and smaller cells, simulations of two-dimensional geometries consisting of generic periodic arrangements of cells of two different sizes, see Figure 2.27, were performed [17]. They comprise a regular hexagonal honeycomb (HC; Figure 2.27, left), serving as reference configuration, clusters of small cells surrounded by large cells (SBS; Figure 2.27, center), and isolated large cells surrounded by small cells (BSB; Figure 2.27, right).

The underlying geometries were constructed by closely packing circles with two different diameters. The cell walls were defined by the contact points and the common tangents of the circles. The vertices were positioned at the intersection points of the so-defined cell walls. The circles can be interpreted as inscribed circles of the polygons forming the foam cells. To establish a relation between the two inhomogeneous topologies the larger of the two incircle radii was chosen to be equal ($r = 2.5$ mm) for both models (see Table 2.5). The incircle radius of the reference honeycomb model was set to be approximately equal to the averaged incircle radius of the two other models. The number of cells was chosen as 28 for the SBS unit cell and 36 for the BSB unit cell. The size of the honeycomb unit cell was chosen to contain a comparable number of 30 cells. With the intention of simulating configurations that appear as “natural” as possible, all three topologies were investigated with perturbed microgeometries. For the large-strain analyses, these perturbations and

Model Topo.	ρ_F [g/cm ³]	\bar{r} [mm]	w_{rel} [%]	c_{rel} [%]	$\sigma_{Y,x}$	$\sigma_{Y,m}$	$\sigma_{Y,y}$	E_x
					$\sigma_{B,x}$	$\sigma_{B,m}$	$\sigma_{B,y}$	E_y
Perfect Hexagonal Honeycomb								
HC perf.	0.1	0.0	0	0	0.10235	3.68765	0.10379	5.30000
					0.69908	0.40527	0.48690	5.30000
Irregular Honeycombs with Different Topologies								
HC irreg.	0.1	0.3	0	0	0.06075	0.12223	0.06612	5.73356
					0.62719	0.56021	0.48249	5.45780
SBS	0.1	0.3	0	0	0.05841	0.12515	0.07197	6.85680
					0.54486	0.35397	0.59102	8.64782
BSB	0.1	0.3	0	0	0.06725	0.14774	0.06319	7.52634
					0.37377	0.25131	0.31546	6.54345

Table 2.6: Selected results of the elastic yield and elastic buckling analyses under uni- (x,y) and biaxial (m) compression. All nominal stresses and the overall elastic moduli are given in [MPa].

additional cell wall wiggles were imposed to trigger deformation localization.

Apart from the different geometry, all simulation parameters were equal to those used for the hexagonal honeycomb models discussed in Section 2.6.2. For the present section an emphasis was put on uniaxial and biaxial compressive deformation in the large strain domain, owing to the importance of these deformation modes in crash protection applications.

2.8.2 Results

In accordance with Table 2.4 for hexagonal honeycombs, Table 2.6 lists selected results for irregular honeycomb models of different topologies and an apparent density of 0.1 g/cm³. The presented absolute values were calculated on the basis of the generic aluminum bulk material described by Table 2.3. For a description of the result parameter identifiers in Table 2.6 see Section 2.6.3.

In comparison with the perfect hexagonal honeycomb, all of the perturbed models show reduced uniaxial and biaxial values of the overall initial yield stress. The maximum relative reduction of the uniaxial overall initial yield stress amounts to approximately 40%. The values of the overall initial yield stress are not ordered consistently; the yield stress in x -direction and the biaxial yield stress are highest for the BSB model while at the same time the yield stress in y -direction is the lowest for this model. Obviously, the scatter caused by the geometrical imperfections is larger than any intrinsic influence of the topology. Furthermore, a large degree of anisotropy is apparent for each model. The largest difference between the highest and the lowest uniaxial yield stress is 14% for the y -direction. Among

groups of identical models the largest difference between the two uniaxial yield stresses is 23% for the model SBS. This model shows both the largest and the smallest uniaxial yield stress among the imperfect models.

With respect to elastic buckling, the model BSB showed the least resistance in uniaxial and biaxial loading situations. This instability was caused by buckling of the long beam members connecting the clusters of small cells in combination with a rotation of the latter. Nevertheless, the buckling stresses were one order of magnitude higher than the initial yield stresses in the uniaxial loading situations. For biaxial loading, the difference was less pronounced, with the biaxial buckling stress of the model BSB exceeding the yield stress by 70%.

The effective elastic stiffness of the imperfect configurations was higher than that of the perfect reference honeycomb, the maximum increase of 63% being recorded for the modulus E_y of model SBS. The hexagonal honeycomb exhibited the lowest stiffness of the imperfect models.

The results presented so far only concerned the elastic behavior and the onset of non-linearity by yielding and by elastic buckling. To examine the influence of the microstructural topology, the collapse and post-collapse behavior of the three honeycomb models was calculated. Figures 2.30–2.32 show the results in form of predicted stress versus strain diagrams for uniaxial compression in both directions as well as for biaxial compression (dashed lines). Additionally, predicted deformed configurations are displayed for selected stages of uniaxial compression in x - and y -direction; arrows indicate the corresponding points on the stress–strain curves. The extension of the initial linear regime is shown as dotted lines. The convergence of the simulations depended on the complexity of the occurring self-contact conditions. Nominal compressive strains of up to 75% could be achieved.

The imperfections induced anisotropic mechanical behavior in all three models. Like the overall initial yield stresses, the initial peak stresses in the two principal directions varied considerably for the individual models. Some simulations showed a distinct initial peak stress marking the onset of cell collapse, while other stress–strain relationships exhibited an extended hardening regime prior to collapse (SBS, x -compression, see Figure 2.32). Besides these types of mechanical responses, behavior close to an ideally plastic one can be found (HC, x -compression, see Figure 2.30), at least up to intermediate compressive strains. The biaxial collapse stresses are consistently higher than the uniaxial collapse stresses. For simulations with compressive strains that extend into the densification regime, a characteristic steep increase of the compressive stress could be observed as soon as most of the cells had collapsed.

2.8.3 Discussion

The most obvious conclusion that can be drawn from results of the linear and buckling analyses (Table 2.6) is that the scatter induced by irregularities of the geometry and by

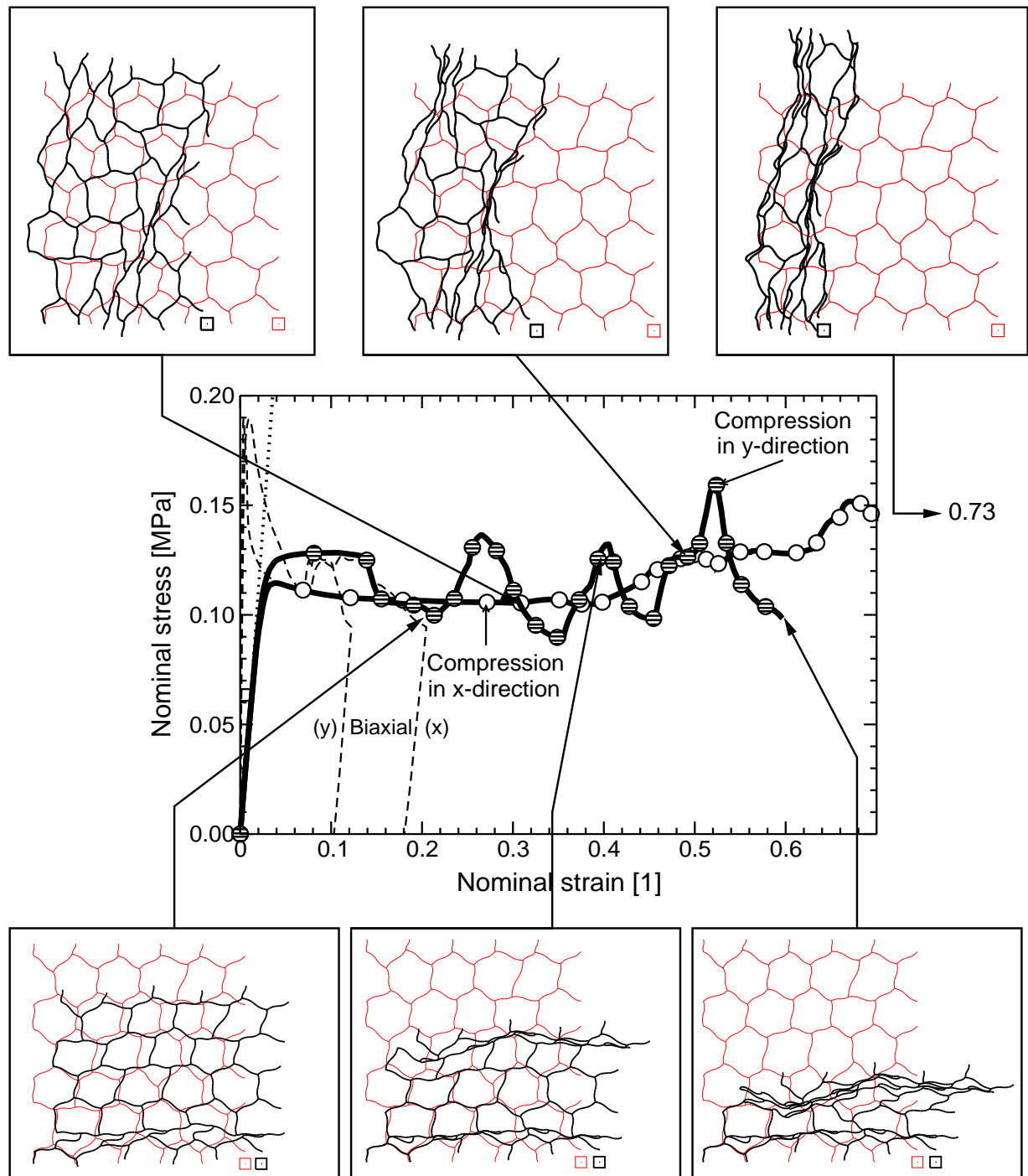


Figure 2.30: Predicted overall stress versus strain diagrams (center) for the imperfect and irregular hexagonal honeycomb model "HC". Plots of the deformed configurations under compression in x -direction (top) and in y -direction (bottom) are supplied.

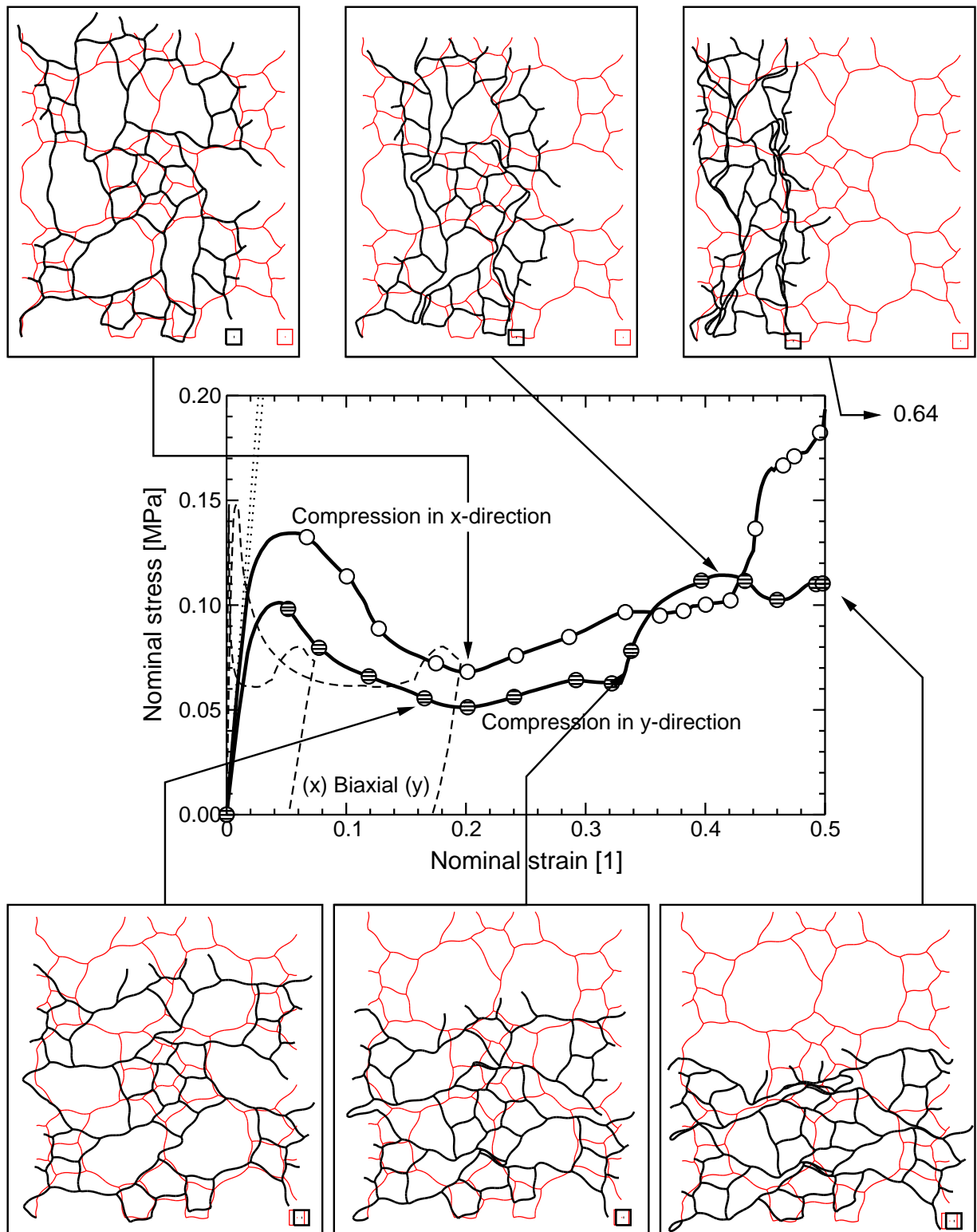


Figure 2.31: Predicted overall stress versus strain diagrams (center) for the imperfect and irregular honeycomb model "BSB". Plots of the deformed configurations under compression in x -direction (top) and in y -direction (bottom) are supplied.

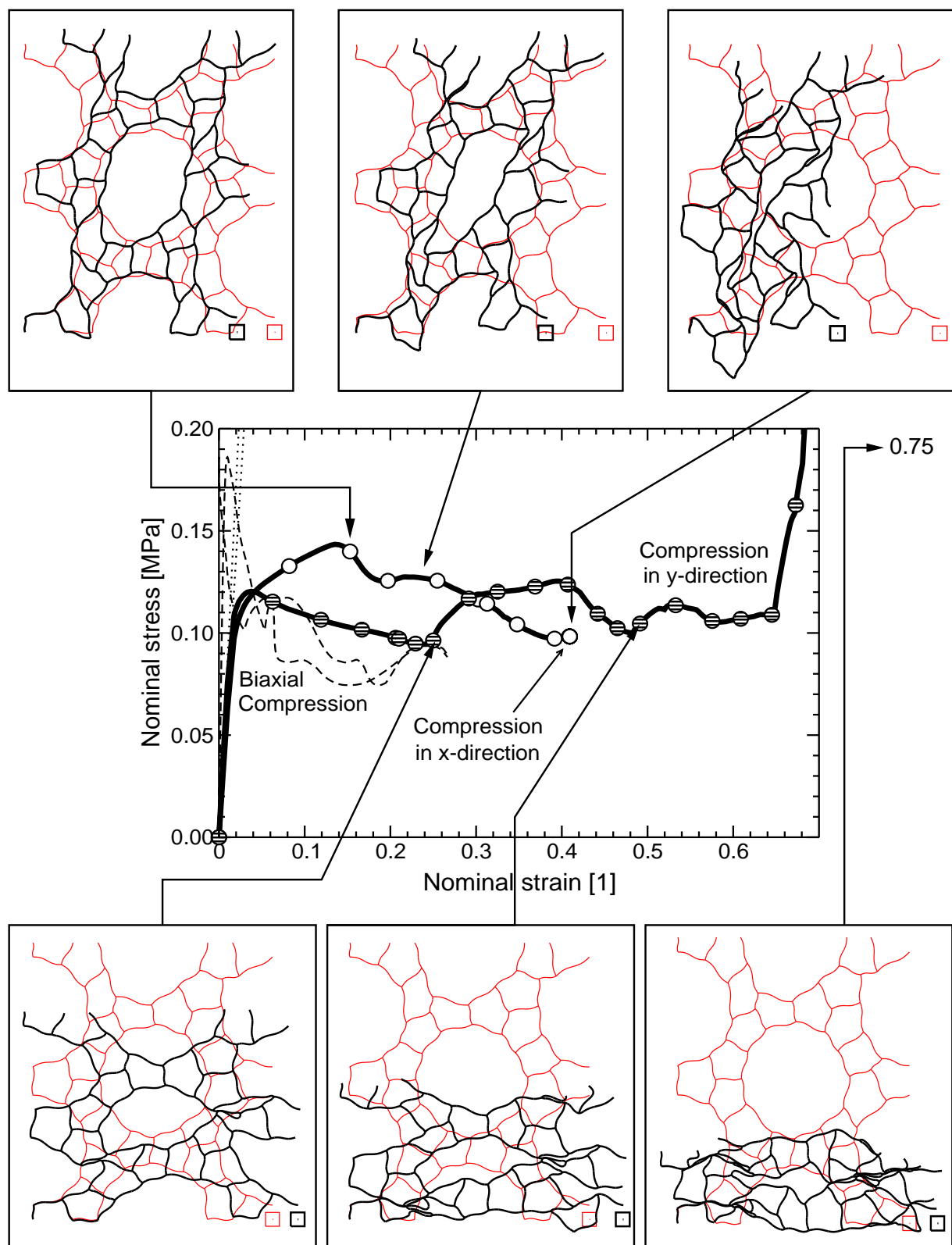


Figure 2.32: Predicted overall stress versus strain diagrams (center) for the imperfect and irregular honeycomb model “SBS”. Plots of the deformed configurations under compression in x -direction (top) and in y -direction (bottom) are supplied.

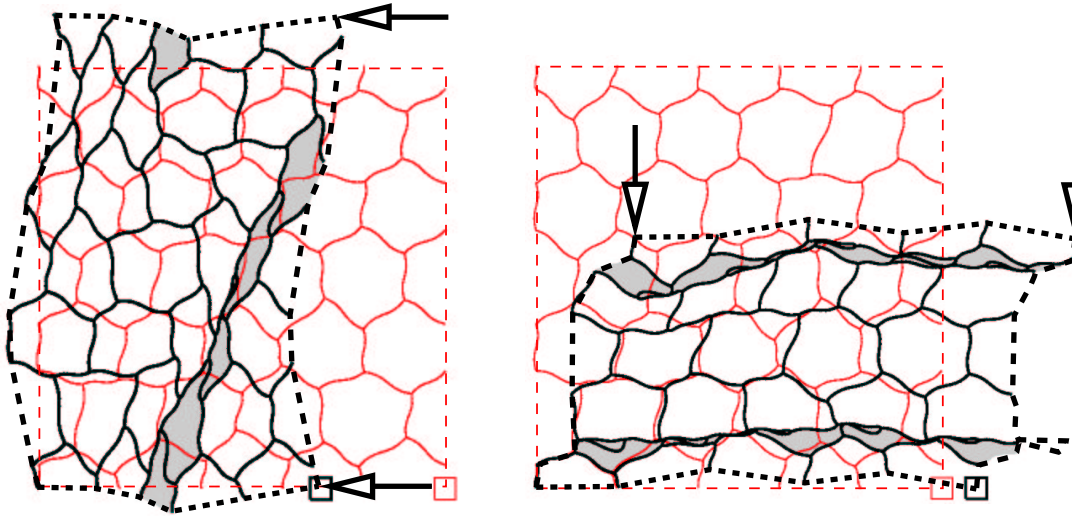


Figure 2.33: Undeformed and deformed configurations (as predicted by unit cells with periodic boundary conditions) of an imperfect hexagonal honeycomb subjected to uniaxial loads applied in the horizontal and vertical directions. Note the occurrence of shear localization (left) and layer-wise collapse (right), respectively.

the cell wall wiggles is stronger than the influence of the micro topology. With respect to the perfect hexagonal honeycomb all other configurations showed reduced overall yield stresses, but increased elastic moduli.

When observing overall stress–strain relationships predicted for uniaxial compression, two qualitatively different deformation and collapse mechanisms become apparent. If shear localization occurs, the microgeometry can deform at nearly constant applied stress through cell wall bending, and, after the collapse of the shear bands, by sliding along the collapsed layer, giving rise to comparably smooth stress–strain curves. If, in contrast, cell wall buckling and extensive layer-wise collapse perpendicular to the loading direction are the dominant mechanisms, the stress–strain relationship shows marked oscillations on account of the sequential collapse of “cell rows” which are incapable of accommodating subsequent deformation by sliding. Figure 2.33 shows deformation modes of the above types for the imperfect hexagonal honeycomb, with the corresponding stress versus strain curves being given in Figure 2.34.

In addition to these general observations on collapse modes some specific rules for the interaction of small and big cells can be identified. Comparing the deformation patterns developed by arrangements SBS and BSB, see Figure 2.35, one can observe that in the latter the clusters of small cells do not contribute very much to the overall deformation and may become obstacles in the densification regime. The framework of small cells surrounding the large ones in model SBS, however, provides more uniform stiffness and deforms more

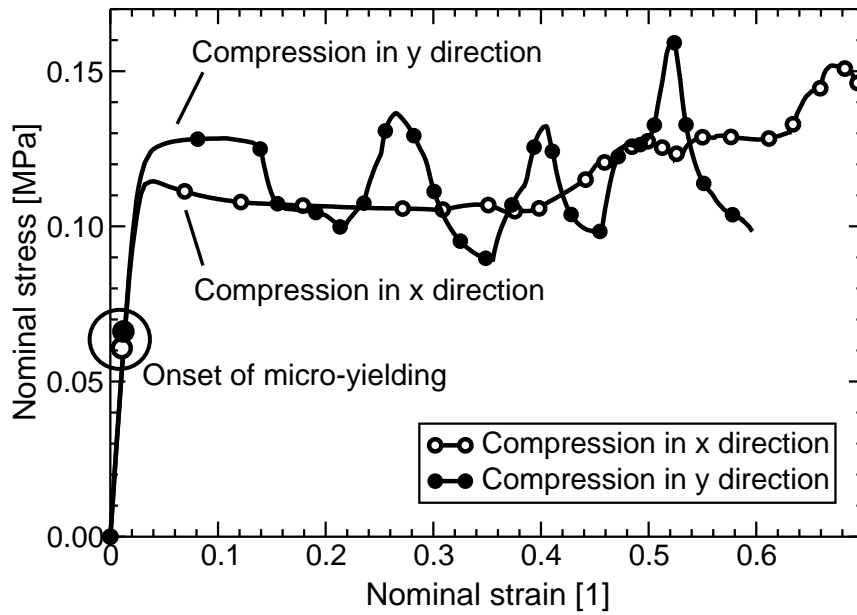


Figure 2.34: Predicted overall stress-strain relationships of an imperfect hexagonal honeycomb [17] corresponding to the deformation modes shown in Figure 2.33.

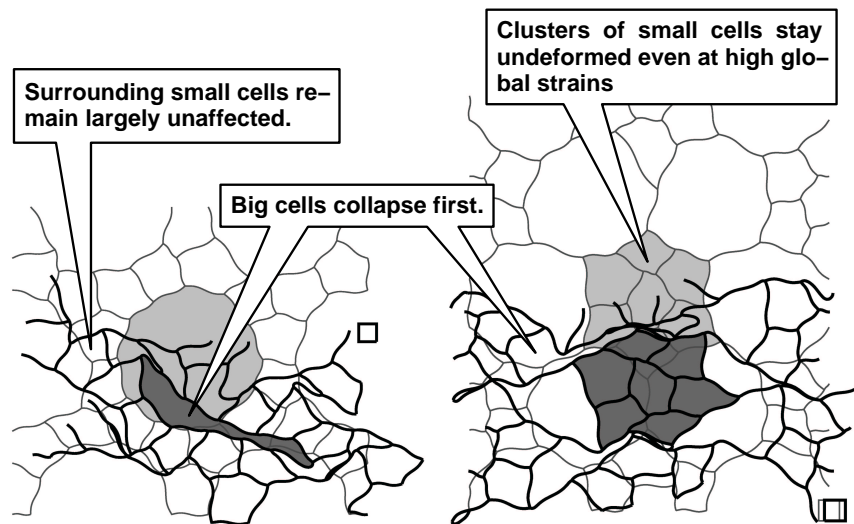


Figure 2.35: Deformed configurations predicted for imperfect models describing small cells surrounding big cells (BSB, left) and big cells surrounding small cells (SBS, right) based on the configurations presented in Figure 2.27.

evenly. In general, clusters of small cells tend to be detrimental to the deformation and energy absorption potential of cellular metals as they typically deform less than their larger neighbors, the longer struts of which confer lower bending stiffness and strength.

These observations lead to the conclusion that whenever smooth stress versus strain relationships are desired, the cell size distribution should be as uniform as possible and the cells should be small compared to the sample or structure to either prevent localization or to limit its detrimental effects.

2.9 Influence of Holes and Solid-Filled Cells

Another group of imperfections in cellular geometries may be generated by eliminating some vertices as well as the cell walls connected to them leading to holes that are larger than typical cell sizes, or by filling selected cells with solid material, compare Figure 2.2.

Experiments by Prakash et al. [87] have shown that the filling of some cells leads to local strengthening of honeycombs and increases the elastic modulus as well as the degree of strain hardening, but reduces the densification strain. The opposite effect is caused by removing individual cells or whole cell clusters as demonstrated by Guo and Gibson [43] in a Finite Element study on intact and damaged honeycombs. They reported on correlations between the undamaged cross sectional area perpendicular to the loading direction and the elastic buckling load as well as the plastic collapse strength. The maximum interaction range between separate defects of this type was found to be about ten cell diameters.

Chen et al. [12] investigated the influence of solid inclusions and holes on the stiffness as well as on the uniaxial and the in-plane hydrostatic yield strength values of perfect honeycombs and two-dimensional arrangements in which some 5% of the cell walls were randomly fractured. Solid inclusions were shown to lead to minor increases of the elastic stiffness and to have a negligible effect on the uniaxial and the in-plane hydrostatic yield strength of both the otherwise perfect and the fractured honeycombs. Because the solid inclusions introduce additional mass, however, the specific properties were negatively affected. Large holes were found to induce cell wall bending in otherwise perfect honeycombs, leading to significant reductions of the bulk modulus and the hydrostatic yield strength. For honeycombs with some missing cell walls the decrease in overall stiffness due to the missing microstructural parts could be estimated from the reduced overall relative density of the honeycomb.

2.10 Influence of Fractured or Missing Cell Walls

Cell walls that are damaged by fracture or that are bodily removed may weaken cellular materials to a considerable extent. Having introduced such defects into regular hexagonal and Voronoi honeycombs, Silva and Gibson [104] reported that the reduction of overall mechanical properties due to the removal of cell walls tends to be 2 to 3 times greater

than that caused by an equivalent (in terms of density) uniform reduction of the cell wall thickness. A typical Voronoi honeycomb was predicted to be, on average, 30–35% weaker than a periodic hexagonal honeycomb of the same density. The same degree of weakening can be obtained by removing 5% of the cell walls.

Experiments on honeycombs [87] showed that removal of cell walls triggers localized deformation because the weakened cells collapse prematurely. Whether or not cells with defects interact to form a common deformation band depends on their distance and the orientation of their offset vector with regard to the loading direction. Albuquerque et al. [3] performed similar experiments on Kevlar honeycombs. In addition to confirming the results of Silva and Gibson [104] and Prakash et al. [87] they found that the compressive behavior is hardly affected by having the defects uniformly dispersed or concentrated in a region, provided the concentration of defects is low.

Upon removing 10% of the cell walls in Voronoi honeycomb models, Silva and Gibson [104] obtained a reduction of the compressive strength by some 40% and found that the stiffness and strength tend to zero when 35% of the cell walls are removed. To study fatigue accumulation in cancellous bone Schaffner et al. [95] removed struts in an open cell model once the lengths of fatigue microcracks in them (assumed to grow according to a Paris law) exceeded a user-specified limit. They found that Voronoi honeycombs are more sensitive to fatigue damage than regular hexagonal geometries. After comparing several types of morphological imperfections in honeycombs Chen et al. [11] identified the removal of cell walls as the most critical of them in terms of reduction of the yield strength.

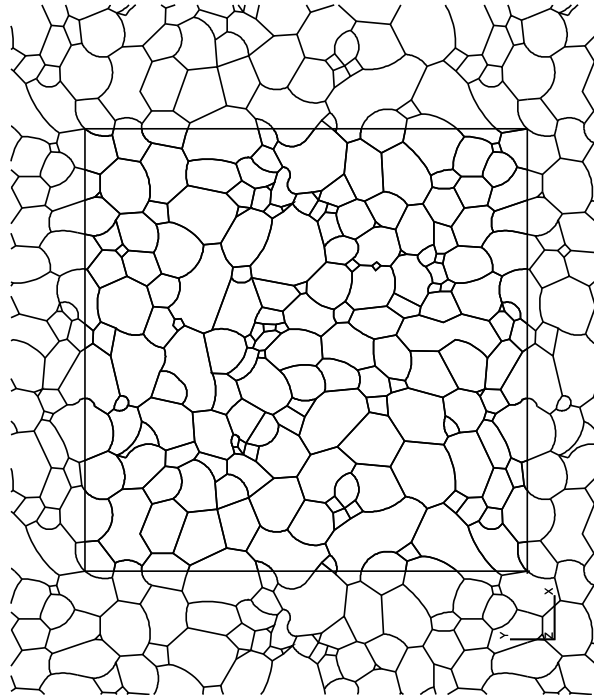


Figure 2.36: Unit cell for a periodic “real structure” honeycomb model [20] adapted from a micrograph given in [39]. Note the wide range of cell sizes, cell shapes and cell wall imperfections.

2.11 Overall Yield and Collapse Surfaces

In Section 2.3 the evaluation of yield surfaces, “generalized yield surfaces” and collapse surfaces from unit cell analyses was discussed. For a given cellular metal, the availability of such data allows multiaxial stress states to be assessed for the onset of inelastic behavior and for the commencement of cell collapse, which defines the initial overall peak force and the start of the plateau region in the overall stress versus strain behavior.

Overall initial yield surfaces for hexagonal honeycombs with corrugated or curved cell walls were mentioned in Section 2.6. Here, some aspects of overall yield and collapse surfaces will be discussed for more realistic microgeometries. To study the behavior of an irregular honeycomb with a “natural” microgeometry, a unit cell was generated on the basis of a section through a sample of closed cell aluminum foam given by Grenestedt [39], suitable adaptations being introduced to support periodic boundary conditions, see Figure 2.36. The prescribed beam thickness was chosen to give an apparent density of 0.1 g/cm^3 in combination with the generic aluminum bulk material properties listed in Table 2.3.

The predicted overall collapse stress surfaces typically surround the overall initial yield surfaces, and for irregular honeycombs the shapes of the two surfaces tend to be somewhat

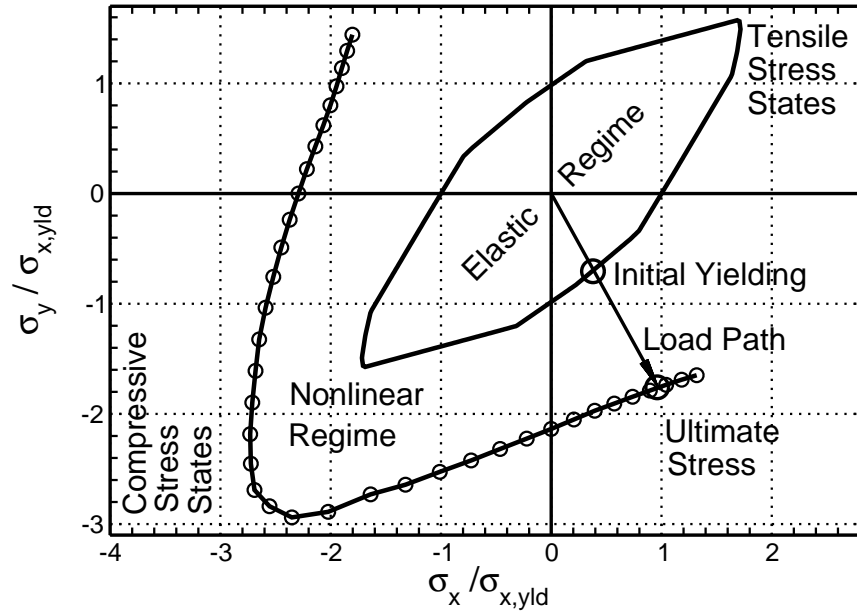


Figure 2.37: Overall yield and collapse surfaces [20] predicted for the real structure honeycomb model presented in Figure 2.36.

similar, compare Figure 2.37. It may be noted that for uniaxial overall stress states, where the dominant local deformation mechanism is bending, the collapse stress exceeds the initial yield stress by a factor of about 2.4, which is far in excess of the value of 1.5 given by simplified beam analysis (assuming ideally plastic beams of rectangular cross section and neglecting stress redistribution).

The collapse surface presented in Figure 2.37 is not given for all possible loading paths, only the purely compressive regime (3rd quadrant) and those parts of the shear regimes being covered, for which the larger principal stress is compressive (2nd and 4th quadrants). These restrictions were necessary because the predicted stress versus strain responses do not allow the extraction of plateau stresses once the tensile principal stresses exceed the compressive ones. To obtain peak stresses and a plateau region from such tension dominated loading paths additional failure criteria, for instance cell wall fracture, would have to be introduced.

By definition, an initial yield surface allows the presence of plastic yielding to be assessed on the basis of linear analyses. This obviously is an important contribution to the development of macroscopic elastoplastic constitutive models. It is not, however, sufficient for carrying out nonlinear studies such as crushing or crash analyses, for which detailed information on the evolution of the yield surface under loading as provided by a hardening law (see Section 4.3) is indispensable and strain rate effects may have to be accounted for. One of the hardening laws used in connection with metallic foams is isotropic hardening [24].

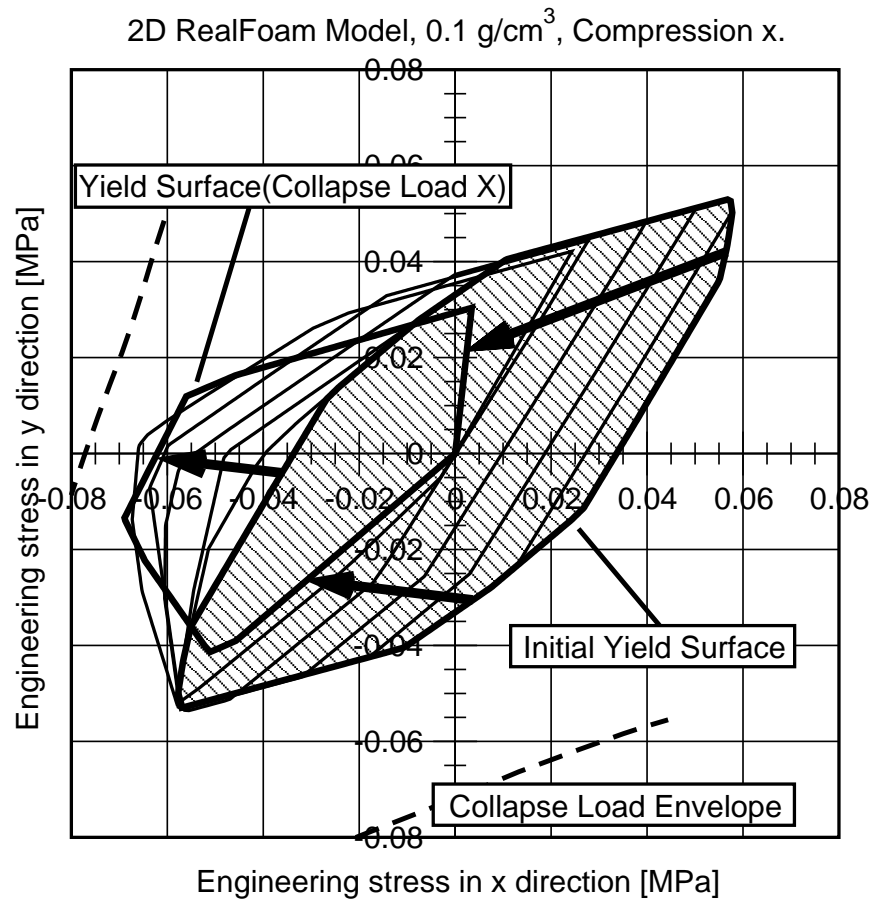


Figure 2.38: Evolution of the overall yield surface under uniaxial compressive loading in x -direction predicted for the real structure honeycomb model presented in Figure 2.36.

It assumes that the origin and the shape of the yield surface stay the same, while its size increases driven by accumulated plastic strains. In the Crushable Foam model [51] mixed hardening is assumed, where the yield surface keeps the same shape while its size can increase (isotropic hardening), and its origin can be shifted (kinematic hardening) so that the hydrostatic tensile yield stress is kept constant.

Micromechanical analyses based on the real structure geometry shown in Figure 2.36 paint a somewhat more complex picture. Derived with the method presented in Section 2.3.2, Figure 2.38 displays predictions for the evolution of the overall yield surface corresponding to progressive uniaxial compressive loading in the x -direction. At several points during the loading sequence the analysis was interrupted, the model was unloaded and then subjected to linear superposition analyses to estimate the onset of nonlinear behavior. This way the yield surface corresponding to the actual state of hardening was generated. The initial hardening behavior was predicted to be essentially kinematic, the yield surface being shifted

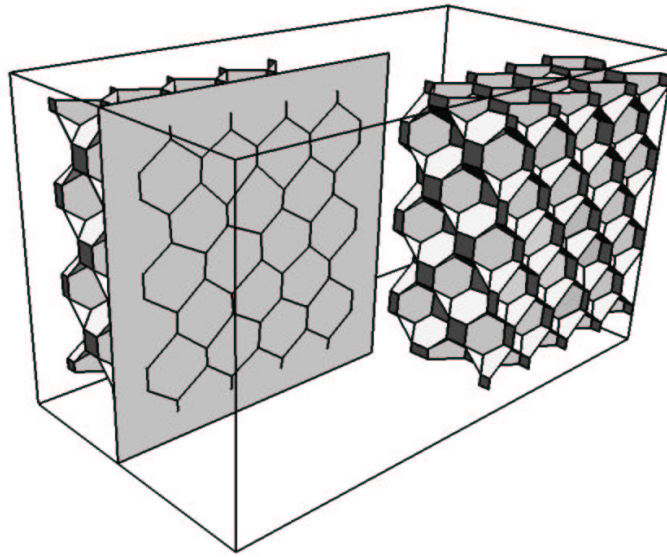


Figure 2.39: Irregular tetrakaidecahedral model for a closed cell foam [20]. As can be seen from the planar section, perturbations were introduced only in the core of the model to allow for the use of symmetry boundary conditions.

in the direction of the applied stress without major changes in shape or size. At elevated compressive stresses, however, the evolving yield surface changes its shape and contracts as well. Because Figure 2.38 is based on the superposition of solutions from linear analyses it cannot account for geometrical nonlinearities, which may be expected to play an increasing role as compressive collapse is approached. Hence, its reliability in the latter regime is not fully clear. Accordingly, the results can be interpreted as clearly favoring kinematic hardening models for low inelastic strains and hinting at possible changes in the hardening behavior for the high strain regime.

As mentioned before, planar models are directly applicable to honeycombs, but are not necessarily directly transferable to real foams that require three-dimensional simulations for quantitative predictions. Denzer developed three-dimensional closed cell microgeometries [20] based on a body-centered cubic arrangement of tetrakaidecahedral cells, using symmetry boundary conditions to limit the computational costs. Initial overall yield surfaces under compressive loading were evaluated for configurations with perfect cell geometry as well as for models with statistically perturbed vertex positions, see Figures 2.3 and 2.39. The general shapes of these yield surfaces are ellipsoidal in the principal stress space, and their major axes are aligned with the hydrostatic axis, compare Figure 2.40. This can be explained by discussing the stress states induced in the cell walls, which are mainly membrane-like for hydrostatic loads (even though regular tetrakaidecahedra are not elasti-

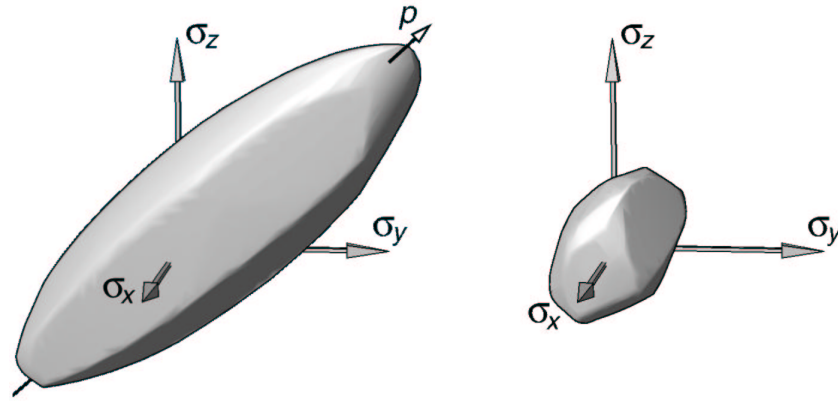


Figure 2.40: Yield surfaces predicted for regular (Figure 2.3) and irregular (Figure 2.39) tetrakaidecahedral closed cell foams [20].

cally isotropic) and characterized by high bending stresses close to the vertices for uniaxial loads, which gives rise to yielding at deviatoric macroscopic stresses that are lower than the hydrostatic macroscopic yield stresses. This load state influence is less pronounced for the imperfect models, where the “aspect ratio” of the yield surface tends to be lower owing to bending moments that are induced by the imperfections and have approximately the same magnitude for uniaxial and hydrostatic applied macroscopic stress states. This behavior is qualitatively similar to predictions obtained from honeycomb models, but the yield surfaces for perfect tetrakaidecahedra are less elongated along the hydrostatic axis than those of perfect honeycombs, compare Figure 2.29.

By projecting selected points of the yield surface shown in Figure 2.40 (left) onto the von Mises equivalent stress versus mean stress plane a standard representation is obtained, see Figure 2.41, that can be readily compared with other results. The projected points can be seen to be scattered around an ellipse, the major axis of which coincides with the mean stress axis, the hydrostatic yield stress being about 2.5 times larger than the uniaxial yield stress. It may be noted that many material laws for foams use yield surfaces that give rise to ellipses when projected to the von Mises equivalent stress versus mean stress plane, among them the model of Deshpande and Fleck [24].

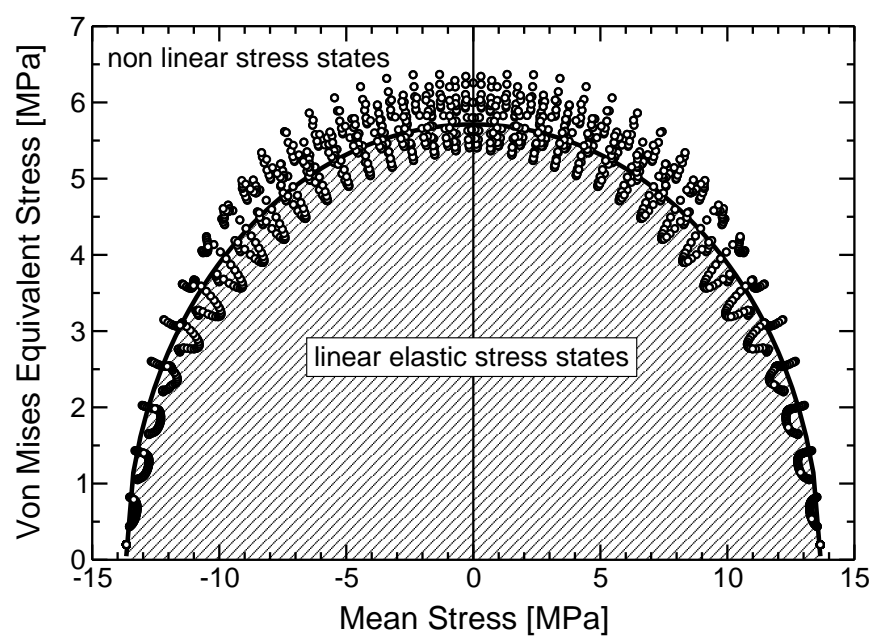


Figure 2.41: Projection of the yield surface shown in Figure 2.40 (left) onto the von Mises equivalent stress versus mean stress plane.

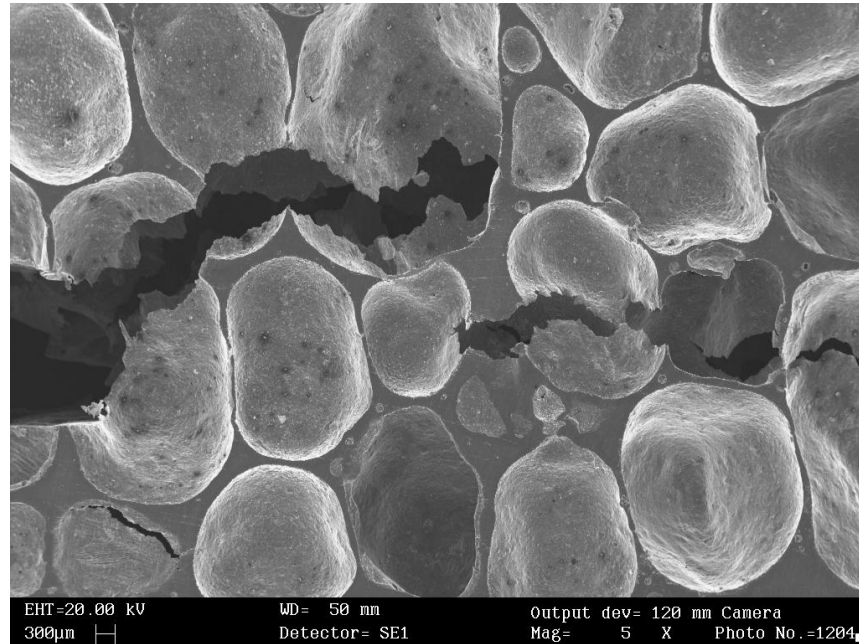


Figure 2.42: Microsection of a closed-cell foam revealing a crack running through the bulk material (Image courtesy of Erich Schmid Institut der Österreichischen Akademie der Wissenschaften).

2.12 Fracture Simulations for Metallic Foams

Unit cell based micromechanical methods give rise to periodic deformation, stress and strain fields and, as a consequence, periodic patterns of damage and cracks. Although this may be acceptable for distributed damage, a useful alternative for studying small samples consists in employing microgeometries that essentially model the whole specimen. Schaffner et al. [95], for example, used a Voronoi honeycomb to study fatigue damage of cancellous bone.

Crack tips in discrete cellular microstructures (Figure 2.42) were studied by Gibson and Ashby [33], who gave expressions for the fracture toughness of brittle honeycombs by considering failure of the first unbroken cell wall in the path of an advancing crack in simple planar and three-dimensional models. An approach in which hexagonal honeycombs are homogenized as a micro-polar elastic material, for which the asymptotic crack tip fields are computed and then used to estimate the displacements and rotations of the cell walls surrounding the crack tip, was developed by Chen et al. [13]. Probably the most flexible approach available at present for studying crack tips in cellular materials, however, is the use of embedding techniques. Such a strategy was followed by Ableidinger [1] for studying the influence of a number of microgeometrical and material parameters on the macroscopic fracture mechanical behavior of a compact tension (CT) specimen made of an open cell

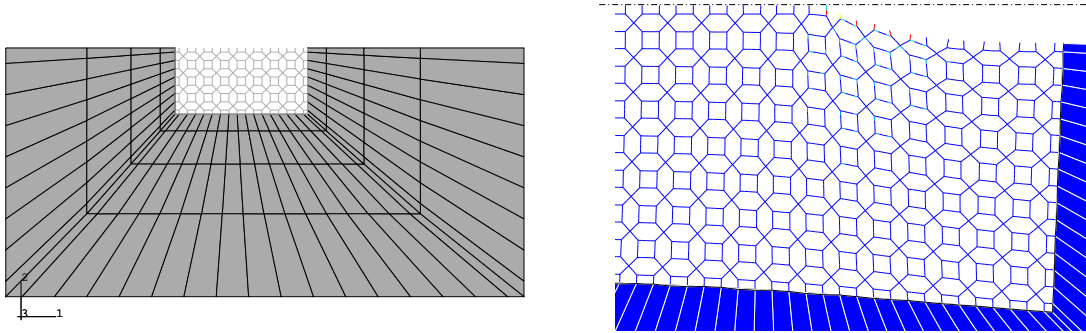


Figure 2.43: Embedded cell model of an open cell foam using a tetrakaidecahedral core and a homogenized outer region (left) and detail of the core around the crack tip (right), from [1]. Note that symmetry with respect to the crack plane is assumed.

aluminum foam subjected to monotonic loading, see also [88].

The region surrounding the crack tip was modeled with a fully resolved, but highly generic, three-dimensional tetrakaidecahedral open cell microgeometry discretized with beam elements. This kernel was embedded into the remainder of the CT specimen, compare Figure 2.43 (left), which was treated as a homogeneous structure with an effective material behavior obtained from unit cell analyses of the same tetrakaidecahedral microgeometry. In the out-of-plane direction the core consisted of a single layer of tetrakaidecahedra, the embedding region having the same thickness, and symmetry boundary conditions were applied at the top and bottom planes, so that the model actually corresponds to an inner layer (plane strain conditions) of the specimen. Tensile loads were applied at the positions of the loading fixtures of the CT specimen, so that the crack proceeded in fracture mode I on the macroscale. Crack propagation at the micro level as resolved in the kernel region was assumed to be caused by sequential ductile failure of the most highly loaded struts, compare Figure 2.43 (right).

From the predicted force versus displacement diagrams of the CT specimens, see Figure 2.44, effective K_I versus Δa (crack resistance) curves as shown in Figure 2.45 were obtained. For this purpose, the macroscopic stress intensity factor K_I was evaluated at each maximum of the force versus displacement curves according to standard expressions for CT specimens, the crack length increments Δa being dictated by the selected microgeometry. Both Figure 2.44 and Figure 2.45 show results for three values of the apparent density of the foam and for two aluminum alloys differing in ductility.

Within such a modeling approach parameters such as the mass density of the foam (which determines the void volume fraction), the size of the cells (which influences the fracture behavior in terms of an internal length scale), the yield strength, and the fracture strain of the bulk material (which govern the ductile damage and failure of the struts) can be varied easily in order to study their respective influences on the fracture behavior of open

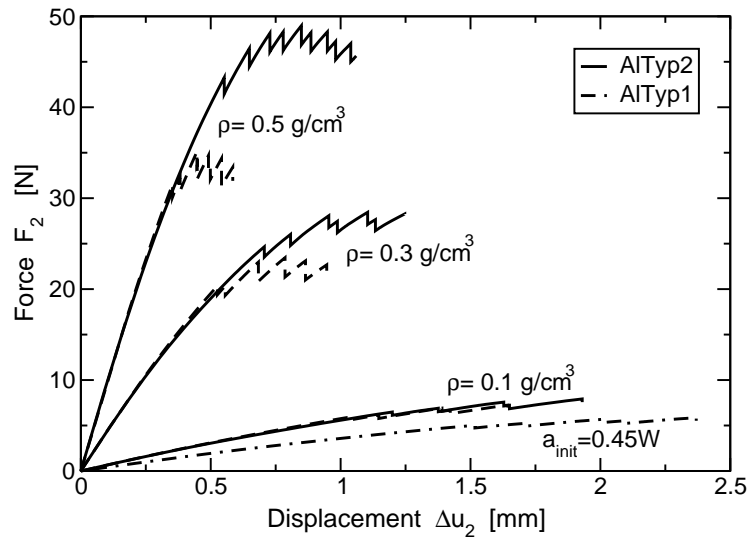


Figure 2.44: Macroscopic force versus displacement curves of CT specimens made of open cell aluminum foams predicted by embedded cell models, see Figure 2.43, for different effective densities and different aluminum alloys [1].

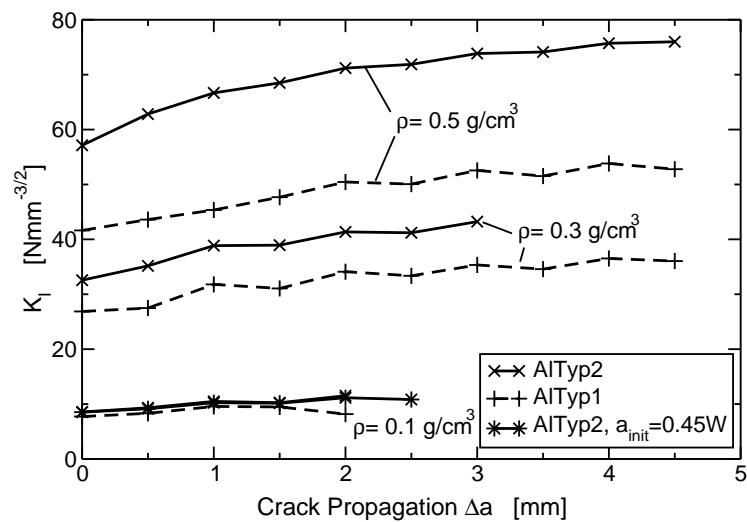


Figure 2.45: Macroscopic crack resistance curves of CT specimens made of open cell aluminum foams predicted by embedded cell models, see Figure 2.43, for different effective densities and different aluminum alloys [1].

cell metallic foams.

2.13 Summary and Outlook

A large body of different micromechanical simulation models and simulation results were presented in this chapter. The interaction of various topologies and imperfections was investigated, and their influence on the effective mechanical behavior of cellular metals was assessed. The employed simulation models were predominantly two-dimensional, but the application of periodic boundary conditions to 3D unit cells was demonstrated, and some results obtained with 3D models were presented. Several pre- and postprocessing methods were developed to ease the generation of models for cellular materials and to provide advanced result evaluation methods.

The future of micromechanical modeling can be expected to see an increased interest in modeling three-dimensional cellular arrangements and in transferring methods that have proven successful in the analysis of planar morphologies into the three-dimensional domain. This process is facilitated by the steadily increasing capabilities of computer hardware and software. Therefore, the advent of micromechanical models, which better capture the behavior of three-dimensional microgeometries (especially for closed cell foams), may be forecast. Larger and more sophisticated three-dimensional micromechanical models will provide more precise information on the behavior of cellular metals under multiaxial loading states. This, together with additional information from corresponding multiaxial experiments, can be expected to lead to new insight into phenomena related to the macromechanics of cellular models and may give rise to the development of more refined constitutive theories.

Chapter 3

Modeling of Mesoscopic Density Inhomogeneities

3.1 Introduction

Safety requirements in vehicle engineering have been raising interest in materials which are suitable for minimizing the contact forces between two colliding bodies while maximizing the amount of kinetic energy that is converted to irrecoverable internal energy. The latter process is generally referred to as energy absorption. To satisfy both of the above demands the material of choice should be able to undergo large compressive deformations at a more or less constant stress level. In addition the material should be of light weight.

Properties like these can be found in metallic foams which exhibit a characteristic non-linear deformation behavior: during the first stages of uniaxial compression the stress rises steeply due to the resistance of the cell walls and struts against axial compression, bending and buckling. After the stress has exceeded the collapse strength of the weakest band of cells, the sequential collapse of cell layers is initiated during which the stress, if at all, increases only slightly, leading to a plateau-like stress-strain regime. This changes drastically as soon as the better part of the cells has collapsed, and their cell walls start to contact each other. Then the densified foam stiffens drastically as soon as it is compacted further.

Generic quasi-static responses of foams under compressive deformation are depicted in Figure 3.2 (right). Considering that the area under the nominal stress versus nominal strain curve is equal to the energy stored in the foam material it becomes clear that the stress-strain behavior is very favorable in terms of high energy absorption at low peak stress levels. Unfortunately, it is at present difficult to produce foam structures of homogeneous density. Therefore, foams are not only heterogeneous in terms of consisting of solid regions and voids, but in many cases also show an inhomogeneous distribution of their apparent density, their mean cell size and other microgeometrical parameters. These

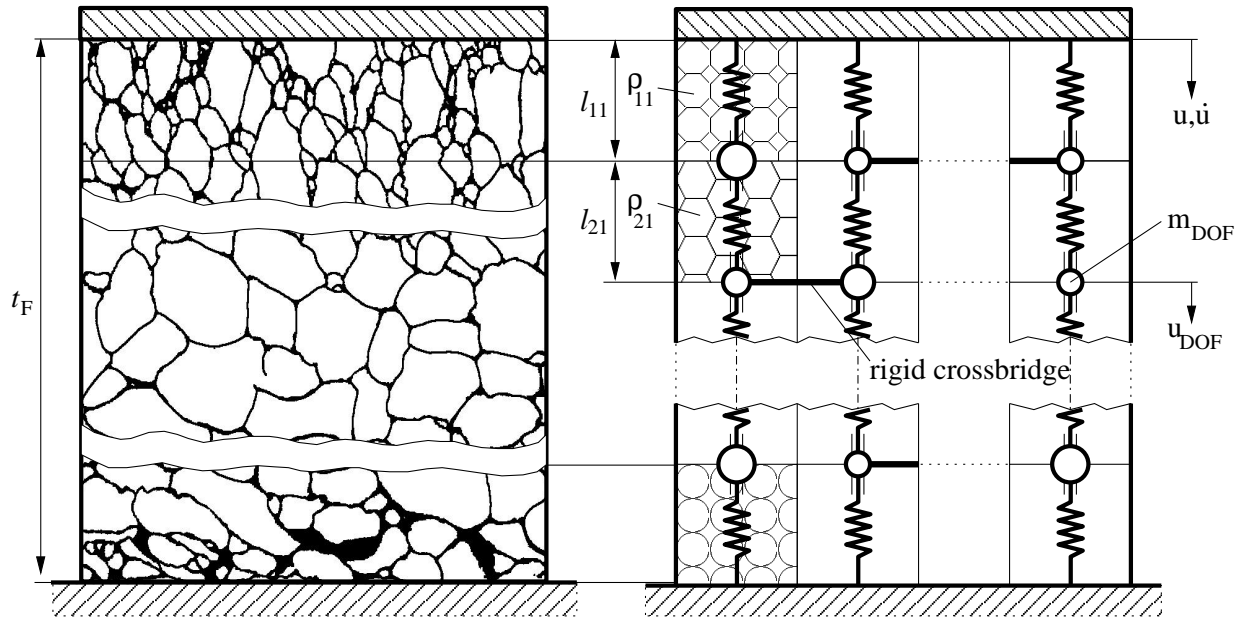


Figure 3.1: Micro-graphical cross-section of an aluminum foam with three regions of differing apparent density (left) and sketch of the simulation model used in the present study (right).

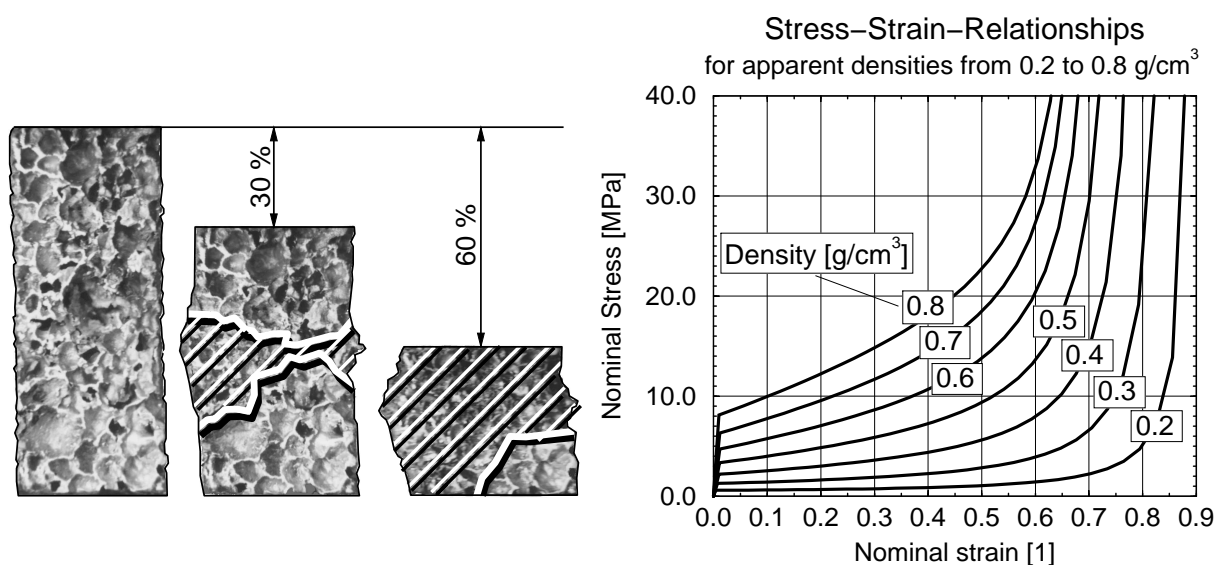


Figure 3.2: Left: three different stages of deformation of a foam specimen; regions of localized deformation are hatched. Right: generic quasi-static stress-strain relationships for aluminum foams within a density range between 0.2 and 0.8 g/cm³ (from [36]).

variations correspond to length scales larger than that of the voids (the microscale) and smaller than that of the samples or components (the macroscale) and are, accordingly, termed mesoscopic inhomogeneities in the following. Figure 3.1 (left) shows such density variations in a cross section of a foam sample.

Shim et al. [102] introduced uniaxial lumped mass–spring mesoscopic models for the simulation of the dynamic uniaxial crushing of foam samples with uniform apparent density. Systems of elastic–plastic springs were employed by Gradinger and Rammerstorfer [36; 38] for studying the compressive force–displacement behavior of crushed specimens with deterministically distributed meso-inhomogeneities. These two approaches were combined by Daxner et al. [18] to assess the influence of inhomogeneous density distributions on the impact response of foam plates with generic variations in the apparent density, the interaction of density inhomogeneities in directions normal to the orientation of the load being also accounted for, see Figure 3.1 (right). Here, these investigations of the influence of mesoscopical inhomogeneities, for example, of the apparent density on the overall mechanical behavior of a crushed foam body are summarized and complemented by a detailed treatise on the dynamics of a rigid mass impacting an (in)homogeneous foam pad.

3.2 Experimental Data

The simulation model proposed in the next section uses experimental data presented by Gradinger [36], who performed a large number of quasi-static uniaxial compression tests for obtaining a correlation between the apparent density and the uniaxial stress–strain relationships of compressed foam samples.

Shim [102] proposed an analytical piece-wise linear and exponential relationship between the nominal stress σ and the nominal strain ε for describing a generic stress–strain relationship for metallic foams under uniaxial compression:

$$\sigma(\varepsilon) = \sigma_0 \begin{cases} \frac{\varepsilon}{\varepsilon_0} & : \quad \varepsilon \leq \varepsilon_0 \\ \exp \frac{a(\varepsilon - \varepsilon_0)}{(a - \varepsilon)^n} - b(\varepsilon - \varepsilon_0) & : \quad \varepsilon_0 < \varepsilon < a \end{cases} \quad (3.1)$$

Below the collapse stress σ_0 , the stress–strain relationship is assumed to be linear. The collapse strain ε_0 marks the end of the linear regime. The initial tangent modulus S_0 can be calculated from $S_0 = \sigma_0/\varepsilon_0$. For strains above the collapse strain the stress–strain relationship is described by an exponential function with an initially flat tangent, which represents a “plateau” in the stress–strain relationship, see Figure 3.2 (right). In [36] the parameters a, b, ε_0, n and the collapse stress σ_0 were adjusted to fit experimental data obtained for an Al99.5 foam. Equation (3.2) shows the resulting set of parameters as

functions of the apparent density ρ , which has to be inserted in $[\text{g}/\text{cm}^3]$:

$$\begin{aligned}
 a(\rho) &= -0.3704 \rho + 1.0000 \\
 b(\rho) &= 6.6964 \rho^2 - 10.2790 \rho + 2.3053 \\
 \varepsilon_0(\rho) &= -0.0459 \rho^2 + 0.0563 \rho - 0.0055 \\
 n(\rho) &= -1.3633 \rho^2 + 1.2243 \rho + 0.3321 \\
 \sigma_0(\rho) &= 12.3430 \times \rho^{1.8807} [\text{MPa}]
 \end{aligned} \tag{3.2}$$

Additionally, Gradinger gives the following regression equation for the dependency of the unloading modulus S_{Rpo} on the apparent density ρ of the metallic foam (in $[\text{g}/\text{cm}^3]$):

$$S_{\text{Rpo}}(\rho) = 14\,000 \rho^{2.2} [\text{MPa}] \tag{3.3}$$

3.3 Method

The proposed simulation model tries to capture mesoscopical variations of the apparent density by partitioning a generic foam specimen into a checker-board like arrangement of regions with approximately uniform apparent density. The foam material is represented by an array of point masses connected by elasto-plastic spring elements in loading direction and rigid cross-bridges transverse to the loading direction. A schematic sketch of the model and the density inhomogeneities it is intended to capture can be found in Figure 3.1. The simulation model was implemented as a stand-alone **Fortran** program.

Similar models were used by Gradinger [36; 38] for quasi-static analyses of layered, inhomogeneous foam volumes and by Shim et al. [102] to investigate the dynamic uniaxial crushing of generic foam blocks with uniform density. Though the model is one-dimensional in principle, the cross-bridges, which couple the point masses transversely and can be understood as regions of either zero or infinite shear stiffness, are intended to take into account the interaction of foam regions that are connected in parallel with respect to the deformation direction. The cross-bridges can either be open or closed, in each case representing an extreme value of the local shear stiffness.

3.3.1 Uniaxial Constitutive Models

Each foam region of mesoscopically homogeneous density is represented by one or more spring elements, the stress-strain relationships of which are defined as functions of the apparent density by Equations (3.1) and (3.2). The mechanical behavior of the springs can be chosen to be nonlinear elastic or elasto-plastic with either elastic or inelastic unloading, the latter meaning an instant relaxation of the spring as soon as shortening occurs. Quasistatic stress-strain relationships for the different material models are shown in Figure 3.3 (left) for the uniaxial compression of a foam volume of $0.5 \text{ g}/\text{cm}^3$ apparent density. Gradinger

determined an average plateau stress of 3.35 MPa for this density. The initial tangent modulus was found to be ≈ 300 MPa, the collapse strain being $\varepsilon_0 = 1.1\%$. The unloading modulus S_{Rpo} according to Equation (3.3) is one order of magnitude higher, that is, slightly above 3 GPa. Choosing the Young's Modulus E_F from those two extremes strongly affects the character of the stress-strain relationships in Figure 3.3 (left), particularly the initial “elastic” regime and the unloading part. It is also obvious from Figure 3.3 (left) that the initial stiffness S_0 restricts the applicable range of the stress-strain curve, since the tangent modulus $d\sigma/d\varepsilon$ can easily become larger than the “elastic” modulus at high strains, which is physically unsound. For the elastic-rigid plastic material model the stress drops to zero as soon as the strain in the spring element drops beneath its current maximum.

The choice of the material model also affects the dynamic behavior of the lumped mass model. In Figure 3.3 (right) a single spring element with the corresponding lumped point mass for an apparent density of 0.5 g/cm^3 attached at one end and a displacement constraint at the other end was subjected to a constant stress of 7.5 MPa. Strain histories for nonlinear elastic (with and without damping), soft and stiff elasto-plastic and elastic-rigid plastic material behavior are depicted. The inertial effects of the lumped mass are clearly visible when comparing the maximum dynamic strain of 66% to the quasi-static solution of 41.5%.

3.3.2 Integration Algorithm

The treatment of dynamic processes requires the formulation and the integration of the equations of motion for the spring/mass system. The equations of motion are integrated using the explicit central difference integration rule. For each degree of freedom (DOF) u_k the state at the time $t + \Delta t$ can be calculated from previously calculated states ${}^{t-\Delta t}u_k$ and tu_k according to:

$${}^{t+\Delta t}u_k = 2 {}^tu_k - {}^{t-\Delta t}u_k + \frac{F_k^{(\text{ext})} - F_k^{(\text{int})}}{m_k} \Delta t^2, \quad (3.4)$$

where for $k = 1$ the external force $F_k^{(\text{ext})}$ is equivalent to the total applied or contact force acting on the lumped mass m_1 of the top foam layer, and equal to zero for all other degrees of freedom. The internal force $F_k^{(\text{int})}$ in Equation (3.4) is the sum of all spring forces acting on the lumped mass k , compressive forces being counted as positive.

The central difference method was chosen mainly for its simplicity and its easy and straightforward implementation. One disadvantage of this explicit integration method is that it is only conditionally stable, that is, the solution may diverge if no precautions are taken. It can be shown [8] that the central difference method is stable if the integration time step Δt is smaller than a critical time step $\Delta t_{\text{crit}} = T_{\text{min}}/\pi$, where T_{min} is the smallest period of the model, corresponding to the highest frequency of free vibration of the whole model. The exact calculation of the smallest period of oscillation can be avoided by using a lower bound $T_{\text{min}}^{(\text{el})}$ instead of the actual T_{min} . This bound is the smallest period of oscillation $T_{\text{min}}^{(\text{el})}$

among all *individual* elements in the model [8]. A related estimate for the critical time step is the shortest time it takes a stress wave to run through any of the individual spring elements in the model (Courant-Friedrichs-Lewy stability condition). Hence, the critical time step is given by $\Delta t_{\text{crit}} \leq \min(l_{ij}/c_{ij})$, where l_{ij} is the length of the spring element (i,j) , and c_{ij} is the one-dimensional wave-speed $c_{ij} = \sqrt{E_{ij}/\rho_{ij}}$ [8].

3.3.3 Damping Algorithm

To eliminate oscillations of unrealistically high frequency an internal damping mechanism can be activated to improve the results of high-speed impact simulations. A basic damping mechanism depending on the elongation rate of the springs was introduced by adding speed proportional internal forces

$$F_{ij}^{(\text{visc})} = -d \cdot A_j \underbrace{(l_{ij}^t - l_{ij}^{t-\Delta t})}_{\dot{l}_{ij}} / \Delta t, \quad (3.5)$$

where A_j is the cross-section of the foam column (j) , l_{ij} is the length of the spring element, and the damping coefficient d relates the elongation velocity \dot{l}_{ij} to the damping force $F_{ij}^{(\text{visc})}$. This simple damping model was introduced to obtain smoother solutions rather than to predict the influence of actual foam material damping characteristics. One shortcoming of Equation (3.5) is that the damping effect is independent of the effective foam density, which may not be the case in reality. To demonstrate the effect of the damping algorithm the decaying oscillation of a lumped mass attached to a spring/damper element is shown in Figure 3.4. The envelope formed by the two dashed lines is defined by the amplitude function $a(t) = \pm u_{\text{init}} \exp(-t d/2m)$ for a freely oscillating mass m with a velocity proportional damping coefficient d and an initial displacement of u_{init} .

3.3.4 Contact Algorithm

During the simulations tensile stress waves were generated by the transition of compression waves from regions of higher local density to regions of lower local density, a configuration that behaves partly like a free end in that one part of the compression wave is reflected as a tensile stress wave whereas the other part continues to propagate through the less dense material as a compression wave.

The tensile stress waves cause tensile effective forces in the spring elements between the foam nodes closest to the surface and the merged foam surface-impact mass node. Since contact between the impact mass and the foam surface is assumed, the foam will separate from the impact mass for a short period of time. The algorithm handling this separation waits for a tensile contact force to act on the impact mass M at time t . As soon as this occurs the combined mass $M + m$ of the impact mass M and the surface node mass m is split up and the impact mass is assigned an own degree of freedom u_M . The impact mass

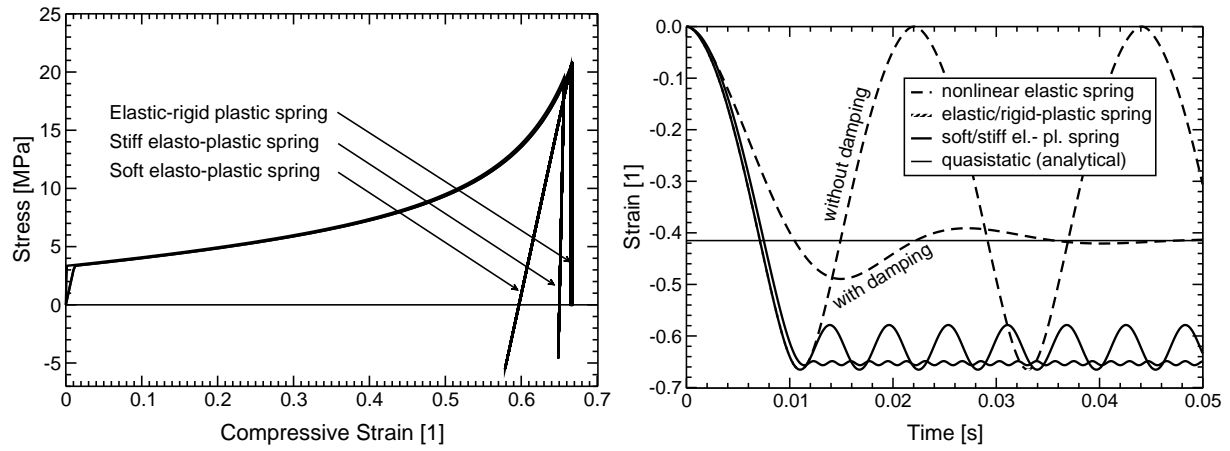


Figure 3.3: Mechanical response of a single spring element for different constitutive models. Left: quasi-static stress-strain diagrams. Right: time-strain histories for a dynamic event.

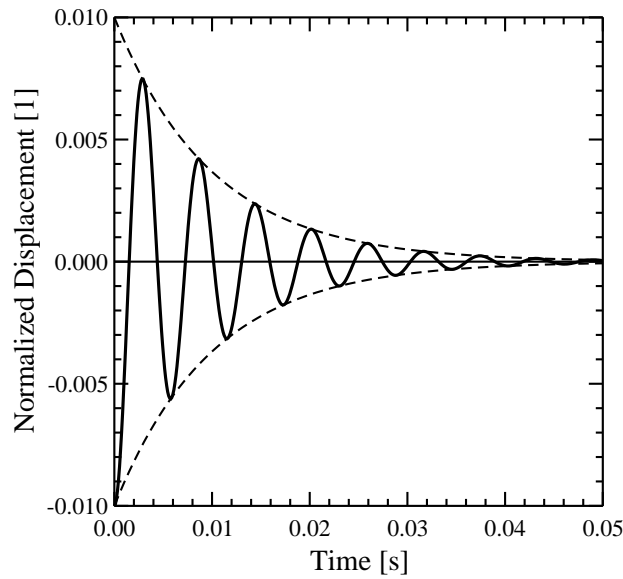


Figure 3.4: Verification of the explicit damping algorithm by comparing the predicted position history of an oscillating mass/spring system with the analytical amplitude function.

is then considered to move free of force, that is, at a constant velocity. The internal force tF now acts on the surface node m exclusively, and the new displacement of the now free surface ${}^{t+\Delta t}u_1$ is calculated accordingly.

As soon as the displacement ${}^{t+\Delta t}u_M$ of the impact mass exceeds the displacement of the surface foam node, ${}^{t+\Delta t}u_1$, the impact mass is added to the foam node mass, and the displacement of the foam node, ${}^{t+\Delta t}u_{M+m}$, is set equal to the displacement of the impact mass at time $t + \Delta t$ and at time t , so that the reunited mass $M+m$ both has the actual displacement ${}^{t+\Delta t}u_M$ and the velocity of the impact mass. The number of DOFs is reduced by one during this procedure. The node mass is considered to be negligibly small compared to the impact mass for this impact event.

3.3.5 Energy Balance

During a dynamic impact event the major part of the initial kinetic energy $E_{\text{kin},1}^{(M)}$ of the impact mass (M) is transferred to the foam material (F). Assuming an *adiabatic* process the principle of conservation of energy demands that

$$E_{\text{kin},1}^{(M)} - E_{\text{kin},2}^{(M)} = W_{\text{ext}} = E_{\text{kin},2}^{(F)} + \Delta U^{(F)}, \quad (3.6)$$

where W_{ext} is the work of the contact forces between impact mass and foam surface and $\Delta U^{(F)}$ stands for the change of internal energy of the foam material. Inserting the integrated equation of motion rewritten as $\Delta E_{\text{kin}}^{(F)} = E_{\text{kin},2}^{(F)} = W_{\text{int}}^{(F)} + W_{\text{ext}}$ into Equation (3.6) results in the equality $\Delta U^{(F)} = -W_{\text{int}}^{(F)}$. In the following the work W_{ext} of the contact forces between impact mass and foam surface will be referred to as the *absorbed energy*. It can be calculated as the integral

$$W_{\text{ext}}(\varepsilon_n) = V_0 \int_0^{\varepsilon_n} \sigma_n(\varepsilon) \, d\varepsilon. \quad (3.7)$$

where nominal strains ε_n and stresses σ_n have to be inserted. V_0 is the undeformed volume of the foam specimen, and ε_n is equal to the nominal strain at the time the impact mass finally separates from the foam.

In terms of crash worthiness, an absorption efficiency A can be defined as the ratio between the actually absorbed energy W_{ext} and the energy absorbed by an ideal absorber W_{ideal} showing a constant stress level σ_n^{max} throughout a compressive deformation:

$$A(\varepsilon_n) = \frac{W_{\text{ext}}(\varepsilon_n)}{W_{\text{ideal}}} = \frac{W_{\text{ext}}(\varepsilon_n)}{\sigma_n^{\text{max}} \varepsilon_n}. \quad (3.8)$$

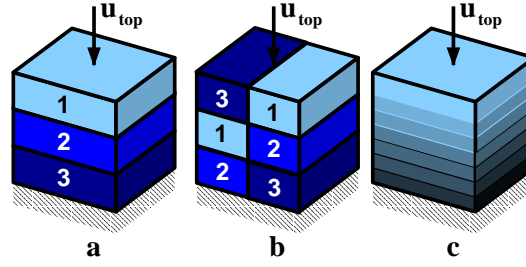


Figure 3.5: The three foam cube models for the quasi-static simulations: three layers in serial arrangement (a), three layers in two parallel columns (b) and linear density distribution (c). The cube edge length is equal to 100 mm.

3.4 Results

3.4.1 Quasi-Static Simulations

The simulation models used for the quasi-static simulations are shown in Figure 3.5. Model (a) consists of three layers with absolute densities of $\rho_1 = 0.2$, $\rho_2 = 0.5$, and $\rho_3 = 0.8$ g/cm³. The relative thicknesses of the layers are determined in such a way that the apparent density ρ_{app} is equal to $\rho_2 = 0.5$ g/cm³. Accordingly, the volume ratio is uniquely defined by the volume fraction of the layer of medium density ρ_2 , that is, V_2/V_{total} , which is also the parameter distinguishing the different simulation results in Figures 3.6 and 3.7.

Figure 3.6 shows the predicted quasi-static stress–strain relationships for volume fractions V_2/V_{total} ranging from 0 to 100%. The relationship for the fully homogeneous foam cube corresponds to the one found for $\rho = 0.5$ g/cm³ in Figure 3.2. The foam model, which contains just two layers of 0.2 and 0.8 g/cm³ density shows two distinct kinks where the collapse stress of either fraction is reached. The fact that half of the foam volume collapses at a very low plateau stress significantly reduces the amount of energy absorbed by the material. This is reflected in Figure 3.7 (left), which shows the absorbed energy of the cube-shaped specimen as a function of strain and the density composition. It becomes obvious that the homogeneous foam absorbs a maximum of energy, whereas the opposite is true for the foam composed of 50% ρ_1 and 50% ρ_3 . The energy absorption efficiency plots in Figure 3.7 (right) show a similar picture, with the efficiency being maximal for the homogeneous foam for strains above 20%. At strains below 20% the lower gradient of the stress–strain curve for ρ_1 results in a higher efficiency of foam models containing a layer of this density. For the special case of a foam composed of three layers of equal volume and of densities ρ_1 , ρ_2 and ρ_3 each, Figure 3.8 displays how the stored energy is distributed between the different regions. The potential of the low density fraction is exhausted at global strains around 25%, indicating that the material has become too densified to be

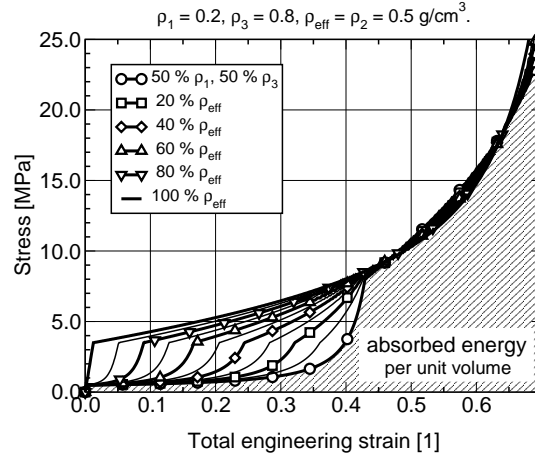


Figure 3.6: Stress versus strain diagrams predicted for foam plates that consist of layers of different density while maintaining the same overall density. The solid line corresponds to a meso-homogeneous plate, the open circles denote a two-layer structure, and all other cases are three-layered arrangements.

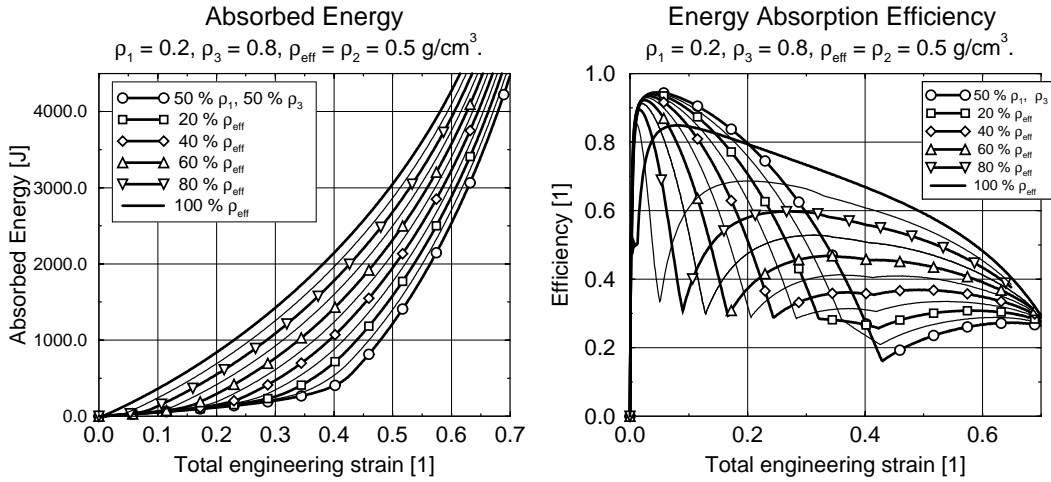


Figure 3.7: Energy absorbed by (left) and energy absorption efficiency (right) of an initially $10 \times 10 \times 10 \text{ cm}^3$ cube-shaped specimen (right) as functions of strain and the distribution of three different densities, model (a).

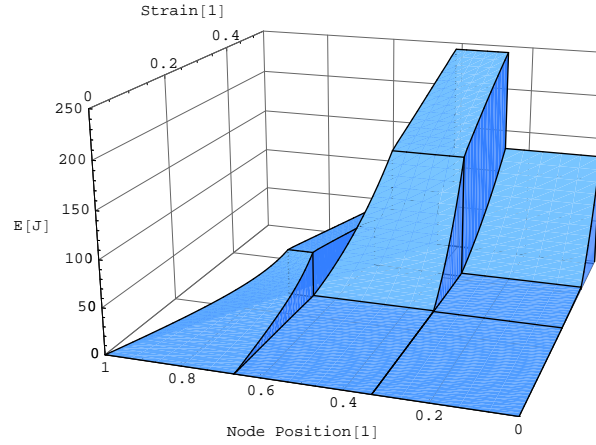


Figure 3.8: Increase of local internal energy (per spring element) as a function of global strain for model (a). The three layers of initially equal thickness have densities of 0.2, 0.5 and 0.8 g/cm³, respectively, from left to right.

compacted further. It is at strains above this value that the other two regions collapse successively and start to absorb energy. At 50% global strain they are still capable of absorbing more energy.

The second simulation model is composed of six geometrically identical cuboids, see Figure 3.5(b). Again three different densities are considered, but now the arrangement of 3 rows and 2 columns allows for a parallel coupling of regions with different densities. In Figures 3.9 and 3.10 the composition of the columns is described by a sequence of two numbers where each digit 1, 2 and 3 stands for a density of 0.2, 0.5 and 0.8 g/cm³, respectively. The apparent density is kept constant at 0.5 g/cm³. Again the most balanced arrangement (123-321) shows the best behavior with respect to energy absorption. At the other end of the scale the most unbalanced combination 123-123 sets the minimum value for the absorbed energy.

The quasi-static model in Figure 3.5(c) is characterized by a linear density distribution with a range from 0.2 to 0.8 g/cm³. Comparing the local strain, Figure 3.11 (left), and the increase of internal energy, Figure 3.11 (right), shows again that layers of low density (right) collapse first and store the main part of the absorbed energy at low global strains. At higher strains the denser regions, which collapse at higher plateau stresses, dominate the energy absorption behavior, while at the same time the deformation and absorption potential of the compacted layers of low density has been exhausted.

The proposed simulation model also allows a random perturbation of the local apparent density. Figure 3.12 shows how different stress versus strain relationships may result from different statistical distributions of the local foam density. In all cases the average density

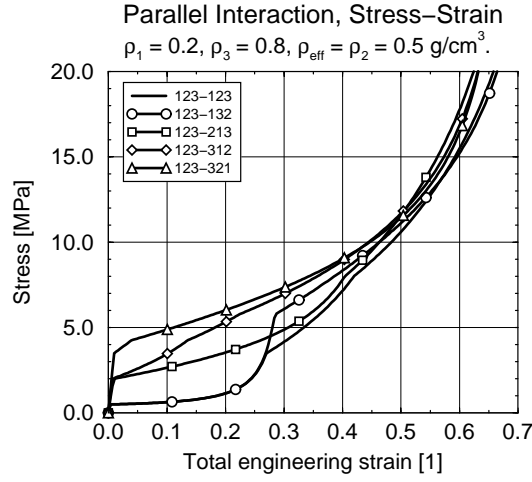


Figure 3.9: Stress-strain relationship as a function of the foam element arrangement, model (b).

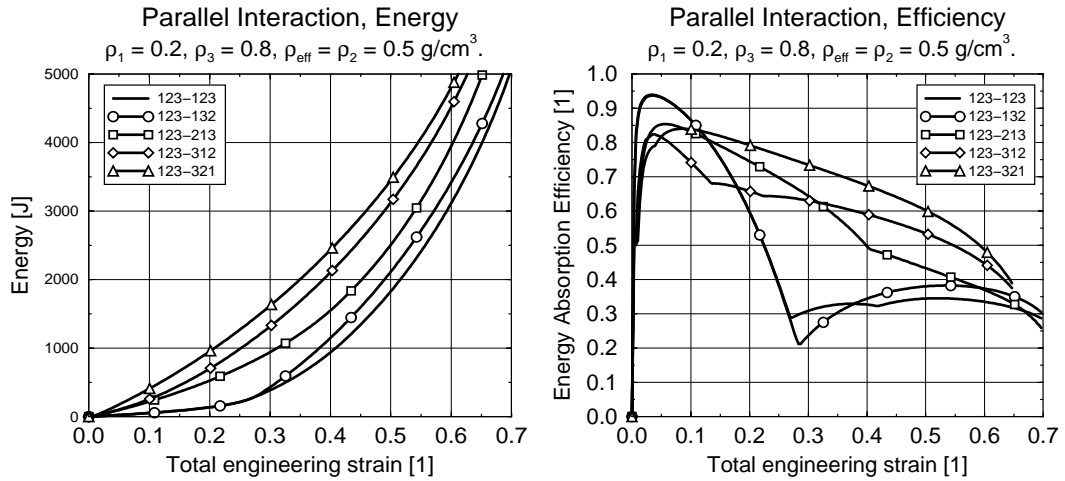


Figure 3.10: Energy absorbed by (left) and energy absorption efficiency (right) of an initially $10 \times 10 \times 10 \text{ cm}^3$ cube-shaped specimen as functions of strain and foam element arrangement, model (b).

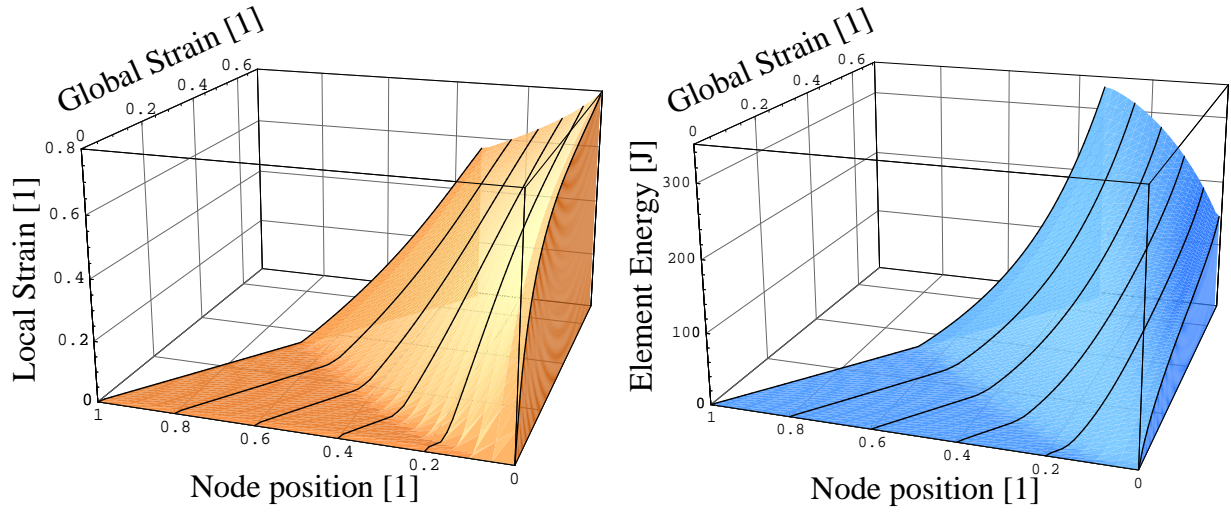


Figure 3.11: Local strain (left) and evolution of local internal energy (per element, right) for a linear density distribution, model (c).

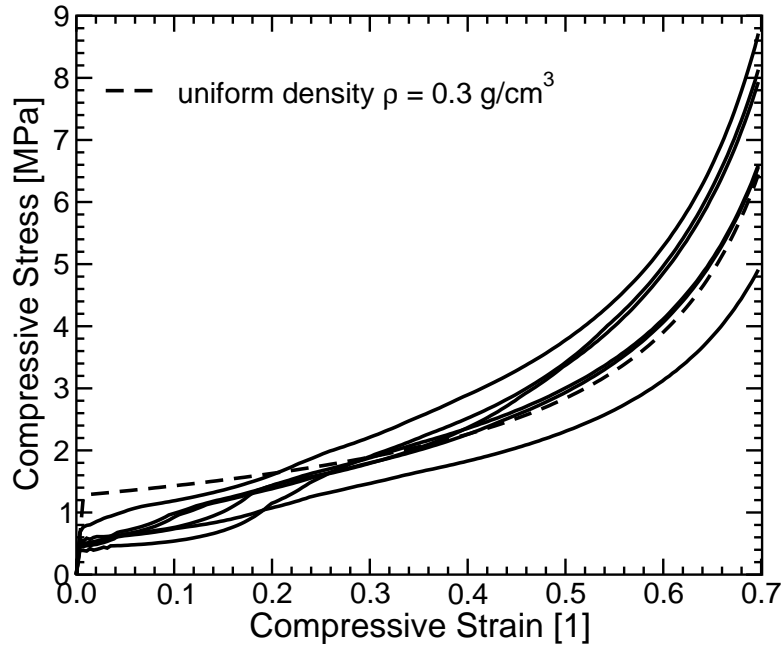


Figure 3.12: Stress versus strain diagrams predicted for several randomly perturbed density distributions having the same average density. The dashed line corresponds to a homogeneous foam specimen of the same apparent density.

was 0.3 g/cm^3 . The dashed line in Figure 3.12 represents the stress versus strain relationship for a model of homogeneous foam density. For compressive strains up to 30% the randomly perturbed foam bodies mostly exhibit lower stresses than the homogeneous model, owing to the localized collapse of layers with an apparent density below the average one. Beyond 30% compressive strain, however, most of the perturbed configurations show more resistance against compression than the homogeneous model.

3.4.2 Dynamic Simulations

As an example for dynamic mesomechanical simulations the impact of a rigid impactor on a foam cube fixed to a rigid wall is considered. The influence of the deformation velocity is restricted to inertial effects: any strain rate influence due to the entrapped gas is neglected assuming closed foam cells filled with an ideal gas under isothermal conditions. Thus, the mechanical contribution of the compression of the entrapped gas is implicitly taken into account by the quasi-static stress-strain relationship as no gas flow is assumed to take place. In addition the strain rate sensitivity of aluminum is considered to be negligible. Since a purely mechanical theory is applied neither the temperature rise due to the increase of internal energy is taken into account nor is any other kind of thermo-mechanical coupling accounted for.

Introduction

Shim et al. illustrated several phenomena pertinent to the dynamic crushing of cellular structures [102]. Figure 3.13 shows the time histories of the normalized positions of selected material points during an uniaxial impact event. The material points are represented by lumped masses in the spring/mass model, and the mass positions are normalized by the foam pad thickness t_F . The actual simulation time is normalized by the time it takes an elastic shockwave to run from the impact end to the rigid wall, as will be discussed later. The material points are represented by lumped masses in the spring/mass model. The graphs were recalculated using the generic parameters presented in [102]: $a = 0.9$, $b = 2.0$, $\varepsilon_0 = 0.05$, $n = 0.4$, and $\sigma_0 = 1.0$. These parameters imply strain-softening, that is, for increasing compressive strain the post-collapse force decreases to a minimum and rises again as the collapse of individual cell layers begins to increase the overall stiffness.

Shim used an elastic-rigid plastic material formulation, where unloading in the post-collapse regime is assumed to be inelastic. The ratio $\bar{m} = m/M$ of the lumped foam masses m to the impact mass M governs the degree of compaction, as can be seen in Figure 3.13: the two diagrams differ in the mass ratio \bar{m} , which was chosen as $1/10$ for the left figure and $1/100$ for the right figure. The impact velocity, normalized by the foam pad thickness t_F , was identical for both simulations and amounted to $\bar{v} = 0.25$.

The ratio between the mass M of the impactor and the lumped mass of the individual foam elements influences the penetration depth of the impactor. For the higher m/M ratio

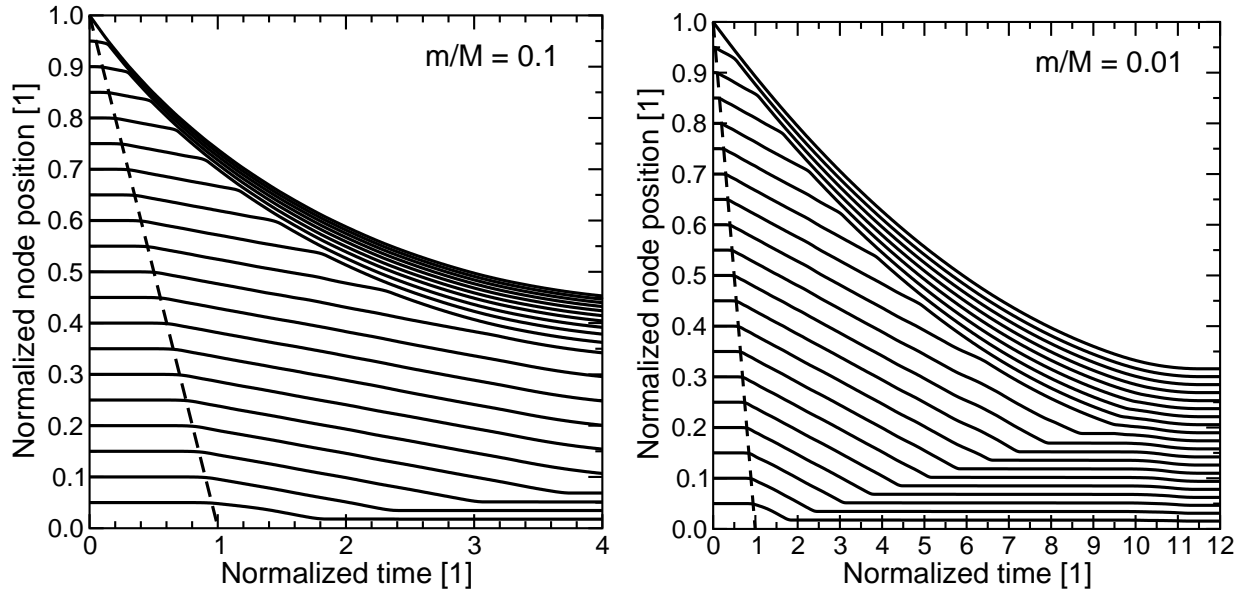


Figure 3.13: Predicted histories of the position of selected material points in a uniform foam sample under impact load (recalculated after Shim et al. [102]).

in Figure 3.13 (left) the inertial forces exerted on the impactor and the layer of compacted material traveling in front of it give rise to very high local strain levels close to the impactor and a crushing deformation mode that localizes in the upper half of the foam body. For a lower ratio m/M the forces necessary to accelerate individual lumped foam masses are lower, leading to lower local stress levels and lower local strains, see Figure 3.13 (right). Since the initial kinetic energy of the impact mass is the same in both simulations, more foam elements have to be compacted to absorb the same amount of energy as the highly compacted surface layers in Figure 3.13 (left). Therefore, the crushed zone in Figure 3.13 (right) is spreading over the whole foam body and shows uniform, but comparably low straining, resulting in a low stress level over a large stroke length.

In both simulations documented in Figure 3.13 elastic and plastic wave propagation phenomena are apparent. The time histories of the normalized positions of individual lumped foam masses show that after a certain time, which is directly proportional to the initial distance between the point masses and the foam surface, the masses suddenly start to travel in impact direction at a velocity which is well below the impact velocity. In Figure 3.13 the intersection of the dashed line with the initially horizontal mass position curves marks the moment of this sudden acceleration impulse, which is the footprint of the elastic compressive stress wave that is initiated at the first moment of impact and travels ahead of the spreading zone of plastic deformation. For a continuum, the elastic wave speed c_{el} can

	Shock wave front	
	↓	
Compressive stress	σ_2	σ_1
Density	ρ_2	ρ_1
Velocity	v_2	v_1
Wave speed	$c \Rightarrow$	

One-dimensional Shock Wave Analysis

Table 3.1: Material state in front (index 1) and behind (index 2) a shock wave front for a one-dimensional shock wave analysis.

be calculated as a function of Young's modulus E and the density ρ :

$$c_{\text{el}} = \sqrt{E/\rho} \quad (3.9)$$

For the particle-spring chain proposed by Shim et al. this translates to the normalized wave speed $\bar{c} = t_{\text{F}}^{-1} \sqrt{(\varepsilon_0 \bar{m})^{-1}}$. The pseudo time it takes the elastic wave to travel through the 20 layers of the model can be calculated to 1.41 s for $\varepsilon_0 = 0.05$ and $\bar{m} = 0.1$ (Figure 3.13, left), and 0.45 s for $\bar{m} = 0.01$ (Figure 3.13, right), which agrees with the simulation results.

At the distal end of the simulation model, the elastic wave is reflected at the rigid wall the model is attached to. At the same time, the bottom of the foam column, which at that time is traveling at a constant speed of $v = \sigma_0/(\rho c_{\text{el}})$ or, in terms of the parameters used by Shim et. al., $\bar{v}_{\text{el}} = t_{\text{F}}^{-1} \sqrt{\sigma_0 \varepsilon_0 / \bar{m}}$, giving $\bar{v}_{\text{el}} = 0.0355$ for $\bar{m} = 0.1$ and $\bar{v}_{\text{el}} = 0.112$ for $\bar{m} = 0.01$, suddenly encounters a rigid obstacle. This has two immediate effects: firstly, the elastic wave is reflected into the material, which at that point shows a stress level σ_0 corresponding to first cell collapse, and, hence, a tangent stiffness, which is far lower than the elastic modulus; secondly, the body of foam, that is traveling behind the elastic wave front, runs into an obstacle. These effects cause the foam layers close to the wall to crush, and a plastic shock wave to originate at the wall.

At the impact end, the impact mass usually has sufficient speed and kinetic energy to outrun the material traveling at \bar{v}_{el} behind the elastic wave front. This causes layer-wise crushing and produces an expanding zone of compacted material in front of the impact area, which is lead by a plastic shock front (see Figure 3.13).

Table 3.1 describes the state of a material before (index 1) and after a shock wave has passed by (index 2). Considering a control volume traveling along with the speed of the shock wave c , the law of momentum conservation yields:

$$(\sigma_2 - \sigma_1) = v_1 (v_1 - c) \rho_1 - v_2 (v_2 - c) \rho_2 \quad (3.10)$$

Material continuity dictates that

$$(c - v_1) \rho_1 - (c - v_2) \rho_2 = 0. \quad (3.11)$$

Equations (3.10) and (3.11) can be used together with the stress-density relationships $\sigma_{1/2} = \sigma(\rho_{1/2})$ defined implicitly by Equation (3.1) for calculating the states in front and behind the wave front. Please note that σ_1 and σ_2 have to be inserted as positive values for *compressive* stresses.

The set of equations (3.10) and (3.11) can be exploited in several ways. For the elastic compression wave, inserting $v_1 = 0$, $\sigma_1 = 0$, $\rho_1 = \rho_0$ for the initial state of the material in front of the elastic wave front, and $\sigma_2 = \sigma_0$ as well as $\rho_2 = \rho_0/(1 + \sigma_2/E)$ for the state behind the shock wave allows solving for the elastic wave speed $c_{el} = \sqrt{E/\rho}$ and the resulting speed $v_{el} = \sigma_0/(\rho c_{el})$ of the material trailing the wave front.

The initial elastic wave is followed by a slower stress wave causing massive local compaction in front of the impact mass. For a real metallic foam the assumption of $\sigma_1 = \sigma_0$, $v_1 \approx 0$, $\rho_1 \approx \rho_0$, and $v_2 \approx v_{\text{impact}}$ is justifiable for the moment of impact. With this simplification the corresponding stress state $\sigma_2 = \sigma_{\text{dyn}}$ can be calculated by numerically solving the equation

$$\sigma_{\text{dyn}} = \sigma_0 + \frac{\rho_1 \rho_2(\sigma_{\text{dyn}})}{\rho_2(\sigma_{\text{dyn}}) - \rho_1} v_{\text{impact}}^2 \quad (3.12)$$

for σ_{dyn} .

It is readily observable that the speed c_{pl} of the plastic wave front is not constant, but gradually decreases to zero as the kinetic energy is absorbed, and the zone of compacted foam between the plastic wave front and the impact mass is increasing and slowing down at the same time (Figure 3.13).

The front of compaction originating from the rigid wall, on the other hand, appears to progress at a constant speed until it meets the impact front. In the idealized example of Shim et al., $\sigma_1 = \sigma_0$, $v_1 = \bar{v}_{el}$, and $\rho_1 = \bar{m}/(1 - \varepsilon_0)$ describe the state of the material between the two plastic wave fronts. The rigid boundary causes v_2 to be zero between the reverse plastic wave front and the wall. Expressing σ_2 as $\sigma_2(\rho_2)$ by means of the stress-strain relationship (3.1) we can solve Equations (3.10) and (3.11) for c_{pl} and ρ_2 , obtaining theoretical values of $\bar{c}_{pl} = 0.027$ for $\bar{m} = 0.1$ and $\bar{c}_{pl} = 0.085$ for $\bar{m} = 0.01$.

After the initialization of a plastic wave front at the rigid wall a zone of compacted material is expanding away from this boundary. In the idealized models of Shim et al. the mass ratio \bar{m} determines whether this wave front meets with the compaction front in front of the impact mass. For the higher normalized mass $\bar{m} = 0.1$ this is not the case (Figure 3.13, left), because the inertial forces resisting the acceleration of the individual lumped foam masses cause higher local compressive strains and, therefore, higher local energy dissipation. At the same time, these forces slow down the lump consisting of the impact mass and the body of compacted foam at a rate that prevents deep penetration of the impactor. For the lower normalized mass $\bar{m} = 0.01$ in Figure 3.13 (right) the inertial forces necessary to accelerate the lumped foam masses are lower, resulting in lower local strains and lower local energy dissipation. The forces acting between impactor and foam pad are too low to prevent the impactor from penetrating until the two compaction fronts meet, and the

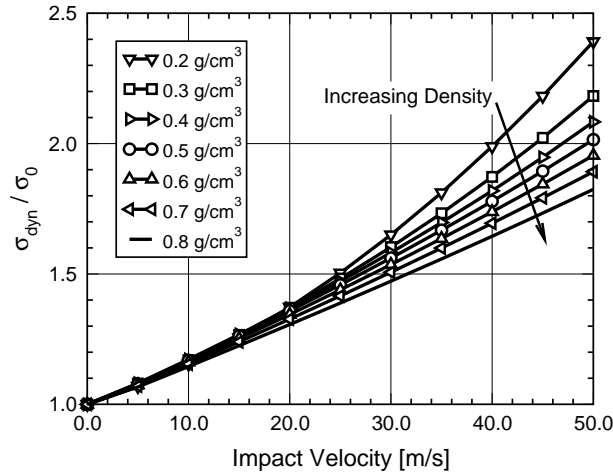


Figure 3.14: Predicted influence of impact velocity and foam density on the initial stress response σ_{dyn} relative to the static collapse stress σ_0 .

foam is compressed in a very uniform manner (Figure 3.13, right). This generic dynamic example shows that, all things like impactor mass M , impact velocity v_{impact} and material behavior being equal, the foam with the lower normalized mass density performs better in terms of uniformity of the compressive strain, the exploitable stroke length, and the stress level exerted on the impactor.

ALULIGHT Foam Pads of Uniform Density

In the previous section, a generic model originally proposed by Shim et al. [102] was investigated to outline the basic mechanisms of elastic and plastic wave propagation that govern a one-dimensional impact event involving a foam pad fixed to a rigid wall and a rigid impact mass striking perpendicularly to the surface of the pad. The material data collected by Gradinger (see [36] and Section 3.2) lend themselves well to a transfer of the theoretical results to more practical examples of uniaxial impact events.

In Equation (3.12) an implicit relationship for the determination of the initial dynamic contact stress σ_{dyn} between an impactor with an absolute velocity v_{impact} and a foam pad was presented. Inserting the density dependent material parameters (3.2) in Equation (3.12) and calculating σ_{dyn} for different impact velocities v_{impact} the influence of the apparent foam density and the impact velocity on the initial contact stress can be predicted. Figure 3.14 shows the relationship between this dynamic stress and the static collapse stress σ_0 as a function of the impact velocity and the foam density. All curves originate at $\sigma_{\text{dyn}} = \sigma_0$ for $v_{\text{impact}} = 0$ m/s. For $v_{\text{impact}} = 30$ m/s the impact stress is about 50% higher than the static

collapse stress, with slightly higher relative stress responses for lower foam densities. At an impact velocity of $v_{\text{impact}} = 50$ m/s the relative difference between the static collapse stress and the dynamic contact stress ranges from approximately 80% for 0.2 g/cm^3 foam density to 140% for 0.8 g/cm^3 foam density. It may be concluded that for the considered brand of aluminum foam the dynamic response of a low density foam is more sensitive to the impact velocity than that of a high density foam.

For the discussion of elastic and plastic wave propagation in an *ALULIGHT* foam pad a new type of diagram is introduced in Figure 3.15. At the bottom of Figure 3.15 a lumped mass position versus time diagram as presented earlier is tilted counter-clockwise and projected to the base of a three-dimensional diagram showing the nominal local strains along its vertical axis. This kind of diagram has the advantage of giving not only a impression of the global deformation, but also of the distribution and the evolution of the local strains. Stress waves leading to a sharp increase in the local strains are clearly discernible as ramps along the time-position curves of individual foam elements. The parameters used for Figure 3.15 were: foam thickness $t_F = 50$ mm; impact mass $M = 10$ kg; impact velocity $v_{\text{impact}} = 10$ m/s; $\rho_{\text{low}} = 0.2 \text{ g/cm}^3$ (dashed area); $\rho_{\text{high}} = 0.3 \text{ g/cm}^3$.

It is easy to visualize the wave propagation phenomena discussed earlier with the proposed diagrams. In Figure 3.16 two low-energy impact events are illustrated as strain surface plots. The two depicted cases differ in the magnitude of the impact mass, M and $2.5M$, respectively, while the impact velocity is identical. Therefore, the kinetic energy to be considered in Figure 3.16 (b) is 2.5 times higher than the one in Figure 3.16 (a). At the moment of impact (time zero) an elastic shock wave starts running through the foam and subjects the material to the collapse stress σ_0 . In Figure 3.16(a) the jump of the local strain from zero to ε_0 is visible as a ramp, which is marked by a circle. At both ends, massive ramps indicate the propagation of the plastic wave fronts from both ends of the model. The slope of the ramp shows how the local strain is decreasing with increasing distance to the foam surface indicating that the body of compacted foam is slowing down gradually leading to less severe dynamic crushing inside the foam pad. The two plastic wave fronts meet roughly in the middle of the foam body resulting in a superposition of the stress waves and very high local strains. The plastic wave originating from the rigid wall subsides shortly afterwards while the impact wave continues to propagate until it is arrested at the rigid wall. The dissipation of the higher impact energy for the configuration in Figure 3.16(b) requires higher degrees of compaction, which manifests itself in the fact that both plastic waves continue to propagate beyond the limits of Figure 3.16(a). The impact wave is reflected both at the rigid wall and the impact mass, higher global and local levels of compression being the consequence. Note, that the *initial* strain levels are the same in both figures, since they depend essentially on the foam density and the impact velocity, both of which are identical.

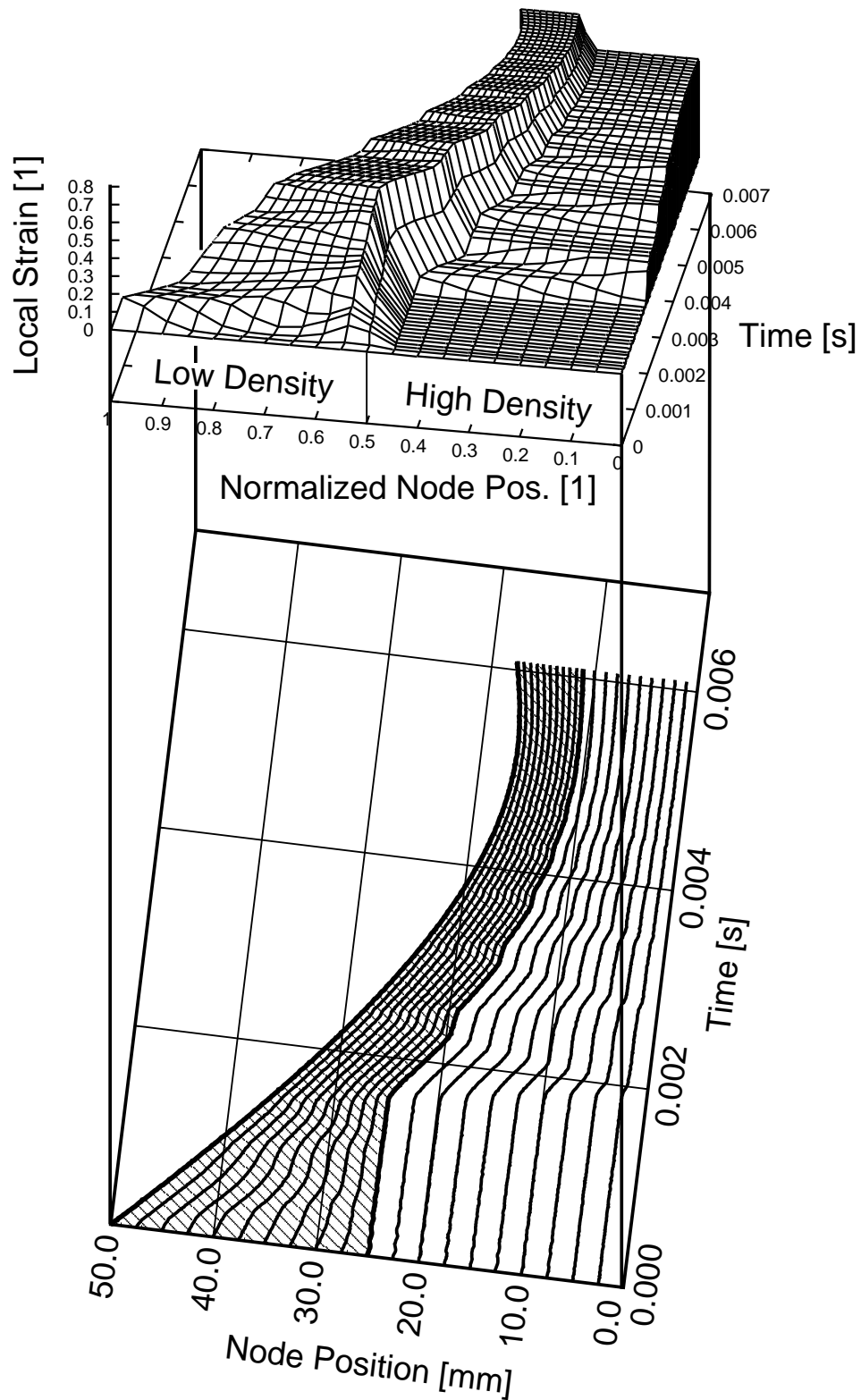


Figure 3.15: Predicted time history of local strains (top) and node positions (bottom) for the impact of a mass on a foam pad consisting of two layers of different apparent foam density.

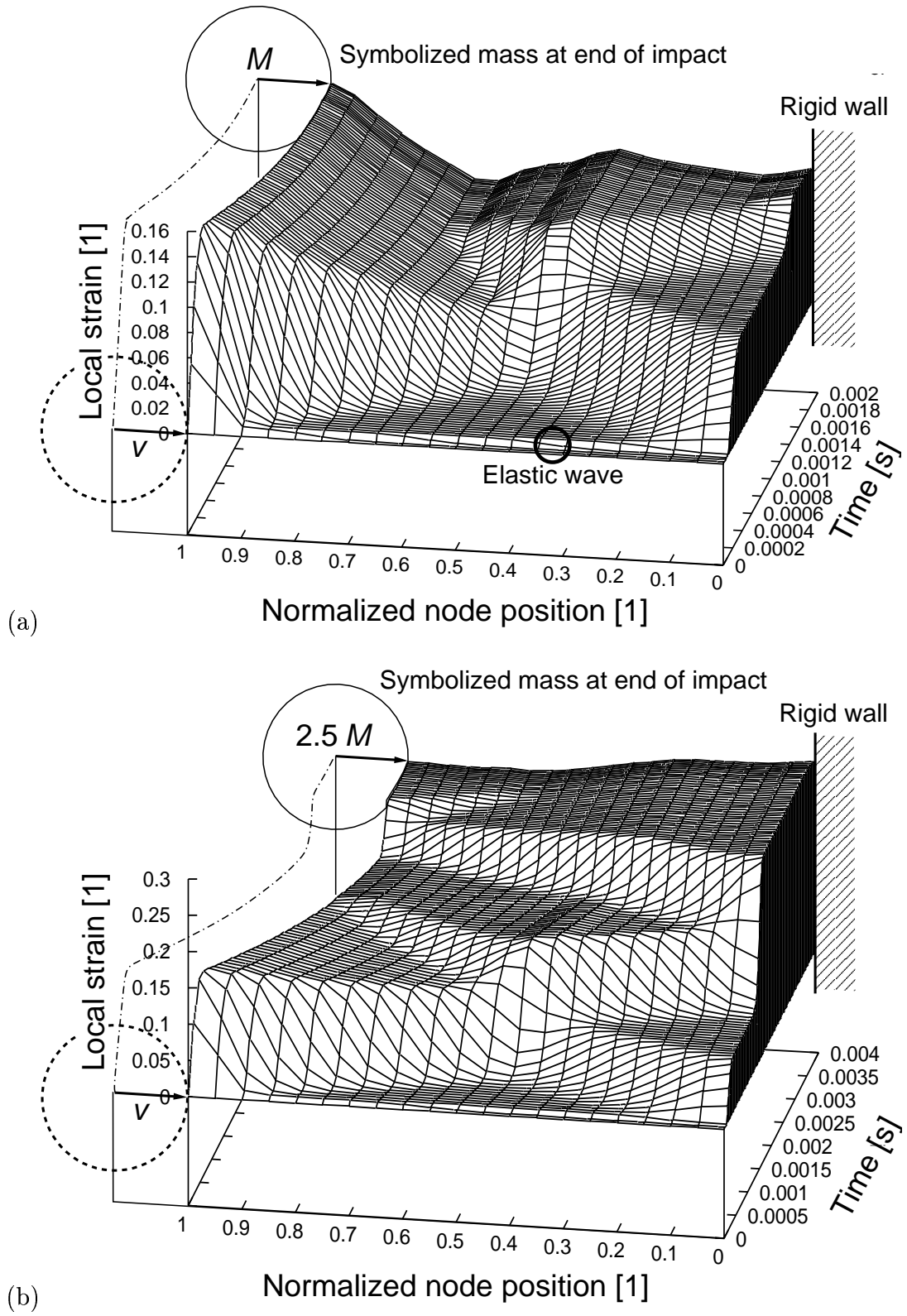


Figure 3.16: Local strain diagrams for impact events of two different kinetic energies.

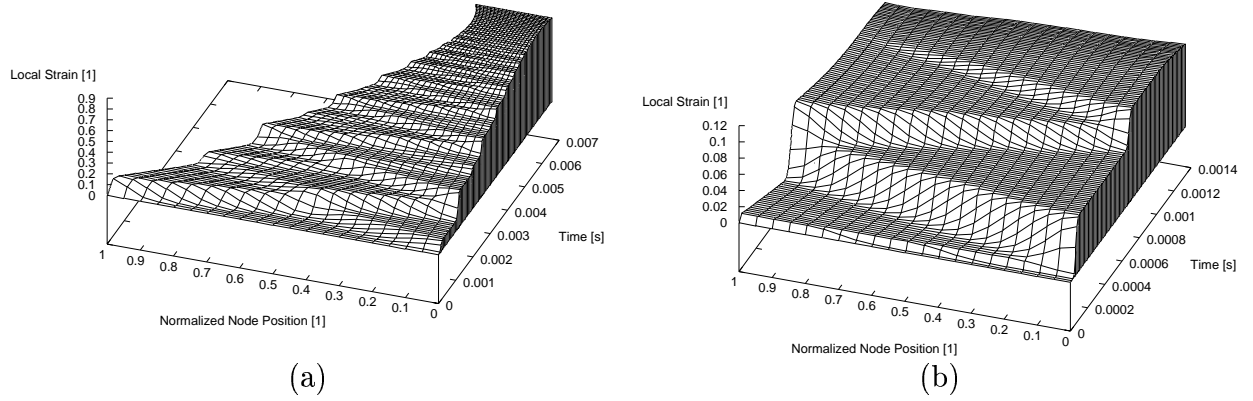


Figure 3.17: Comparison of the local strain histories for the foam layers with (a) 0.2 g/cm^3 and (b) 0.85 g/cm^3 density.

Global Influence of Density Variation

To transfer the above considerations to a more realistic setting, an idealized head impact event, as it may occur in the context of passenger protection in automotive engineering, was simulated. The impact mass M and velocity v_{impact} were set to 10 kg and 10 m/s, respectively. A cube-shaped foam pad with a constant foam layer thickness of $t_F = 50$ mm and a base area of 100×100 mm was assumed. With this configuration dynamic simulations were performed for varying apparent foam densities.

Figure 3.17 shows the strain surface plots for two extremes of the density range, $\rho_{F,\min} = 0.2 \text{ g/cm}^3$ and $\rho_{F,\max} = 0.85 \text{ g/cm}^3$. The foam pad with the low density, Figure 3.17(a), shows the characteristic zig-zag pattern of plastic waves originating and being reflected at the impact mass and the rigid wall. Since the stepwise increase of the local strain as indicated by the “ramps” in Figure 3.17(a) corresponds to jumps of the local stress, a stepwise increase of the contact stress at the top of the foam body may be expected from the ascending left border of the strain surface plot in Figure 3.17(a). The predicted time histories of the contact stress support this conclusion, see Figure 3.18. For the low density of 0.2 g/cm^3 several stress waves arrive at the impact mass and cause steps in the contact stress history. The fact that several compression waves run through the foam pad corresponding to the strain surface plot in Figure 3.17(a) means that at any time the strain distribution in the foam pad is comparably uniform. This can be emphasized by comparing the dynamic stress-strain relationship for $\rho_F = 0.2 \text{ g/cm}^3$ with the quasi-static one, which is marked in Figure 3.19 by a dashed line.

Subjecting a pad of foam of 0.85 g/cm^3 density to the same impact load leads to a drastically different result. Figure 3.17(b) shows the local strain surface plot for this initial density. The most surprising finding from this diagram is that the sudden acceleration of

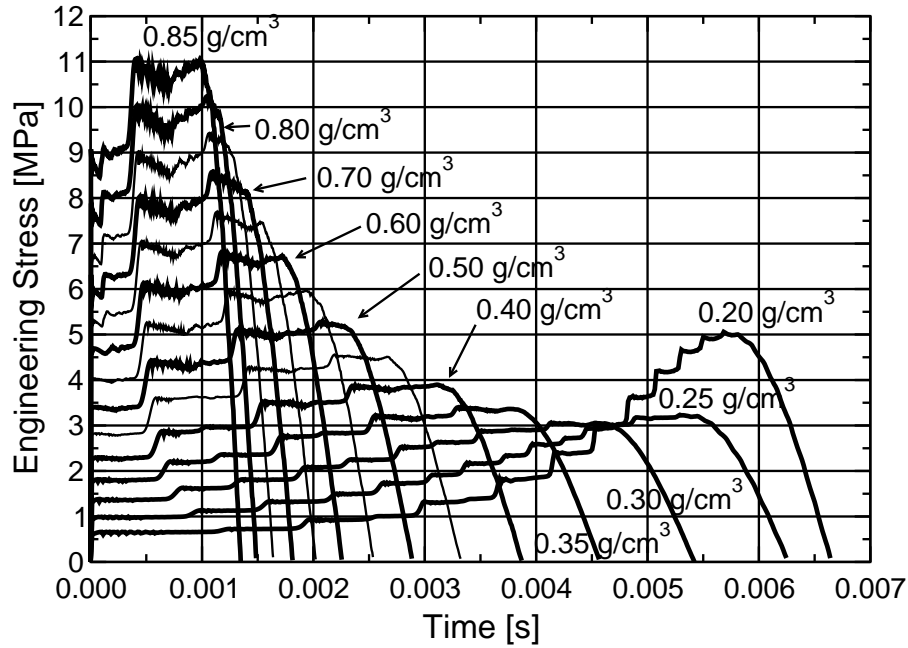


Figure 3.18: Predicted stress histories for the impact of a mass of 10 kg at a velocity of 10 m/s on foam layers of 50 mm thickness and different densities.

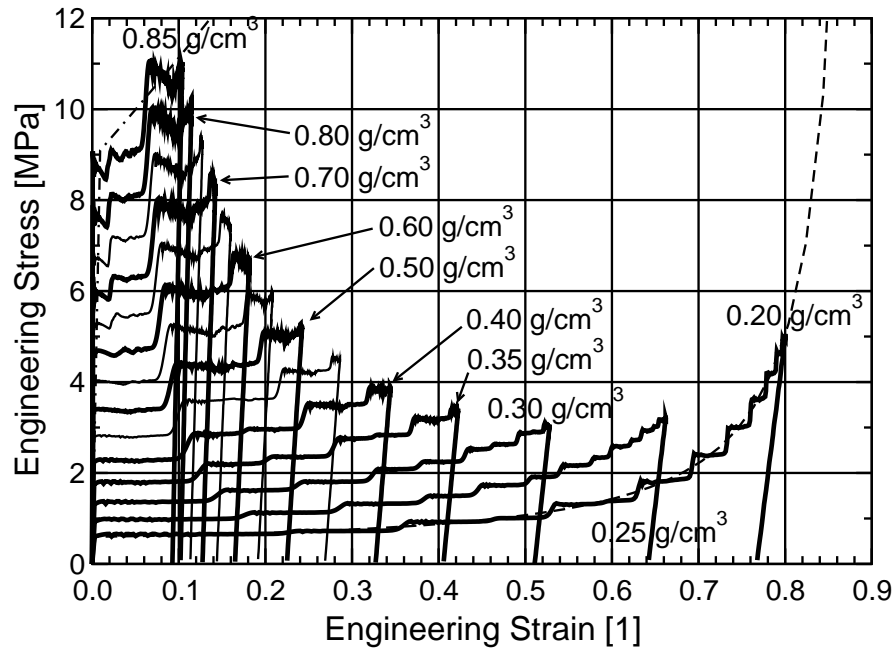


Figure 3.19: Predicted contact stress-global strain relationships for the impact of a mass of 10 kg at a velocity of 10 m/s on foam layers of 50 mm thickness and different densities.

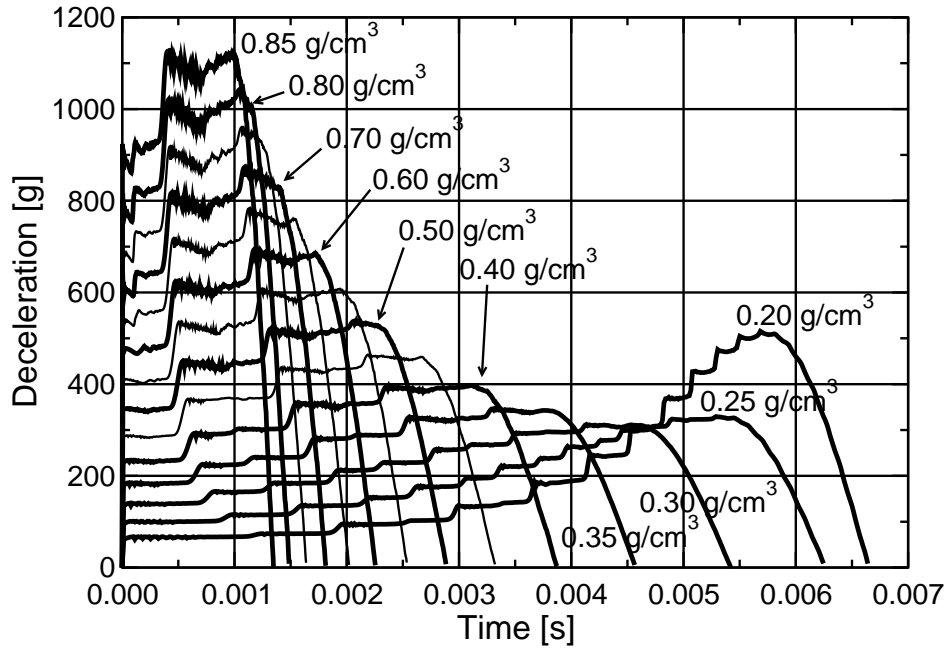


Figure 3.20: Predicted deceleration histories for the impact of a mass of 10 kg at a velocity of 10 m/s on foam layers of 50 mm thickness and different densities.

the foam surface layers does not lead to the formation of a plastic wave front the reason being that the velocity $v_{el} = 9.92$ m/s of the material trailing the elastic shock wave front is almost identical to the impact speed of $v_{impact} = 10$ m/s. As the elastic shock wave reaches the distal end of the model, the reflection of the elastic stress wave and the kinematic boundary condition cause compressive strains beyond the collapse strain ε_0 and a wave of plastic compression to run back towards the impact mass, which, at that time, perceives only the static collapse stress $\sigma_0 = 9.1$ MPa as the foam's mechanical response. This changes as soon as the plastic shock wave reaches the foam surface and is reflected at the rigid impact mass raising the instantaneous stress level to 11 MPa. Comparing this stress response to the quasi-static one (the dash-dotted line in the upper left hand corner of Figure 3.19) shows that the contact stress experienced by the impact mass jumps from the collapse stress directly to a maximum level. The final peak of the dynamic stress–global strain curve (Figure 3.19) is very close to the quasistatic stress–strain relationship indicating that the strain distribution is almost uniform over the thickness of the foam pad, which can also be seen from Figure 3.17(b).

To judge the severity of the impact events from a biomechanical viewpoint it is advantageous to describe the impact event in terms of a deceleration history. Figure 3.20 shows the corresponding diagrams for the problems under consideration. It is obvious that the foam pads of high density show high initial stresses, which increase only slightly in the course of the impact. The reason for this is the high rate of energy dissipation at the

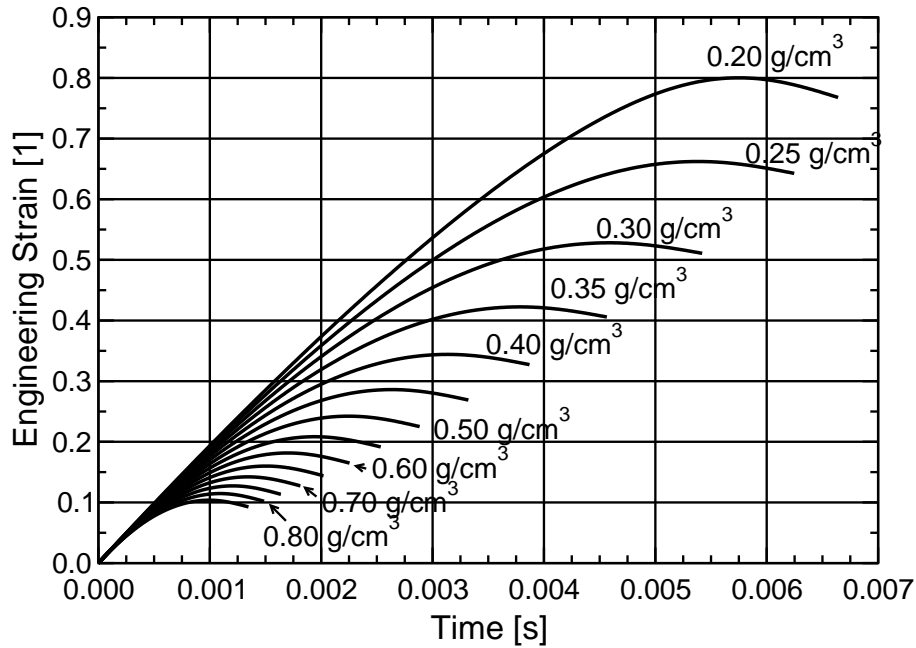


Figure 3.21: Predicted strain histories for the impact of a mass of 10 kg at a velocity of 10 m/s on foam layers of 50 mm thickness and different densities.

increased plateau stress, which reduces the necessary stroke length and, in turn, the global strain. The high decelerations caused by high-density foam pads are also visible from the high initial curvature of the predicted global strain versus time curves in Figure 3.21. Owing to the large decelerations, the impact events last considerably shorter for high density foam paddings. The low density foams represented in Figure 3.20, on the other hand, show impact events lasting several milliseconds, during which the deceleration is steadily increasing. In the case of a foam of 0.2 g/cm^3 density the final deceleration reaches almost half of the magnitude of the peak acceleration experienced for the maximum density due to low initial energy dissipation rate and the resulting high degree of compaction at the end of the impact. For the considered impact parameters the most advantageous density with respect to a minimization of the highest appearing deceleration is about 0.3 g/cm^3 . The fulfillment of other injury criteria may require a different combination of impact duration and deceleration history.

Influence of Foam Pad Thickness

So far, the apparent density ρ_F of the foam material was varied, while the thickness t_F of the foam pad was kept fixed. Certain damage or injury criteria may put restrictions on the maximum contact stress experienced by a body hitting a metal foam layer. If, for example, the maximum allowable contact stress is around 1 MPa, a foam density beyond

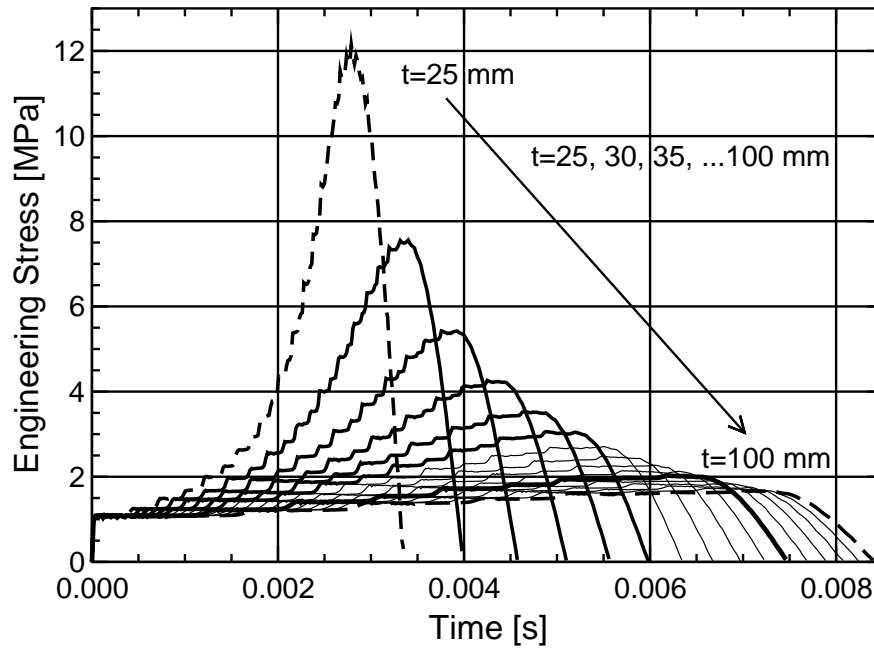


Figure 3.22: Predicted stress histories for the impact of a mass of 10 kg at a velocity of 10 m/s on foam layers of 0.25 g/cm^3 density and different densities.

0.25 g/cm^3 is undesirable since it would imply a plateau stress above 1 MPa. But even if the plateau stress is below the required maximum, the actual maximal contact stress is still largely influenced by the thickness t_F of the foam layer, as will be discussed in this section.

In the following, the relationship between the foam pad thickness and the predicted history of the contact stress is demonstrated for the example of a cuboid with a base area of $100 \times 100 \text{ mm}$ and a constant density of 0.25 g/cm^3 . The impact load was identical to the previous example ($M = 10 \text{ kg}$; $v_{\text{impact}} = 10 \text{ m/s}$). The foam pad thickness was varied between 25 and 100 mm.

Figure 3.22 shows the time history of the contact stresses experienced by the impact mass, and Figure 3.23 displays the contact stresses in terms of deceleration histories. The initial response of the foam is the same for all thickness values and oscillates between 1.0 and 1.1 MPa. This compares well to the quasistatic collapse stress of 0.91 MPa for $\rho_F = 0.25 \text{ g/cm}^3$ multiplied by the dynamic load amplitude magnifier of approximately 120% as documented in Figure 3.14. The subsequent evolution of the contact stress and the deceleration show the strong influence of the available stroke length on the occurring stress levels. For the thick (100 mm) foam pads a large degree of absolute deformation was possible at a rather low strain of 40%, compare Figure 3.24. Consequently, the maximum stress remained below 1.5 MPa and the energy absorption efficiency A above 80%. For the thin (25 mm)

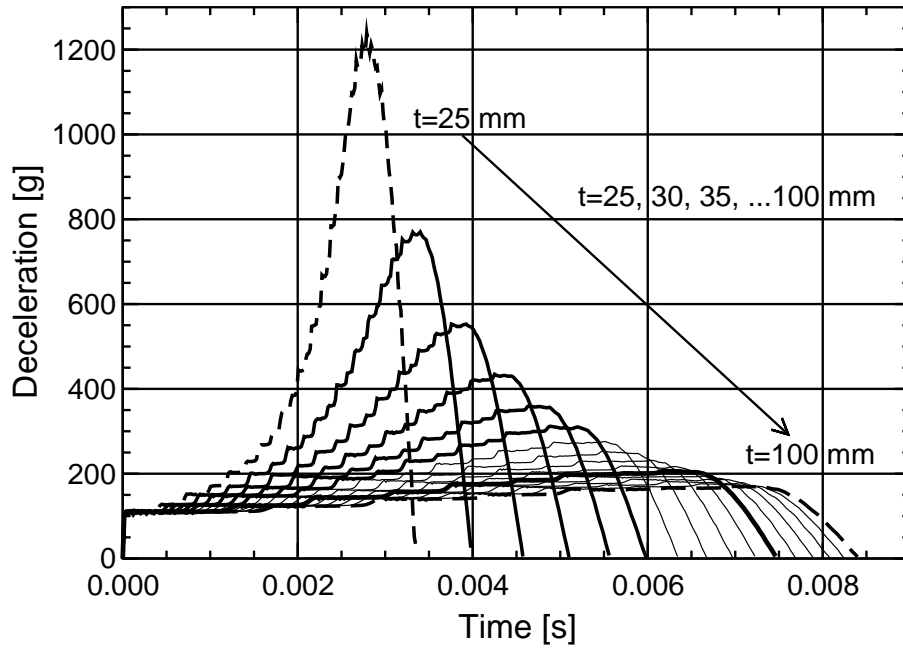


Figure 3.23: Predicted acceleration histories for the impact of a mass of 10 kg at a velocity of 10 m/s on foam layers of 0.25 g/cm^3 density and different thicknesses.

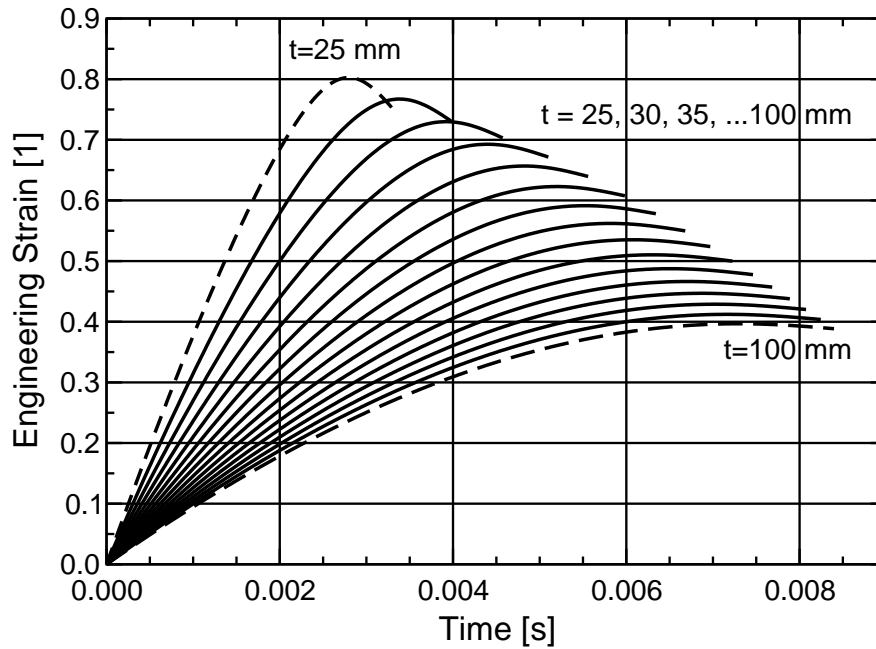


Figure 3.24: Predicted overall strain histories for the impact of a mass of 10 kg at a velocity of 10 m/s on foam layers of 0.25 g/cm^3 density and different thicknesses.

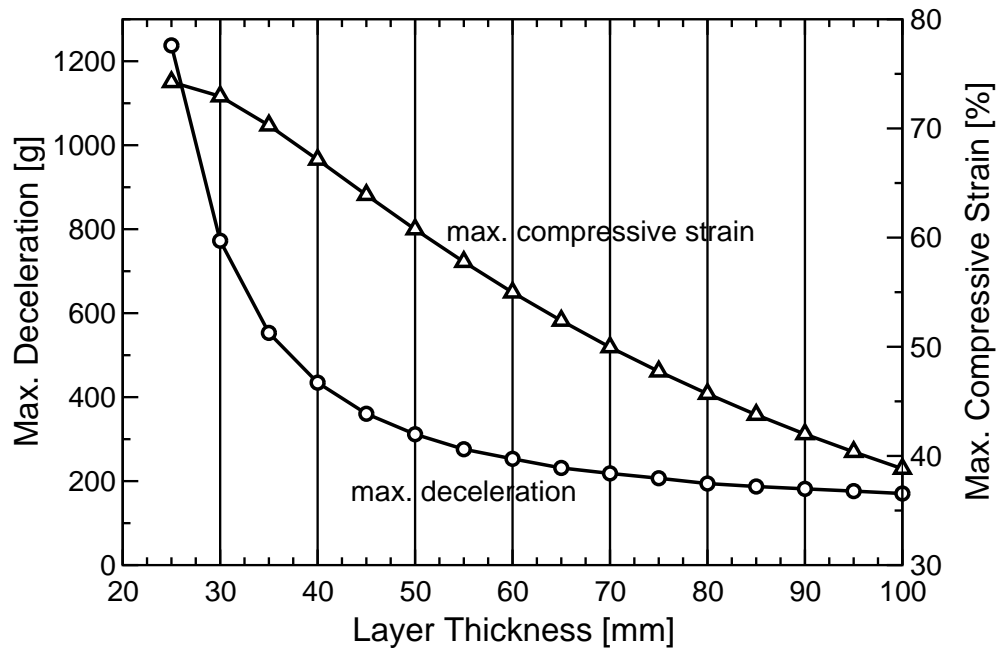


Figure 3.25: Predicted maximum deceleration and maximum compressive strain as functions of layer thickness (impact mass 10 kg; velocity 10 m/s; foam density 0.25 g/cm³).

foam pad the available stroke length was considerably smaller resulting in higher strain ($\approx 80\%$) and stress levels (≈ 12 MPa). At the same time, the energy absorption efficiency was reduced to $A = 5\%$!

It follows that a thick foam layer is desirable for reaching large stroke lengths and for keeping both the levels of compaction and the stress levels low, as illustrated by Figure 3.25. For actual applications, restrictions on the available design space or weight considerations will, unfortunately, favor configurations of less than ideal thickness.

Layered Foam Pads of Non-Uniform Density

After the investigations of various configurations with uniform apparent foam densities we now study the case of simulation models consisting of two layers of equal thickness (25 mm each) but differing density (0.20 g/cm³ and 0.35 g/cm³). The model is hit by a rigid mass of 1 kg traveling at a speed of 30 m/s. The two possible stacking orders of the two layers are considered.

As predicted by the analytical derivation the instantaneous stress is significantly higher if the impact mass hits the layer of high density first (see Figure 3.26). The subsequent stress–time history depends on the way the stress waves are reflected at the impact mass, the density boundary, and the rigid wall. In Figure 3.27 the time history of the local

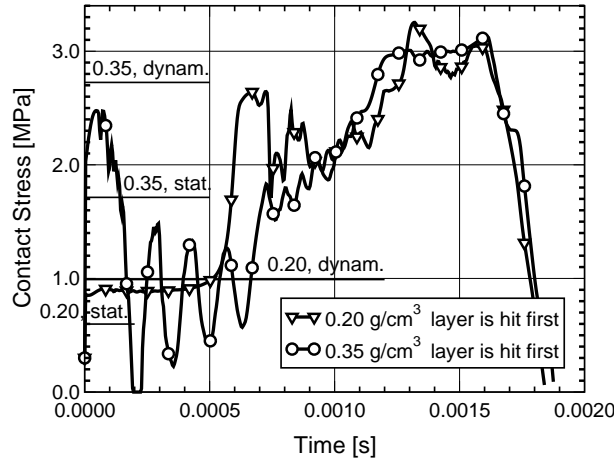


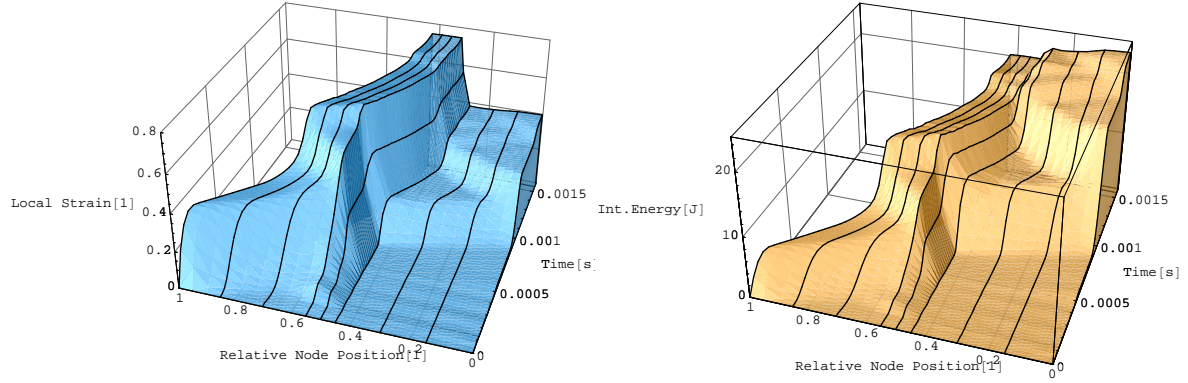
Figure 3.26: Contact stress between a mass of 1 kg having an impact speed of 30 m/s and a foam pad composed of two equally thick layers of 0.20 g/cm^3 and 0.35 g/cm^3 density. The two possible stacking orders of the layers are simulated.

strains and the evolution of the local internal energy can be seen. Apart from the basic wave propagation and reflection phenomena described previously the wave reflection at the density boundary influences the dynamic response of the model. It is noteworthy that the internal energy absorbed by the layer of higher density exceeds that of the softer layer, although the latter is deformed considerably more. It is also noticeable that two or three wave reflections are sufficient for generating fairly uniform local strains in each of the two layers.

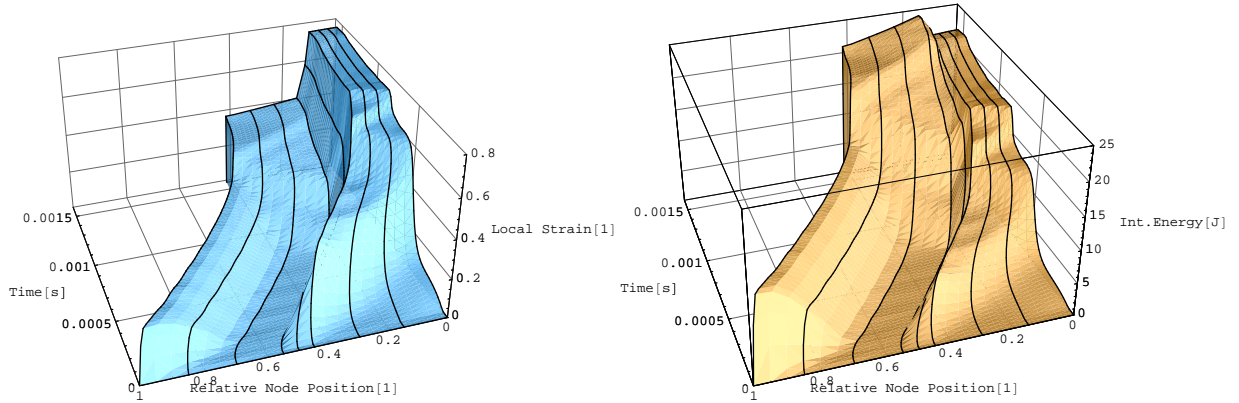
3.5 Summary

The influence of meso-inhomogeneities of the apparent density on the quasi-static and dynamic energy absorption behavior of aluminum foam was examined. The results are of particular interest when metallic foam is applied as protective padding. Strong meso-inhomogeneities reduce the energy absorption efficiency, because they lead to strain localization resulting in a decrease of the initial collapse and plateau stress and a less pronounced plateau region [18; 38], as can be seen from Figure 3.6. This holds true for density variations occurring in the loading direction and perpendicularly to it [18]. Accordingly, for such applications it is desirable to tune foam production technologies for achieving uniform density distributions.

When a metallic foam is treated as a homogenized material, inertia effects [6] lead to wave propagation phenomena which are governed by the interaction of foam density, layer thick-



Impact mass hits layer of LOW density first



Impact mass hits layer of HIGH density first

Figure 3.27: Local strain history (left) and evolution of internal element energy (right) for the impact of a mass of 1 kg at a speed of 30 m/s on a 50 mm thick foam layer. The foam pad is composed of a 25 mm thick layer of 0.20 g/cm^3 density and a 25 mm thick layer of 0.35 g/cm^3 density. Different stacking orders are considered.

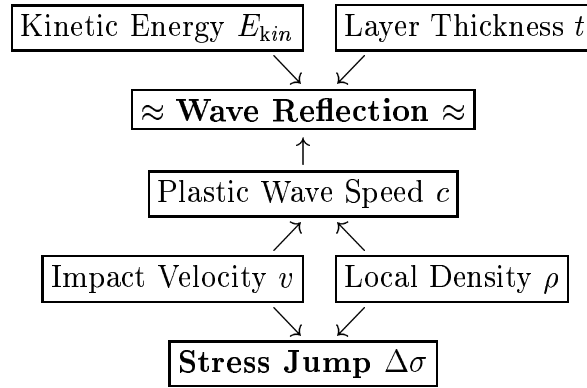


Figure 3.28: Factors determining the dynamic response of a foam layer of thickness t and local density ρ to the impact of a mass of velocity v and kinetic energy E_{kin} .

ness, impact energy and impact velocity [18]. These interacting factors are summarized in Figure 3.28. At moderate impact speeds such inertia effects give rise to an impact resistance that exceeds the static collapse strength only slightly, compare Figure 3.14. Nevertheless, the dynamic effects of wave reflection and wave superposition are noticeable under these conditions, as is evident in Figure 3.26, where the stacking order of foam layers with different densities is shown to influence the time histories of impact stresses significantly. The results obtained with simulations, that treat cellular metals as homogenized materials, however, will have to be compared to dynamic tests to make sure that no artificial inertia effects are introduced by the homogenization approach. Possibly, the mass density used for the homogenized material may have to be adjusted to closely fit the experimental results for dynamic events.

Mesosopic mass-spring models as described above are restricted to specific load cases and, in general, cannot handle arbitrary multiaxial loading paths. More generalized mesoscopic simulations can be carried out by using the Finite Element method with standard volume elements, see Chapter 4.

Chapter 4

Macroscopic Modeling of Metallic Foams

4.1 Introduction

From the perspective of structural modeling and simulation an efficient method of modeling metallic foam material in components, which are much larger than individual foam cells, is desirable. The difference in length scale between individual cells and foamed components impedes the modeling of microgeometrical details of the foam structure, because (a) a discretization of actual components down to the level of individual cells is out of the scope of current hard- and software technology, and (b) the algorithmic effort to create such large-scale microgeometrical models would be tremendous; a preprocessor suitable for this task would have to be capable of incorporating the available statistical information on cell size and cell orientation distribution in a meaningful way to reverse engineer a corresponding micro-structure.

Sometimes micro CT scans are used to generate microstructural models of foams [93] or bone [2], often by a direct transformation of individual CT data points (Voxels) to cuboid Finite Elements [65]. But, as in the case of a potential statistics-based microstructural modeling strategy, the length scale difference between the microstructure and the component poses severe characterization problems, because it is not yet technically possible to produce CT scans from component sized objects with high enough spatial resolution to render the microstructure in sufficient detail. Therefore, although examples of large scale Finite Element simulations, that can be directly compared to identical experimental setups, do exist for 2D honeycomb structures, compare the work of Papka and Kyriakides [79; 80; 81; 82], this approach is infeasible for typical 3D foams.

As a consequence, a continuum formulation for foams is applied, that is, the material is treated as if it did not consist of separate solid and gaseous phases, but rather represents a homogeneous medium, which fills the foam parts of the structure as if a solid, virtual

material was distributed uniformly in space instead of the discrete structure of the foam skeleton. This approach is backed up by the theory of asymptotic homogenization of periodic microstructures which is routinely applied to heterogeneous materials [110]. All these methods deal with local deformation mechanisms only insofar as their influence on the macromechanical behavior of the material is sought to be captured as accurately as possible. Sometimes it is not necessary to consider micromechanical mechanisms at all, for example when the macroscopic behavior of the material is modeled based solely on macroscopic experiments without any information on the micromechanical processes being available. In this case, often only overall properties, for instance the effective density, are used to describe mechanical parameters of, in most cases, specific brands of metallic foams [36; 38].

As was shown in the previous sections micromechanical considerations can nevertheless be useful to derive generic relationships, for example between the effective foam density and the effective stiffness [34], which can then be fitted to experimental results and provide some physical background for phenomenological approaches.

4.2 Nonlinear Macroscopic Behavior of Metallic Foams

Before mathematical models for the macromechanical behavior of metallic foams will be discussed in Section 4.3, some macromechanical phenomena characteristic of metallic foams will be presented in the following along with a survey of corresponding experimental results.

4.2.1 Behavior under Uniaxial Compression

Uniaxial Compression Behavior in Compression Direction

The uniaxial compression test is by far the most popular and most frequently performed test for metallic foams, see, for example, Degischer et al. [21]. Therefore, the mechanical behavior of metallic foams under uniaxial compression is very well documented. A discussion of the inelastic mechanical behavior in loading direction was already presented in Chapter 2 for the microscale and in Chapter 3 for the overall behavior.

Plastic Poisson's Ratio

Metallic foams can be compressed to very large axial strains. At the same time they do not show excessive lateral expansion, indicating a high degree of compressibility. Visual inspection of compressed foam samples, see, for example, Figure 3.2 (left), Markaki and Clyne [67], or Seeliger [99], even leads to the conclusion that there is no lateral expansion at all.

Foam Brand	Density $\rho_{F,rel}$	Yield Surface Shape Param. α	Plastic Poisson's ratio ν_{pl}	Source
<i>DUOCEL</i>	7.0%	1.58	0.150	[24]
<i>DUOCEL</i>	7.0%		0.052	[35]
<i>ALPORAS</i>	8.0%		0.024	[35]
<i>ALPORAS</i>	8.4%	2.08	0.010	[24]
<i>ALPORAS</i>	16.0%	1.35	0.230	[24]

Table 4.1: Plastic Poisson's ratios ν and selected yield surface shape parameters α (see Section 4.3.4) for open (*DUOCEL*^(TM)) and closed-cell (*ALPORAS*^(TM)) aluminum foam.

The relationship between longitudinal compression and transverse expansion is expressed in elastic and plastic Poisson's ratios, ν and ν_{pl} , respectively. The plastic Poisson's ratio ν_{pl} is defined as the negative ratio of the transverse logarithmic plastic strain to the longitudinal logarithmic plastic strain under uniaxial compression.

Shaw and Sata [101] report a plastic Poisson's ratio of 0.17 for closed cell aluminum foam. Deshpande and Fleck measured values of the plastic Poisson's ratio for three different metallic foams [24]. Their results are listed in Table 4.1 along with results of Gioux et al. [35], who found distinctly smaller values of ν_{pl} for comparable foams. Motz and Pippan [72] confirm the approximation of vanishing lateral expansion at high compressive strains, but observe a plastic Poisson's ratio of $\nu_{pl} = 0.35$ in the small strain regime between tensile yielding and fracture of the closed-cell aluminum foam *ALPORAS*. This result was found to compare favorably with Finite Element simulations of tetrakaidecahedral unit cell models [1].

Seeliger [99] found the plastic Poisson's ratio of closed-cell aluminum foam to increase monotonously from initially zero to 0.33 at 80% nominal compressive strain.

The abstraction of vanishing plastic Poisson's ratio for the compression of metallic foams is attractive and an often used assumption. In the interpretation of Poisson's ratios larger than zero care has to be taken with regard to the admissible strain range which might be comparatively small or even tensile. The influence of the plastic Poisson's ratio in Finite Element simulations will be discussed later.

4.2.2 Behavior under Hydrostatic Load

As soon as hydrostatic loads are imposed on cellular metals, their mechanical behavior begins to differ most significantly from the one observed in solid metals: whereas the latter generally retain a constant volume during plastic deformation, cellular metals can undergo large volumetric deformation due to the compressibility of their gaseous phase.

With respect to macromechanical modeling of metallic foams it is, therefore, important to characterize the effective behavior of the material under multiaxial loads. Unfortunately, the cellular nature of foams poses practical difficulties in the execution of experiments, since the surface of a foam specimen generally does not constitute a skin that can bear distributed (pressure) loads. Owing to this experimental problems, less data exists on the multiaxial behavior of metallic foams compared to the wealth of data for uniaxial loading.

Triantafillou et al. [113] submitted an open-cell aluminum foam ($\rho_F = 0.135 \text{ g/cm}^3$) to axisymmetric loading by applying tensile radial stresses and, simultaneously, compressive or tensile axial stresses. They found that an analytical failure surface derived in a companion paper by Gibson et al. [32] could be fitted well to the experimental failure stress states. As a particularly noteworthy result Triantafillou et al. determined the failure stress under hydrostatic tension and found it to be roughly equal to both the tensile and the compressive uniaxial failure stress of the examined foam material, which amounted to 1.77 and 1.70 MPa, respectively.

Gioux et al. [35] investigated the failure of open-celled aluminum foam (*DUOCEL*, $\rho_{F,\text{rel}} = 7\%$) and closed-cell aluminum foam (*ALPORAS*, $\rho_{F,\text{rel}} = 8\%$) under biaxial and (axisymmetric) triaxial loading. The average hydrostatic compressive collapse stress was essentially equal to the uniaxial compressive collapse stress for the open-cell foam and 30% higher than the uniaxial compressive collapse stress for the closed-cell foam. The data showed considerable scatter owing to variations in the apparent density of the specimens.

Deshpande and Fleck [24] investigated the yield behavior of two aluminum alloy foams (*ALPORAS*, $\rho_{F,\text{rel}} = 8.4\%$ and 16% ; *DUOCEL*, $\rho_{F,\text{rel}} = 7\%$) under axisymmetric compressive stress states. They found that the magnitude of the hydrostatic yield strength was consistently 20% lower than the uniaxial yield strength. Furthermore, they explored the evolution of the yield surface by repeated unloading and re-loading on different stress paths. More details on their results and the constitutive theory they inspired can be found in Section 4.3.5.

Hanssen [47] and Müllerschön [27] examined the hydrostatic behavior of *HYDRO* aluminum foam. They observed that the hydrostatic plateau stress was approximately of the same magnitude as the plateau stress measured for uniaxial loading. Seeliger [99] reports a hydrostatic compressive yield strength, which is $2/3$ of the uniaxial compressive yield strength for an AlSi7 foam of 0.34 g/cm^3 density.

The cited studies do not show a consistent trend with regard to the relationships between the uniaxial collapse stress and the hydrostatic collapse stress of the materials. The measured hydrostatic collapse stresses approach the values of the uniaxial collapse stresses within a range of $\pm 1/3$ of the latter values. It can be concluded that in the absence of specific triaxial experimental data, the hydrostatic strength can be estimated to be equal to the uniaxial strength of the materials.

4.2.3 Macroscopic Tensile Loading and Fracture

While metallic foams behave primarily in a ductile way under compression, they exhibit a semi-brittle behavior under uniaxial tension resulting in rupture of specimens at a strain of only a few percent, preceded by a linear elastic and an elasto-plastic regime with strain-hardening.

Thornton and Magee [111] found that the tensile yield strength of aluminum foam is in most cases lower than the compressive yield strength, with the relative difference increasing with increasing density. Sugimura et al. [109] concluded from their evaluation of flexure tests performed on *ALPORAS* foam ($\rho_F \approx 0.2 \text{ g/cm}^3$) that the tensile yield strength of the material was about 30% higher than the compressive yield strength at the same uniaxial strain. McCullough et al. [68] determined the tensile yield strength of *ALULIGHT* foam of $\rho_F = 0.65 \text{ g/cm}^3$ density; the measured tensile strength was at most 20% above the compressive one. Andrews et al. [4] performed uniaxial tension and compression tests on several different foam products and found tensile strengths, which are up to 20% lower than the compressive ones, with the exception of *ALCAN* foam, which behaved brittle in tension and showed a tensile ultimate strength less than half of its compressive collapse stress. In good agreement with these findings, Olurin et al. [78] report ultimate tensile strengths that are within 25% of the compressive plateau stresses for *ALPORAS* and *ALCAN* foam. Gioux et al. [35] report the tensile failure strength of *DUOCEL* ($\rho_{F,\text{rel}} = 7\%$) and *ALPORAS* ($\rho_{F,\text{rel}} = 8\%$) foam to be consistently 8% higher than the compressive yield strength. Motz and Pippan [72] performed tensile tests on *ALPORAS* foam ($\rho_F = 0.25$ and 0.4 g/cm^3) and determined yield stresses of 0.71 MPa and 1.79 MPa, and ultimate stresses of 1.70 MPa and 3.95 MPa, respectively, indicating a ratio of over 1:2 of yield stresses to ultimate stresses. Hanssen [47] reports tensile failure stresses, that are more or less equal to the initial plateau stress in compression for aluminum foam produced by Hydro Aluminium AS ($\rho_F = 0.2$ to 0.5 g/cm^3).

Most experiments cited above place the tensile strength of metallic foams within $\pm 25\%$ of the compressive strength. After the ultimate stress is reached, cracks start to propagate through the material leading to a sharp drop in the nominal stress-strain relationship and, eventually, total rupture of the specimen at strains of a few percent. Depending on the foam production technology this behavior can be highly anisotropic and different strength values can be found for longitudinal, transverse, and through-thickness directions [68].

The material behavior under compressive and under tensile uniaxial loading differs so significantly that a foam constitutive model intended for general application should take both hardening (densification) and fracture into account. First steps into this direction are documented by Schluppkotten [96], who extended the constitutive model proposed by Deshpande and Fleck [24] with an isotropic damage model, albeit with the intention of modeling polymeric foams.

4.2.4 Strain-Rate and Impact Velocity Effects

Since metallic foams are a candidate material for energy absorption related applications such as passenger or pedestrian protection [60] and protective packaging, it is indispensable to discuss their behavior under dynamic loading. According to Hall et al. [44] strain rates between 10^2 s^{-1} and 10^3 s^{-1} have to be expected in parts of automobiles' structures during impact events.

From a theoretical standpoint the following potential sources for strain-rate or impact velocity dependent mechanical effects can be identified:

- **Strain rate sensitivity of the cell-wall material:**

Dynamic compression tests by Dannemann and Lankford [16] show a noticeable influence of the strain rate on the flow stress of solid Al 6101 samples.

Deshpande and Fleck [23] demonstrated how the overall and the local strain rates are related by means of the idealized open-cell model of Gibson and Ashby [34]. They find that the strain rate in the outer fibers of the cell wall is approximately an order of magnitude lower than the macroscopic strain rate indicating that a potential strain-rate dependency of the cell wall material is attenuated by the foam micro-kinematics.

- **Micro-inertial effects:**

Micro-inertial forces effects contribute to an increased dynamic strength of cellular materials by resisting the buckling of the cell walls [23], causing a pronounced initial peak in the stress strain relationship. Deshpande and Fleck [23] do not note this initial peak in their experiments and conclude that micro-inertial effects do not have a strong impact on the deformation of metallic foams, since they deform primarily by cell wall bending (as opposed to buckling) due to numerous imperfections in the microstructure.

- **Shock wave propagation:**

Shock wave propagation effects were discussed in detail in Chapter 3. Their influence can be assessed by treating the metallic foam as a homogeneous material. For this reason, macroscopic modeling with continuum elements will capture shock wave phenomena without additional measures.

- **Viscous effects; entrapped gas flow:**

Deshpande and Fleck [23] consider the case of a gas, which is perfectly enclosed in the foam skeleton, as the upper bound for the contribution of the viscous strain rate effects due to gas flow and the inhibition thereof. They found the stress increase caused by the compression of an enclosed gas having an initial pressure, which is equal to the environmental pressure, to be only of a few percent of the static yield stress. It can, therefore, be safely assumed that for gas-filled foams gas flow effects do not add a pronounced strain rate dependence, especially in the initial response to dynamic loading.

While it is possible to predict the influence of the described dynamic effects within a certain margin of error, only experiments can give insight into their interaction in the real material. Most experiments fall in one of the two following categories:

1. Direct impact tests,
2. Split-Hopkinson Pressure Bar (SHPB) tests.

For a description of the two methods and a comparison of their relevance with regard to the testing of metallic foams see Deshpande and Fleck [23].

Yu et al. [119] performed high-strain rate testing including Split-Hopkinson Pressure Bar tests on Al6061 foam samples of a relative density of 10% to 30% produced by a powder-metallurgical route. Comparing the dynamic test results to quasistatic test results they claim that, although considerable data scatter exists, the initial peak stress of the samples is essentially independent of the strain rate.

Mukai et al. [73; 74] investigated the dynamic response of closed-cell aluminum foam (*ALPORAS*) and open-cell magnesium foam at dynamic strain rates over 10^3 s^{-1} . They found that the plateau stress of both foams exhibited a strong strain rate sensitivity leading to a two-fold increase of the plateau stress. For an *ALPORAS* foam of 10% relative density, testing of samples of $9 \times 9 \times 6 \text{ mm}^3$ dimension gave quasi-static collapse stresses between 1.5 and 2 MPa and dynamic collapse stresses between 2.5 and 3 MPa for an overall strain rate of $2.5 \times 10^3 \text{ s}^{-1}$, which corresponds to an initial impact velocity of 15 m/s.

Paul and Ramamurty [83] obtained strain rate sensitivities m for the exponential relationship $\sigma_t \propto (\dot{\epsilon}_t)^m$ between the true stress σ_t and the true strain rate $\dot{\epsilon}_t$ by switching nearly instantaneously between two (overall) strain rates during a compression test. The strain rate sensitivity m was shown to increase with the magnitude of the strain rate jump $\Delta\dot{\epsilon}_t$ and the true strain, at which the rate jump was prescribed. For their $25 \times 25 \times 50 \text{ mm}^3$ *ALPORAS* specimens they obtained m values between 0.005 and 0.015. For comparatively low strain rates of $1.6 \times 10^{-1} \text{ s}^{-1}$ they found an increase of the first peak stress by as much as 25% compared to a reference experiment performed at a strain rate of 10^{-3} s^{-1} . In this context they emphasize the difference between the overall (nominal) strain rate and the local strain rate in bands of localized deformation. Furthermore, an extrapolation of their results seems to be in good agreement with the results of Mukai et al. [74] for much higher strain rates.

Performing SHPB experiments on cylindrical aluminum foam specimens (height: 12 mm; diameter: 18 mm) produced by the Fraunhofer process, Hall et al. [44] found it impossible to distinguish any strain rate influence on the flow stress from the scatter inherent in the tested material, although they achieved strain rates as high as $2.0 \times 10^3 \text{ s}^{-1}$. They also imply that SHPB tests on foam material should be evaluated with great caution since foams violate some of the fundamental assumptions of the standard evaluation procedure.

Deshpande and Fleck [23] performed both SHPB and impact type experiments on *ALU-LIGHT* ($\rho_{F,\text{rel}} = 0.17$ to 0.4) and *DUOCEL* foams ($\rho_{F,\text{rel}} = 0.07$). They used cylindrical

specimens of 10 mm diameter and length. In the SHPB test they achieved strain rates up to $5.0 \times 10^3 \text{ s}^{-1}$ corresponding to a maximum impact velocity of 50 m/s. Employing a simple, one-dimensional shock model introduced by Reid and Peng [90] they stated that a noticeable (in terms of a 20% increase of the plateau stress) effect of shock propagation mechanisms has to be expected at impact velocities exceeding 50 m/s. Correspondingly, they did not expect any strain-rate effect to be discernible from strength scatter due to density inhomogeneities in their experiments, for which this scatter was also found to be of the order of 20%. It appears that the number of experiments reported in [23] was not large enough to show a consistent trend to higher dynamic plateau stresses for increasing strain rates. Deshpande and Fleck, therefore, excluded significant strain rate effects on the examined foam materials.

Dannemann and Lankford [16] investigated samples of closed-cell aluminum foam (*ALPORAS*; relative densities of 7.4% and 15%), open-cell aluminum foam (*DUOCEL*; relative density of 7%), and solid Al6061 samples with the SHPB method. The tests revealed negligible strain-rate dependence of the yield strength for the low density open-cell aluminum foam at $\dot{\epsilon} = 1.2 \times 10^3 \text{ s}^{-1}$ as well as for the solid 6101 aluminum material at $\dot{\epsilon} = 9.1 \times 10^2 \text{ s}^{-1}$. In contrast, a distinct strain rate dependence ($\dot{\epsilon} \leq 2.5 \times 10^3 \text{ s}^{-1}$) of the yield stress was demonstrated for the closed-cell *ALPORAS* foam samples (length: 25.4 mm; diameter: 23.6 mm) and attributed primarily to viscous effects like the flow of the entrapped gas through ruptured cell walls. Unfortunately, their diagrams are not very clear and show a large degree of scatter. The tendency, however, appears to be the same as in the investigation of *ALPORAS* foam by Mukai et al. [74]. The achieved strain rate corresponds to a comparably high impact velocity of 63.5 m/s.

Hanssen et al. [47] fired a projectile fitted with strain gauges against a stationary foam target (aluminum foam by Hydro Aluminium AS) reaching velocities of up to 15 m/s. They found the dynamic force peak to be as much as 50% higher than the quasi-static one. The relationship between the impact velocity and the increase of the peak force appears to be linear in the investigated ranges of velocities ($\leq 15 \text{ m/s}$) and strain ($\leq 30\%$).

This brief summary of recent experimental evidence pro and contra the existence of a distinct rate-dependence of the mechanical behavior of metallic foams may cause some confusion, since it proves that conflicting observations and opinions exist among researchers. It may well be that strain-rate effects exist, but are hidden by experimental scatter caused by small sample sizes and material inhomogeneities. In this case the calibration of the material data itself will be a more serious problem than capturing the strain-rate dependence.

4.3 Constitutive Modeling

4.3.1 Some Basic Conventions

The local stress state in a solid body can be described by a symmetric second-rank tensor $\boldsymbol{\sigma} = [\sigma_{ij}]$ called the stress tensor. Three scalar properties I_1 , I_2 , and I_3 , which are invariant with respect to a rotation of the reference frame, can be found for any stress tensor. These invariants are defined as:

$$I_1 = \sigma_{kk} \quad (4.1)$$

$$I_2 = \frac{1}{2} (\sigma_{ii} \sigma_{kk} - \sigma_{ij} \sigma_{ij}) \quad (4.2)$$

$$I_3 = \det \boldsymbol{\sigma} \quad (4.3)$$

It is possible to find a reference frame 1-2-3 for which all non-diagonal, that is, shear stress components σ_{ij} vanish identically. The remaining diagonal, that is, normal stress components $\sigma_1 = \sigma_{11}$, $\sigma_2 = \sigma_{22}$, and $\sigma_3 = \sigma_{33}$ are called the principal stresses. They can be found by solving the characteristic equation

$$\det(\boldsymbol{\sigma} - \sigma \mathbf{I}) = -\sigma^3 + I_1 \sigma^2 - I_2 \sigma + I_3 = 0, \quad (4.4)$$

Expressing the principal invariants in terms of the principal stresses gives:

$$I_1 = \sigma_1 + \sigma_2 + \sigma_3 \quad (4.5)$$

$$I_2 = \sigma_1 \sigma_2 + \sigma_2 \sigma_3 + \sigma_1 \sigma_3 \quad (4.6)$$

$$I_3 = \sigma_1 \sigma_2 \sigma_3 \quad (4.7)$$

It often proves advantageous to decompose the stress tensor $\boldsymbol{\sigma}$ into a hydrostatic part, which is described by the volumetric (spherical, hydrostatic) component

$$\sigma_m = \frac{1}{3} I_1, \quad (4.8)$$

the negative value ($-\sigma_m$) of which corresponds to the hydrostatic pressure p , and a deviatoric part \mathbf{s} , the components s_{ij} of which are defined as:

$$s_{ij} = \sigma_{ij} - \sigma_m \delta_{ij}, \quad (4.9)$$

where δ_{ij} is the Kronecker delta symbol, which takes the values $\delta_{ij} = 1$ for $i = j$, and $\delta_{ij} = 0$ for $i \neq j$. As for the full stress tensor $\boldsymbol{\sigma}$ three invariants J_1 , J_2 , and J_3 can be defined for the deviatoric stress tensor \mathbf{s} . The first invariant J_1 of the deviatoric stress tensor vanishes identically. The second invariant J_2 is given as $J_2 = \frac{1}{2} s_{ij} s_{ij}$ and plays an important role in metal plasticity, where the von Mises equivalent stress

$$\sigma_e = \sqrt{3 J_2} \quad (4.10)$$

is a scalar measure for the stress state regarding the tendency of a material to yield, provided that the material can be described by the theory of J_2 plasticity, as it is the case for most solid metals. In these cases, the von Mises stress can be compared to the uniaxial yield stress of the material to determine whether yielding of the material occurs under an applied general stress state (compare the discussion in Section 2.3.2).

4.3.2 Formal Introduction to Elasto-Plasticity

In this section a brief, formal introduction to the constitutive modeling of inelastic and, in particular, elasto-plastic material behavior [64] will be presented. The state of local deformation in the material is described by a strain tensor ϵ . Generalized constitutive laws commonly express the strain tensor ϵ in terms of the instantaneous stress tensor σ , the temperature T , and internal variables S_i :

$$\epsilon = f(\sigma, T, S_i) \quad (4.11)$$

The internal variables S_i describe the internal structure of the material during the deformation process. Examples for internal variables are accumulated plastic strains for rate independent plasticity and creep strains for time-dependent inelastic behavior. The constitutive description of the material requires evolution equations for the internal variables:

$$\frac{dS_i}{dt} = g_i(\sigma, T, S_i) \quad (4.12)$$

Equations (4.11) and (4.12) constitute a coupled system of equations that form the constitutive law. Time-integration can be performed to calculate the actual strain state $\epsilon(t)$.

A specialized case of these generalized constitutive equations is the theory of rate independent, incremental plasticity (“flow theory”). This theory has been applied successfully to predict the inelastic mechanical response of a wide range of materials including solid metals as well as metallic foams. The principal premise is that the strain tensor ϵ can be split into an elastic part ϵ_{el} and a plastic part ϵ_{pl} , where the former is the instantaneous elastic response depending only on the local stress state: $\epsilon_{el} = \epsilon_{el}(\sigma)$. The tensor of plastic strains ϵ_{pl} represents inelastic, time-independent strain components that cannot be recovered by elastic unloading.

Incremental plasticity theory assumes a purely elastic response for stress states σ , for which a material specific *yield function* $F(\sigma, S_i)$ returns values lower than zero. Plastic deformation implies fulfilling the *yield criterion* $F(\sigma, S_i) = 0$, which defines a surface in the (6-dimensional) stress space that is referred to as *yield surface*. As soon as the yield criterion $F(\sigma, S_i) = 0$ is fulfilled the material is accumulating plastic strains ϵ_{pl} at a rate, which is defined by the incremental plastic *flow rule*

$$d\epsilon_{pl} = d\epsilon_{pl}(\sigma, d\sigma, S_i). \quad (4.13)$$

Often, the flow rule is defined in terms of the gradient of a flow potential $G(\boldsymbol{\sigma})$:

$$d\boldsymbol{\epsilon}_{ij}^{\text{pl}} = d\lambda \frac{\partial G(\boldsymbol{\sigma})}{\partial \sigma_{ij}} \quad (4.14)$$

where $d\lambda$ is the nonnegative increment of the plastic flow multiplier λ , which can be determined using a *consistency condition* expressing the fact that in the case of plastic loading the stress state always remains on the yield surface [64]. Those special forms of Equation (4.14), for which the yield function $F(\boldsymbol{\sigma})$ assumes the role of the flow potential, that is, $G \equiv F$, are called *associated* flow rules.

For loading in the plastic range the stress state always remains on the yield surface, the size, the location and the shape of which can change according to the applied constitutive theory. This evolution of the yield surface is driven by the evolution of the internal variables S_i , which, in turn, is governed by *hardening laws* and temperature changes, compare Equation (4.12).

4.3.3 Constitutive Laws for Metallic Foams - Overview

The effective mechanical behavior of foam can be described by constitutive theories such as plasticity theory under the condition that the overall dimensions of the structures made of foam are at least one or two orders of magnitude larger than the typical size of single foam cells.

Linear Elastic Behavior

For small elastic deformations, the tensor of elastic strains $\boldsymbol{\epsilon}_{\text{el}}$ can be related to the stress tensor $\boldsymbol{\sigma}$ by a generalized form of Hooke's Law:

$$\boldsymbol{\sigma} = \mathbf{E} \boldsymbol{\epsilon}_{\text{el}}, \quad (4.15)$$

which constitutes a linear relationship involving the fourth-rank tensor of elasticity \mathbf{E} .

As long as only the linear elastic response of a structure is of interest, homogenized cellular metals are fairly easy to deal with. For the special case of an isotropic, linear elastic material, two material parameters λ and μ , which are known as the Lamé coefficients, are necessary for the calibration of the generalized Hooke's law $\sigma_{ij} = E_{ijkl} \varepsilon_{kl}$ and the formulation of the tensor of elasticity E_{ijkl} :

$$E_{ijkl} = \lambda \delta_{ij} \delta_{kl} + \mu (\delta_{ik} \delta_{jl} + \delta_{il} \delta_{jk}), \quad (4.16)$$

The Lamé coefficients λ and μ can be expressed in terms of the Young's modulus E and the Poisson's ratio ν as:

$$\lambda = \frac{E\nu}{(1+\nu)(1-2\nu)} \quad (4.17)$$

$$\mu = \frac{E}{2(1 + \nu)} \quad (4.18)$$

Here, the need for a definition of Young's modulus for cellular metals arises. Some experimental results indicate that typical metallic foams may not possess an elastic regime under compression, but rather begin to deform irreversibly at stresses which are low compared to their collapse or plateau stresses. Thus, it is not fully clear, to what extent cellular metals can be treated as linear elastic materials in structural analyses.

Elasto-Plastic Constitutive Laws

The most distinguishing feature of the macroscopic mechanical behavior of cellular materials is their ability to yield under states of pure hydrostatic pressure and to acquire volumetric plastic deformations when being loaded beyond this yield limit. This characteristic behavior is not supported by the classical J_2 plasticity theories for solid metals, which assume that the volume of a volume element remains constant during plastic deformation. Therefore, new constitutive laws had to be developed for cellular materials.

A comprehensive overview of material laws for the simulation of metallic foams was compiled by Hanssen et al. [46; 47]. They describe and compare constitutive formulations proposed by Schreyer et al. [98], Ehlers et al. [25; 26], Deshpande and Fleck [24], Miller [70], HKS [53] and then proceed to validate constitutive formulations implemented in the Finite Element code LS-DYNA [45]. In his thesis [96] on crash simulation involving polymeric foams Schluppkotten additionally surveyed material laws implemented in the Finite Element codes RADIOSS and PAMCrash. Chen and Lu [10] proposed a stress potential for metallic foams in connection with an associated flow rule and demonstrated excellent agreement with the multi-axial experimental results of Deshpande and Fleck [24].

The individual constitutive models differ in the mathematical formulation of the yield surface, the plastic flow rule and the history dependence of the hardening function. In the following, the Crushable Foam constitutive law(s) provided by the Finite Element code ABAQUS will be discussed in greater detail.

4.3.4 The ABAQUS Crushable Foam Models

Constitutive theories, or material laws, are typically implemented into displacement controlled Finite Element codes as algorithms, which, essentially, return the stress response of the material to an imposed strain increment. In the Finite Element code ABAQUS [53] the phenomenological Crushable Foam constitutive models can be considered for the macroscopic simulation of metallic foams. The original Crushable Foam model, which was characterized by volumetric hardening, was developed for PU foams, but an application and calibration of this model for metallic foams is possible. In [24] Deshpande and Fleck proposed an isotropic constitutive model for metallic foams, which was, subsequently, implemented as an ABAQUS user material subroutine by Chen [9] and is included as a standard

constitutive model with the explicit Finite Element code **ABAQUS/Explicit** from Revision 6.2 onwards.

Both models feature a yield surface which can be represented as an ellipse in the mean/effective¹ stress plane (see Figures 4.1 and 4.2). The yield surface of the Crushable Foam model with isotropic hardening, Figure 4.2, is symmetrical with respect to compressive and tensile stress states. Furthermore, it evolves by uniform scaling in all directions (isotropic hardening). An associated flow rule is used, and the plastic Poisson's ratio is generally not equal to zero. The Crushable Foam material, on the other hand, is characterized by a constant tensile hydrostatic yield stress, which causes the origin of the yield surface to move along the hydrostatic axis as the yield surface expands during hardening (Figure 4.1). The non-associated flow rule governing this constitutive model is defined such that plastic Poisson's effects are suppressed.

Crushable Foam Model with Volumetric Hardening

The yield surface of the **ABAQUS** Crushable Foam material law with volumetric hardening is defined in terms of the von Mises equivalent stress σ_e and the hydrostatic pressure p ($= -\sigma_m$):

$$F_{\text{vol}}(\sigma_e, p) = \sqrt{(\sigma_e)^2 + \alpha^2(p - p_0)^2} - B = 0 \quad (4.19)$$

As mentioned before, Equation (4.19) defines an ellipse in the effective stress versus pressure plane, as shown in Figure 4.1. Along the hydrostatic axis the ellipse is bounded by the tensile hydrostatic yield pressure $p_t^{(0)}$ in the tensile regime and the instantaneous compressive hydrostatic flow pressure p_c , which is initially equal to the compressive yield pressure $p_c^{(0)}$ for the initial yield surface. In the Crushable Foam law with volumetric hardening, the tensile hydrostatic yield pressure $p_t^{(0)}$ is assumed to remain constant throughout the evolution of the yield surface and, therefore, during any plastic deformation process. Furthermore, the shape of the yield surface, expressed by the shape parameter α in (4.19) is assumed to be a constant. Other important points on the circumference of the elliptical projection of the yield surface are the point corresponding to the initial shear yield stress $(0, \tau_y^{(0)}\sqrt{3})$ and the point $(\sigma_{yc}^{(0)}/3, \sigma_{yc}^{(0)})$ marking the onset of yielding under uniaxial compressive loading.

For the description of individual foam materials two specific input parameters, k and k_t , have to be known:

$$k = \frac{\sigma_{yc}^{(0)}}{p_c^{(0)}} \quad \text{and} \quad k_t = \frac{p_t^{(0)}}{p_c^{(0)}}. \quad (4.20)$$

¹In this notation, which is widely used in the literature, both the “mean” and the “effective” stresses, σ_m and σ_e , denote stresses on the macroscopic level, and “effective stress” denotes the effective (in the sense of macroscopic) von Mises equivalent stress.

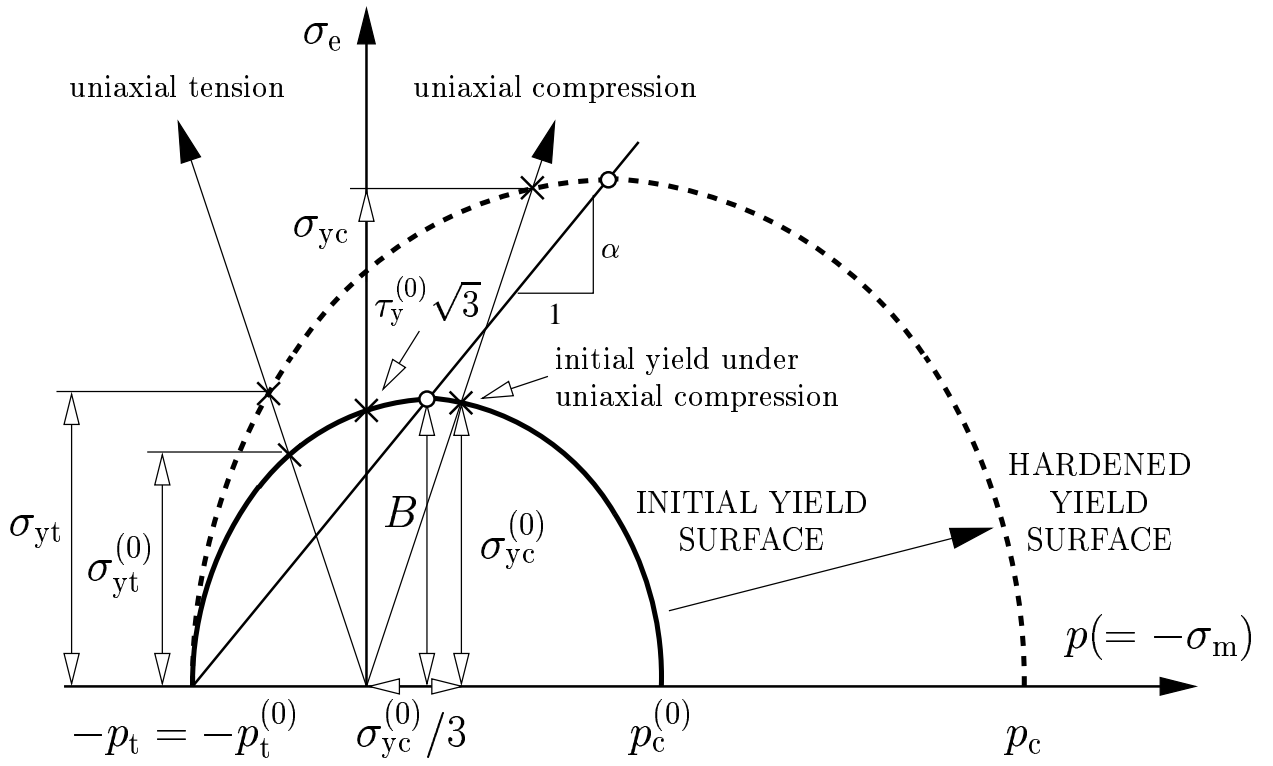


Figure 4.1: Crushable Foam model with volumetric hardening [53]; yield surface in the $\sigma_m - \sigma_e$ plane.

The shape parameter (aspect ratio) α then follows as:

$$\alpha = \frac{3k}{\sqrt{(3k_t + k)(3 - k)}} \quad (4.21)$$

The parameter B in Equation (4.19) represents the length of the (vertical) σ_e axis of the yield ellipse. It is related to the length of the hydrostatic axis ($p_c + p_t^{(0)}$) via the shape parameter α , which is the aspect ratio of the ellipse:

$$B = \alpha \frac{p_c + p_t^{(0)}}{2} \quad (4.22)$$

The center of the yield ellipse, which moves along the hydrostatic axis during volumetric hardening, is situated at the mid-point of the fixed tensile yield pressure and the variable compressive flow pressure:

$$p_0 = \frac{p_c - p_t^{(0)}}{2} \quad (4.23)$$

In addition to the uniaxial compressive yield stress $\sigma_{yc}^{(0)}$, two additional data items from the following list have to be known (or appropriate assumptions have to be made) to allow the calibration of the input parameters:

- Initial tensile yield stress in uniaxial tension $\sigma_{yt}^{(0)}$
- Initial yield stress in simple shear $\tau_y^{(0)}$
- Initial yield stress under hydrostatic pressure $p_c^{(0)}$
- Initial yield stress under hydrostatic tension $p_t^{(0)}$

Since tension tests on metallic foams are becoming a standard procedure (see Section 4.2.3) and some data exists on the hydrostatic yielding of metallic foams (see Section 4.2.2) it is appropriate to utilize the respective material parameters to determine the hydrostatic yield strength $p_t^{(0)}$ required for the calculation of the **ABAQUS** input parameter k_t :

$$p_t^{(0)} = \frac{p_c^{(0)} \sigma_{yc}^{(0)} \sigma_{yt}^{(0)}}{3 p_c^{(0)} (\sigma_{yc}^{(0)} - \sigma_{yt}^{(0)}) + \sigma_{yc}^{(0)} \sigma_{yt}^{(0)}} \quad (4.24)$$

The evolution of the yield surface is controlled by a plastic strain measure ε_{eqv}^{pl} , which is equal to the compressive volumetric part $-\varepsilon_{vol}^{pl}$ of the tensor of the plastic strains ϵ_{pl} for the volumetric hardening model. While the hydrostatic tensile strength $p_t^{(0)}$ remains constant throughout any plastic deformation process, the hydrostatic compressive strength p_c evolves as a function of the equivalent plastic strain $p_c = p_c(\varepsilon_{eqv}^{pl})$. This hardening function is material dependent and can be obtained from a uniaxial compressive test under

the assumption of zero plastic Poisson's ratio, that is, the uniaxial plastic strain being equal to the volumetric plastic strain.

The flow rule is a non-associated flow rule defined in terms of the total derivative of a flow potential function G_{vol} :

$$d\epsilon^{\text{pl}} = d\epsilon_{\text{eqv}}^{\text{pl}} \frac{\partial G}{\partial \sigma} \quad (4.25)$$

For the Crushable Foam model with volumetric hardening, the flow potential function $G_{\text{vol}}(\sigma_e, p)$ is given as:

$$G_{\text{vol}} = \sqrt{(\sigma_e)^2 + \frac{9}{2} p^2} \quad (4.26)$$

and the increment of the equivalent plastic strain $d\epsilon_{\text{eqv}}^{\text{pl}}$ is defined as:

$$d\epsilon_{\text{eqv}}^{\text{pl}} = \frac{\sigma : d\epsilon^{\text{pl}}}{G} \quad (4.27)$$

with the operator $(:)$ representing the scalar product of two tensors, that is, the sum of the products of corresponding elements. The flow rule (4.25) in connection with the particular form (4.26) of the flow potential gives a direction of plastic flow that is identical to the stress direction for radial loading paths in the stress space. This implies that loading in any principal direction does not cause plastic strains in directions perpendicular to the loading direction. Hence, the plastic Poisson's ratio ν_{pl} is assumed to vanish. There is experimental evidence showing that this is a reasonable assumption at least for finite, compressive deformation, see Section 4.2.

4.3.5 Crushable Foam Model with Isotropic Hardening

The Crushable Foam model with isotropic hardening was originally proposed by Deshpande and Fleck [24], who performed compression tests on aluminum foam prescribing multiaxial (axisymmetric) stress states. By successive loading and unloading on different loading paths they located points on the yield surface. By repetition of this procedure for several stages of pre-deformation they obtained information about the evolution of the yield surface for increasing plastic strains. Note that this experimental procedure was very similar to the numerical method proposed in Section 2.3.2. The experimentally determined points on the yield surface could be approximated very well by an ellipse in the origin of the effective stress/hydrostatic pressure plane. Accordingly, their mathematical definition of the yield surface $F_{\text{iso}}(\sigma_e, p) = 0$ took the form of an ellipse:

$$F_{\text{iso}}(\sigma_e, p) = \sqrt{(\sigma_e)^2 + \alpha^2 p^2} - B = 0 \quad (4.28)$$

where α determines the shape (aspect ratio) and B determines the size of the yield surface. The shape factor α can be found by inserting the quotient $k = \sigma_{\text{yc}}^{(0)} / p_c^{(0)}$ of the absolute

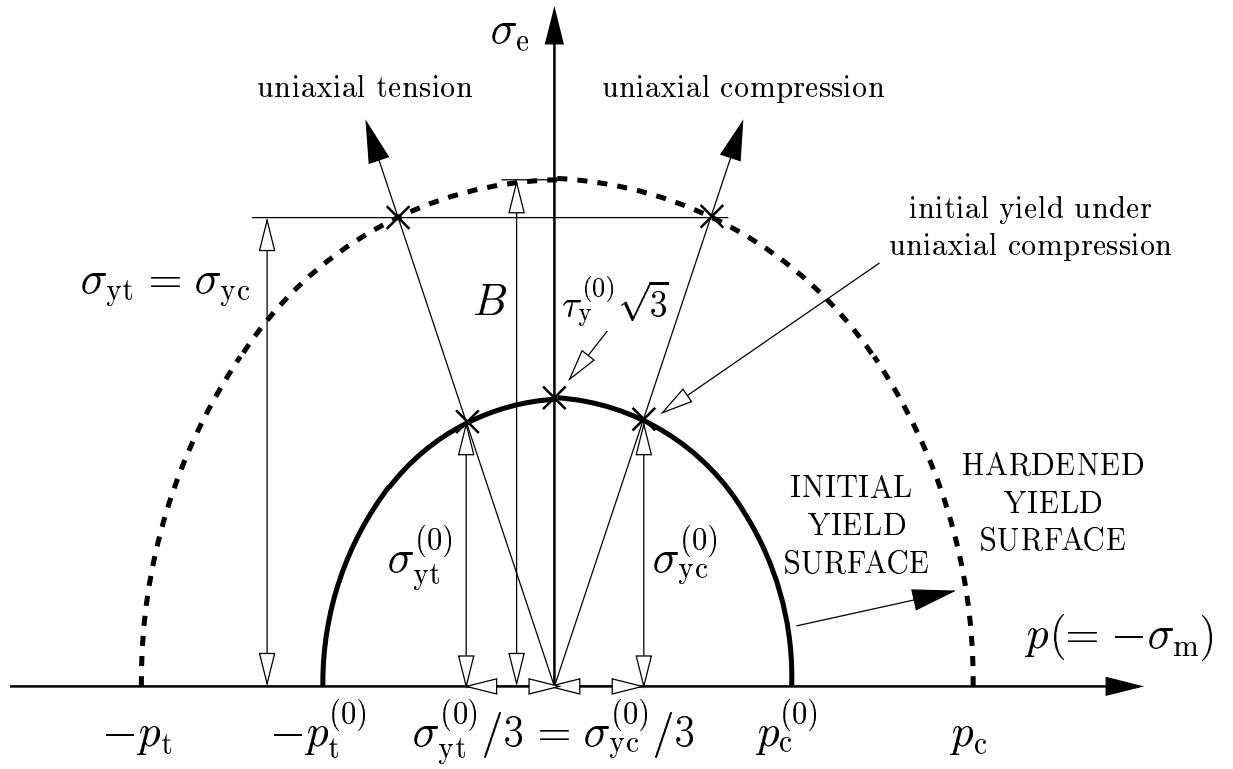


Figure 4.2: Crushable Foam model with isotropic hardening [53]; yield surface in the $\sigma_m - \sigma_e$ plane.

value of the initial yield stress in uniaxial compression $\sigma_{yc}^{(0)}$ and the initial yield strength in hydrostatic compression $p_c^{(0)}$ into the expression

$$\alpha = \frac{3k}{\sqrt{9 - k^2}} \quad (4.29)$$

The yield surface size parameter B , defined as the length of the deviatoric half axis of the initial yield surface, can then be calculated as a function of either $p_c^{(0)}$ or $\sigma_{yc}^{(0)}$:

$$B = \alpha p_c^{(0)} = \sigma_{yc}^{(0)} \sqrt{1 + \left(\frac{\alpha}{3}\right)^2} \quad (4.30)$$

A factor $k = 0$ results in $\alpha = 0$ and recovers the von Mises yield surface. Deshpande and Fleck [24] found that for uniaxial loading paths the yield surfaces changed primarily in size while maintaining essentially the same elliptic shape. They dubbed their material law “Self-Similar” constitutive model as a consequence, thereby indicating isotropic hardening.

The flow potential G_{iso} used in the Crushable Foam material law with isotropic hardening is defined by:

$$G_{iso} = \sqrt{(\sigma_e)^2 + \beta^2 p^2}, \quad (4.31)$$

where

$$\beta = \frac{3}{\sqrt{2}} \sqrt{\frac{1 - 2\nu_{pl}}{1 + \nu_{pl}}}. \quad (4.32)$$

Note, that for $\beta = \alpha$ the condition $G_{iso} = F_{iso}$ for *associated* plastic flow is fulfilled. For vanishing plastic Poisson’s ratio $\nu_{pl} = 0$, the parameter β assumes a value of $\sqrt{9/2} \approx 2.12$. With the two parameters α and β it is possible to independently adjust the size of the yield surface and the plastic Poisson’s ratio.

The incremental flow rule is given by:

$$d\epsilon_{pl} = d\lambda \frac{\partial G_{iso}}{\partial \sigma}. \quad (4.33)$$

in accordance with Equation (4.14).

The hardening of the foam is described by the relationship $\sigma_{yc} = \sigma_{yc}(\epsilon_{eqv}^{pl})$, where ϵ_{eqv}^{pl} is the equivalent plastic strain. The evolution of the equivalent plastic strain ϵ_{eqv}^{pl} is defined through

$$d\epsilon_{eqv}^{pl} = \frac{\sigma : d\epsilon^{pl}}{\sigma_{yc}(\epsilon_{eqv}^{pl})} \quad (4.34)$$

which means that the work performed by the increment of the equivalent plastic strain and the instantaneous uniaxial yield stress is the same as the work performed by the increment of the full plastic strain tensor and the full stress tensor. For uniaxial tension or compression, transverse expansion does not contribute to the plastic work. In this

case, Equation (4.34) simplifies to $d\varepsilon_{\text{eqv}}^{\text{pl}} = \sigma_{\text{yc}} d\varepsilon^{\text{pl}}/\sigma_{\text{yc}}$, and the equivalent plastic strain is equal to the absolute value of the uniaxial plastic strain. Therefore, the relationship $\sigma_{\text{yc}} = \sigma_{\text{yc}}(\varepsilon_{\text{eqv}}^{\text{pl}})$ can be found directly from the stress–strain diagram of a uniaxial compression test. In contrast to the Crushable Foam model with volumetric hardening the isotropic hardening model experiences hardening during pure shear deformation.

4.3.6 Discussion

Existing material laws for metallic foams are adequate for modeling simple deformation histories and predominantly radial stress paths. More complex mechanical processes such as successive perpendicular loading will require more sophisticated modeling techniques to account for the anisotropy caused by changing loading or deformation directions, see Deshpande and Fleck [24] and Hanssen [47].

Perhaps the most restricting feature about the available foam models is the absence of appropriate fracture models. Metallic foams are very prone to softening and premature failure when experiencing tensile stress states, the overall behavior being governed by progressive failure of the cell walls in this regime. Progressive fracture of cell walls governs the behavior of metallic foams in this situation. Since fracture is often observed in real-world applications of metallic foams, the introduction of corresponding simulation methods will be a major advance.

A correct calibration of the material parameters based on experimental data is indispensable for the success of any Finite Element simulation. In most cases, a uniaxial compressive test is the minimum requirement for this calibration. For more sophisticated constitutive models additional data on the yield surface shape and the hardening behavior has to be provided by the user. This requires information about the mechanical behavior of the material under multi-axial loading conditions. Since multi-axial experimental data is scarce the user must rely on appropriate assumptions, which can be derived either from micromechanical FE simulations or via parameter identification techniques (that is, by minimizing the discrepancy between simulations and experimental results).

Fortunately, applications, in which hydrostatic loading conditions prevail, are rare. To illustrate this, an application will be presented in the following, for which the uniaxial compressive stress–strain relationship is the most influential material property: the impact of a large object onto a relatively thin foam layer (padding).

4.4 Low Energy Impact on Metallic Foam Paddings

4.4.1 Introduction

Safety requirements in vehicle engineering have been raising interest in materials which are suitable for minimizing the contact forces between two colliding bodies while maximizing the amount of kinetic energy that is converted to irrecoverable energy. The latter process is generally referred to as energy absorption. The material of choice should be able to undergo large compressive deformations at a more or less constant stress level. In addition it should be of light weight.

At present paddings made of organic foams, which exhibit relatively low strength, are widely used for impact protection. Due to their low plateau stress levels, these foams have to undergo comparatively large deformations to absorb the kinetic energy of impacting body parts. In some situations, however, the available design space is too small to allow for the provision of an organic foam layer of sufficient depth. Metallic foams are candidate materials for use in such cases because they exhibit a higher collapse strength while preserving the deformation characteristics of a cellular material, in particular a long plateau of nearly constant stress in the stress–strain diagram (see Figure 3.2).

Typically, the impact events under consideration will include an impacting object of roughly cylindrical (for example knee) or spherical shape (for example head) and a comparably thin foam padding. Safety regulations like the *Federal Motor Vehicle Safety Standards*, see, for instance, [76], provide standardized test set-ups for the assessment of the crashworthiness of vehicle interiors. Body parts are abstracted by simple geometrical shapes of standardized dimension and mass to make safety tests and the associated results comparable to the prescribed safety requirements.

For complementing the testing of real structures and for supporting the design of new energy absorption structures as well as the development of new materials, numerical simulations are performed, see, for instance, Kretz and Götzinger [60], or Schluppkotten et al. [97]. In this section, the performance of aluminum foam as a protective material is assessed by simulating a head impact event as described by FMVSS 201 [76]. At the same time, the performance of the ABAQUS constitutive models for crushable foams and their parameter sensitivity are investigated in this potential field of application for metallic foams.

4.4.2 Method

The following crush and crash simulations are related to a potential real-world application of metallic foams by the specification of the standardized head impact test set-up described in the *Federal Motor Vehicle Safety Standard* FMVSS 201 [76]. In this international occupant safety standard, the injury potential of head impacts on interior surfaces of automobiles is assessed.

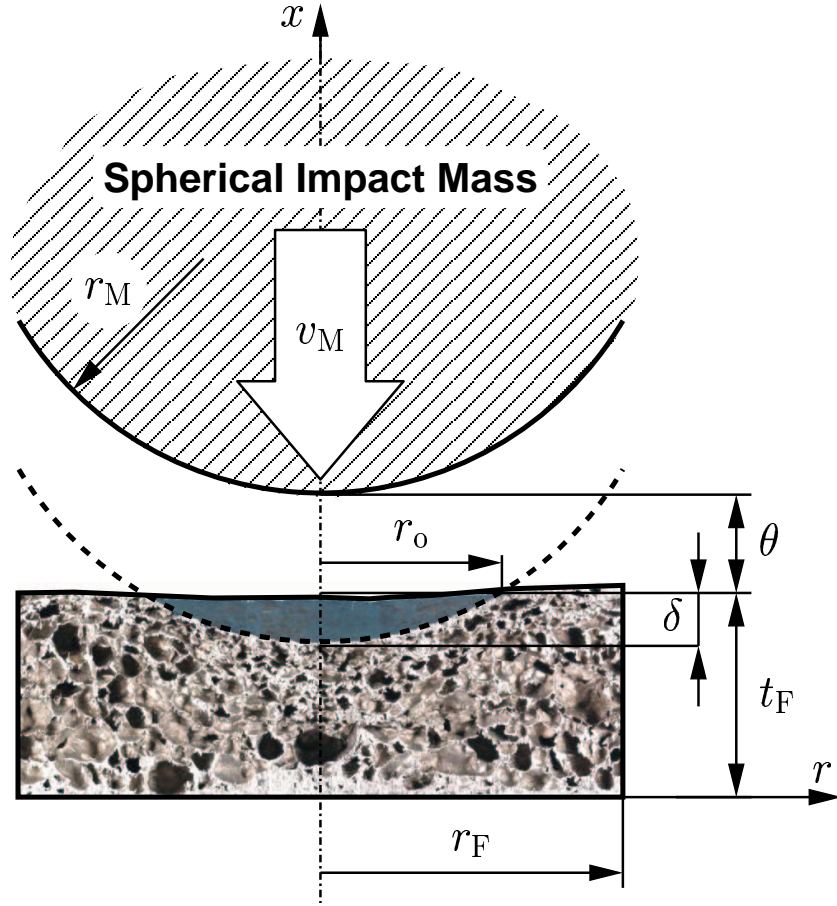


Figure 4.3: Schematic diagram showing the impact simulation setup.

The test can be described as the collision between a freely moving, rigid sphere representing the head of an adult and structures enclosing the passenger compartment of the automobile. The spherical impactor is characterized by the following parameters (compare Figure 4.3):

- Impactor diameter $r_M = 82.5$ mm (165 mm diameter),
- Impactor mass $m_M = 6.8$ kg,
- Impact velocity $v_M = 6.7$ m/s (≈ 24 km/h).

The initial kinetic energy K of the impact sphere amounts to $K = m_M v_M^2 / 2 = 152.6$ J.

A sketch of the impact situation is provided in Figure 4.3. Here, the foam pad thickness t_F and the foam pad radius r_F are identified. The maximum indentation depth is denoted as δ . The radius r_o of the impact area can be expressed as a function of the radius of the

impact sphere r_M and of the impact depth δ :

$$r_o = \sqrt{r_M^2 - (r_M - \delta)^2} \quad (4.35)$$

The initial offset θ between sphere and foam surface completes the set of geometrical parameters. For the Finite Element simulations axisymmetric models were created. The impact sphere was modeled by means of a rigid, analytical surface. The foam pad was represented by a mesh of axisymmetric 4-node continuum elements with bilinear interpolation functions. Frictionless contact between the analytically described sphere and the top surface of the uppermost element layer was prescribed.

Both quasi-static and dynamic simulations were performed. Wherever possible, the implicit Finite Element code **ABAQUS/Standard 6.2** was used. For certain ranges of input parameters all attempts to achieve a convergent solution with **ABAQUS/Standard 6.2** failed. For these cases, the simulations were performed with the more robust forward integration method of **ABAQUS/Explicit 6.2**. For the quasistatic analyses, the simulation time interval was set to 0.1 seconds. Comparison with longer simulation intervals did not reveal any significant strain rate effect, and the simulations could, therefore, be considered quasistatic.

To model the constitutive behavior of the foam material, the **ABAQUS** Crushable Foam material was used with both the volumetric and the isotropic hardening options. The hardening behavior was described by the analytical stress–strain relationship (3.1) in combination with density dependent function parameters (3.2) as defined by Gradingier for the uniaxial compression of a typical aluminum foam [37], see Section 3.2. The necessary conversion of the nominal compressive strain ε_c to the true compressive plastic strain ε_{pl} was performed by the equation

$$\varepsilon_{pl} = -\ln(1 - \varepsilon_c) - \sigma_{yc}/E \quad (4.36)$$

Here, σ_{yc} denotes the *true* instantaneous compressive yield stress ($\sigma_{yc} > 0$). Care for the proper conversion of experimentally determined *nominal* stresses to true stresses has to be taken for non-zero plastic Poisson’s ratios ν_{pl} . The Young’s modulus E was chosen equal to the unloading modulus defined in Equation (3.3). The nominal stress–strain curves were truncated where the tangent modulus became equal to the elastic modulus. The rest of the stress–strain regime was described by linear extrapolation to 99% nominal strain with the tangent modulus being equal to the elastic modulus. The elastic Poisson’s ratio ν was set to zero.

For the various simulations described below, the following reference parameters apply if not otherwise noted:

- reference initial uniaxial compressive yield stress of $\sigma_{yc}^{(0)} = 1$ MPa;
- reference initial hydrostatic yield stresses $p_c^{(0)} = p_t^{(0)} = 1$ MPa.
- reference thickness of the foam pad $t_F = 25$ mm;

- reference indentation δ in quasistatic simulations: 20 mm, or 80% of the reference thickness;
- radius of the foam pad r_F equal to radius of the sphere: $r_M = r_F$;
- vertical displacement constraints at the bottom of the foam plate;
- radial displacement constraints at the bottom and the outside of the plate.

Complementing the Finite Element simulations a simple analytical model is proposed assuming that the reaction force $F(\delta)$ can be approximated by integrating the local, axial stress σ_{xx} over the impact area:

$$F = \int_0^{r_o} 2\pi r \sigma_{xx}(r) dr \quad (4.37)$$

Assuming that the axial strain $\varepsilon_{xx}(r)$ at a given distance r from the axis of rotation is uniform over the thickness of the pad, the local stress becomes a function of r only. Kinematic considerations provide the magnitude of the local compressive axial strain $\varepsilon_{xx}^{(c)}$ as a function of r , the radius of the sphere r_M , and the indentation depth δ :

$$\varepsilon_{xx}^{(c)}(r) = \frac{\delta - r_M + \sqrt{r_M^2 - r^2}}{t_F} \quad (4.38)$$

In the following sections the influence of several material and geometrical parameters on the overall force-indentation behavior of the described impact configuration will be examined in quasistatic and dynamic simulations.

4.4.3 Results

Examination of the Reference Configuration

The first simulations, based on the reference configuration as outlined in the previous section, are intended to demonstrate the influence of the choice of the kinematic boundary conditions on the overall force-indentation behavior and the importance of material models suitable to simulate pressure sensitive materials.

Two different kinematic boundary conditions were considered: (a) a model without any radial constraints as a model for a plate of finite radius r_F and frictionless contact with the rigid foundation (vertical displacement constraints at the bottom of the foam part), and (b) a model with radial displacement constraints representing an integrated plate tied to the foundation by adhesive or metallic bonding.

For the Crushable Foam material with volumetric hardening, the force-indentation diagrams in Figure 4.4 show little difference between the two boundary configurations for

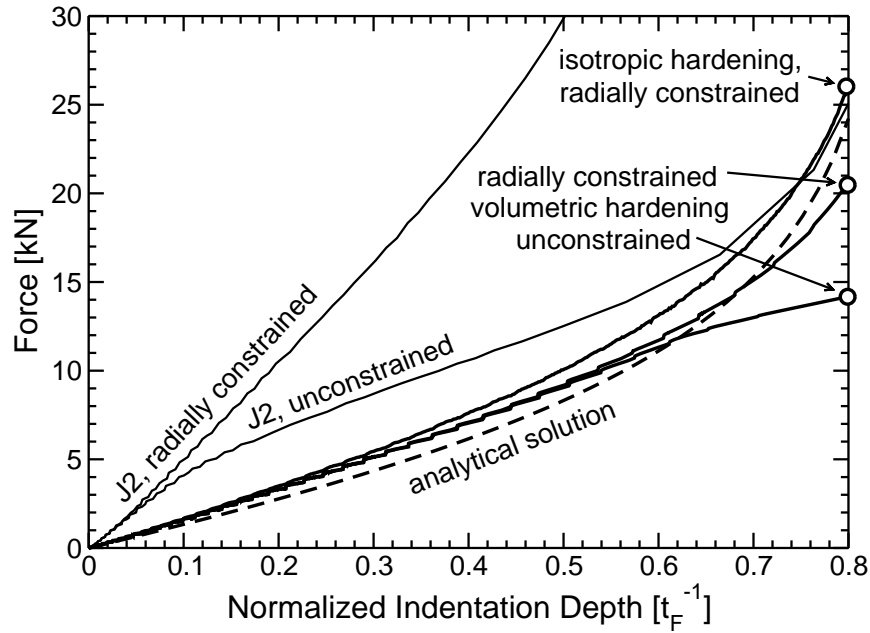


Figure 4.4: Predicted force-indentation relationships for different constraint conditions and constitutive models.

normalized indentation depths of up to 60%. Beyond this indentation depth the predicted reaction forces begin to diverge with the constrained model showing an exponential increase of the indentation force while the unconstrained model shows a slight drop in the tangential stiffness.

The difference is even more marked, if, for the sake of completeness, the Crushable Foam material law (with volumetric hardening) is replaced with classical, plastically incompressible J_2 plasticity. Here, the initial response is distinctly stiffer than for the Crushable Foam model. In the unconstrained model, the tangential stiffness drops at about 10% normalized indentation and remains roughly equal to the corresponding tangent stiffness predicted by the simulations with the Crushable Foam material. In the physically more reasonable constrained configuration, however, the force-indentation response remains essentially linear and, thus, unnaturally stiff.

The difference between the two simulations using the Crushable Foam model with volumetric hardening has to be sought in the respective accumulation of volumetric plastic strains and the associated degree of hardening for different boundary conditions. The deformed Finite Element meshes and the contour plots of the plastic volumetric strain fields for both configurations (Figure 4.5) show that the unconstrained mesh is able to escape volumetric plastic compression by radial expansion. The constrained model lacks this degree of freedom along parts of its boundary and, therefore, is forced to undergo volumetric plastic

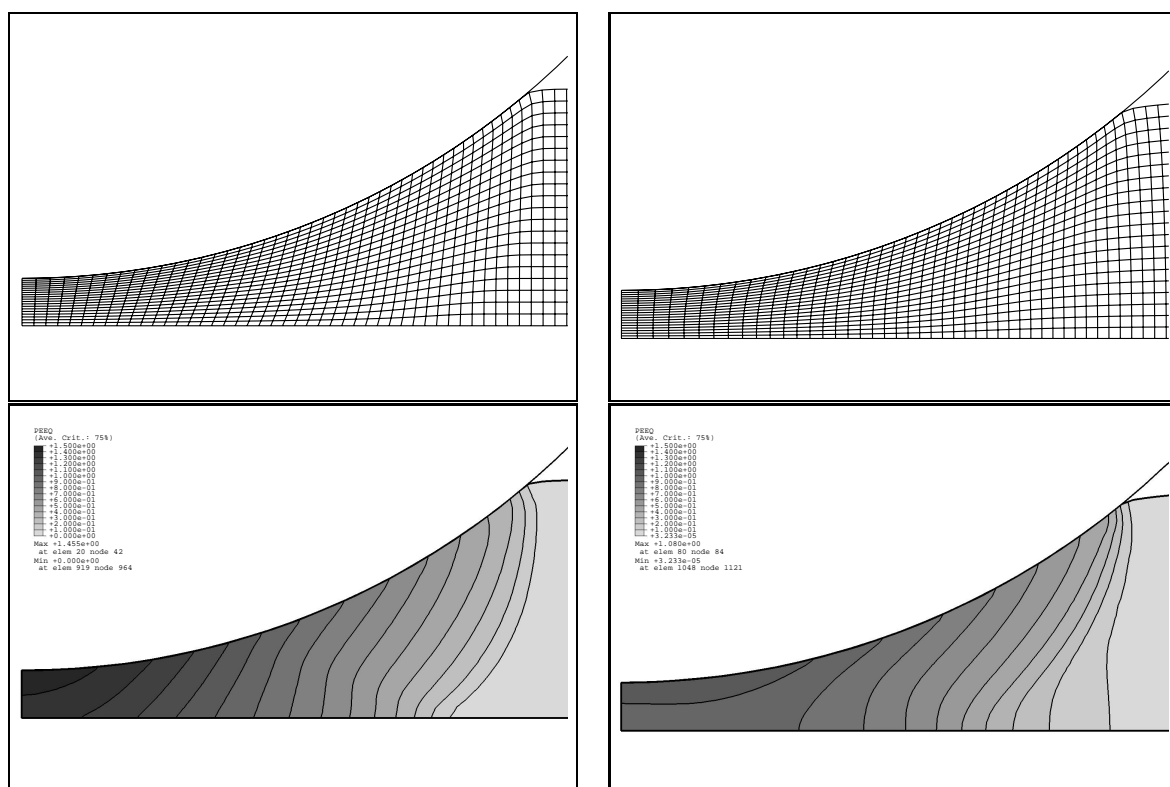


Figure 4.5: Deformed meshes and predicted volumetric plastic strain for a radially constrained model (left) and a model without radial deformation constraints (right).

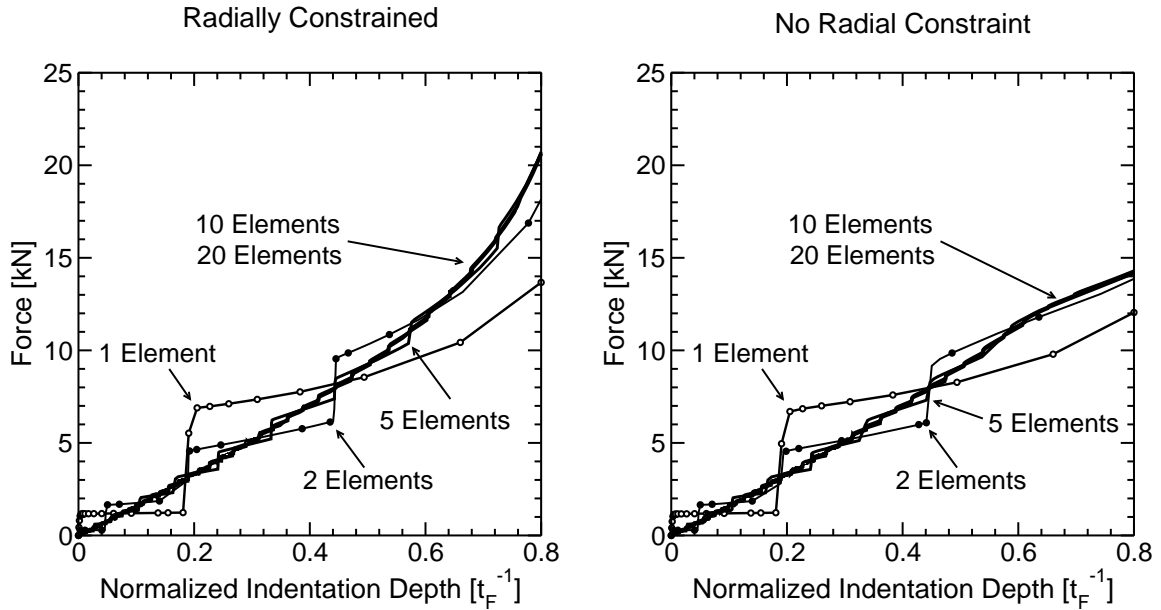


Figure 4.6: Predicted force-indentation relationships for different constraint conditions and different degrees of mesh refinement, expressed by the number of elements over the foam pad thickness.

straining corresponding to uniaxial compression with vanishing plastic Poisson's ratio.

This may be the reason why the analytical model (represented by the dashed line in Figure 4.4) as introduced in Section 4.4.2 predicts a force-indentation response that is very similar to the constrained Finite Element model, notwithstanding a slight underestimation of the actual reaction force at high indentations. Figure 4.4 also contains a force-indentation diagram obtained using the Crushable Foam model with isotropic hardening and radial displacement constraints. Starting off at the same initial stiffness as the foam law with volumetric hardening, the isotropic hardening model predicts higher indentation forces for increasing strains. A closer look at Equation (4.34), which drives the evolution of the equivalent plastic strain in the case of isotropic hardening, reveals, that hardening can be caused by shear deformation in this model, giving rise to a higher degree of hardening than is observable in a model with hardening being driven exclusively by the evolution of the volumetric plastic strain.

Influence of Mesh Refinement

An investigation of the influence of the mesh refinement on the qualitative character of the force-indentation diagrams is suitable for explaining the phenomenon of stair-like force jumps in the indentation responses, as they can be observed in some publications [60]. In

contrast to force jumps owing to the wave propagation and reflection phenomena outlined in Chapter 3, steps in the quasistatic force-indentation curves can be attributed to the finite discretization of the contact surface in radial direction.

Figure 4.6 illustrates the beneficial influence of an increasing mesh refinement on the smoothness of the force-indentation diagram of the radially constrained (left) and the unconstrained reference model (right). The number of elements in the thickness direction of the foam pad distinguishes the individual curves. Since equilateral 4-node elements were used, a high mesh refinement in thickness direction implies a high mesh refinement in radial direction, which is advantageous for resolving the extension of the contact area sufficiently fine for obtaining a smooth force diagram. Increasing the mesh refinement from 10 to 20 elements did not result in any visible improvement; 10 elements in plate thickness were, consequently, chosen as the reference mesh refinement.

As was outlined previously, it is not easy to determine experimentally the material parameters associated with the behavior of cellular materials under hydrostatic loads. The following sections are devoted to the quantification of the sensitivity of crush simulations with spherical indenters to variations of the hydrostatic compressive and/or tensile yield stress, $p_c^{(0)}$ and $p_t^{(0)}$, respectively, and the plastic Poisson's ratio ν_{pl} in the case of isotropic hardening.

Sensitivity to Variations of the Hydrostatic Compressive Yield Stress

The first parameter subjected to a systematic variation is the initial hydrostatic compressive yield pressure $p_c^{(0)}$. The theoretical limit for $p_c^{(0)}$ is one third of the uniaxial compressive yield strength $\sigma_{yc}^{(0)}$. Figure 4.7 shows predicted force-indentation diagrams for values of the compressive yield pressure ranging from 0.40 to 100 MPa. The uniaxial compressive and tensile hydrostatic yield stresses were kept constant at 1 MPa.

For $p_c^{(0)}$ values below the uniaxial compressive yield stress the *implicit* solution method failed to converge. An explicit simulation produced results in this range, but for $p_c^{(0)}$ values very close to the theoretical limit the explicit simulation produced very ragged reaction force-indentation curves, and the deformed mesh showed hourglassing effects. These results were omitted from Figure 4.7.

With regard to the set of reference parameters $\sigma_{yc}^{(0)} = p_c^{(0)} = p_t^{(0)} = 1$ MPa, an increase of the initial hydrostatic compressive yield strength resulted in a slight decrease of the overall reaction force (-3.4% for $p_c^{(0)} = 100$ MPa). There was no relevant additional decrease for $p_c^{(0)}$ values beyond 5 MPa. Decreasing $p_c^{(0)}$ leads to increased force levels. At $p_c^{(0)} = 0.4$ MPa the reaction force was 21% higher than the reference force.

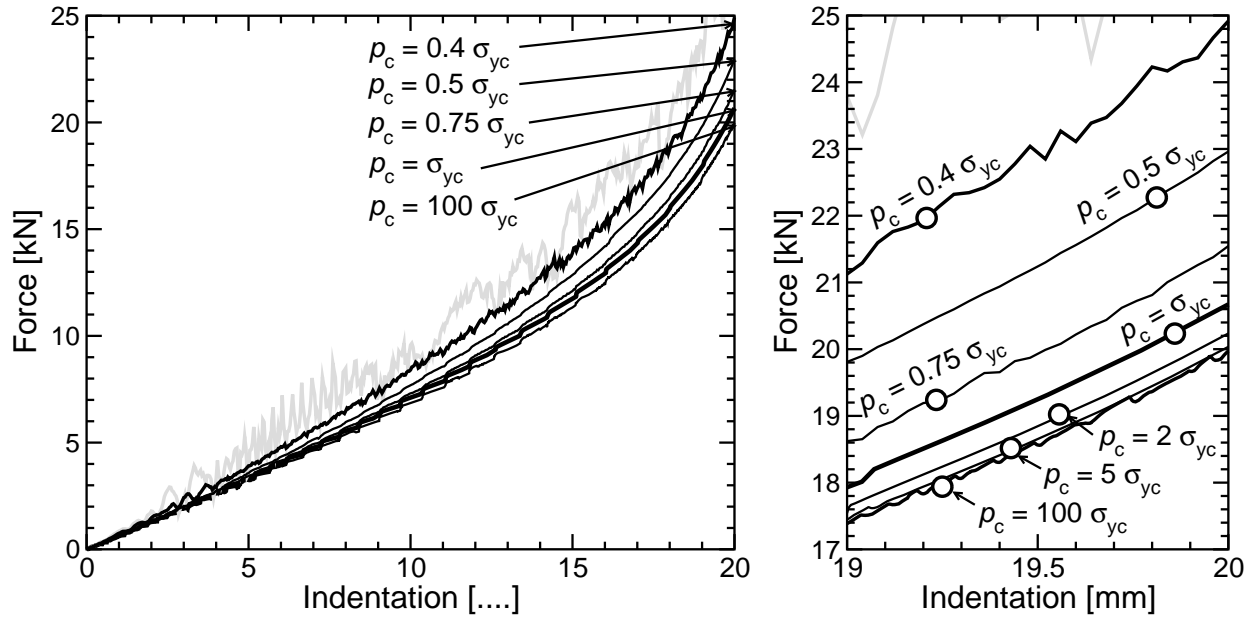


Figure 4.7: Predicted force-indentation relationships for different values of the initial hydrostatic compressive yield pressure $p_c^{(0)}$.

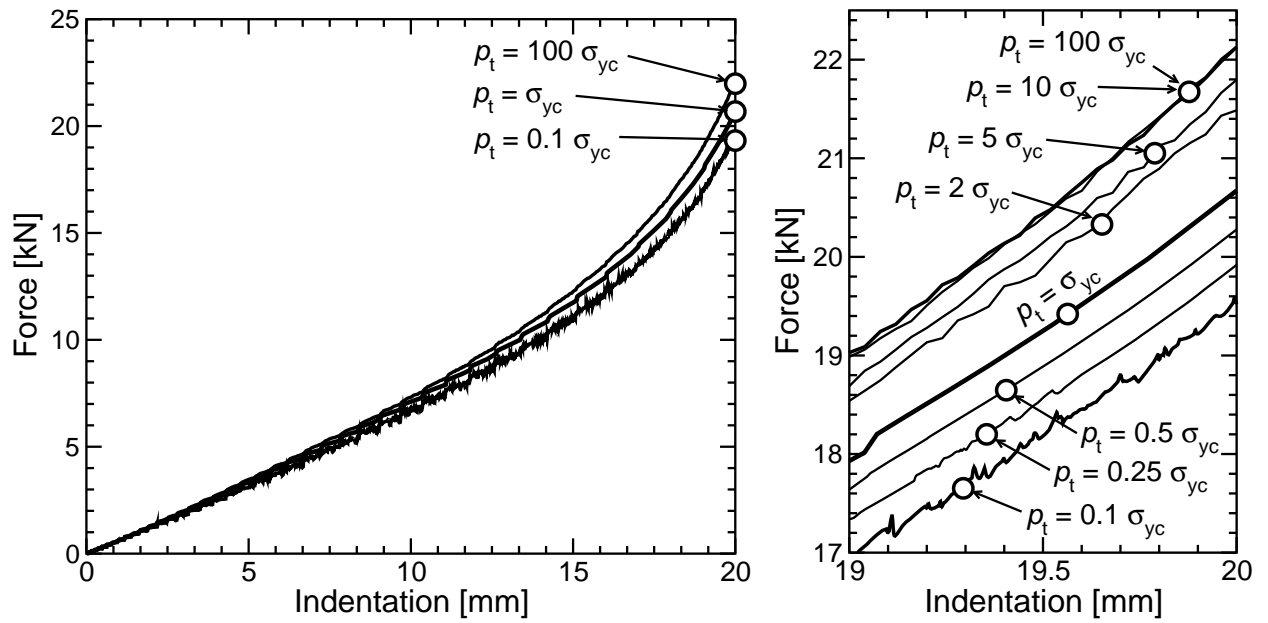


Figure 4.8: Predicted force-indentation relationships for different values of the initial hydrostatic tensile yield pressure $p_t^{(0)}$.

Sensitivity to Variations of the Hydrostatic Tensile Yield Stress

The volumetric hardening option of the ABAQUS Crushable Foam material law allows for different tensile and compressive initial hydrostatic yield stresses. Figure 4.8 shows predicted force-indentation diagrams for tensile hydrostatic yield stresses between 0.1 and 100 MPa at constant uniaxial compressive and compressive hydrostatic yield stresses of 1 MPa, respectively.

For $p_t^{(0)}$ values of 5, 10, and 100 MPa convergence could not be obtained with the standard implicit integration scheme of ABAQUS/Standard. Again, the explicit integration scheme of ABAQUS/Explicit proved to be more robust and provided results up to the desired indentation depth.

Compared to the result for the reference parameter set $\sigma_{yc}^{(0)} = p_c^{(0)} = p_t^{(0)} = 1$ MPa, a reduction of the initial hydrostatic tensile yield strength caused a slight decrease of the overall reaction force (-5% for $p_c^{(0)} = 0.1$ MPa). Increasing $p_c^{(0)}$ leads to increased force levels. At $p_c^{(0)} = 100$ MPa the reaction force was 7% higher than the reference force.

Simultaneous Variation of the Hydrostatic Tensile and Compressive Yield Stress

Besides a separate variation of the constant tensile hydrostatic yield stress $p_t^{(0)}$ and the initial compressive hydrostatic yield stress $p_c^{(0)}$, a simultaneous variation of these two yield surface parameters is possible. With increasing values of $p_c^{(0)}$ and $p_t^{(0)}$ the shape of the initial yield surfaces turns into an elongated ellipse aligned with the hydrostatic axis in the mean/effective stress plane.

The influence of a simultaneous variation for the values of the two hydrostatic strength parameters on the overall quasistatic force-indentation response was also investigated. Since for the used set of parameters the *initial* yield surface is symmetric with respect to the origin, it was possible to use both the volumetric and the isotropic hardening model; a vanishing plastic Poisson's ratio $\nu_{pl} = 0$ was assumed for both models.

Figure 4.9 shows predicted force-indentation diagrams for a range of values of $p_c^{(0)} = p_t^{(0)}$ between 0.4 and 100 MPa. With respect to the reference reaction force for $p_c^{(0)} = p_t^{(0)} = \sigma_{yc}^{(0)} = 1$ MPa an increase of the hydrostatic strength to 100 MPa leads to an increase of 1.5% for the volumetric hardening model and a decrease of 4.4% for the isotropic hardening model. A reduction of the hydrostatic strength to 0.4 MPa resulted in a relative increase of the peak reaction force by 18.4% for the volumetric hardening model and by 46.1% for the isotropic hardening model.

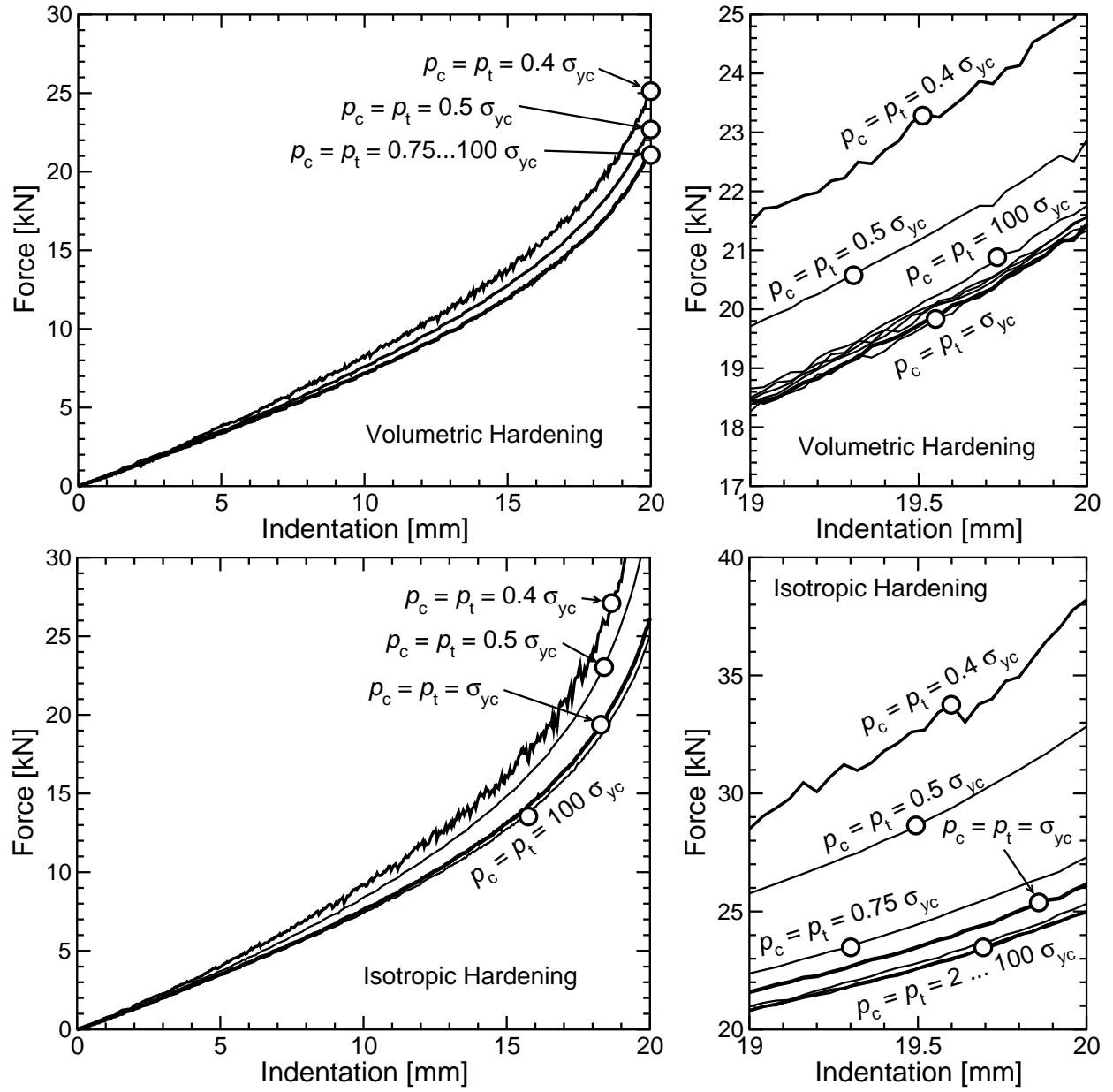


Figure 4.9: Predicted force-indentation relationships for equal values of the initial hydrostatic compressive $p_c^{(0)}$ and tensile yield pressures $p_t^{(0)}$; volumetric hardening (top); isotropic hardening (bottom).

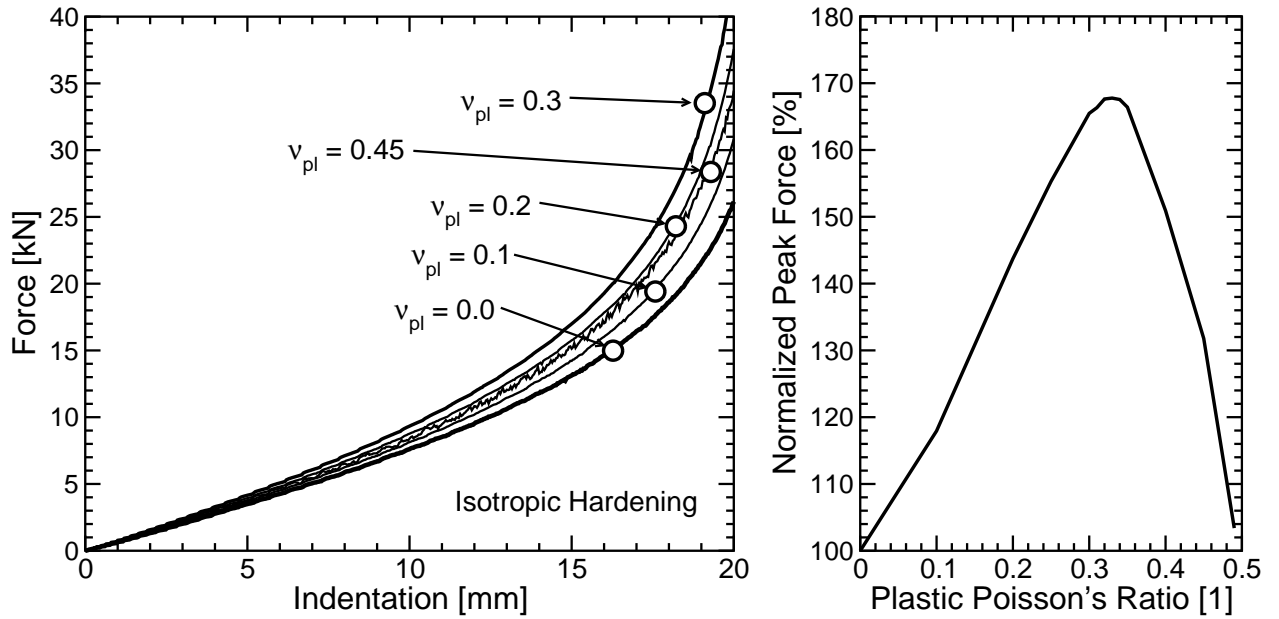


Figure 4.10: Left: predicted force-indentation relationships for different plastic Poisson's ratios ν_{pl} and isotropic hardening. Right: normalized peak forces in terms of ν_{pl} .

Variation of the Plastic Poisson's Ratio for Isotropic Hardening

The formulation of the Crushable Foam law with isotropic hardening allows for the variation of the plastic Poisson's ratio ν_{pl} (for volumetric hardening, $\nu_{pl} \equiv 0$ is assumed).

Figure 4.10 shows the influence of a variation of the plastic Poisson's ratio ν_{pl} in the interval $0 \leq \nu_{pl} < 0.5$ on the predicted mechanical behavior of the quasistatic reference indentation simulation. The theoretical limit of $\nu_{pl} = 0.5$ forbids any volumetric plastic compression (analogous to J_2 plasticity); a simulation with this restriction could not be executed owing to numerical difficulties.

Plotting the peak reaction force over the prescribed plastic Poisson's ratio (Figure 4.10, right) reveals two different regimes. For ν_{pl} values between 0.0 and 0.33, an increase of ν_{pl} results in an increase of the peak reaction forces. At 80% nominal compressive strain the peak force for $\nu_{pl} = 0.33$ is 70% higher than the peak force for $\nu_{pl} = 0$. For ν_{pl} values above 0.33, further increasing ν_{pl} causes the peak reaction force to decrease towards the value for $\nu_{pl} = 0.0$. A similar relationship between the plastic Poisson's ratio and the axial stress can be observed in the simulation of a uniaxial compression test with lateral expansion constraints, see Section 4.4.4, where it will be shown that the value of ν_{pl} maximizing the reaction force for arbitrary states of compression can be determined in consideration of work hardening mechanisms.

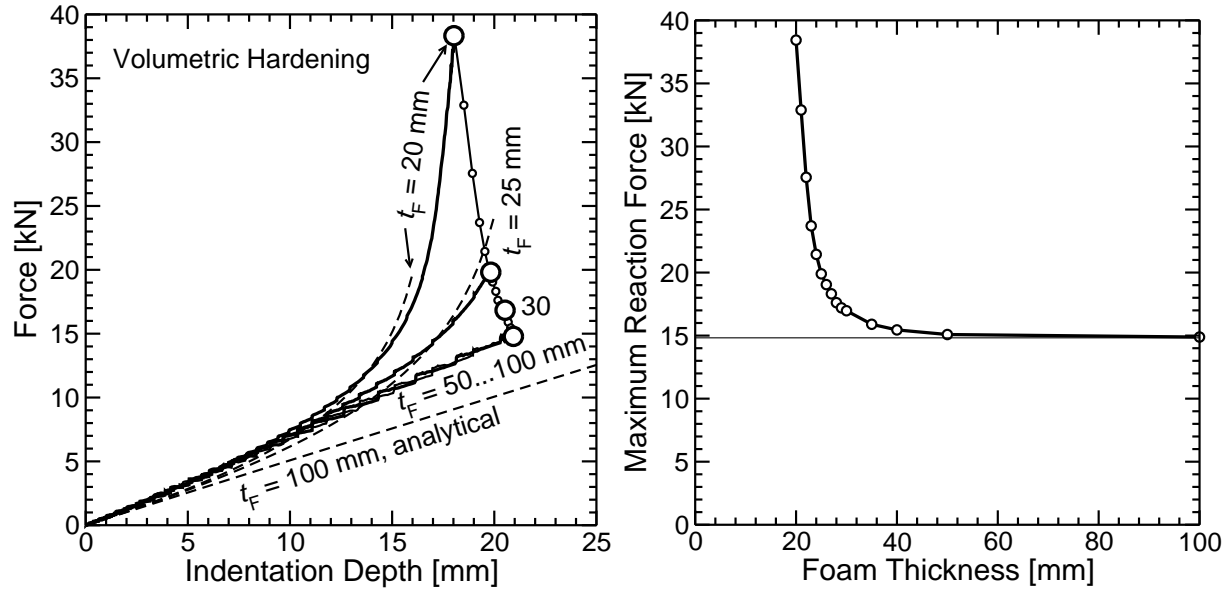


Figure 4.11: Left: predicted force-indentation relationships for foam pads of different thickness. The curves terminate at the point of maximum dynamic indentation. Right: peak indentation force as a function of the foam pad thickness.

Variation of the Foam Thickness in Dynamic Situations

So far, the influence of parameters necessary for the calibration of the Crushable Foam material law was studied in quasistatic simulations. Now, the influence of a geometrical parameter, namely the foam pad thickness t_F , on the results of an impact simulation will be considered.

In the following simulation series, the Crushable Foam constitutive model with volumetric hardening was calibrated with the reference material parameter set ($\sigma_{yc}^{(0)} = p_c^{(0)} = p_t^{(0)} = 1$ MPa). The impact of a rigid sphere of standardized mass and velocity on foam pads of different thickness was simulated. Figure 4.11 shows the simulation results as overall force-displacement plots (left) and as a peak force versus foam thickness diagram (right). Besides the Finite Element simulation results, selected force-displacement graphs obtained with the analytical solution (4.37) are presented and will be subjected to discussion.

The maximum reaction force appears for the minimum foam pad thickness of $t_F = 20$ mm. In this thickness regime, the peak force is highly sensitive to changes in thickness: an increase of the foam pad thickness to 25 mm reduces the predicted peak force by almost 50%! Above 25 mm thickness, the thickness-peak force relationship quickly approaches a limit value of 15 kN, only 25% below the peak force for $t_F = 25$ mm. It can be concluded,

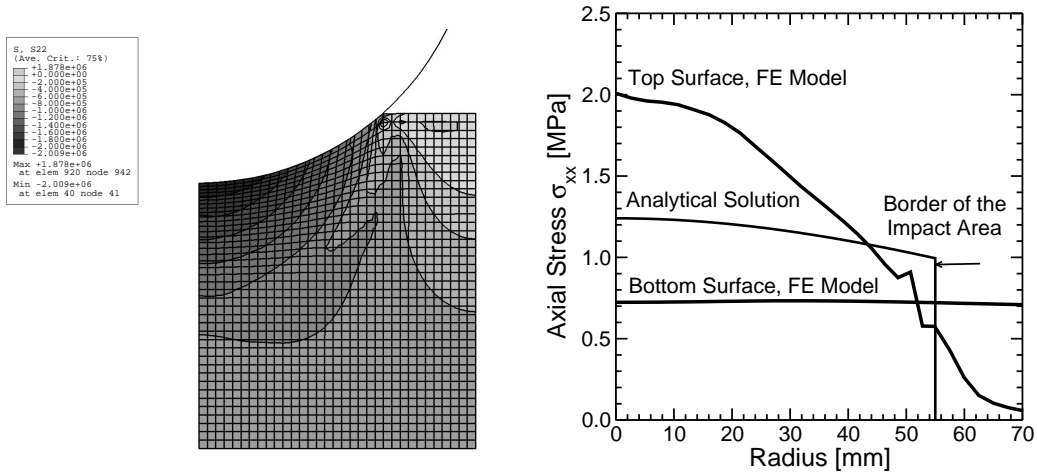


Figure 4.12: Predicted distribution of axial stresses in a 100 mm thick foam pad at the moment of maximum indentation of a spherical impactor; Left: contour plot; Right: radial stress distributions.

that at small original thickness values, a slight increase of the foam thickness can be very beneficial, whereas for thick foam pads even large thickness increments do not have a noticeable influence on the peak force.

Figure 4.11 contains three force–displacement graphs predicted by the analytical solution, Equation (4.37), for $t_F = 20, 25$ and 100 mm. They are discernible as dashed lines. For foam pads of small thickness, the analytical solutions agree very well with the simulation results. Beyond a foam pad thickness of 50 mm, however, the peak force predicted by the Finite Element simulation does not drop further with increasing thickness, while the analytical model continues to show a decreasing peak force for increasing thickness t_F . For investigating this difference in behavior, a comparison between the two models is provided for $t_F = 100$ mm in Figure 4.12. The contour plot of the axial normal stress σ_{xx} (S_{22}) in the deformed configuration (Figure 4.12, left) indicates, that the crash deformation localizes in the upper half of the Finite Element model. There is no apparent interaction between the stress field in the upper half of the pad and the distal wall. A plot of the axial normal stress along the bottom and the top surface of the Finite Element model versus the radial distance from the rotational axis of symmetry, Figure 4.12 (right), confirms this statement. It shows a parabolic stress distribution at the top surface, but a uniform stress distribution at the bottom surface. The analytical model, assuming uniform stress in thickness direction, predicts stress levels between these two extremes, that is, lower than the actual stresses acting on the impact sphere. Hence, neglecting the effects of strain localization clearly reduces the analytically predicted peak force.

With increasing distance between the localized deformation field and the distal wall, bound-

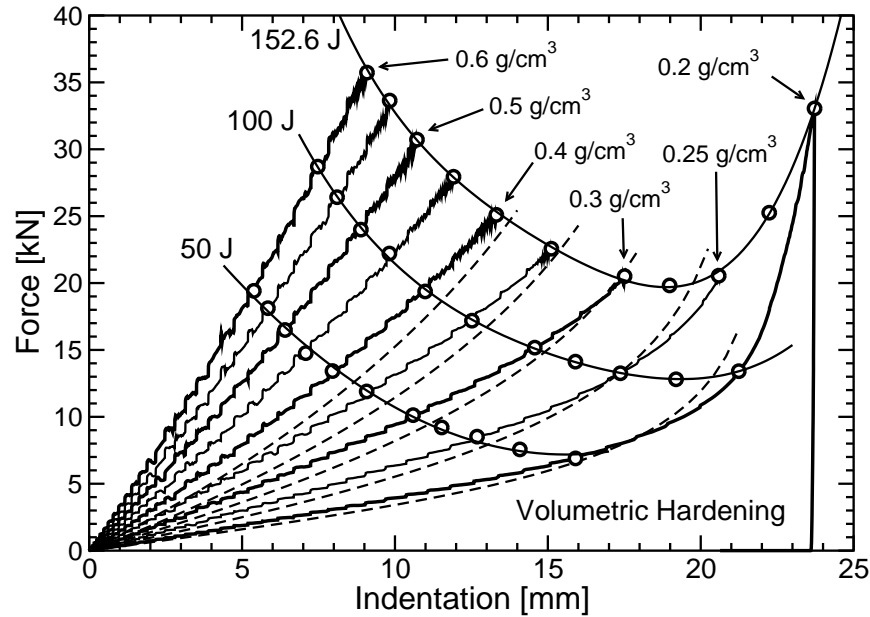


Figure 4.13: Predicted force-indentation relationships for the dynamic impact of a spherical impactor on foam pads of different apparent density.

ary effects begin to diminish and the peak indentation force converges towards a lower limit.

Variation of the Foam Density in Dynamic Situations

As shown in Chapter 3, the apparent foam density has a very strong influence on the uniaxial force-displacement behavior of metallic foams. The same effect is observable in crash simulations involving a spherical indenter. Figure 4.13 shows predicted force-indentation graphs for the dynamic impact of a rigid spherical impactor on foam pads of apparent densities ρ_F ranging from 0.2 g/cm^3 to 0.6 g/cm^3 . Starting from zero at the moment of impact the reaction force rises exponentially until a peak reaction force and the maximum indentation depth are reached. The force-indentation diagram for the foam of 0.2 g/cm^3 apparent density shows how the reaction force drops sharply to zero after the maximum indentation was reached. This drop marks the end of the deceleration period and the beginning of the acceleration of the impact mass in the opposite direction by forces created by the release of the stored elastic energy. As soon as the impactor separates from the foam surface the contact force vanishes. This elastic spring-back regime was omitted in the other curves for more visual clarity.

The area under the force-indentation curves equals the work performed by the contact forces between the impactor and the foam pad. The overwhelming part of the kinetic

energy, which initially amounts to 152.6 J, is dissipated by plastic deformation, while a minor part is stored as elastic strain energy. At the moment of standstill, the initial kinetic energy of the impact mass is fully stored in the foam material. The corresponding peak reaction force values, parameterized by the apparent foam density, are connected by a line in Figure 4.13. In addition to this envelope of the predicted force-indentation curves, indentation states, for which the stored energies amount to 50 and 100 J, respectively, are marked in Figure 4.13.

With respect to the minimization of the injury potential of the impact situation, the peak load appearing during impact should be minimized. If the free parameter is the apparent foam density then a diagram like Figure 4.13 can be evaluated to find the density that corresponds to the lowest peak load sustained during an impact event driven by a given amount of kinetic energy [60]. For the considered head impact, the lowest peak load is approximately 20 kN for an optimum density of 0.275 g/cm³. This optimum density value is very close to the one obtained in the uniaxial simulations investigated in Chapter 3. As in previous examples, the analytical solution based on Equation 4.37 gives surprisingly good predictions for the overall force-indentation behavior, compare the dashed lines in Figure 4.13.

4.4.4 Discussion

Influence of Hydrostatic Yield Parameters

In Figure 4.14, the relative difference between the predicted and the reference peak indentation force at an indentation depth of $0.8 t_F$ is plotted versus the prescribed hydrostatic strength parameters $p_c^{(0)}$ and $p_t^{(0)}$. The absolute force offsets have been normalized by the reference indentation force for volumetric hardening. Thus, it becomes obvious that the peak force for the reference parameter set $p_c^{(0)} = p_t^{(0)} = \sigma_{yc}^{(0)} = 1$ is approximately 20% higher for isotropic hardening, although the two hardening data sets were identical; in particular, the plastic Poisson's ratio ν_{pl} was set to zero for isotropic hardening. This shows, that for equal material data and equal simulation configurations the isotropic hardening behavior predicts slightly higher force values than the volumetric one owing to (a) the contribution of shear stresses and strains to the expansion of the yield surface, and (b) the symmetric expansion of the yield surface in the compressive and the tensile hydrostatic regimes.

The strongest influence of a variation of the hydrostatic strength parameters can be observed for low $p_c^{(0)}$ values, representing initial yield surfaces, the long axis of which is parallel to the effective strain axis in the σ_m - σ_e diagram. For yield surfaces of this shape small increments of the hydrostatic, compressive yield stress lead to large increments of the uniaxial compressive and the shear yield stresses. It will be shown below, that these stress states cover large regions of the stress field and, therefore, make the simulations sensitive to variations of the corresponding yield stress properties. Within the range of practical

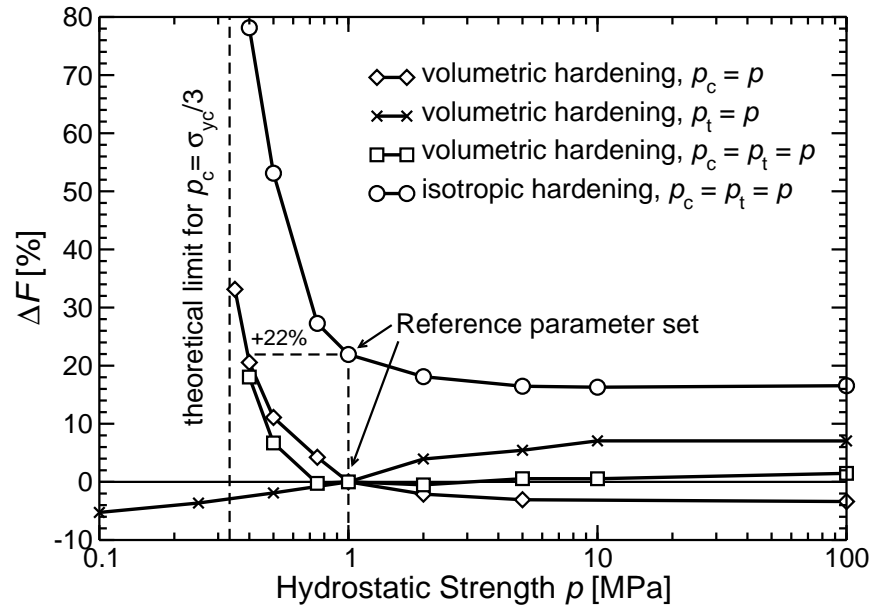


Figure 4.14: Relative difference between the reference indentation force for $p_c^{(0)} = p_t^{(0)} = \sigma_{yc}^{(0)} = 1$ MPa (volumetric hardening) and predicted indentation forces for different hydrostatic strength values and constitutive models.

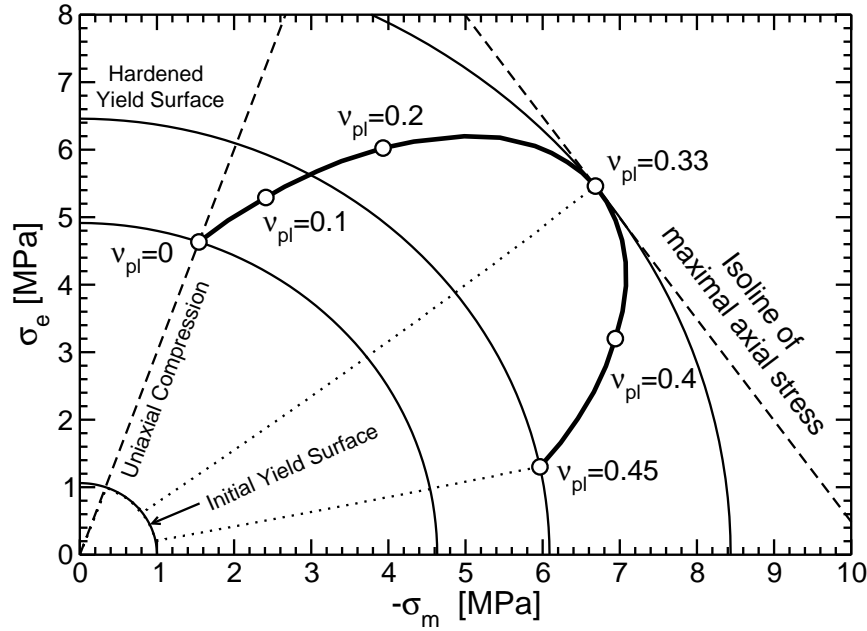


Figure 4.15: Dependence of the axisymmetric stress state on the plastic Poisson's ratio ν_{pl} in a radially constrained uniaxial compression simulation, visualized by projection to the mean/effective stress plane. The prescribed nominal axial strain is 70%.

hydrostatic yield stress values discussed in Section 4.2.2, a variation of only -5/+10% has to be expected for the peak indentation force for the given configuration.

Influence of the Plastic Poisson's Ratio

For the isotropic hardening model, the plastic Poisson's ratio has been shown to exert considerable influence on the overall force-indentation behavior. At $\nu_{pl} = 0.33$ a maximum force was predicted by the indentation simulation. Subjecting the Crushable Foam material with isotropic hardening to uniaxial compression and radial deformation constraints gives a similar relationship between ν_{pl} and the axial compression force. The thick solid line in Figure 4.15 connects axisymmetric stress states, which are evaluated for the same uniaxial compressive strain and parameterized by the Poisson's ratio. The dotted lines show stress paths for two selected plastic Poisson's ratios ($\nu_{pl} = 0.33$ and $\nu_{pl} = 0.45$) and monotonically increasing, purely uniaxial compressive strain.

To relate the stress states to the corresponding state of the yield surface, a projection to the mean/effective stress plane was chosen. In the case of an uniform axisymmetric stress state with $\sigma_{\theta\theta} = \sigma_{rr}$ this transformation is performed by:

$$\sigma_e = |\sigma_{xx} - \sigma_{rr}| \quad (4.39)$$

$$\sigma_m = \frac{\sigma_{xx} + 2\sigma_{rr}}{3} \quad (4.40)$$

In this representation, isolines of constant axial stress σ_{xx} can be described by the linear equation

$$\sigma_e(\sigma_m) = \frac{3}{2}(\sigma_{xx} - \sigma_m). \quad (4.41)$$

Maximizing σ_{xx} under the constraint that the stress state resides on the yield surface leads to the condition that the isoline, Equation (4.41), touches the yield surface in the point corresponding to the maximized axial yield stress (and the corresponding radial stress). From this follows that the largest axial stress is associated with the “largest” yield surface, that is, the maximum degree of hardening. Maximizing $d\varepsilon_{eqv}^{pl}$ in Equation (4.34) for arbitrary uniaxial hardening tables $\sigma_{yc}(\varepsilon_{eqv}^{pl})$ means maximizing the plastic dissipation energy increment ($\boldsymbol{\sigma} : d\boldsymbol{\epsilon}_{pl}$). The principle of maximum plastic dissipation applies to associated plastic flow, for which the yield surface F_{iso} and the flow potential G_{iso} are symmetric. Comparing Equations (4.28) and (4.31) shows that this condition is fulfilled for $\alpha = \beta$ and, consequently, for

$$\nu_{pl} = \frac{1}{6}(3 - k^2). \quad (4.42)$$

For the examined case of $k = 1$, the highest degree of hardening occurs at $\nu_{pl} = 1/3$, as was observed in Figures 4.10 and 4.15.

Stress Fields and Stress Evolution

So far, the evaluation of the simulation results was primarily based on a discussion of the overall force–displacement response of the sphere/foam system. To understand the reaction of the foam material in the considered impact situation it is advantageous to discuss the stress and deformation fields in the model in more detail.

The instantaneous stress state can be visualized by stress vector plots, in which the length and the direction of vectors graphically represents the magnitude of the principal stresses, and the orientation of the vectors shows the orientation of the principal stresses axes. Figure 4.16 shows a corresponding plot for an early stage of a typical impact simulation.

Directly under the impact mass uniaxial compressive deformation prevails. The maximum degree of hardening occurs at the foam surface below the center of the impact mass. Both stresses and strains are largest at the surface of the foam and decrease with increasing depth under the impact zone. The zones of equal compressive strain in the impact direction have the shape of an inverted cone with the impact area as its base.

Tensile principal stresses occur at the surface of the foam pad just outside the border of the contact area. The tensile principal stress axes are oriented parallel to the (deformed) surface. The highest value of tensile principal stresses is reached at the border of the impact area. Here, the occurrence of cracks can be expected as schematically indicated in

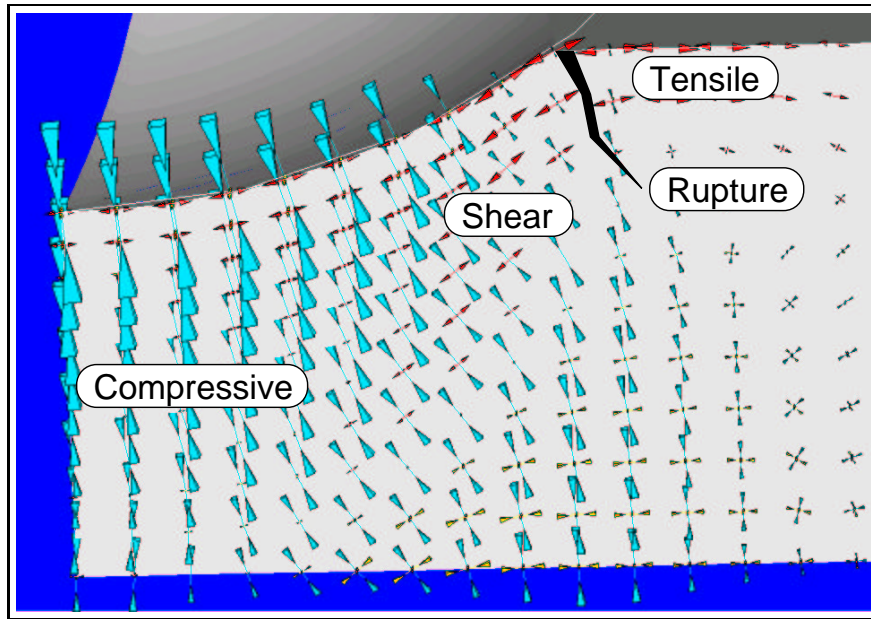


Figure 4.16: Plot of predicted principal stress vectors, partitioned into different characteristic stress domains.

Figure 4.16. Material points just inside the border of the impact area undergo the highest amount of shear deformation.

The observation of the instantaneous stress distributions indicates the prevalence of uniaxial stress states in the considered impact event. This means that the simulation should not be very sensitive to changes in the hydrostatic parameters of the material. Additionally, the principal stress axes keep roughly the same orientation during the indentation. Therefore, strong anisotropy effects do not occur.

Besides the multiaxial nature of the instantaneous stress states, the history of local stress states is an important aspect of the simulation. The evolution of local stress states is best visualized as a curve in the mean/effective stress diagram used commonly when describing pressure dependent material laws; in Figure 4.17, the predicted evolution of stress states in selected material points of the foam target is followed during the impact event. This data can be used to assess which level of complexity of the flow rule and the hardening law is required for performing satisfactory simulations.

Essentially, radial paths in stress space indicate that simple isotropic constitutive laws suffice for describing the local material state, whereas distinct changes in the direction of the stress paths signal that phenomena such as anisotropic hardening will have to be considered. Furthermore, softening due to fracture of cell walls may occur when stress states enter tensile regimes.

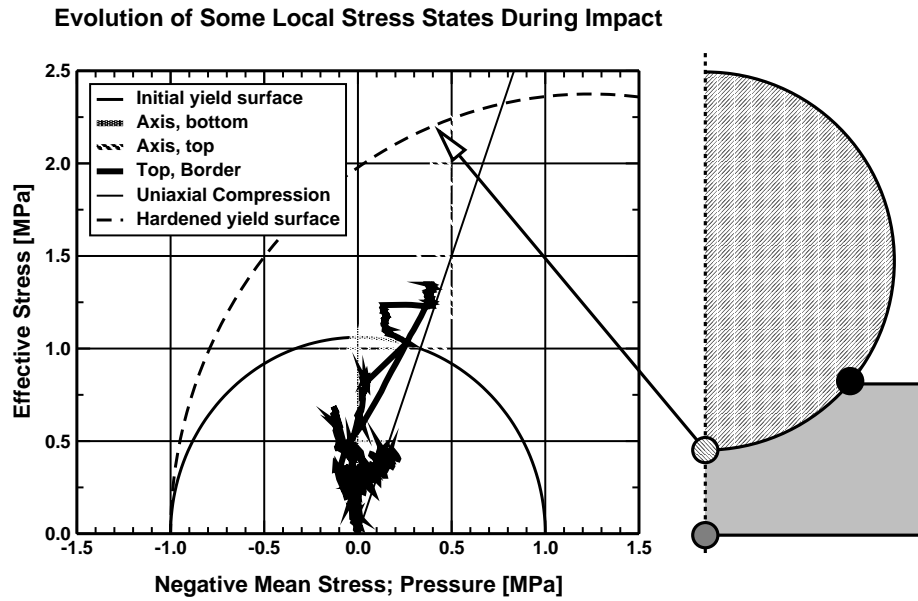


Figure 4.17: Stress states of selected material points visualized as paths in the von Mises equivalent versus mean stress plane during a typical impact event.

Figure 4.17 shows stress history paths for three different material points. These stress paths lie mostly between the axis of uniaxial compression (inclination 3:1) and the vertical axis that represents pure shear, indicating that these two types of loading will dominate the local deformation of the foam. The “Axis, top” line in Figure 4.17 is associated with a point under the center of the impact mass. It is surrounded by an ellipse, which is the projection of the Crushable Foam yield surface corresponding to the highest value of the hardening parameter, in this case the accumulated volumetric plastic strain. Uniaxial stress states can be seen to prevail in the impact event considered here, indicating that the simulation should not be very sensitive to changes of the hydrostatic parameters of the material.

These findings narrow down the requirements for constitutive laws to be employed in crash simulations involving a comparatively thin padding and a large impactor. They explain the relatively small influence of the shape of the yield surface on the overall force-indentation relationship and the surprisingly good predictions of the uniaxial analytical model.

4.4.5 Conclusions

In this section, the simulation of low-energy impact events with selected constitutive models was demonstrated. Because of the geometrical relation between the curved impact mass

and the thin foam layer, the local deformation and stress states were predominantly in the uniaxial compressive and shear like domain. The orientations of the principal axes of the stress tensor did not change significantly, and anisotropy effects could, therefore, be neglected. Furthermore, the influence of hydrostatic material parameters was not very pronounced under these conditions; the simulations were rather insensitive to variations of these parameters within reasonable ranges.

The Crushable Foam constitutive model with isotropic hardening allows for the specification of the plastic Poisson's ratio ν_{pl} . The peak indentation force is approximately equal for $\nu_{pl} = 0$ and $\nu_{pl} \approx 0.5$. Between those limiting values, the peak force reached a maximum if the condition of associated flow is fulfilled. For equal uniaxial and hydrostatic yield stresses this is the case for a plastic Poisson's ratio of $1/3$, where the peak force was 70% above the reference value. This significant influence has to be kept in mind with regard to the calibration of material data.

In addition, the simulation results were very sensitive to changes of the kinematic boundary conditions and the thickness of the foam pad. Radial kinematic constraints lead to a strong increase of the reaction force for indentation depths exceeding 60% foam pad thickness. Increasing the foam pad thickness has a strong effect for foam pads of low thickness and a diminishing effect for foam pads of high thickness. In the former case, the thickness influences the degree of compaction, and, thereby, the degree of hardening directly. In the latter case, the diminishing interaction between the impact zone and the distal surface leads to a decoupling of the foam thickness and the dynamic peak load.

Another strong influence can be contributed to the apparent density of the foam. For the examined reference configuration, a distinct optimum in the density range existed with regard to a minimization of the peak load experienced by an impactor hitting the metallic foam padding. It can be expected that such an optimal density exists for similar configurations, see, for example, [60] and Chapter 3.

4.5 Design Optimization with Metallic Foams

4.5.1 Introduction

Nature, well known for her economic use of sparse resources, relies on cellular materials such as wood or bone to set up load-bearing structures (for example endo- and exoskeletons) in living beings. The reason for this preference lies in the high specific stiffness and strength of this kind of materials. Another characteristic of porous or cellular materials is the fact that their mechanical properties are scalable by changing their effective density. In living beings biological growth processes exploit this possibility by adapting the mechanical properties of tissue in response to changing loading conditions. Apart from changes of the microstructure, the most apparent change is the increase or decrease of the local effective density.

Engineers are inspired by the intricate biological structures, that were optimized by evolution in the course of hundreds of millions of years, and they are looking for engineering materials with similar advantageous properties [58]. With growing knowledge about the mechanical performance of cellular metals and, in particular, of metallic foams, methods for the design of foam components for applications such as packaging, energy absorption and sandwich structures have evolved significantly [6; 31; 33]. The ability of cellular metals to compete with other materials can be underlined by emphasizing their multifunctionality [29; 30]. Furthermore, it was shown that in certain structures, such as cylindrical sandwich shells, metallic foam cores are more weight efficient than other stiffening concepts [56]. In studies dealing with the design and optimization of metallic foam components usually a foam of uniform density is assumed.

Metallic foams show some potential for being produced with controlled spatial variations of their density, introducing inhomogeneities on a mesoscale as defined in Chapter 3. In the case of foams produced via powder metallurgical routes the foaming process, and, as a consequence, the final density distribution may be controlled by suitable choices of the distribution of the blowing agent and of process parameters such as temperature and pressure. This suggests employing such foams as graded materials in space filling lightweight structures designed in analogy to cancellous bone, a functionally graded biological material that displays increased density in regions of high loading, compare Figure 1.1 (left).

In a study by Reiter [91] algorithms are presented which simulate the natural adaptation of bone to applied loads. Figure 4.18 (left) shows the bone density distribution as predicted by the program FAROB. The calculated density distribution agrees well with the density distribution found in an actual femur (Figure 4.18, right). Bone typically shows regions of dense material, that is, cortical bone, and of foam-like material, that is, spongy (trabecular) bone. It was shown that in many cases bones represent stiffness optimized structures. Hence, it was a natural step to try simulating the bone remodeling processes and to transfer the concepts and corresponding algorithms to technical applications within the framework of functionally graded materials [92]. Some production routes [34] for metal-

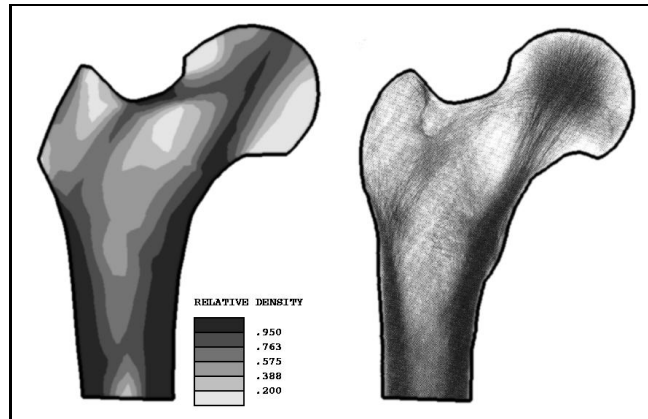


Figure 4.18: Left: density distribution in the proximal femur as predicted by numerical bone remodeling simulation [85]. Right: Radio-graph of a typical human femur [62].

lic foams are undergoing development aimed at allowing the realization of spatially varying micro-structures and apparent mass densities, leading to position dependent stiffness and strength properties. This opens up the possibilities of employing them as graded materials in space filling lightweight structures and of approximating the natural path of “optimization” followed by bone configurations for making functionally graded foams and for the formation of *in situ* sandwich structures made of aluminum (Figure 1.1, right).

4.5.2 Method

The method proposed in this study is based on the premise that the global behavior of structures can be improved by achieving certain stress or strain conditions on the local level. In many design cases, an improvement of a structure is related to a reduction of its total mass while maintaining or improving important parameters like stiffness or strength. The design objective in these cases is the improvement of the weight-specific properties of the structure. Depending on the parameter domain of the problem this can imply the optimization of part dimensions, shapes of parts with a given topology or an optimization of the topology itself. Sophisticated methods try to optimize the geometry (that is, size or shape) and the topology of a structure at the same time. The existence of a structural shape implies that the structure is defined by the geometry and the topology of the boundary of a volume of solid material. For practical reasons, only shapes, which do not extend beyond a predefined design space, are considered.

Metallic foams offer a different route for the improvement (or the optimization) of structures, since they can be produced not only in fairly arbitrary shapes, but also with a varying local apparent density. Recognizing the local apparent density as an important

design variable in structures consisting of or containing metallic foam, a method to adapt the local density in a way, that is beneficial for the overall behavior of the structure, was sought. In the research field of biomechanics, an appropriate method was proposed by Reiter [91]. This method predicts the growth of bone in living beings by simulating the adaptation of the apparent bone density to stress fields caused by external loads. The basic assumption behind this algorithm is that bone can react to a *local* stimulus related to the stresses or the strains in the trabecular microstructure. In the case of bone remodeling this stimulus is often chosen to be an averaged local strain energy density in the trabecular structure of the spongy bone.

In the context of the present investigation two different scalar mechanical properties were considered as the driving forces for the density adaptation process:

1. the homogenized strain energy density and
2. an equivalent stress for the homogenized material.

These two properties were related to nominal values to calculate a stimulus and, consequently, a proportional rate of change of the local foam density. For a local mechanical parameter v , which is desired to converge towards a nominal, stationary value v_{stat} , the stimulus S can be determined by:

$$S(t) = \frac{v(t) - v_{\text{stat}}}{(v_{\text{stat}})^{s_w}} \quad (4.43)$$

The numerator of this expression corresponds to the stimulus definition proposed by Reiter [91], whereas the denominator was supplemented in this work to allow for a calculation of the stimulus in terms of absolute or relative, that is, dimensionless values. To this end the exponent s_w was introduced, which acts like a switch, yielding a stimulus in absolute values for $s_w = 0$, or a dimensionless quantity for $s_w = 1$. Calculating a relative stimulus simplifies the calibration of the adaptation parameters, therefore s_w was kept at a value of 1 throughout the present study.

The goal of the proposed algorithm lies in improving the global behavior of structures by satisfying a local stationarity condition $v - v_{\text{stat}} = 0$, where v is a state variable such as the spatially varying homogenized equivalent stress, and v_{stat} is a constant global stationary value. The stimulus S expresses by how much the actual value v differs from the aspired stationary value v_{stat} . If the difference is severe then the density of the foam changes at a high rate, whereas the rate of change of the foam diminishes in the vicinity of the density that corresponds to the locally optimal configuration. This is achieved by solving the initial value problem

$$\frac{d\rho_F}{dt} = c S(t), \quad (4.44)$$

where $d\rho_F/dt$ is the rate of the change of the apparent foam density, $S(t)$ is the time-dependent stimulus as introduced in Equation (4.43) and c is a factor for controlling the

speed of the density adaptation process. Appropriate initial conditions, often in the form of an initially uniform density distribution $\rho_F(t_0) = \rho_{F,0}$, complete the problem. Equation (4.44) is an ordinary first-order differential equation describing the evolution of the local apparent density $\rho_F(t)$. The rate of change of the density is a linear function of the stimulus $S(t)$. This approach has been used in a number of studies on bone remodeling, for example, in the work of Reiter [91] or in Pettermann et al. [85], where t has the character of a real time. For the present models t may be viewed as a fictitious time.

So far little has been said about the relevance of the two different state variables, the local strain energy density and the local equivalent stress, and about their respective nominal values. Pedersen [84] states that structures, which exhibit a uniform distribution of the strain energy density in the loaded condition, are optimized with respect to weight specific stiffness. This leads to the choice of the homogenized strain energy U_F as a variable v and a constant homogenized strain energy $U_{F,\text{eq}}$ as a nominal value v_{stat} in Equation (4.43). The rate Equation (4.44) causes the density ρ_F to decrease as soon as the actual strain energy density is below the nominal one and to increase as soon as U_F is higher than $U_{F,\text{eq}}$. It is worth restating that a spatial distribution $U_F(x, y, z)$ of the homogenized strain energy density, which converges locally to a stationary value $U_{F,\text{eq}}$, is equivalent to an increase of the specific stiffness.

The other state variable under consideration is an equivalent stress σ_{eqv} , which is, in connection with a density-dependent yield stress $\sigma_{F,\text{yld}}(\rho_F)$, a scalar measure that can be used to determine whether a material deforms inelastically or not. For a structure made of metal, inelastic deformation usually implies plastic deformation, and in many design cases these non-reversible deformations are undesirable. Within the framework of plasticity theory stress tensors are translated into a scalar equivalent stress, which can be compared to a yield stress representing the limit of purely elastic deformation under uniaxial loading. Assuming that such a yield stress exists for metallic foams we can apply the proposed procedure to improve the strength of a structure made of or containing metallic foam by gradually changing the local apparent density of the homogenized material such that, ultimately, the local stress state shows the desired safety against yielding everywhere in the structure. This procedure is known as “fully stressed design” and regarded as an intuitive way to optimize the strength of a structure.

In the treatment of porous or cellular materials a distinction has to be made between quantities v_S related to the solid phase and effective or homogenized quantities v_F which can be defined on a length-scale, where the material does not act like a structure, that is, an arrangement of cell walls, struts, and vertices, but rather as a homogeneous material with individual cells being indistinguishable from a mechanical point of view (compare the discussion in Section 4.1). The field of homogenization theory deals with the transition between these two length-scales. For an isotropic material with a statistically uniform microstructural topology the apparent density is the governing material property. It has proven advantageous to relate homogenized quantities v_F and bulk material quantities v_S

by power laws of the form

$$\frac{v_F}{v_S} = \alpha \left(\frac{\rho_F}{\rho_S} \right)^\beta \quad (4.45)$$

with the relative density $\rho_{F,\text{rel}} = \rho_F/\rho_S$ being the governing parameter. The dimensionless constants α and β depend on foam-specific microgeometrical parameters. Gibson and Ashby [34] suggested an exponent β_E of 2 for scaling the elastic modulus of open cell foams, while they assigned an exponent β_σ of 1.5 to the yield stress $\sigma_{F,\text{yld}}$. In the same work, several more refined micromechanical models are presented to take into account the microtopology, that is, open or closed cell microstructures, or the distribution of the material between cell walls and corners as well as edges. We assume that a relationship such as Equation (4.45) can describe the actual dependence of an effective material property $v_{i,F}$ on the relative apparent density $\rho_{F,\text{rel}}$ reasonably well within a given density range $[\rho_{F,\text{min}}, \rho_{F,\text{max}}]$.

If the bulk material density ρ_S and the mechanical bulk material properties $v_S^{(i)}$ are unknown, but scaling relations are available in terms of absolute parameter values v_F and the absolute foam density ρ_F , then the scaling parameters α and β can be used directly as soon as the bulk material density ρ_S and the bulk material parameter $v_S^{(i)}$ are both set to 1.0. Equation (4.45) then becomes

$$v_F = \tilde{\alpha} \rho_F^\beta \quad (4.46)$$

As mentioned in Section 3.2, Gradinger and Rammerstorfer [36] presented power laws similar to Equation (4.46), which were obtained for an aluminum foam of the brand *ALULIGHT*^(TM) in an extensive experimental program. This aluminum foam is produced via a powder metallurgical route holding a potential for controlling the foaming process, and, therefore, the final density distribution by a suitable choice of the distribution of the blowing agent and the process parameters, for example the time histories of temperature and pressure. In [36] the results of a large number of uniaxial compression tests was expressed by the following regression formula for the macroscopic uniaxial compressive yield stress $\sigma_{F,\text{yld}}$

$$\sigma_{F,\text{yld}}(\rho_F) = 12.343 \rho_F^{1.8807} [\text{MPa}], \quad (4.47)$$

which was considered to be equal to the collapse stress σ_0 . A similar relationship for the initial tangent modulus E_F was derived as:

$$E_F(\rho_F) = 892.32 \rho_F^{1.3212} [\text{MPa}]. \quad (4.48)$$

The absolute apparent foam density ρ_F has to be inserted in $[\text{g/cm}^3]$ in both equations. Equations (4.47) and (4.48) are valid for a density range of $0.2 < \rho_F < 0.8 \text{ g/cm}^3$. In addition to the initial modulus E_F , an unloading modulus of

$$S_{\text{Rpo}}(\rho_F) = 14\,000 \rho_F^{2.2} [\text{MPa}] \quad (4.49)$$

was measured. Equations (4.47) to (4.49) will be used to demonstrate the adaptation process for an existing aluminum foam. The homogenized foam material is assumed to be

isotropic and linear elastic for stress states inside the yield surface. The elastic Poisson's ratio ν is chosen as 0.3.

Since an important characteristic of foam is its pressure sensitivity, a suitable stress measure has to be found for strength optimization. If isotropic behavior can be assumed then it is advantageous to express the yield criterion $\sigma_{\text{eqv}} = \sigma_{\text{F,yld}}$ in terms of the invariants of a stress tensor $\boldsymbol{\sigma}$. A suitable stress measure for assessing the influence of the deviatoric stress components is defined in classical metal plasticity by the von Mises equivalent stress:

$$\sigma_e = \sqrt{\frac{3}{2} s_{ij} s_{ij}}, \quad (4.50)$$

with s_{ij} being the deviatoric components $s_{ij} = \sigma_{ij} - \sigma_m \delta_{ij}$ of the local stress tensor $\boldsymbol{\sigma}$. An alternative formulation of Equation (4.50), namely $\sigma_e = (3 J_2)^{1/2}$, incorporates the second invariant $J_2 = \frac{1}{2} s_{ij} s_{ij}$ of the deviatoric stress tensor and motivates the designation “ J_2 -plasticity” for a theory of yielding for materials that do not yield under pure hydrostatic stress states. In contrast to the behavior of solid metals, hydrostatic pressure can cause yielding of a porous or foamed metal. Thus, the influence of the mean stress

$$\sigma_m = \frac{1}{3} \sigma_{kk} = \frac{1}{3} I_1 \quad (4.51)$$

has to be taken into account along with the equivalent deviatoric stress σ_e . Here, $I_1 = \sigma_{11} + \sigma_{22} + \sigma_{33}$ denotes the first invariant of the local stress state $\boldsymbol{\sigma}$. For the interaction of deviatoric and hydrostatic stress components an equivalent stress measure was proposed by Deshpande and Fleck [24]:

$$\sigma_{\text{eqv}}^2 = \frac{1}{1 + (\xi/3)^2} (\sigma_e^2 + \xi^2 \sigma_m^2) \quad (4.52)$$

The corresponding yield surface, which is defined by the yield condition $\sigma_{\text{eqv}} = \sigma_{\text{F,yld}}$, is of elliptical shape in the (σ_m, σ_e) stress space. The shape parameter ξ defines the aspect ratio of the ellipse², and $\sigma_{\text{F,yld}}$ is the yield strength of the foam under uniaxial compression. The hydrostatic yield strength $\sigma_{m,\text{yld}}$ is given by $\sigma_{m,\text{yld}} = \sigma_{\text{F,yld}} [(1 + (\xi/3)^2)^{1/2}]/\xi$. For $\xi = 0$ Equation (4.52) simplifies to $\sigma_{\text{eqv}} = \sigma_e$, and the equivalent stress σ_{eqv} is equal to the von Mises equivalent stress σ_e . The definition of a local equivalent stress σ_{eqv} and a density dependent yield stress $\sigma_{\text{F,yld}}$ are sufficient for performing density adaptation in order to achieve a fully stressed design as outlined previously.

The choice of a nominal strain energy density $U_{\text{F,eq}}$ for an adaptive improvement of the specific stiffness of a foam structure is less straightforward and requires some additional considerations. It will be shown later that a structure of high specific stiffness tends to be clearly partitioned in regions of maximum and minimum foam densities. Assuming that only the regions of maximum apparent foam density carry the applied load, a nominal

²The parameter ξ in Equation (4.52) is equivalent to the parameter α in the definition of the equivalent stress according to Deshpande and Fleck [24] and the ABAQUS Crushable Foam law with isotropic hardening.

strain energy density $U_{F,eq}$, that ensures that the yield criterion $\sigma_{eqv} \geq \sigma_{F,yld}$ is not fulfilled in regions of maximum foam density, can be considered an appropriate target value. In the case of the yield criterion for metallic foams proposed by Fleck and Deshpande [24] it is indeed possible to find an appropriate strain energy density, since for $\xi > 0$ the yield surface is closed and convex in the 6-dimensional space of the components of the stress tensor. The total strain energy density U_F can be split up into a contribution U_V representing the elastic energy stored by changing the volume of an volume element, yielding

$$U_V(\sigma_m) = \frac{3(1-2\nu)}{2E}(\sigma_m)^2 \quad (4.53)$$

for an isotropic material and a contribution U_{Sh} corresponding to the elastic energy stored by changing the shape of the volume element:

$$U_{Sh}(\sigma_e) = \frac{1+\nu}{3E}(\sigma_e)^2 \quad (4.54)$$

Here, we are looking for a nominal strain energy density $U_{F,eq}$ that is lower or equal to the minimum of all strain energy density values for stress states on the yield surface. In other words, we want to minimize $U_F = U_V + U_{Sh}$ under the condition that the yield criterion is fulfilled. Since U_V , U_{Sh} , and σ_{eqv} can be expressed in terms of the mean stress σ_m and the von Mises equivalent stress σ_e this minimum can be found fairly easily. For $\rho_F = \rho_{F,max} = 0.8 \text{ g/cm}^3$ and $\xi = 1.5$ the sought nominal strain energy density $U_{F,eq}$ is equal to the strain energy density $U_F(\sigma_{m,yld})$ for a foam volume having a density of $\rho_{F,max}$ and being loaded by the hydrostatic yield stress $\sigma_{m,yld}$. If the strain energy density U_F is below this threshold $U_{F,eq}$, and the foam density is $\rho_{F,max}$ then yielding will not occur.

Another approach for the determination of a nominal strain energy density is the consideration of a uniaxial stress state which corresponds to the uniaxial yield stress $\sigma_{F,yld}$. In the following it will be shown that upon trying to improve the specific stiffness of a structure with spatially varying stiffness one often ends up with a framework of struts formed by regions of maximum density. Assuming that these stiff struts are the load bearing parts of the structure and that uniaxial stress states predominate in a framework topology, the choice of a nominal value

$$U_{F,eq} = \frac{(\sigma_{F,yld})^2}{2E_F}, \quad (4.55)$$

which is the elastic energy density at the uniaxial yield stress $\sigma_{F,yld}$ of a foam of maximum admissible density $\rho_{F,max}$, has some physical relevance.

4.5.3 Implementation

The stress-strain relationship $\boldsymbol{\sigma} = \mathbf{E} \boldsymbol{\epsilon}$ for a linear elastic material and the differential equation (4.44) governing the adaptation process were implemented as a user material subroutine in the Finite Element code ABAQUS. A user material subroutine (UMAT) essentially takes a strain increment as an argument and returns a stress increment as a function

of the strain increment and the local material state. The strain increments, which are supplied by *ABAQUS*, are updated iteratively until global mechanical equilibrium is achieved. Due to the discretization of the continuum problem the material state is evaluated only at a finite number of integration points.

The evolution of the local, homogenized density ρ_F is evaluated by integrating Equation (4.44) incrementally using the explicit integration scheme:

$$\rho_F(t + \Delta t) = \rho_F(t) + \frac{d\rho_F}{dt} \Delta t. \quad (4.56)$$

In the implementation of this incremental integration scheme, the rate of change of the density $|d\rho_F/dt|$ is limited by a maximum value $(\dot{\rho}_F)_{\max}$. This parameter and the factor c in Equation (4.44) govern the convergence behavior of the optimization process. The use of an explicit integration scheme requires the parameters c and $(\dot{\rho}_F)_{\max}$ to satisfy additional convergence conditions. If the multiplier c for the stimulus or the time increment is chosen too large then the solution will oscillate around the equilibrium state. If too high a value is selected for $(\dot{\rho}_F)_{\max}$ then the force equilibrium iterations of the Finite Element solver will fail to converge.

A reasonable value for the cut-off rate of change of the foam density $(\dot{\rho}_F)_{\max}$ can be derived by specifying the minimum number of increments n_{inc} necessary to raise the density at a material point from the minimum density $\rho_{F,\min}$ to the maximum density $\rho_{F,\max}$. For a time increment size Δt a maximum rate $(\dot{\rho}_F)_{\max}$ of

$$(\dot{\rho}_F)_{\max} = \frac{\rho_{F,\max} - \rho_{F,\min}}{n_{\text{inc}} \Delta t} \quad (4.57)$$

follows. In the present study, the number of increments n_{inc} was set to 10. Since the step time has no physical meaning in the case of topology optimization (as opposed to, for example, bone remodeling,) the time increment size Δt was set to 1.0. The rate multiplier c in equation (4.44) was chosen such that the lowest possible relative stimulus, namely $(0 - v_{\text{stat}})/v_{\text{stat}} = -1$ leads to the highest rate of density reduction $-(\dot{\rho}_F)_{\max}$. It follows that $c = (\dot{\rho}_F)_{\max}$.

With the definition of a user material subroutine the density adaptation process is performed on the integration-point level. A comparison of this method to other approaches (element based, node based) is given in the work by Jacobs et al. [57]. It should be mentioned that the integration-point approach can put severe restrictions on the choice of the Finite Element type. The integration order of conventional Gauss quadrature can be too low for the case of high density gradients. It was shown in a single element test (bilinear, 4 node, two dimensional solid) that the assembly of the Finite Element stiffness matrix can lead to physically unreasonable stress states in the integration points if the integration order is too low to capture high stiffness gradients throughout the element. This problem is tied to the existence of multiple integration points per element. Finite Elements with a single integration point are the logical exception. Therefore, only two element types with

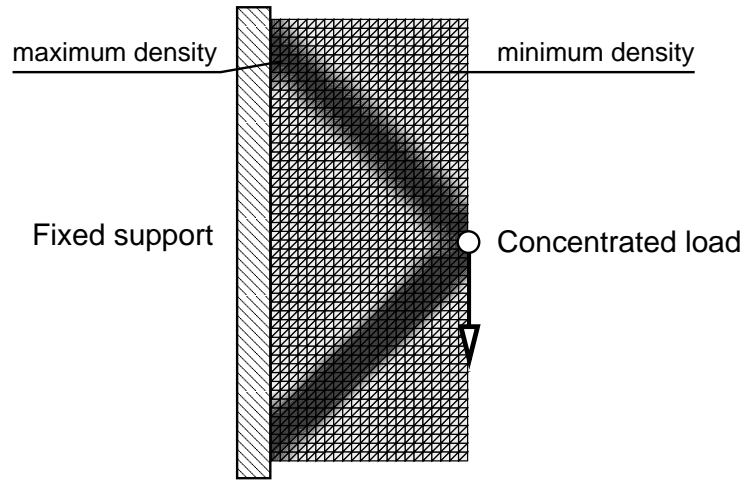


Figure 4.19: Deep cantilever beam example.

one integration point were used in the present study, namely 2D constant strain triangles and 3D axisymmetric triangles.

The simulations were started with a uniform density distribution. The analyses were continued until the density changes fell below a chosen convergence limit.

4.5.4 Results

Structures of High Specific Stiffness

In the following some basic configurations characterized by different admissible design spaces and different loading as well as kinematic boundary conditions will be investigated. Beam-like topologies are very common in engineering. Consequently, some standard cases for topology optimization are defined by beam-like design spaces and single concentrated or distributed loads. Depending on the symmetry and the boundary conditions of the problem deep or short cantilever beams as well as bridge-like beams supported at two or more points can be distinguished. For these configurations many reference solutions for stiffness and strength optimized topologies exist [28; 50]. Here, some similar problems were examined to allow for a comparison of the obtained solutions to the ones found in the literature and, thus, to verify the proposed method as well as to find the characteristics inherent to a optimization process based on metallic foams.

The first design problem involves a clamped, deep cantilever beam with a single load at the center of the long free edge (Figure 4.19). An adaptation of the density distribution with the goal of achieving a uniform apparent strain energy density was performed. The value of the nominal strain energy density $U_{F,eq}$ was chosen to be equal to the strain energy density

for the uniaxial yield stress of a foam volume having the maximum density $\rho_{F,\max}$. This choice was motivated by the assumption that the adaptation process would lead to a two-bar truss, which is considered the stiffness optimized reference solution for this problem. The concentrated load was chosen to lead to a reasonable thickness of the two trusses, which involved the calculation of the relationship between the magnitude of the load and the stress in the two trusses. The elastic modulus E_F was calculated as a function of the apparent density ρ_F according to Equation (4.49), that is, the unloading modulus S_{Rpo} was used in place of E_F . The input parameters for this and the following simulations are summarized in Table 4.2.

The resulting converged density distribution is depicted in Figure 4.19. The density adaptation process effectively produced the desired reference solution of a two-bar truss. The “bars” represent regions, where foam of the highest admissible density $\rho_{F,\max}$ was accumulated, while the rest of the design space is filled with foam of the lowest admissible density $\rho_{F,\min}$. The thickness of the bars is approximately 75% of the analytically predicted one. This ratio remains valid even if the minimum density is set to a value close to zero, and, consequently, the supporting effect of the regions of low density is vanishing. Examining the deformed configuration of the problem one finds that the “bars” undergo shear and, to a lesser extent, bending deformation. Therefore, they do not act like ideal truss members, but more like thick beams with finite shear and bending stiffnesses, the influence of which manifests itself in the slightly reduced thickness of the bars.

If the dimensions of the design space are changed such that the length of the feasible region becomes larger than the height then we arrive at a design problem commonly referred to as short cantilever beam. Figure 4.20 shows the density distribution after a strain energy driven adaptation simulation was performed for the clamped beam with a central concentrated load at the short free edge. For this example the nominal strain energy density was chosen to be the lowest one for which yielding can occur in regions of maximum density (as discussed in Section 4.5.3). The resulting density distribution is more complicated than the one presented for the deep cantilever beam problem, but it shares an important characteristic, namely the distinct partitioning of the design space into regions filled with material of low and of high density. This truss-like topology is typical for stiffness optimization problems. Again, the solution of the problem corresponds well with reference solutions [50]. A slight asymmetry is noticeable between the two outer diagonal members: the top flange is interrupted by a comparatively wide section of intermediate density. The inner truss-like members, which are arranged in the shape of an “X”, also exhibit this intermediate density. Upon closer observation, the grey areas in the contour density plot turn out to be a checkerboard-like arrangement of elements with maximum and minimum foam density. The cause for this pattern and the implications of this finding will be discussed in greater detail in the following section.

To document the convergence behavior of the algorithm a history plot of the averaged strain energy density is shown in Figure 4.21. The two curves in Figure 4.21 correspond to two different *initial* densities $\rho_{F,0}$, namely $\rho_{F,\min}$ and $\rho_{F,\max}$. At selected points in

Input Parameters for (Self) Adaptive Material			
No.	Input Parameter P_i	Value	Unit
1	Remodeling mode flag 0 ... no remodeling (lin. elast.) 1 ... strain energy based 2 ... eqv. stress based	1 or 2	
2	Absolute density of the bulk material ρ_S	"1.0"	g/cm ³
3	Minimum admissible foam density $\rho_{F,\min}$	0.2	g/cm ³
4	Maximum admissible foam density $\rho_{F,\max}$	0.8	g/cm ³
5	Poisson's number ν	0.3	
6	Young's modulus of the solid bulk material E_S (also: Young's modulus for linear elastic mode if $P_1 = 0$)	"1.0"	MPa
7	Young's modulus scaling factor α_E : ... unloading:	14000	
	... initial:	892.32	
8	Young's modulus scaling exponent β_E : ... unloading:	2.2000	
	... initial:	1.3212	
9	$P_1 = 1$... Equilibrium strain energy density $U_{S,\text{eq}} (= U_{F,\text{eq}})$	0.00256	MPa
	$P_1 = 2$... Yield stress of (fictitious) solid material σ_{yS}	"1.0"	MPa
10	$P_1 = 1$... Strain energy scaling factor α_U	1.0	
	$P_1 = 2$... Yield stress scaling factor α_σ	12.343	
11	$P_1 = 1$... Strain energy scaling exponent ($U_{S,\text{eq}} = U_{F,\text{eq}}$) β_U	0.0	
	$P_1 = 2$... Yield stress scaling exponent β_σ	1.8807	
12	$P_1 = 1$... Density weighting factor in Bone Remodeling [91] a_1	0.0	
	$P_1 = 2$... Shape parameter for self similar foam model ξ	1.5	
13	Necrosis limit for Bone Remodeling [91] (not implemented)	—	
14	Density reduction rate multiplier c_{dec}	0.06	$\frac{\text{g/cm}^3}{\Delta t}$
15	Density increase rate multiplier c_{inc}	0.06	$\frac{\text{g/cm}^3}{\Delta t}$
16	Maximum density reduction rate, Eq. (4.57): $\dot{\rho}_{\text{dec}}$	0.06	$\frac{\text{g/cm}^3}{\Delta t}$
17	Maximum density increase rate, Eq. (4.57): $\dot{\rho}_{\text{inc}}$	0.06	$\frac{\text{g/cm}^3}{\Delta t}$
18	Lazy zone half width for Bone Remodeling [91]	0.0	
19	Stimulus switch: 0 ... absolute stimulus s_w 1 ... relative stimulus	1	

Table 4.2: Input parameters for the ABAQUS User Material subroutine describing self-adaptive density remodeling.

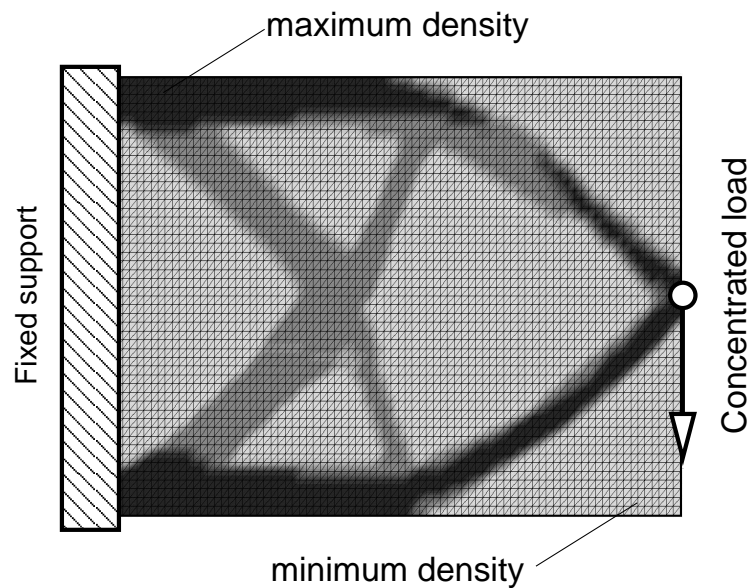


Figure 4.20: Short cantilever beam example.

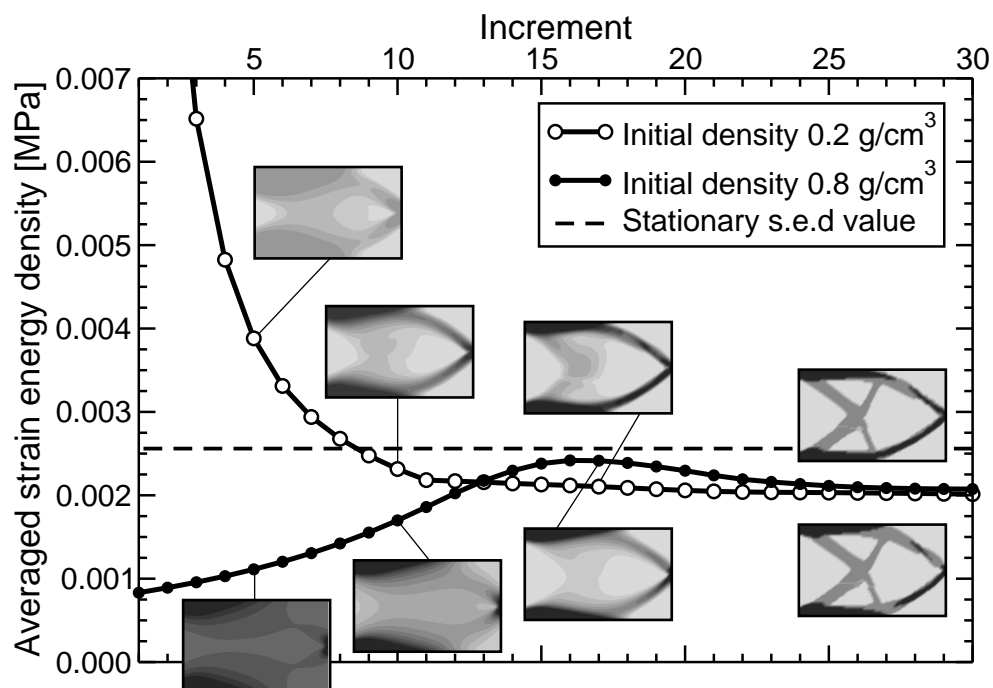


Figure 4.21: Evolution of the averaged strain energy density for different starting conditions in the short cantilever beam example.

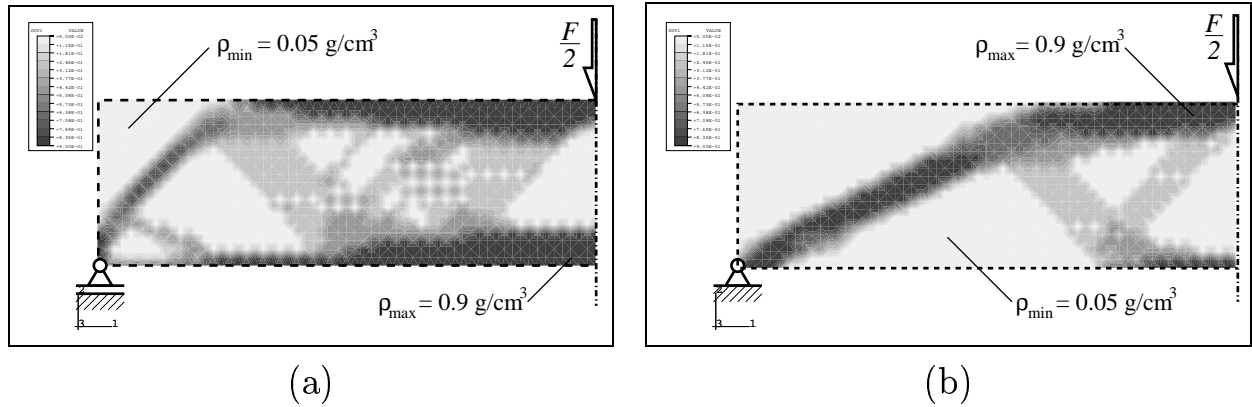


Figure 4.22: Density distributions of a stiffness optimized symmetric plane stress beam under a central load F with free (a) and fixed supports (b) [19].

the simulation history, contour plots of the apparent density are also given. Towards the right side of the diagram, the two converged configurations are depicted which are almost identical indicating that the solution is not sensitive to the choice of the initial density. The history of the averaged strain energy density for $\rho_{F,0} = \rho_{F,\min}$ shows steadily decreasing energy density values. This is favorable since minimizing compliance defined as the work done by a set of given loads against the displacements at mechanical equilibrium is equivalent to minimizing the total elastic energy of the structure [28]. Starting at the other end of the density range, $\rho_{F,0} = \rho_{F,\max}$, results in an initially stiffer structure in terms of absolute values. The mass-specific stiffness, however, is less favorable since a lot of surplus material is distributed in regions with low stress levels. In the course of the simulation this excessive material is degraded, and after passing through a maximum close to the nominal strain energy density the averaged strain energy density converges to the value obtained for the simulation starting at minimum initial density.

In [19] stiffness improved configurations were presented for the problem of a beam, which is supported on both ends and loaded by a vertical force along the symmetry plane (Figure 4.22). Free and fixed supports were considered and led to distinctly different density distributions. For the fixed supports in Figure 4.22(b) a clean planar framework appears in the course of the adaptation process, while in the case of free supports a sandwich-like structure with cover sheets of variable thickness and a core of intermediate density emerges, see Figure 4.22(a). Here, the kinematic boundary conditions govern the adaptation process leading to a sandwich topology for the bending dominated problem of horizontally movable supports.

Tackling true sandwich structures with the proposed method leads to similar configurations showing regions of intermediate, but uniform density. In Figure 4.23 a symmetric beam is covered by a shell consisting of bulk material ($E = E_s$). Furthermore, a distributed load

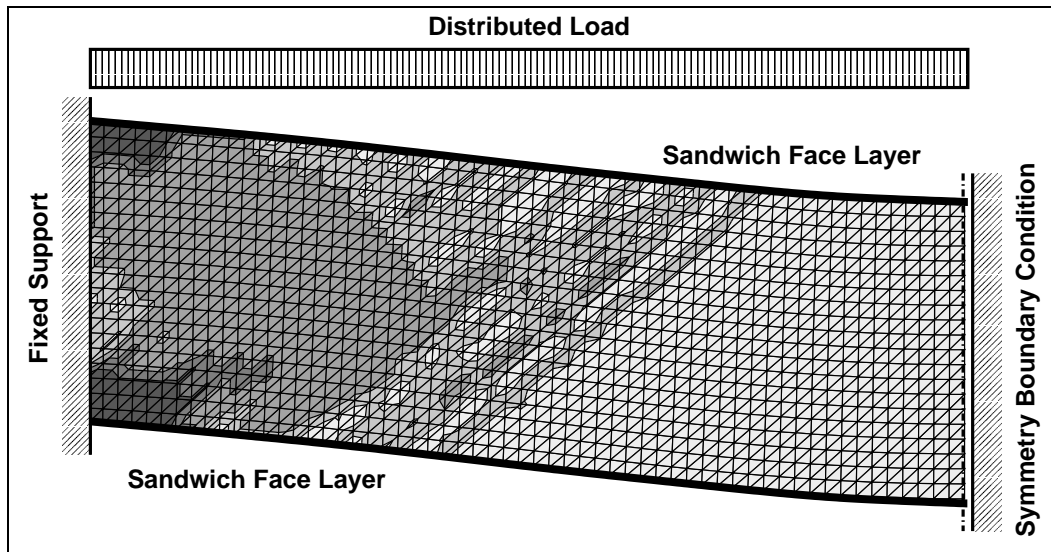


Figure 4.23: Sandwich beam with improved specific stiffness due to a functionally graded metallic foam core [114].

is assumed, and fixed supports are prescribed for this example. A stiffness optimization of this configuration was performed in [114]. The depicted solution showed better weight specific stiffness than an analytically optimized configuration which was restricted to having a density distribution that was variable only in thickness direction [114].

Structures of High Specific Strength

In this section some examples of structures with a high specific strength, obtained by following the axiom of fully stressed design, will be presented. Here, the local foam density is changed until the local equivalent stress matches the strength of the material as closely as possible, therefore avoiding the usage of dense material in regions of low stress levels. In the simulations under consideration the lower initial (tangent) modulus as defined in Equation (4.48) was used. This fact will be of great importance in the discussion of the results.

The beam that was presented earlier in Figure 4.22 is treated again with the density adaptation method, but now with the object of achieving a high specific strength instead of a high specific stiffness. The result is shown in Figure 4.24. The most obvious difference to the results presented earlier is the smoothness of the density distribution, with soft gradients instead of a stepwise change of the apparent density such as it predominates in the truss-like structures of high specific stiffness. Figure 4.24 shows how highly stressed regions such as the supports and the lower and upper regions in the middle of the beam accumulate the highest local foam densities, while nearly stress-free regions like the top

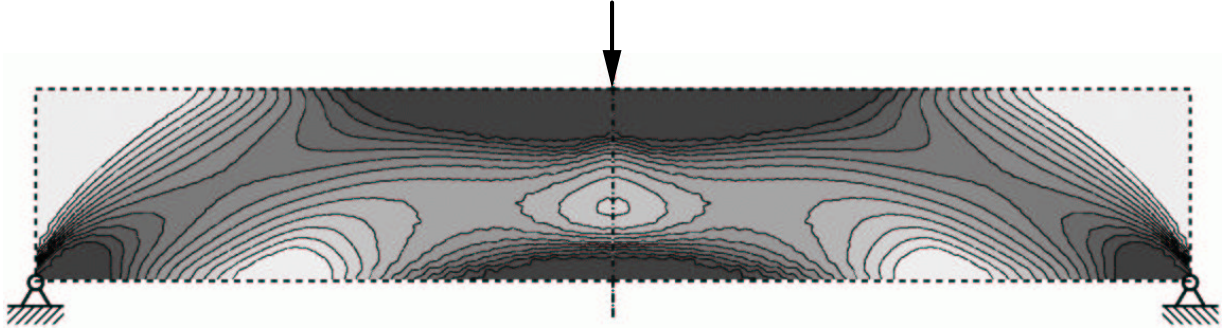


Figure 4.24: Strength optimized symmetric beam with fixed supports under a central load.

corners are filled with foam of minimal density. The whole layout reminds of an arched bridge with a bottom flange, both of which exhibit high foam density and are connected by a core of gradually changing intermediate density.

In [19] the effects of stress concentrations around a hole in the center of a square plate are investigated with respect to their influence on the strength optimization process. Figure 4.25 shows the density distributions obtained for a plate which was subjected to a distributed load q on the top surface. Here, a distinction was made between the von Mises equivalent stress and the equivalent stress for foam plasticity proposed by Deshpande and Fleck [24]. The shape parameter ξ for the yield criterion was chosen to be 1.5. To effect three-axial stress states plane strain conditions were prescribed.

The stress concentration around the hole gives rise to an accumulation of high density material, which forms two symmetric columns oriented in loading direction and bounded by the hole on the inner side and a region of low foam density on the outside. Another area reinforced by foam of high density developed close to that sector of the circular hole which is parallel to the loaded area. Here, the material accumulation is the result of a concentration of tensile stresses perpendicular to the loading direction. Figure 4.25 allows for a comparison of the two different yield criteria with respect to their effect on the evolved density configurations. The foam specific equivalent stress, Equation (4.52), proves to be more sensitive to the distributed load applied to the top of the model as it is indicated by the layer of increased density, which spans across the whole width of the top of the model, and the horizontal bands of denser material that reinforce the center region of the plate right above the hole.

To provide a situation, where triaxial stress states are even more dominant, a circular plate such as the one presented in Figure 4.26 was considered. The circumferential boundary of the plate was fixed, and a constant pressure p was applied to the top surface of the model. The magnitude of this pressure was set to 50% of the uniaxial yield strength of a foam of the highest admissible density: $p = \frac{1}{2}\sigma_{F,yld}(\rho_{F,max})$. To get an impression of the

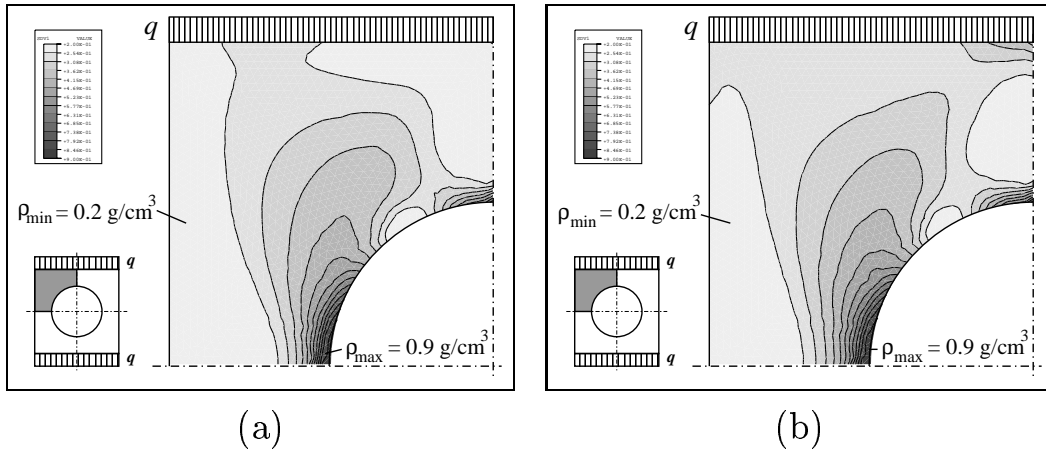


Figure 4.25: Strength optimized symmetric plane strain plate with a central hole under a distributed load q in the vertical direction. The optimized density distributions for J_2 -plasticity (a) and foam plasticity (b) are shown. Due to the symmetry of the problem only one quarter of the model is depicted [19].

influence of the shape parameter ξ in this case, ξ was varied from $\xi = 0.0$ (von Mises yield criterion) to $\xi = 3.0$ in steps of $\Delta\xi = 0.5$. The six resulting density distributions are shown as axisymmetric cross-sections in Figure 4.26.

For the uniform initial configuration, the stresses σ_{xx} in axial direction are equal to $-p$ at the top surface and decline with an almost constant gradient until they vanish at the bottom surface. The radial stresses σ_{rr} reach values slightly higher than $\pm 2p$ due to the circumferential bending moment in the middle of the plate and the reaction moment at the clamped lateral area. In the center of the plate the circumferential stresses $\sigma_{\theta\theta}$ are equal to the radial ones. With increasing radius they decline and change their sign to rise again to values of approximately $\pm p$ due to Poisson's effect. The shear stresses σ_{rx} are distributed parabolically in thickness direction and rise linearly from 0 in the center of the plate to values around p close to the lateral area, where the parabolic stress distribution is disturbed by the kinematic boundary conditions. How these initial stress distributions and the yield surface shape parameter ξ affect the final density distribution can be seen in Figure 4.26.

For von Mises plasticity ($\xi = 0$), the deviatoric components of the stress tensor are critical. Regions of high foam density can, accordingly, be found in regions of high shear stresses, as is observable from the dark regions in the density contour plot in Figure 4.26(a). The nearly hydrostatic stress conditions along the axis of the plate do not result in high von Mises equivalent stresses, and, therefore, only thin layers of high-density foam can be found at the top and at the bottom of the central part of the plate, where the bending stresses in radial and circumferential direction are the dominant components of the stress tensor. It is

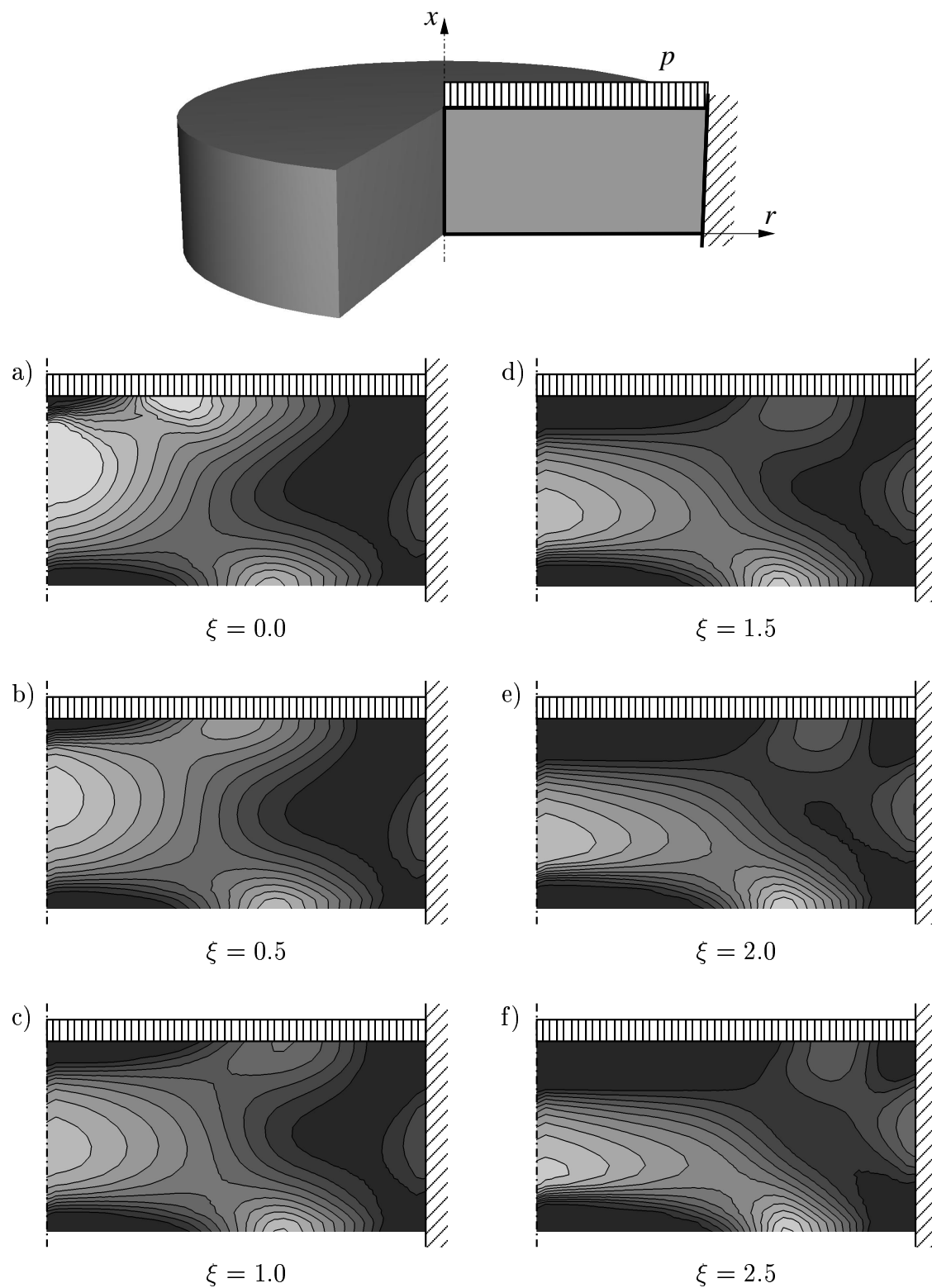


Figure 4.26: Optimized foam density distributions in the cross-section of a thick, circular plates under uniform pressure for different yield surface shape parameters ξ .

remarkable that the layer of high density is more extended at the bottom of the plate, where no surface pressure was applied. Here, a plane stress state with $\sigma_{rr} = \sigma_{\theta\theta} \approx 2p$ results in von Mises equivalent stresses that have a stronger deviatoric effect than the stress state at the loaded surface, where the pressure in the third direction induces a higher triaxiality and a lower von Mises equivalent stress. In the initial configurations the von Mises stress is lower than the yield stress of the highest foam density, but the increase of the foam density along the surface of the plate leads to stress redistribution and, ultimately, to the formation of layers with maximal density.

With increasing ξ , the influence of the hydrostatic part of the stress tensor becomes more pronounced. A closer investigation of the configuration for $\xi = 2.5$, Figure 4.26(e), reveals that in the regions with the initially highest shear stresses material with a less than maximum density suffices to prevent yielding. At the top surface, where the applied pressure acts in combination with the compressive bending stresses a massive layer of high foam density can be found. At the bottom of the plate the axial stresses are dropping to zero and the biaxial tensile bending stress state produces a foam layer that is only slightly more extended than the corresponding region in Figure 4.26(a). At the outer edges of the plate the radial and circumferential bending stress concentrations cause the density to reach the maximum admissible value.

4.5.5 Discussion

The proposed method makes innovative use of the capabilities of **ABAQUS** with regard to modeling the constitutive behavior of materials. It is intended to represent a material that adapts to mechanical loading. While certainly not an optimization in the strict mathematical sense, the self-adapting material subroutine can be used for a quick assessment of the potential effects of other, more refined topology optimization methods. Apart from the necessary restrictions on element types, this requires no change to the Finite Element model itself. The implementation as an **ABAQUS** UMAT makes pre- and post-processing steps within the iteration loop obsolete. This leads to a speed increase by a factor of up to 8 in comparison to comparable stand-alone remodeling and optimization programs (for example **FAROB** by Reiter [91]).

Two different optimization goals were pursued in the previous section: the maximization of the specific stiffness by achieving a uniform homogenized strain energy density and the maximization of the specific strength by means of a fully stressed design. Apart from the different definitions of the stimuli, the density dependent moduli of elasticity E_F was defined differently in the two cases. For the strength adaptation, the lower initial tangent modulus (4.48) was used, while for the stiffness adaptation the higher unloading modulus (4.49) was chosen to model the elastic behavior. This proved to be influential for the character of the density distributions, which is truss-like for stiff structures and continuous with smooth gradients in the case of structures of high specific strength.

Density distributions, which are of the same binary nature as the one presented as examples

of structures of high specific stiffness, are well known and investigated in the biomechanical research field of bone remodeling, which deals with the functional adaptation of living bone tissue to changing load conditions. In the case of bone remodeling the strain energy density $U_{B,S}$ in the trabecular solid bone material is assumed to be relevant for adaptation, that is, $S_B(t) = U_{B,S} - U_{B,S,stat}$ acts as a stimulus. The relation between the apparent and the bulk density values for bone are similar to Equation (4.45) and given by

$$U_{B,S} = \frac{U_B}{\rho_{B,rel}^{\beta_U}} \quad (4.58)$$

and

$$E_B = E_{B,S} \rho_{B,rel}^{\beta_E}. \quad (4.59)$$

Harrigan [48] and Reiter [91] state that in such cases the condition $\beta_E < \beta_U$ must be fulfilled to ensure the stability of remodeling solutions with smooth density gradients. Stable density distributions are insensitive to perturbations of the local density, meaning that these perturbations tend to decay with time, whereas perturbations of instable configurations cause the local density to diverge to either minimal or maximal density values. In the case of an initially non-uniform stress field this means that the Finite Element solutions tend towards the formation of a framework of plane/space trusses on the global level, and to the local appearance of “checkerboard” density patterns, wherein adjacent elements alternate between the maximum and minimum density.

If the condition $\beta_E < \beta_U$ is applied to the problem of stiffness improvement of foam structures as treated here, because of $\beta_U = 0$ (the homogenized strain energy density is used instead of the bulk value) and $\beta_E > 0$, this stability condition is violated as in many similar situations in topology optimization.

The density configurations in Figures 4.24 to 4.26, which exhibit continuous density distributions with comparably shallow gradients, show that smooth and stable density distributions were obtained for a yield stress related stimulus and the low β_E from Equation (4.48). To derive a stability condition like $\beta_E < \beta_U$ by dimensional analysis we first note that $U \propto \sigma^2/E$. Substituting the yield stress $\sigma_{F,yld}$ for σ and the effective Young’s modulus E_F for E we arrive at the relationship $U \propto \sigma_{F,yld}^2/E_F$. Both arguments on the right hand side of this proportionality equation depend on the relative foam density $\rho_{F,rel}$. Expanding both terms and introducing the respective scaling exponents β we obtain

$$U \propto \frac{(\rho_{F,rel})^{2\beta_\sigma}}{(\rho_{F,rel})^{\beta_E}} = (\rho_{F,rel})^{2\beta_\sigma - \beta_E} \quad (4.60)$$

Substituting $(2\beta_\sigma - \beta_E)$ for β_U in the stability condition $\beta_U > \beta_E$ gives $2\beta_\sigma - \beta_E > \beta_E$ and, hence, $\beta_\sigma > \beta_E$ as the stability condition for the fully stressed design adaptation method. This condition is indeed fulfilled for the considered exponents $\beta_\sigma = 1.8807$ and $\beta_E = 1.3213$. Although Equation (4.60) is just a coarse approximation, the above consideration indicates that the strength optimization leads to stable and smooth solutions for the chosen parameters.

For cases of structures with high specific stiffness distributed load and boundary conditions had a smoothening effect on the density distribution despite the prevalence of the described instability issues on the local level (compare Figure 4.23). Metallic foams seem to be more suited for the construction of stiff structures under such conditions than for design cases dominated by concentrated loads and point-like supports.

It should be mentioned that in practice ideal conditions like uniform strain energy density or full exploitation of the load bearing capacity can hardly be achieved. This is a consequence of the constraints that are put on the density range, with material prevented to vanish completely at one end of the density range and material, which is over-stressed, but has already reached the highest admissible density value at the other end. A distinct lump of high-density foam indicates that the load-bearing capacity of the design space is exceeded and inserts of solid material are necessary to distribute the applied load.

4.5.6 Summary

An algorithm for an optimization of distributions of the apparent density in structures made of functionally graded cellular materials was proposed. This algorithm, which can be described as a self-adapting material, was implemented into an ABAQUS User Material subroutine (UMAT). This implies that it acts on the integration point level, where it converges locally to a stationary condition for which a user defined state variable reaches a nominal value. This value is in most cases related to the local homogenized mass density by a power law. The exponent of this power law governs the numerical stability of the solutions with respect to small variations in the local density. This indicates that the character of the solutions is strongly influenced by the actual elastic properties and their density dependence. Choosing an appropriate adaptation criterion can provide solutions that represent foam structures of high specific stiffness or strength.

It was shown that strength optimizations with material parameters, that are typical for metallic foams, lead to continuous solutions showing density gradients, which may indeed be realizable by suitable processing technologies (compare Figure 4.24). Local stress concentrations like loading points or supports may have to be reinforced with solid inserts in practical applications. Attempts to optimize the specific stiffness of foam structures resulted in the formation of discrete structures such as frameworks of struts. This indicates that cellular metals may not be ideal for stiffness-optimized structures, at least in the presence of concentrated loads. For sandwich beams with foam cores as studied by Vonach et al. [114] smooth mesoscopic density distributions were obtained for stiffness optimized configurations under distributed loads.

As the processing technologies for foamed metals are improved, and the production of foamed structures with non-uniform density becomes feasible, studies like the one presented here may give useful information about potential improvements for the density distributions in such structures. Future developments may incorporate the optimization of the shape of the foam filled region, which was tied to a rigid design space in the present study, and the

simultaneous optimization of the thickness of a shell of solid material, which encloses the foam core to form integrated, sandwich-like components as displayed in Figure 1.1 (right).

Chapter 5

Conclusions

It is generally difficult to decide on which length scale the simulation of the thermo-mechanical behavior of metallic foams has to be performed to achieve optimum results and reliable predictions for the real performance of the material. One of the potential applications of metallic foam, namely sandwich cores, may serve to illustrate this difficulty: in thickness direction sandwich cores possess a limited number of cell layers, suggesting a microstructural simulation approach that fully resolves the discrete microstructure of the material. On the other hand, the in-plane dimensions of the core are typically much larger than the core thickness and, hence, the average cell size, thus favoring a macroscopic simulation approach considering that it is infeasible to model microstructures containing thousands of individual foam cells within present computational capabilities. These macroscopic approaches describe the discrete microstructure via a homogeneous reference material, the effective behavior of which closely approaches that of the original microstructure. In many cases such macroscopic descriptions can give excellent approximations of the behavior of the cellular material. They have to be adapted to capture the essential micromechanical features while keeping the computational cost for modeling component-size metallic foam structures within reasonable bounds.

To identify the necessary abstractions on the macromechanical level and the governing mechanisms on the micromechanical level, it is advantageous to perform the simulation of metallic foams on both levels and to transfer results from one level to the other. The present thesis attempts to cover different strategies for modeling the mechanical behavior of cellular metals. On the microstructural level, several methods for advanced pre- and post-processing of 2D and 3D models were proposed to capture the influence and the interaction of imperfections and irregularities in ways that promote a deeper understanding of foam micromechanics than existing approaches. With crash-protection applications in mind, a special emphasis was put on predictions of the micromechanical behavior for large compressive strains. By applying homogenization methods the results were expressed in terms of effective/overall quantities and, therefore, made accessible for comparison to macromechanical results. Macromechanical characteristics like oscillations in the plateau region

of the overall stress–strain relationships were correlated to micromechanical processes. In some way, results from experimental results drive the development of more sophisticated microstructural models, because a result that can be *explained* weighs more heavily than plain data; for cellular materials, investigations on the microstructural level are the richest source of qualitative information.

On the other hand, not all microstructurally based mechanical phenomena have to be considered for simulating the mechanical behavior of a metallic foam structure successfully. To demonstrate this, the predictive quality of two constitutive laws was evaluated for a standard impact protection situation. The requirements for constitutive laws are tied to their intended application, and in the case of large objects impacting thin foam layers these requirements were shown to be modest.

Even easier to deal with are problems where inelastic behavior can, in principle, be excluded by appropriate dimensioning of the metallic foam components. In these cases, metallic foams can be modeled with linear elastic constitutive theories, which, for the simplest case of isotropic elasticity, require only two parameters for the calibration of the material data. On the basis of such approaches, it is possible to exploit the scalability of the elastic properties by a controlled variation of the apparent density for designing structures with optimized distributions of the local apparent density. A method suitable for the prediction of such weight-efficient density distributions was presented and parallels to the self-adaptation capability of living cellular tissue (bone) were discussed.

The scope of the present thesis demonstrates that many different strategies are applicable for modeling the mechanical behavior of cellular metals. In view of the engineering potential of metallic foams and the research challenges they pose, it appears safe to say that studies of these materials on all length scales discussed above will remain a fertile field for future research. The immediate challenge on the micromechanical level will be the introduction of larger, more representative 3D models of the cellular microstructure. On the macromechanical level, the implementation of robust and reliable algorithms for the modeling of damage and fracture has great potential for improving the predictive quality of simulations involving metallic foam components.

Bibliography

- [1] Ableidinger, A.: *Some Aspects of the Fracture Behavior of Metal Foams*. Diploma thesis, Vienna University of Technology, Vienna. 2000.
- [2] Adachi, T., Tsubota, K., Tomita, Y., and Hollister, S. J.: Trabecular surface remodeling simulation for cancellous bone using microstructural voxel finite element models. *J. Biomech. Eng. ASME*, **123**:403–409. 2001.
- [3] Albuquerque, J. M., Fátima Vaz, M., and Fortes, M. A.: Effect of missing walls on the compression behaviour of honeycombs. *Scr. Mater.*, **41**:167–174. 1999.
- [4] Andrews, E., Sanders, W., and Gibson, L. J.: Compressive and tensile behaviour of aluminum foams. *Mat. Sci. Eng.*, **A270**:113–124. 1999.
- [5] Andrews, E. W., Gibson, L. J., and Ashby, M. F.: The creep of cellular solids. *Acta Mater.*, **47**(10):2853–2863. 1999.
- [6] Ashby, M. F., Evans, A. G., Hutchinson, J. W., and Fleck, N. A.: Metal foams: a design guide. Tech. rep., Engineering Department, University of Cambridge, Cambridge, UK. Version 4. August 1998.
- [7] Ashby, M. F., Seymour, C. J., and Cebon, D.: A database of metal foams and honeycombs. In: Banhart, J., ed., *Metallschäume*, pp. 199–216. Verlag MIT, Bremen. 1997.
- [8] Bathe, K.-J.: *Finite Element Procedures*. Prentice-Hall, Upper Saddle River, NJ. 1996.
- [9] Chen, C.: Manual for a UMAT user subroutine. Technical Report CUED/C-MICROMECH/TR.4, Dept. of Engineering, Cambridge University, Cambridge. 1998.
- [10] Chen, C. and Lu, T. J.: A phenomenological framework of constitutive modelling for incompressible and compressible elasto-plastic solids. *Int. J. Sol. Struct.*, **37**:7769–7786. 2000.
- [11] Chen, C., Lu, T. J., and Fleck, N. A.: Effect of imperfections on the yielding of two-dimensional foams. *J. Mech. Phys. Solids*, **47**:2235–2272. 1999.

- [12] Chen, C., Lu, T. J., and Fleck, N. A.: Effect of inclusions and holes on the stiffness and strength of honeycombs. *Int. J. Mech. Sci.*, **43**:487–504. 2001.
- [13] Chen, J. Y., Huang, Y., and Ortiz, M.: Micromechanical fracture analysis of cellular materials: a strain gradient model. *J. Mech. Phys. Solids*, **46**:789–828. 1998.
- [14] Christensen, R. M.: Mechanics of cellular and other low-density materials. *Int. J. Sol. Struct.*, **37**:93–104. 2000.
- [15] Crisfield, M. A.: *Non-Linear Finite Element Analysis of Solids and Structures*, vol. 2. John Wiley, Chichester, UK. 1997.
- [16] Dannemann, K. A. and Lankford, J.: High strain rate compression of closed-cell aluminium foams. *Mat. Sci. Eng.*, **A293**:157–164. 2000.
- [17] Daxner, T., Böhm, H. J., and Rammerstorfer, F. G.: Influence of micro- and meso-topological properties on the crash-worthiness of aluminium foams. In: Banhart, J., Ashby, M. F., and Fleck, N. A., eds., *Metal Foams and Porous Metal Structures*, pp. 283–288. Verlag MIT, Bremen. 1999.
- [18] Daxner, T., Böhm, H. J., and Rammerstorfer, F. G.: Mesoscopic simulation of inhomogeneous metallic foams with respect to energy absorption. *Comp. Mat. Sci.*, **16**:61–69. 1999.
- [19] Daxner, T., Böhm, H. J., and Rammerstorfer, F. G.: Adaptation of density distributions for optimising aluminium foam structures. *Mater. Sci. Technol.*, **16**:935–939. 2000.
- [20] Daxner, T., Denzer, R., Böhm, H. J., Rammerstorfer, F. G., and Maier, M.: Simulation des elasto-plastischen Verhaltens von Metallschaum mit Hilfe von 2D und 3D Einheitszellen-Modellen. *Mater.-wiss. u. Werkst.-techn.*, **31**:447–450. 2000.
- [21] Degischer, H. P., Galovsky, U., Gradinger, R., and Kretz, R.: Über mechanische Eigenschaften von Aluminiumschäumen. In: Banhart, J., ed., *Metallschäume*, pp. 79–90. Verlag MIT, Bremen. 1997.
- [22] Denzer, R. and Maier, M.: Numerical simulation of the micromechanical energy absorbing mechanism of aluminium foams. In: *Proc. ECCM 99*. Munich. 1999.
- [23] Deshpande, V. S. and Fleck, N. A.: High strain rate compressive behaviour of aluminium alloy foams. *Int. J. Impact. Eng.*, **24**:277–298. 2000.
- [24] Deshpande, V. S. and Fleck, N. A.: Isotropic constitutive models for metallic foams. *J. Mech. Phys. Solids*, **48**:1253–1283. 2000.
- [25] Ehlers, W. and Droste, A.: A continuum model for highly porous aluminium foam. *Techn. Mech.*, **19**(4):341–350. 1999.

- [26] Ehlers, W. and Droste, A.: FE simulation of metal foams based on the macroscopic approach of the Theory of Porous Media. In: Banhart, J., Ashby, M. F., and Fleck, N. A., eds., *Metal Foams and Porous Metal Structures*, pp. 299–302. Verlag MIT, Bremen. 1999.
- [27] Ehlers, W., Müllerschön, H., and Klar, O.: On the behaviour of aluminium foams under uniaxial and multiaxial loading. In: Banhart, J., Ashby, M. F., and Fleck, N. A., eds., *Metal Foams and Porous Metal Structures*, pp. 255–262. Verlag MIT, Bremen. 1999.
- [28] Eschenauer, H. A. and Olhoff, N.: Topology optimization of continuum structures. *Appl. Mech. Rev.*, **54**(4):331–390. 2001.
- [29] Evans, A. G., Hutchinson, J. W., and Ashby, M. F.: Multifunctionality of cellular metal systems. *Prog. Mat. Sci.*, **43**:171–221. 1999.
- [30] Evans, A. G., Hutchinson, J. W., Fleck, N. A., Ashby, M. F., and Wadley, H. N. G.: The topological design of multifunctional cellular metals. *Prog. Mat. Sci.*, **46**:309–327. 2001.
- [31] Gibson, L. J.: Modelling the mechanical behavior of cellular materials. *Mater. Sci. Engng.*, **A110**:1–36. 1989.
- [32] Gibson, L. J., Ashby, M., Zhang, J., and Triantafyllou, T. C.: Failure surfaces for cellular materials under multiaxial loads — I. Modelling. *Int. J. Mech. Sci.*, **31**(9):635–663. 1989.
- [33] Gibson, L. J. and Ashby, M. F.: *Cellular Solids: Structure and Properties*. Pergamon Press, Oxford, UK. 1988.
- [34] Gibson, L. J. and Ashby, M. F.: *Cellular Solids: Structure and Properties*. Cambridge University Press, Cambridge, New York, Melbourne, 2nd edn. 1997.
- [35] Gioux, G., McCormack, T. M., and Gibson, L. J.: Failure of aluminum foams under multiaxial loads. *Int. J. Mech. Sci.*, **42**:1097–1117. 2000.
- [36] Gradinger, R. C.: *Das mechanische Verhalten von Aluminiumschaum bei Druck- und Crushbelastung — Experimente und numerische Simulation*. Diploma thesis, Vienna University of Technology, Vienna. Sep. 1997.
- [37] Gradinger, R. C., Kretz, R., Degischer, H. P., and Rammerstorfer, F. G.: Deformation behaviour of aluminium foam under compressive loading. In: *JUNIOR-EUROMAT, 26-30 August 1996*. Lausanne, Switzerland. 1996.
- [38] Gradinger, R. C. and Rammerstorfer, F. G.: On the influence of meso-inhomogeneities on the crush worthiness of metal foams. *Acta Mater.*, **47**(1):143–148. 1999.

- [39] Grenestedt, J. L.: Influence of wavy imperfections in cell walls on elastic stiffness of cellular solids. *J. Mech. Phys. Solids*, **46**(1):29–50. 1998.
- [40] Grenestedt, J. L.: Effective elastic behavior of some models for ‘perfect’ cellular solids. *Int. J. Sol. Struct.*, **36**:1471–1501. 1999.
- [41] Grenestedt, J. L. and Bassinet, F.: Influence of cell wall thickness variations on elastic stiffness of closed cell cellular solids. *Int. J. Mech. Sci.*, **42**:1327–1338. 2000.
- [42] Grenestedt, J. L. and Tanaka, K.: Influence of cell shape variations on elastic stiffness of closed cell cellular solids. *Scr. Mater.*, **40**:71–77. 1999.
- [43] Guo, X. E. and Gibson, L. J.: Behavior of intact and damaged honeycombs: A finite element study. *Int. J. Mech. Sci.*, **41**:85–105. 1999.
- [44] Hall, I. W., Guden, M., and Yu, C.-J.: Crushing of aluminum closed cell foams: density and strain rate effects. *Scr. Mater.*, **43**(6):515–521. 2000.
- [45] Hallquist, J. O.: *LS DYNA Theoretical Manual*. Livermore Software Technology Corporation, Livermore, CA. 1998.
- [46] Hanssen, A. G.: *Structural crashworthiness of aluminium foam-based components*. Ph.D. thesis, Norges Tekniske Høgskole, Trondheim, Norway. June 2000.
- [47] Hanssen, A. G., Hopperstad, O. S., Langseth, M., and Ilstad, H.: Validation of constitutive models applicable to aluminium foams. *Int. J. Mech. Sci.*, **44**(2):359–406. 2002.
- [48] Harrigan, T. P. and Hamilton, J. J.: Necessary and sufficient conditions for global stability and uniqueness in finite element simulations of adaptive bone remodeling. *Int. J. Sol. Struct.*, **31**(1):97–107. 1994.
- [49] Hashin, Z.: Analysis of composite materials — a survey. *J. Appl. Mech.*, **50**:481–505. 1983.
- [50] Hassani, B. and Hinton, E.: *Homogenization and Structural Topology Optimization*. Springer, London, UK. 1999.
- [51] HKS: *ABAQUS/Standard Theory Manual, Version 5.8*. Hibitt, Karlsson & Sorensen, Inc., Pawtucket, Rhode Island. 1998.
- [52] HKS: *ABAQUS/Standard User’s Manual, Version 5.8*. Hibitt, Karlsson & Sorensen, Inc., Pawtucket, Rhode Island. 1998.
- [53] HKS: *ABAQUS/Standard Theory Manual, Version 6.2*. Hibitt, Karlsson & Sorensen, Inc., Pawtucket, Rhode Island. 2001.

- [54] Hollister, S. J., Brennan, J. M., and Kikuchi, N.: A homogenization sampling procedure for calculating trabecular bone effective stiffness and tissue level stress. *J. Biomech.*, **27**:433–444. 1994.
- [55] Hughes, T.: *The Finite Element Method*. Prentice-Hall, Englewood Cliffs, NJ. 1987.
- [56] Hutchinson, J. W. and He, M. Y.: Buckling of cylindrical sandwich shells with metal foam cores. *Int. J. Sol. Struct.*, **37**:6777–6794. 2000.
- [57] Jacobs, C. R., Levenston, M. E., Beaupré, G. S., Simo, J. C., and Carter, D. R.: Numerical instabilities in bone remodeling simulations: The advantages of a node based finite element approach. *J. Biomech.*, **28**(4):449–459. 1995.
- [58] Krach, W., Daxner, T., and Rammerstorfer, F.: Metallic foams vs. human bones - a comparison of structure and mechanical properties. *Proceedings Materials Week 2000*, Paper 1160, URL: <http://www.materialsweek.org/proceedings/index.htm>. 2000.
- [59] Kraynik, A. M., Nielsen, M. K., Reinelt, D. A., and Warren, W. E.: Foam micromechanics. structure and rheology of foams, emulsions, and cellular solids. In: Sadoc, J. F. and Rivier, N., eds., *Foams and Emulsions*. Kluwer Academic Publishers, Dordrecht. 1999.
- [60] Kretz, R. and Götzinger, B.: Energy absorbing behaviour of aluminium foams: head impact test on an A-pillar of a passenger car. In: Banhart, J., Ashby, M. F., and Fleck, N. A., eds., *Cellular Metals and Metal Foaming Technology*, pp. 433–444. Verlag MIT, Bremen. 2001.
- [61] Kriszt, B., Foroughi, B., Faure, K., and Degischer, H. P.: Deformation behaviour of aluminium foam under uniaxial compression (a case study). In: Banhart, J., Ashby, M. F., and Fleck, N. A., eds., *Metal Foams and Porous Metal Structures*, pp. 241–246. Verlag MIT, Bremen. 1999.
- [62] Kummer, B. K. F.: Biomechanics of bone: Mechanical properties, functional structure, functional adaptation. In: Fung, Y. C., Perrone, N., and Angliker, M., eds., *Biomechanics: Its Foundation and Objectives*, pp. 237–271. Prentice Hall, Englewood Cliffs, NJ. 1972.
- [63] Lu, T. J. and Chen, C.: Thermal transport and fire retardance properties of cellular aluminium alloys. *Acta Mater.*, **47**(5):1469–1485. 1999.
- [64] Lubliner, J.: *Plasticity Theory*. Macmillan Publishing Company, New York. 1990.
- [65] Maire, E., Wattebled, F., Buffière, J. Y., and Peix, G.: Deformation of a metallic foam studied by x-ray computed tomography and finite element calculations. In: Clyne, T. W. and Simancik, F., eds., *Metal Matrix Composites and Metallic Foams*, pp. 68–73. Wiley–VCH, Weinheim. 2000.

- [66] Mang, H. and Hofstetter, G.: *Festigkeitslehre*. Springer-Verlag, Vienna. 2000.
- [67] Markaki, A. E. and Clyne, T. W.: The effect of cell wall microstructure on the deformation and fracture of aluminium-based foams. *Acta Mater.*, **49**:1677–1686. 2001.
- [68] McCullough, K. Y. G., Fleck, N. A., and Ashby, M. F.: Uniaxial stress-strain behaviour of aluminium alloy foams. *Acta Mater.*, **47**(8):2323–2330. 1999.
- [69] Meguid, S. A., Cheon, S. S., and El-Abbasi, N.: Fe modelling of deformation localization in metallic foams. *Finite Elements in Analysis and Design*, **38**:631–643. 2002.
- [70] Miller, R. E.: A continuum plasticity model for the constitutive and indentation behaviour of foamed metals. *Int. J. Mech. Sci.*, **42**:729–754. 2000.
- [71] Mills, N. J. and Zhu, H. X.: The high strain compression of closed-cell polymer foams. *J. Mech. Phys. Solids*, **47**:669–695. 1999.
- [72] Motz, C. and Pippan, R.: Deformation behaviour of closed-cell aluminium foams in tension. *Acta Mater.*, **49**:2463–2470. 2001.
- [73] Mukai, T., Kanahashi, H., Higashi, K., Yamada, Y., Shimojima, K., Mabuchi, M., Miyoshi, T., and Nieh, T.: Energy absorption of light-weight metallic foams under dynamic loading. In: Banhart, J., Ashby, M. F., and Fleck, N. A., eds., *Metal Foams and Porous Metal Structures*, pp. 353–358. Verlag MIT, Bremen. 1999.
- [74] Mukai, T., Kanahashi, H., Miyoshi, T., Mabuchi, M., Nieh, T., and Higashi, K.: Experimental study of energy absorption in a closed-celled aluminum foam under dynamic loading. *Scr. Mater.*, **40**(8):921–927. 1999.
- [75] Müller, R. and Rügsegger, P.: Three-dimensional finite element modelling of non-invasively assessed trabecular bone structures. *J. Med. Engng. Phys.*, **17**:126–133. 1995.
- [76] National Highway Traffic Safety Organisation: Occupant protection in interior impact. Federal Motor Vehicle Safety Standard (FMVSS) 49 CFR §571.201, NHTSA, Department of Transportation. 1997.
- [77] Nye, J. F.: *Physical Properties of Crystals*. Oxford University Press, Oxford, UK. 1985.
- [78] Olurin, O. B., Fleck, N. A., and Ashby, M. F.: Deformation and fracture of aluminium foams. *Mat. Sci. Eng.*, **A291**:136–146. 2000.
- [79] Papka, S. D. and Kyriakides, S.: In-plane compressive response and crushing of honeycomb. *J. Mech. Phys. Solids*, **42**(10):1499–1532. 1994.

- [80] Papka, S. D. and Kyriakides, S.: Experiments and full-scale numerical simulations of in-plane crushing of a honeycomb. *Acta Mater.*, **46**(8):2765–2776. 1998.
- [81] Papka, S. D. and Kyriakides, S.: In-plane biaxial crushing of honeycombs–Part I: Experiments. *Int. J. Sol. Struct.*, **36**:4367–4396. 1999.
- [82] Papka, S. D. and Kyriakides, S.: In-plane biaxial crushing of honeycombs–Part II: Analysis. *Int. J. Sol. Struct.*, **36**:4397–4423. 1999.
- [83] Paul, A. and Ramamurty, U.: Strain rate sensitivity of a closed-cell aluminum foam. *Mat. Sci. Eng.*, **A281**:1–7. 2000.
- [84] Pedersen, P.: On thickness and orientational design of orthotropic materials. *Struct. Opt.*, **3**:69–78. 1991.
- [85] Pettermann, H. E., Reiter, T. J., and Rammerstorfer, F. G.: Computational simulation of internal bone remodeling. *Arch. Comp. Meth. Eng.*, **4**:295–323. 1997.
- [86] Ponte Castañeda, P. and Suquet, P.: Nonlinear composites. In: van der Giessen, E. and Wu, T. Y., eds., *Advances in Applied Mechanics 34*. Academic Press, New York. 1998.
- [87] Prakash, O., Bichebois, P., Bréchet, Y., Louchet, F., and Embury, J. D.: A note on the deformation behavior of two dimensional model cellular structures. *Phil. Mag.*, **A73**:739–751. 1996.
- [88] Rammerstorfer, F. G. and Böhm, H. J.: Finite element methods in micromechanics of composites and foam materials. In: Topping, B. H. V., ed., *Computational Mechanics for the Twenty-First Century*, pp. 145–164. Saxe-Coburg Publications, Edinburgh. 2000.
- [89] Rammerstorfer, F. G. and Böhm, H. J.: Composite engineering. Lecture Notes, Institute of Lightweight Structures and Aerospace Engineering, Vienna University of Technology. 2002.
- [90] Reid, S. R. and Peng, C.: Dynamic uniaxial crushing of wood. *Int. J. Impact. Eng.*, **19**(5–6):531–570. 1997.
- [91] Reiter, T.: *Functional Adaptation of Bone and Application in Optimal Structural Design*, vol. 145 of *VDI Fortschrittsberichte, Reihe 17*. VDI Verlag, Düsseldorf. 1996.
- [92] Reiter, T. and Rammerstorfer, F. G.: Simulation of natural adaptation of bone material and application in optimum composite design. In: Pedersen, P., ed., *Optimal Design with Advanced Materials*, pp. 25–36. Elsevier, Amsterdam. 1993.

- [93] Roberts, A. P. and Garboczi, E. J.: Elastic moduli of model random three-dimensional closed-cell cellular solids. *Acta Mater.*, **49**:189–197. 2001.
- [94] Santosa, S. P. and Wierzbicki, T.: On the modeling of crush behavior of a closed-cell aluminum foam structure. *J. Mech. Phys. Solids*, **46**(4):645–669. 1998.
- [95] Schaffner, G., Guo, X. D. E., Silva, M. J., and Gibson, L. J.: Modelling fatigue damage accumulations in two-dimensional voronoi honeycombs. *Int. J. Mech. Sci.*, **42**:645–656. 2000.
- [96] Schluppkotten, J.: *Ein Beitrag zur methodischen Integration von neuen Werkstoffen in die Fahrzeugcrashberechnung*, vol. 16 of *IVW-Schriftenreihe*. Institut für Verbundwerkstoffe GmbH, Kaiserslautern. 2001.
- [97] Schluppkotten, J., Paßmann, R., Cheng, C., and Maier, M.: Erfahrungen mit ABAQUS/Explicit bei der Modellierung des crashrelevanten Verhaltens von Polymerschaumstoffen. In: *Proc. ABAQUS User Meeting, Essen (D), October 1, 1999*. Universität GH-Essen. 1999.
- [98] Schreyer, H. L., Zuo, Q. H., and Maji, A. K.: An anisotropic plasticity model for foams and honeycomb. *J. Eng. Mech. ASCE*, **120**(9):1913–1930. 1994.
- [99] Seeliger, H.-W.: *Entwicklung und Programmierung eines Materialmodells für elasto-plastische Metallschäume*. Ph.D. thesis, University of Bremen. 2000.
- [100] Seitzberger, M., Rammerstorfer, F. G., Gradinger, R., Degischer, H.-P., Blaimschein, M., and Walch, C.: Experimental studies on the quasi-static axial crushing of steel columns filled with aluminium foam. *Int. J. Sol. Struct.*, **37**:4125–4147. 2000.
- [101] Shaw, M. C. and Sata, T.: The plastic behavior of cellular materials. *Int. J. Mech. Sci.*, **112**:469–478. 1966.
- [102] Shim, V. P. W., Tay, B. Y., and Stronge, W. J.: Dynamic crushing of strain-softening cellular structures - a one-dimensional analysis. *J. Eng. Mat. Tech. ASME*, **112**:398–405. 1990.
- [103] Shulmeister, V., Van der Burg, M. W. D., Van der Giessen, E., and Marissen, R.: A numerical study of large deformations of low-density elastomeric open-cell foams. *Mech. Mat.*, **30**:125–140. 1998.
- [104] Silva, M. J. and Gibson, L. J.: The effects of non-periodic microstructure and defects on the compressive strength of two-dimensional cellular solids. *Int. J. Mech. Sci.*, **39**(5):549–563. 1997.
- [105] Silva, M. J., Hayes, W. C., and Gibson, L. J.: The effects of non-periodic microstructure on the elastic properties of two-dimensional cellular solids. *Int. J. Mech. Sci.*, **37**(11):1161–1177. 1995.

- [106] Simone, A. E. and Gibson, L. J.: Effects of solid distribution on the stiffness and strength of metallic foams. *Acta Mater.*, **46**(6):2139–2150. 1998.
- [107] Simone, A. E. and Gibson, L. J.: The effects of cell face curvature and corrugations on the stiffness and strength of metallic foams. *Acta Mater.*, **46**(6):3929–3935. 1998.
- [108] Smit, R. J. M., Brekelmans, W., and Meijer, H.: Prediction of the mechanical behavior of non-linear heterogeneous systems by multi-level finite element modeling. *Comput. Methods Appl. Mech. Eng.*, **155**:181–192. 1998.
- [109] Sugimura, Y., Meyer, J., He, M. Y., Bart-Smith, H., Grenestedt, J., and Evans, A. G.: On the mechanical performance of closed cell Al alloy foams. *Acta Mater.*, **45**(12):5245–5259. 1997.
- [110] Suquet, P. M.: Elements of homogenization for inelastic solid mechanics. In: Sanchez-Palencia, E. and Zaoui, A., eds., *Homogenization Techniques in Composite Media*, pp. 194–278. Springer-Verlag, Berlin. 1987.
- [111] Thornton, P. H. and Magee, C. L.: The deformation of aluminum foams. *Metall. Trans. A*, **6A**:1253–1263. 1975.
- [112] Torquato, S., Gibiansky, L. V., Silva, M. J., and Gibson, L. J.: Effective mechanical and transport properties of cellular solids. *Int. J. Mech. Sci.*, **40**:71–82. 1998.
- [113] Triantafillou, T. C., Zhang, J., Shercliff, T. L., Gibson, L. J., and Ashby, M. F.: Failure surfaces for cellular materials under multiaxial loads — II. Comparison of models with experiment. *Int. J. Mech. Sci.*, **31**(9):665–678. 1989.
- [114] Vonach, W. K., Daxner, T., and Rammerstorfer, F. G.: In-situ sandwiches with optimized metal foam cores. In: Meyer-Piening, H. R. and Zenkert, D., eds., *Sandwich Construction 5*, pp. 291–300. EMAS, Solihull, UK. 2000.
- [115] Warren, W. E. and Kraynik, A. M.: Linear elastic behavior of a low-density Kelvin foam with open cells. *J. Appl. Mech.*, **64**:787–794. 1997.
- [116] Williams, R. E.: Space-filling polyhedron: its relation to aggregates of soap bubbles. *Science*, **161**:276–277. 1968.
- [117] Wolfram, S.: *The Mathematica Book*. Wolfram Media/Cambridge University Press, Cambridge, 4th edn. 1999.
- [118] Young, W. C. and Budynas, R. G.: *Roark's Formulas for Stress and Strain*. McGraw-Hill, New York, NY, 7th edn. 2002.
- [119] Yu, C.-J., Dennis Claar, T., Eifert, H. H., Hall, I. W., Franz, R. E., Leighton, K. T., and Hasson, D. F.: Deformation energy absorption of metal foams at high strain rates. In: Banhart, J., Ashby, M. F., and Fleck, N. A., eds., *Metal Foams and Porous Metal Structures*, pp. 347–352. Verlag MIT, Bremen. 1999.

- [120] Zhang, J. and Ashby, M. F.: Buckling of honeycombs under in-plane biaxial stresses. *Int. J. Mech. Sci.*, **34**(6):491–509. 1992.
- [121] Zhu, H. X., Hobdell, J. R., and Windle, A. H.: Effects of cell irregularity on the elastic properties of open-cell foams. *Acta Mater.*, **48**:4893–4900. 2000.
- [122] Zhu, H. X., Hobdell, J. R., and Windle, A. H.: Effects of irregularity on the elastic properties of 2d voronoi honeycombs. *J. Mech. Phys. Solids*, **49**:857–870. 2001.
- [123] Zhu, H. X., Knott, J. F., and Mills, N. J.: Analysis of the elastic properties of open-cell foams with tetrakaidecahedral cells. *J. Mech. Phys. Solids*, **45**(3):319–343. 1997.
- [124] Zhu, H. X., Mills, N. J., and Knott, J. F.: Analysis of the high strain compression of open-cell foams. *J. Mech. Phys. Solids*, **45**(11/12):1875–1904. 1997.
- [125] Zienkiewicz, O. C. and Taylor, R. L.: *The Finite Element Method*. Butterworth-Heinemann, Oxford, UK. 2000.

Curriculum Vitae

Name : Thomas Daxner
Date of birth : March 9, 1970
Place of birth : Gmunden, Austria
Citizenship : Austrian

Education

09-1980 – 06-1988 “Bundesgymnasium” (high school) in Gmunden, Austria; graduation with honors.
10-1988 – 10-1997 Studies of Mechanical Engineering at the Vienna University of Technology, Austria (interrupted by “Zivildienst”).
06-1995 – 07-1995 IAESTE exchange student at the Laboratory of Thermal Turbo-machines, National Technical University of Athens, Greece.
10-1996 – 08-1997 “Zivildienst” (alternative civilian service) at the Arbeiter-Samariterbund Traun, Austria.
10-1997 Graduation in Mechanical Engineering at the Vienna University of Technology (Degree: Diplomingenieur).
Additional degree in Biomedical Engineering.

Professional Development

10-1997 – 07-2001 Research assistant at the ILFB; employed within the BRITE/EURAM research project EAMLIFe (“Energy Absorbing Materials for Low Impact Forces”) funded by the Commission of the European Union, and within several other projects.
since 08-2001 “Vertragsassistent” (Assistant Professor) at the ILFB.